UNIVERSITÉ DU QUÉBEC À MONTRÉAL

ÉTUDE DU MÉCANISME DE L'AUTO-ASSEMBLAGE DE L'ISLET AMYLOID POLYPEPTIDE ET DES MODULATEURS DE L'AMYLOÏDOGÉNÈSE

THÈSE
PRÉSENTÉE
COMME EXIGENCE PARTIELLE
DU DOCTORAT EN BIOCHIMIE

PAR
VO THANH PHUONG TRANG NGUYEN

NOVEMBRE 2020

UNIVERSITÉ DU QUÉBEC À MONTRÉAL
Service des bibliothèques

Avertissement

La diffusion de cette thèse se fait dans le respect des droits de son auteur, qui a signé le formulaire *Autorisation de reproduire et de diffuser un travail de recherche de cycles supérieurs* (SDU-522 – Rév.10-2015). Cette autorisation stipule que «conformément à l'article 11 du Règlement no 8 des études de cycles supérieurs, [l'auteur] concède à l'Université du Québec à Montréal une licence non exclusive d'utilisation et de publication de la totalité ou d'une partie importante de [son] travail de recherche pour des fins pédagogiques et non commerciales. Plus précisément, [l'auteur] autorise l'Université du Québec à Montréal à reproduire, diffuser, prêter, distribuer ou vendre des copies de [son] travail de recherche à des fins non commerciales sur quelque support que ce soit, y compris l'Internet. Cette licence et cette autorisation n'entraînent pas une renonciation de [la] part [de l'auteur] à [ses] droits moraux ni à [ses] droits de propriété intellectuelle. Sauf entente contraire, [l'auteur] conserve la liberté de diffuser et de commercialiser ou non ce travail dont [il] possède un exemplaire.»

REMERCIEMENTS

Tout d'abord, je tiens à remercier mon directeur de recherche, le professeur Steve Bourgault, de m'avoir donné l'opportunité d'être membre de son équipe dès le début de l'ouverture de son laboratoire. J'aimerais le remercier pour toutes ses idées, pour ses conseils judicieux et pour son soutien moral et financier tout au long de mon parcours académique à l'UQAM. Il a grandement contribué à mon récent succès. Ce fut une expérience extraordinaire et enrichissante. Il me faut également souligner la contribution considérable de mes collègues (anciens et actuels) de laboratoire, Carole Anne, Mathieu, Noé, Billel, Mathew, Ximena, Mélanie, Elizabeth, Mathilde, Guillaume, Soultan, Dominic et Laurie, pour leur soutien moral et leurs aides. Chacun d'entre vous a grandement participé à rendre mes années agréables et mémorables.

J'aimerais aussi remercier les organismes subventionnaires, le GRASP, la fondation UQÀM, le regroupement PROTEO, le centre de recherche Pharmaqam, le Conseil de recherches en sciences naturelles et en génie du Canada (CRSNG), pour leur soutien financier.

Finalement, je tiens à remercier sincèrement la famille de ma tante au Canada (chú Nghĩa, má Út et Diane) qui m'est si précieuse. Sans vous je ne serais pas où je suis aujourd'hui. À mes parents qui se sont sacrifiés pour mon avenir. J'aimerais remercier particulièrement mon amie et collègue Margaryta pour son soutien moral et ses encouragements. Enfin, un grand merci à mon copain, Hwai-Chien. Ton amour et ton soutien me sont indispensables. Merci simplement d'exister et de m'endurer jusqu'à maintenant.

TABLE DES MATIÈRES

LISTE DES FIGURES viii
LISTE DES TABLEAUX xii
LISTE DES ABRÉVIATIONS, SIGLES ET ACRONYMES xiii
RÉSUMÉ xv
CHAPITRE I INTRODUCTION 1
1.1 Maladies associées au mauvais repliement des protéines 1
1.1.1 Maladies associées à une perte de fonction biologique 3
1.1.2 Maladies associées à un gain d'une fonction toxique 4
1.2 Fibres amyloïdes 7
1.2.1 Structure et propriétés des fibres amyloïdes 7
1.2.2 Mécanisme de formation des fibres amyloïdes 11
1.2.3 Facteurs qui modulent l'auto-assemblage amyloïde 13
1.2.4 Toxicité des assemblages 17
1.2.5 Fibres amyloïdes fonctionnelles 20
1.3 Islet Amyloid Polypeptide (IAPP) 23
1.3.1 Diabète de type II et dépôts amyloïdes d'IAPP 23
1.3.2 Biosynthèse de l'IAPP 25
1.3.3 Rôles physiologiques de l'IAPP 27
1.3.4 Phylogénie de l'IAPP 31
1.3.5 Structures secondaires de l'IAPP 34
1.4 Fibres amyloïdes d'IAPP 37
1.4.1 Structure (supra)moléculaire des fibres amyloïdes d'IAPP 37
1.4.2 Mécanismes de l'auto-assemblage amyloïde de l'IAPP 41
1.5 Cytotoxicité de l'IAPP 48

1.6 Inhibiteurs et modulateurs de l'amyloïdogénèse 55
1.6.1 Stabilisation des états non-amyloïdogéniques 55
1.6.2 Inhibiteurs de la croissance des fibres amyloïdes 56
1.6.3 Inhibiteurs des interractions avec les cofacteurs de l'amyloïdogénèse 60
1.6.4 Les anticorps dirigés contre les assemblages amyloïdogéniques 60
1.7 Problématique, hypothèse et objectifs 61
1.7.1 Hypothèse 62
1.7.2 Objectifs 63
CHAPITRE II ARTICLE I: « ROLE OF SITE-SPECIFIC ASPARAGINE DEAMIDATION IN ISLET AMYLOID POLYPEPTIDE AMYLOIDOGENESIS: KEY CONTRIBUTIONS OF RESIDUES 14 AND 21 » 64
2.1 Résumé 67
2.2 Abstract 68
2.3 Introduction 69
2.4 Materials and Methods 73
2.4.1 Peptide Synthesis and Purification 73
2.4.2 IAPP Sample Preparation 74
2.4.3 Kinetics of Amyloid Formation 74
2.4.4 Circular Dichroism Spectroscopy 75
2.4.5 Transmission electron microscopy 76
2.4.6 Atomic force microscopy 76
2.4.7 Cytotoxicity Assay 77
2.5 Results 78
2.5.1 Effect of Asn Deamidation on the Kinetics of Self-Assembly 78
2.5.2 Effect of Asn Deamidation on the conformational transition 81
2.5.3 Effect of Asn Deamidation on the supramolecular architecture of amyloids 82
2.5.4 Deamidation of Asn-14 triggers amyloidogenesis by unmodified IAPP 84
2.5.5 IAPP deamidated at position 21 co-assembles into amyloid fibrils with WT-IAPP 85

2.5.6 Effect of Asn Deamidation on IAPP-mediated cytotoxicity 87
2.6 Discussion 90
2.7 Supporting Information 94
CHAPITRE III ARTICLE II: «OLIGOMER-LIKE FIBRILS: TRANSMISSIBLE PROTEOTOXIC SPECIES EXPANDING THE DIVERSITY OF AMYLOID ASSEMBLIES » 101
AVANT-PROPOS DU CHAPITRE III 103
3.1 Résumé 106
3.2 Abstract 107
3.3 Introduction 108
3.4 Materials and Methods 111
3.4.1 Synthesis, Purification and Sample preparation 111
3.4.2 Preparation of oligomers and fibrils 111
3.4.3 Kinetics of amyloid formation 112
3.4.4 Seeding experiments 113
3.4.5 Fluorescence spectroscopy (ThT and ANS) 113
3.4.6 Circular dichroism spectroscopy 113
3.4.7 Attenuated Total Reflectance-Fourier Transform Infrared Spectroscopy 114
3.4.8 Powder X-Ray Diffraction 114
3.4.9 Transmission electron microscopy 114
3.4.10 Atomic force microscopy 115
3.4.11 Solid-state nuclear magnetic resonance 115
3.4.12 Dot Blot 116
3.4.13 Cell viability 116
3.4.14 Caspase-3 activity assay 117
3.4.15 Lactate Dehydrogenase (LDH) release assay 118
3.4.16 Preparation of large unilamellar vesicles 119
3.4.17 Calcein leakage assay 119
3.4.18 Confocal microscopy 120
3.4.19 Proteinase K digestion 120

3.4.20 Statistical analysis 121
3.4.21 Data availability..... 121
3.5 Results 121
3.5.1 Shifting the toxicity of amyloid fibrils with a single N-to-Q substitution. .. 121
3.5.2 Supramolecular characterization of cytotoxic fibrils 125
3.5.3 Kinetics of self-assembly and time-resolved analysis of cytotoxicity 129
3.5.4 N21Q fibrils share conformational characteristics with prefibrillar toxic oligomers..... 132
3.5.5 N21Q fibrils disrupt plasma membrane 134
3.5.6 The oligomer-like toxic conformation of N21Q fibrils propagates to WT IAPP..... 137
3.6 Discussion 139
3.7 Supporting Information..... 143
CHAPITRE IV ARTICLE III: «LOW GENERATION ANIONIC DENDRIMERS MODULATE ISLET AMYLOID POLYPEPTIDE SELF-ASSEMBLY AND INHIBIT PANCREATIC β-CELL TOXICITY » 161
4.1 Résumé..... 164
4.2 Abstract 165
4.3 Introduction 166
4.4 Materials and Methods..... 170
4.4.1 Dendrimers synthesis, purification and characterization..... 170
4.4.2 Peptide synthesis and IAPP sample preparation 170
4.4.3 Amyloid formation monitored by thioflavin T fluorescence 171
4.4.4 Circular dichroism spectroscopy 172
4.4.5 Atomic force microscopy 173
4.4.6 Cell toxicity assay..... 173
4.5 Results and discussion..... 174
4.5.1 Synthesis of low generation dendrimers..... 174
4.5.2 Effect of low generation dendrimers on IAPP amyloid formation..... 175
4.5.3 Modulation of amyloid assembly by low generation sulfated dendrimers monitored by atomic force microscopy 180

4.5.4 Modulation of IAPP conformational transition by low generation sulfated dendrimers 182
4.5.5 Anionic low generation dendrimers inhibit IAPP-induced pancreatic β-cells toxicity. 183
4.6 Conclusion 187
4.7 Supporting Information 190
CHAPITRE V DISCUSSION GÉNÉRALE 193
CONCLUSION ET PERSPECTIVES 211
BIBLIOGRAPHIE 214
ANNEXE I 264
ANNEXE II 302

LISTE DES FIGURES

Figure		Page
1.1	Illustration schématique des conformations pouvant être adoptées par une chaîne polypeptidique suite à sa biosynthèse.	2
1.2	Organisation structurale des fibres amyloïdes.	8
1.3	Détection des dépôts amyloïdes par le rouge de Congo.	9
1.4	Détection des fibres amyloïdes par la Thioflavin T.	10
1.5	Mécanismes de formation des fibres amyloïdes.	13
1.6	Biosynthèse et maturation de l'IAPP.	26
1.7	Rôles de l'IAPP sur l'homéostasie de glucose.	28
1.8	Représentation schématique du récepteur à calcitonine et des récepteurs de l'IAPP.	30
1.9	Exemples de structures secondaires de l'IAPP.	36
1.10	Structure (supra)moléculaire des fibres amyloïdes d'IAPP.	40
1.11	Toxicité de l'IAPP en fonction du temps d'auto-assemblage.	49
1.12	Mécanismes associés à la perturbation membranaire induite l'auto-assemblage de l'IAPP.	51
1.13	Représentation schématique de l'implication de la cascade de l'amyloïdogénèse de l'IAPP dans le diabète de type 2.	53
2.1	(A) Asn deamidation via the hydrolysis of the succinimide intermediate. (B) Sequence of human IAPP with Asn residues in red bold. IAPP has a disulfide bond between Cys-2 and Cys-7 and a C-α-amidated C-terminus.	71
2.2	Effect of site-specific Asn deamidation on the kinetics of IAPP amyloid formation.	80
2.3	Effect of site-specific Asn deamidation on the conformational transition of IAPP.	82

2.4 Effect of site-specific Asn deamidation on the morphology of IAPP assemblies. 83

2.5 [N14D] IAPP accelerates unmodified IAPP amyloid formation. 85

2.6 Effect of [N21D] IAPP on unmodified IAPP amyloid formation. 87

2.7 Effect of site-specific Asn deamidation on IAPP-induced cytotoxicity 89

S2.1 Kinetics (T_{50}) of amyloid assembly of IAPP and its deamidated derivatives 92

S2.2 Figure S2.1 Kinetics (T_{50}) of amyloid assembly of IAPP and its deamidated derivatives. 94

S2.3 Effect of site-specific Asn deamidation on the conformational transition of IAPP 95

S2.4 Effect of Asn-14 deamidation on the morphology of amyloid fibrils.Kinetics of amyloid formation of fully deamidated IAPP derivatives monitored by ThT fluorescence. 96

S2.5 Effect of [N21D] IAPP and rIAPP on IAPP amyloid formation. 97

S2.6 rIAPP inhibits hIAPP amyloid formation. 98

S2.7 Effect of Asn deamidation on IAPP-induced cytotoxicity. 99

S2.8 Effect of Asn deamidation on the kinetics of IAPP-induced cytotoxicity. 100

3.1 Modulating the toxicity of IAPP fibrils with an N-to0Q substitution at position 21 123

3.2 Characterization of N21Q cytotoxic fibrils 127

3.3 SS-NMR spectra of N21Q and WT IAPP fibrils 129

3.4 Kinetics of self-assembly and time-ressolved analysis of cytotoxicity 131

3.5 N21Q fibrils exhibit oligomer-like conformation and expose residue F23 on the surface. 134

3.6 N21Q fibrils disrupt lipid vesicles and plasma membrane 136

3.7 The oligomer conformation of N21Q fibrils propagates to IAPP 138

S3.1 Cytotoxicity of IAPP and N21Q fibrils measured by the LIVE/DEAD assay 143

S3.2 Fibril toxicity over extended self-assembly periods 144

S3.3 Cytotoxicity of isolated IAPP and N21Q fibrils 145

S3.4 Thermodynamic stability of IAPP and N21Q fibrils 146

S3.5 Stability of IAPP and N21Q fibrils against proteinase K proteolysis 147

S3.6 Mean and median values of length, height and Young's modulus of IAPP and N21Q fibrils 148
S3.7 Characterization of IAPP and N21Q fibrils after lyophilization 149
S3.8 Secondary ^{13}C chemical shifts of Ala13, Phe23 and Val32 150
S3.9 Kinetics of amyloid formation 151
S3.10 Cytotoxicity and lipid membrane perturbation induced by monomers 152
S3.11 Characterization of IAPP oligomers 153
S3.12 Characterization of IAPP oligomers by ELISA 154
S3.13 TEM-immunogold labelling of IAPP and N21Q fibrils 155
S3.14 Toxicity of IAPP and N21Q assemblies on CHO K1 cells 156
S3.15 Characterization of N21Q seeds 157
S3.16 Electron microscopy images of IAPP assemblies seeded with N21Q fibrils 158
S3.17 Cytotoxicity of N21Q fibrillar seeds at low concentrations 159
S3.18 Seeding of N21Q self-assembly with IAPP amyloid fibrils 160
4.1 Primary structure of human IAPP and chemical structures of surface low generation dendrimers used in the present study. 169
4.2 Effects of low generation dendrimers on IAPP amyloid fibril formation monitored by ThT fluorescence. 176
4.3 Low generation sulfated dendrimers modulate IAPP amyloid fibril formation. 181
4.4 Conformational transition of IAPP modulated by low generation sulfonated dendrimers. 183
4.5 Inhibition of IAPP-induced cytotoxicity on β-pancreatic cells by low generation dendrimers. 185
S4.1 Effects of polyhydroxyl low generation dendrimers on IAPP amyloid fibril formation monitored by ThT fluorescence. 190
S4.2 Effect of polyamine G1 dendrimer on IAPP amyloid fibril formation monitored by ThT fluorescence. 190
S4.3 Effect of the glycosaminoglycan mimetic, eprodisate (sodium propane-1,3-disulfonate) on IAPP amyloid fibril formation monitored by ThT fluorescence. 191

S4.4 Concentration-effect of IAPP on the viability of INS-1 pancreatic β-cells..... 192

5.1 Distribution électrostatique impliquant les résidus Arg-11, Ans-14 et His-18 lorsque l'IAPP adopte sa conformation secondaire en hélice-α..... 198

5.2 Acides aminés (naturels et non naturels) ainsi que leur chaîne latérale utilisée dans notre étude. 202

5.3 Représentation hypothétique du diagramme d'énergie de l'auto-assemblage de l'IAPP et des différents dérivés..... 204

5.4 Structure des fibres du variant N21Q analysée par cryo-EM..... 208

LISTE DES TABLEAUX

Tableau		Page
1.1	Exemples de maladies associées à une perte de fonction biologique en lien avec un mauvais repliement protéique.	3
1.2	Exemples de maladies associées à un gain d'une fonction toxique et protéine majeure des dépôts insolubles.	6
1.3	Facteurs pouvant affectant la formation des fibres amyloïdes.	16
1.4	Exemples d'assemblages amyloïdes fonctionnels.	22
1.5	Séquence primaire des peptides de la famille de la calcitonine.	29
1.6	Séquence primaire d'IAPP de différentes espèces.	34
1.7	Effets de substitutions de la séquence de l'IAPP sur l'auto-assemblage amyloïde.	45
1.8	Exemples de molécules pouvant inhiber la formation de fibres amyloïdes d'IAPP.	57
4.1	Effects of low generation G0 and G1 dendrimers on IAPP amyloid formation.	177

LISTE DES ABRÉVIATIONS, SIGLES ET ACRONYMES

ACN	Acétonitrile
AFM	Microscopie à force atomique
AM	Adrénomudélline
ANS	Acide 8-anilino-1-naphtalènesulfonique
Aβ	Amyloïde-β
CD	Spectroscopie de dichroïsme circulaire
CFTR	Régulateur de conductance transmembranaire de la fibrose kystique
CGRP	Peptides associés aux gènes de la calcitonine (*calcitonin-gene-related peptide*)
CR	Rouge de Congo
CT	Calcitonine
CTR	Récepteur de calcitonine
DMSO	Dimethyl sulfoxide
DOPC	1 2-dioleoyl-sn-glycero-3-phosphocholine
DOPG	1,2-Dioleoyl-sn-glycero-3-phospho-rac-(1-glycerol)
DPPC	1,2-Dipalmitoyl-sn-glycero-3-phosphocholine
DPPG	1,2-Dipalmitoyl-sn-glycero-3-phospho-rac-(1-glycerol)
EDT	Éthanedithiol
EGCG	(-)-épigallocatéchine gallate
EPR	Résonnance paramagnétique électronique
FlAsH	Fluorogenic probe fluorescein arsenical hairpin
FTIR	Spectroscopie infrarouge à transformée de Fourrier
GAGs	Glycosaminoglycanes

GPCRs	Récepteurs couplés aux protéines G
HCTU	2-(6-chloro-1-H-benzotriazole-1-yl)-1,1,3,3-tetramethylaminium hexafluorophosphate
HFIP	Hexafluoroisopropanol
IAPP	Islet amyloid polypeptide
IDP	Peptide intrinsèquement désordonné
NEPTMs	Modifications post-traductionnelles non enzymatiques
POPC	1-palmitoyl-2-oleoyl-glycero-3-phosphocholine
POPS	1-palmitoyl-2-oleoyl-glycero-3-phospho-L-serine
RAMPs	Protéines modifiant l'activité des récepteurs (*receptor activity-modifying proteins*)
RE	Réticulum endoplasmique
rIAPP	IAPP de rat
RP-HPLC	Chromatographie liquide à haute performance à phase inverse
SDS	Dodécylsulfate de sodium
ssRMN	Résonance magnétique nucléaire à l'état solide
T2DM	Diabète de type 2
TEM	Microscopie électronique à transmission
TFA	Acide trifluoroacéttique
TFE	Trifluroéthanol
ThT	Thioflavine-T
WT	Type sauvage, wild-type
XRD	Diffraction des rayons X
α-syn	α-synucléine

RÉSUMÉ

Le mauvais repliement et l'auto-assemblage des peptides et protéines en fibres amyloïdes insolubles sont intrinsèquement associés à un large éventail de maladies, notamment la maladie d'Alzheimer et le diabète de type II (T2DM). Bien que les dépôts amyloïdes aient été caractérisés il y a plus d'un siècle, la structure précise des espèces protéiques provoquant la mort cellulaire et la dégénérescence tissulaire demeure encore inconnue. L'objectif de ce projet de thèse consiste à élucider les déterminants moléculaires modulant l'auto-assemblage amyloïde de l'*islet amyloid polypeptide* (IAPP) afin de mieux comprendre les caractéristiques physicochimiques et conformationnels de ce processus et d'identifier les espèces quaternaires cytotoxiques. L'agrégation de l'IAPP, une hormone peptidique composée de 37 résidus, et son dépôt subséquent sous forme d'amyloïdes insolubles dans les îlots pancréatiques sont associés à la progression du T2DM. Premièrement, nous avons évalué l'effet de la désamidation de l'asparagine, une modification post-traductionnelle non-enzymatique, sur l'amyloïdogénèse de l'IAPP et la toxicité sous-jacente. À cet égard, en combinant des analyses biophysiques à l'étude cinétique de l'auto-assemblage, nous avons observé que la conversion de l'Asn en Asp ou en isoAsp a un faible impact sur les positions 22, 31 et 35. Nos résultats exposent des contributions clés des résidus Asn aux position 14 et 21 dans le processus de d'auto-assemblage de l'IAPP. Cette première étude a permis de cibler l'Asn-21 afin de déterminer les protagonistes moléculaires et conformationnels associés à la cytotoxicité du peptide. Deuxièmement, en modifiant sélectivement la position Asn21, nous avons identifié de nouvelles conformations quaternaires cytotoxiques et révélé le rôle de charnière moléculaire joué par cette position. Notamment, la substitution de l'Asn21 par une Gln (N21Q) a conduit à la formation de fibres amyloïdes hautement toxiques avec des caractéristiques prototypiques des oligomères cytotoxiques, incluant une faible affinité envers la sonde thioflavine-T, une hydrophobicité de surface élevée, une grande flexibilité et la présence d'un épitope conformationnel reconnu par l'anticorps anti-oligomère A11. Les propriétés oligomériques des nanofilaments de N21Q, qui sont préservés lors de l'allongement des fibres, sont transmissibles à l'IAPP sauvage. L'identification de fibres cytotoxiques matures avec des caractéristiques oligomériques élargit la diversité et la complexité des amyloïdes et ces assemblages *oligomer-like* stables représentent une occasion unique d'élucider les caractéristiques structurales associées aux pathologies amyloïdes. Troisièmement, nous avons développé de nouveaux échafaudages moléculaires flexibles, soit des dendrimères de faible génération, afin de moduler le

large ensemble conformationnel et l'amyloïdogénèse de l'IAPP. En outre, les dendrimères polysulfatés de génération G0 inhibent la formation d'amyloïde, tandis que les G1 accélèrent considérablement l'auto-assemblage de l'IAPP en longues fibres amyloïdes. Ces dendrimères polysulfatés G0 et G1 protègent les cellules β-pancréatiques contre la toxicité induite par l'IAPP. Ces résultats mettent en évidence que l'inhibition de la conversion structurale secondaire et l'accélération de la formation de fibres amyloïdes constituent des stratégies thérapeutiques prometteuses afin de réduire la toxicité pancréatique associée aux amyloïdes. Dans son ensemble, cette thèse ouvre de nouvelles perspectives mécanistiques supportant la conception de composés nanomoléculaires pour manipuler l'auto-assemblage de peptides amyloïdogéniques nativement désordonnés.

Mots-clés : islet amyloid polypeptide, fibres amyloïdes, auto-assemblage, oligomères, cytotoxicité, désamidation d'asparagine, dendrimères.

.

CHAPITRE I

INTRODUCTION

1.1 Maladies associées au mauvais repliement des protéines

Le repliement des protéines en une structure tridimensionnelle précise est crucial pour leurs fonctions biologiques. L'ensemble de ce processus est finement régulé par un réseau complexe constitué de protéines chaperonnes et autres protéines auxiliaires au repliement (Alexandrescu, 2005 ; Chaudhuri et Paul, 2006; Lindquist et Kelly, 2011 ; Yang *et al.*, 2016) (Figure 1.1). Nonobstant un contrôle strict de ce réseau, de nombreuses protéines n'arrivent pas à atteindre ou à maintenir leur(s) conformation(s) native(s). Lorsque les protéines dénaturées ou mal repliées ne peuvent pas être repliées convenablement par les protéines chaperonnes, elles sont généralement redirigées vers le protéasome ou les lysosomes pour dégradation (Figure 1.1). Parfois, certaines protéines mal repliées peuvent échapper au processus de dégradation et ceci peut mener à des complications pathologiques. En effet, de nombreuses maladies sont associées au mauvais repliement des protéines. Ces maladies peuvent être définies soit comme une perte de fonction biologique (*loss-of-function*) ou un gain d'une fonction toxique (*gain-of-toxic-function*) (Herczenik et Gebbink, 2008).

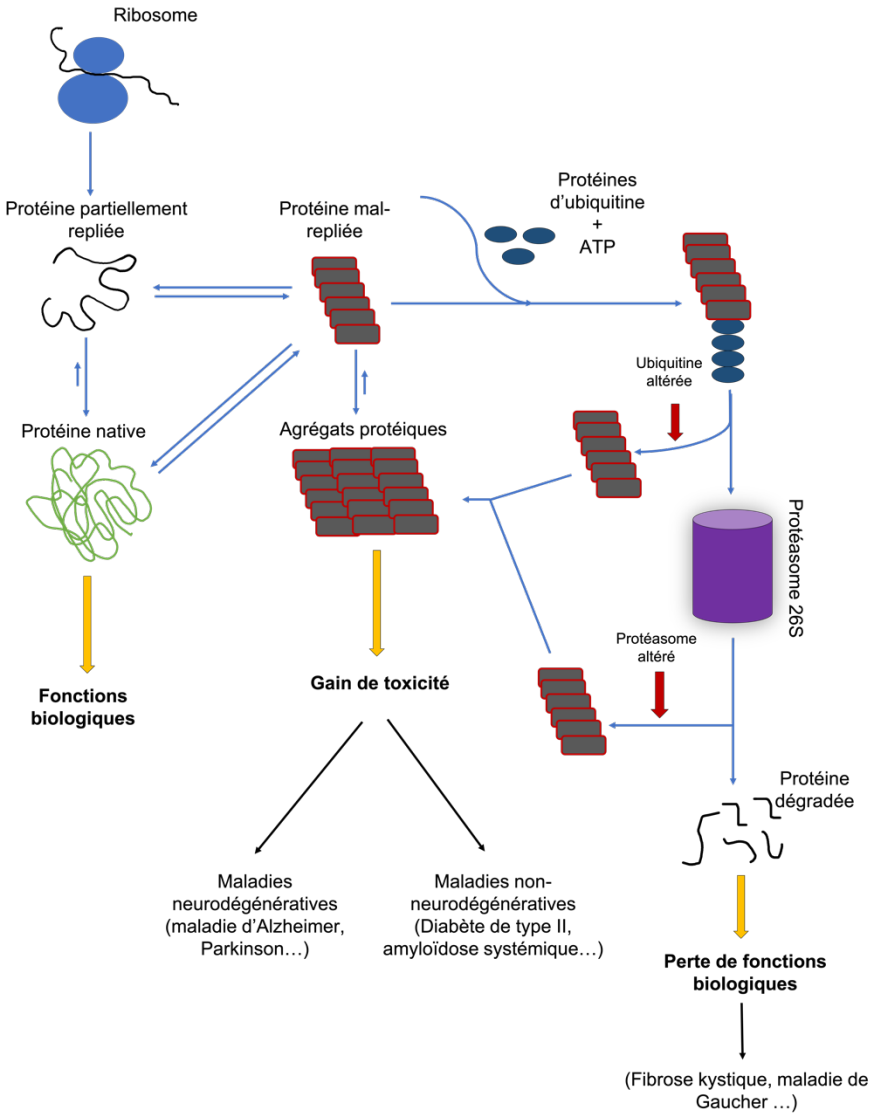


Figure 1.1 Illustration schématique des conformations pouvant être adoptées par une chaîne polypeptidique suite à sa biosynthèse.

Toutes les conformations et leurs interconversions sont soigneusement régulées dans l'environnement biologique au moyen du réseau de chaperonnes et de protéases. La chaîne polypeptidique nouvellement synthétisée est convertie en protéine native qui peut alors exercer ses fonctions biologiques. Le mauvais repliement de protéines peut être associé à une perte de fonction biologique ou un gain d'une fonction toxique. L'agrégation des protéines peut entraîner la formation de fibres amyloïdes, de dépôts de type natif ou de dépôts amorphes, qui sont associés à des états pathologiques lorsqu'ils se forment de manière incontrôlée. Figure adaptée de (Chaudhuri et Paul, 2006).

1.1.1 Maladies associées à une perte de fonction biologique

Les maladies associées à une perte de fonction sont généralement causées par des mutations qui affectent le repliement des protéines. Ainsi, les protéines affectées par la mutation sont dégradées de façon excessive, ce qui provoque une perte de leur(s) fonction(s) biologique(s) et conduit à des physiopathologies (Figure 1.1). La mucoviscidose, également connue sous le nom fibrose kystique en est un exemple. Cette maladie autosomique récessive affecte plusieurs organes, dont les poumons qui sont gravement atteints (Rafeeq et Murad, 2017). La fibrose kystique est causée par une, ou quelques, mutation(s) du gène codant pour la protéine de régulateur de conductance transmembranaire de la fibrose kystique (CFTR). Cette protéine membranaire est responsable du transport du chlorure et de l'eau à travers les cellules productrices de mucus. Une dégradation excessive de cette protéine associée à son mauvais repliement affecte les activités des canaux chlorure et sodium des épithéliums. Ceci résulte en un mucus épais et collant, obstruant ainsi les voies pulmonaires et entraînant de graves infections pulmonaires (Griese *et al.*, 2008; Rafeeq et Murad, 2017). D'autres exemples de maladies associées à une perte de fonction biologique sont présentés dans le tableau 1.1.

Tableau 1.1 Exemples de maladies associées à une perte de fonction biologique en lien avec un mauvais repliement protéique.

Maladie	Protéine associée	Référence
Fibrose kystique	CFTR	(Rafeeq et Murad, 2017)
Maladie de Gaucher	Glucocérébrosidase	(Aerts *et al.*, 2019)

Hypogonadisme hypogonadotrope	Hormone de libération de gonadotrophine hypothalamique (GnRH)	(Stamou et Georgopoulos, 2018)
Diabète insipide néphrogénique	Récepteur de l'arginine vasopressine (AVPR2)	(Christ-Crain *et al.*, 2019)
Maladie pulmonaire obstructive chronique	α-1-antitrypsine	(Silverman *et al.*, 2013; Vignaud *et al.*, 2015)
Maladie de Fabry	α-galactosidase	(Chan et Adam, 2018)
Rétinite pigmentaire	Rhodopsine	(Sudharsan et Beltran, 2019)

1.1.2 Maladies associées à un gain d'une fonction toxique

Les maladies associées à un gain de fonction toxique surviennent lorsqu'une protéine mal repliée change de conformations secondaire, tertiaire et/ou quaternaire et s'agrège. Ceci conduit à la formation d'oligomères, de protofilaments, de fibres amyloïdes et/ou de corps d'inclusions, qui nuit à la fonction cellulaire et tissulaire (Figure 1.1). Ces maladies peuvent être divisées en deux principaux groupes : les neurodégénératives et les non-neurodégénératives, ce dernier groupe incluant les amyloïdoses systémiques et les amyloïdoses localisées (Tableau 1.2) (Chiti et Dobson, 2017).

Les maladies neurodégénératives ont été les premières maladies identifiées associées au mauvais repliement. La maladie d'Alzheimer est l'exemple le plus connu de ce type de maladie neurodégénérative, affichant une prévalence élevée chez les personnes âgées. Chez les patients atteints de la maladie d'Alzheimer, des agrégats protéiques insolubles formés principalement du peptide amyloïde-β s'accumulent et forment des plaques séniles dans le cerveau. Selon l'hypothèse de la cascade amyloïde, qui a été introduite pour la première fois en 1991 par John Hardy et David Allsop (Hardy et

Allsop, 1991), le peptide amyloïde-β, résultant du clivage de la protéine précurseur amyloïde (APP) par des β- et γ-sécrétases, subi divers changements conformationnels et s'agrège en assemblages de protéines de haut poids moléculaire, ce qui provoque une neurotoxicité (Greenberg *et al.*, 2020).

Les amyloïdoses sont un groupe de maladies non-neurodégénératives associées au mauvais repliement des protéines, dans lesquelles les agrégats de protéines s'accumulent de façon systémique ou locale dans certains organes ou tissus (tableau 1.2). L'amyloïdose systémique la plus répandue est l'amyloïdose systémique primaire, dans laquelle les chaînes légères d'immunoglobulines, ou des fragments de celles-ci, qui sont produites par les plasmocytes, forment des amyloïdes. Ces dépôts amyloïdes s'accumulent dans pratiquement tous les organes du corps, induisant diverses complications, incluant des insuffisances cardiaques congestives et rénales, de l'hépatosplénomégalie, des neuropathies et des lésions cutanées (Merlini *et al.*, 2018). Le diagnostic de cette maladie est assez difficile : elle nécessite une analyse histologique et la caractérisation du clone plasmocytaire sous-jacent (Martinez-Naharro *et al.*, 2020). Dans d'autres maladies, les dépôts protéiques peuvent être localisés dans un organe particulier, on parle alors d'amyloïdose localisée. Les symptômes apparaissent comme le résultat d'un dommage progressif de l'organe affecté, par exemple le diabète de type II ou la cataracte dans lesquels le pancréas et l'œil sont respectivement affectés (Herczenik et Gebbink, 2008). À l'exception des amyloïdoses à la transthyrétine, aucune thérapie efficace n'est disponible pour les maladies associées aux dépôts amyloïdes (Zaman *et al.*, 2019).

Certaines de ces maladies sont associées à la fois à un gain d'une fonction toxicité et à une perte de fonction biologique, telles que la maladie de Parkinson ou le diabète de type II (Silverman *et al.*, 2013; Winklhofer *et al.*, 2008). De plus, les dépôts protéiques retrouvés dans les tissus des patients sont principalement sous forme d'agrégats fibrillaires, connus sous le nom de fibres amyloïdes (Benson *et al.*, 2018).

Tableau 1.2 Exemples de maladies associées à un gain d'une fonction toxique et protéine majeure des dépôts insolubles.

Maladie	Protéine associée	Organes affectés	Référence
Maladies neurodégénératives			
Maladie d'Alzheimer	Amyloïde-β (Aβ)	Cerveau	(Murphy et LeVine, 2010)
Maladie de Parkinson	α-synucléine dans les corps de Lewy	Cerveau	(Mehra *et al.*, 2019)
Maladie de Huntington	Huntingtine dans les corps de Huntington	Cerveau	(Wyant *et al.*, 2017)
Encéphalopathie spongiforme	Prion	Cerveau, système nerveux périphérique	(Casalone et Hope, 2018)
Polyneuropathie familiale amyloïde	Transthyrétine	Système nerveux périphérique	(Adams *et al.*, 2020)
Amyloïdose systémique			
Amyloïdose à chaîne légère	Chaîne légère d'immunoglobuline	La plupart des tissus	(Merlini *et al.*, 2018)
Amyloïdose systémique sénile	Transthyrétine	Microvasculature	(Coelho *et al.*, 2016)
Amyloïdose ApoAII	Apolipoprotéine AII	Cœur, rein	(Prokaeva *et al.*, 2017)
Amyloïdose liée à l'hémodialyse	β_2-microglobuline	Système ostéo-articulaire	(Scarpioni *et al.*, 2016)
Amyloïdose héréditaire du lysozyme	Lysozyme	Foie, rein	(Pleyer *et al.*, 2015)
Amyloïdose localisée			
Diabète de type II	Islet amyloid polypeptide (IAPP)	Pancréas	(Akter *et al.*, 2016)
Cataracte	Crystalline	Oeil	(Andley, 2009)
Amyloïdose cornéenne	Lactoferrinre	Cornée	(Al-Shehah *et al.*, 2010)
Cancer médullaire de la thyroïde	Calcitonine	Thyroïde	(Pacini *et al.*, 2010)

1.2 Fibres amyloïdes

1.2.1 Structure et propriétés des fibres amyloïdes

Les fibres amyloïdes, qu'elles soient extraites de patients ou assemblées *in vitro*, sont sous forme de filaments non-ramifiés affichant un diamètre d'environ 7 à 13 nm et une longueur pouvant atteindre le micromètre, comme observé par microscopie électronique à transmission (TEM) (Figure 1.2A) ou par la microscopie à force atomique (AFM) (Nguyen *et al.*, 2015; Paravastu *et al.*, 2008 ; Tycko et Wickner, 2013). Initialement détecté par la diffraction des rayons X, et plus récemment par la spectroscopie infrarouge à transformée de Fourrier (FTIR) et par résonnance magnétique nucléaire à l'état solide (ssRMN), ces fibres présentent une structure quaternaire en feuillets-β-croisés, dans laquelle les brins-β des monomères sont orientés perpendiculairement à l'axe de la fibre et sont assemblés en feuillets β qui s'étendent sur la longueur de fibre. Une distance inter-brin de 4.7 Å et une distance inter-feuillet de 10 Å sont caractéristiques de ces assemblages (Figure 1.2B) (Eanes et Glenner, 1968; Eisenberg et Jucker, 2012 ; Paravastu *et al.*, 2008 ; Sunde et Blake, 1997; Zandomeneghi *et al.*, 2004). L'organisation des brins-β peut être parallèle (Chan *et al.*, 2005; Ladner *et al.*, 2010) ou antiparallèle (Cerf *et al.*, 2009; Okada *et al.*, 2019; Xu *et al.*, 2016) et ces derniers sont stabilisés par des contacts intermoléculaires, et plus particulièrement par un dense réseau de ponts hydrogène impliquant les groupements amine (N-H) et carbonyle (C=O) du squelette peptidique (Figure 1.2C). Quant à l'arrangement inter-feuillet, il est stabilisé par diverses interactions intermoléculaires, impliquant les chaînes latérales des acides aminés, telles que des interactions hydrophobes ou électrostatiques, des liaisons hydrogène, des forces de Van der Waals et/ou des empilements π-π.

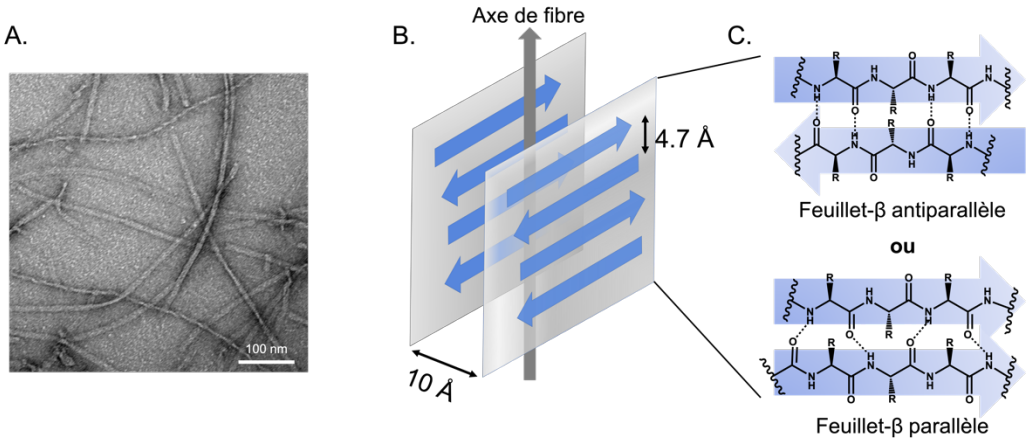


Figure 1.2 Organisation structurale des fibres amyloïdes.

A. Image en microscopie électronique à transmission représentative des fibres amyloïdes d'IAPP préparées in vitro. B. Représentation schématique de la structure quaternaire en feuillets-β-croisés, dans laquelle les brins β sont orientés perpendiculairement à l'axe des fibres et sont assemblés en feuillets-β qui s'étendent sur toute la longueur des fibres. C. L'organisation des brins-β dans un feuillet peut être antiparallèle ou parallèle et ces derniers sont stabilisés par des contacts intermoléculaires, plus particulièrement des ponts hydrogène.

Cette organisation supramoléculaire peut être détectée par des sondes fluorescentes, telles que le rouge de Congo (CR), la thioflavine-T (ThT) ou leurs dérivés (Nilsson, 2004).

Encore de nos jours, la détection histopathologique de la présence des amyloïdes dans des coupes tissulaires est effectuée à l'aide du rouge de Congo (CR), un colorant pourpre utilisé dans l'industrie du textile. Le CR est connu pour sa biréfringence en couleur vert pomme lorsqu'il interagit avec des agrégats amyloïdes sous la lumière polarisée (Figure 1.3). Malheureusement, le processus de coloration au rouge Congo est laborieux et nécessite plusieurs étapes de lavage, conduisant à une faible reproductibilité (Howie *et al.*, 2008).

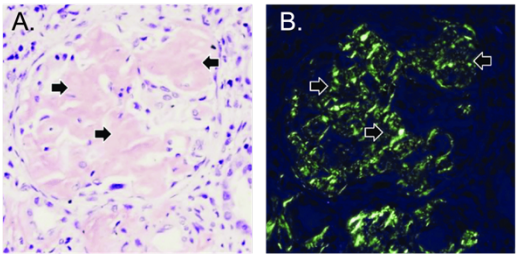


Figure 1.3 Détection des dépôts amyloïdes par le rouge de Congo.

A. Une microphotographie démontrant l'accumulation d'Apolipoprotéine AII (flèches) dans un glomérule rénal. B. Microscopie polarisante révélant une biréfringence vert pomme des dépôts amyloïdes (flèches). Figure adaptée de (Nayer, 2014).

En 1959, Vassar et Culling ont démontré le potentiel de la microscopie à fluorescence pour le diagnostic des fibres amyloïdes. Ils ont été les premiers à décrire l'utilisation du colorant benzathiole thioflavine-T comme marqueur fluorescent puissant de l'amyloïde en histologie (Kelenyi, 1967; Vassar et Culling, 1959). Les recherches menées à la fin des années 1980 et au début des années 1990 ont élargi la gamme d'applications de la ThT, de l'histologie à la caractérisation *in vitro.* Les groupes de recherche de Naiki et de LeVine ont été parmi les premiers à caractériser en profondeur les spectres de fluorescence et les propriétés de liaison du ThT aux structures amyloïdes (LeVine, 1995 ; LeVine, 1993; LeVine, 1997; Naiki *et al.*, 1989 ; Naiki *et al.*, 1990 ; Naiki *et al.*, 1991). Ils ont démontré que, lors de la liaison aux fibres amyloïdes, la ThT présente un décalage significatif du maximum d'excitation (de 385 nm à 450 nm) et du maximum d'émission (de 445 nm à 482 nm) et que la fluorescence de la ThT ne provient que de la sonde liée aux agrégats amyloïdes (LeVine, 1993; Naiki *et al.*, 1989). Ce décalage drastique de la fluorescence de la ThT résulte de l'immobilisation sélective d'un sous-ensemble de conformères de ThT (Dzwolak et Pecul, 2005; Loksztejn et Dzwolak, 2008). En effet, la ThT se comporte comme un *molecular rotor*. En solution, les anneaux de benzylamine et de benzathiole de ThT tournent librement autour de leur

liaison carbone-carbone partagée (Figure 1.4A). Cette rotation éteint rapidement les états excités générés par l'excitation des photons, provoquant une faible émission de fluorescence pour la ThT libre (Figure 1.4B). En revanche, l'immobilisation de la rotation interne de la ThT préserve l'état excité, résultant en un rendement quantique élevé de fluorescence (Stsiapura *et al.*, 2007). De la même manière, les fibres amyloïdes sont susceptibles de présenter un site de liaison à la ThT qui restreint stériquement le pouvoir rotatif de la sonde, conduisant ainsi à une augmentation marquée de la fluorescence du ThT (Figure 1.4B) (Voropai *et al.*, 2003). La ThT est un des outils d'évaluation les plus couramment utilisés pour détecter la formation des fibres amyloïdes. De plus, elle est utilisée pour étudier une grande variété d'amyloïdes telles que l'Aβ, l'insuline, l'α- synucleine, *etc*. (Aliyan *et al.*, 2019).

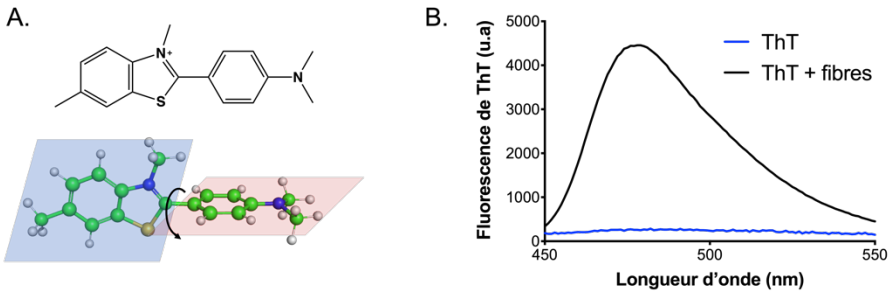


Figure 1.4 Détection des fibres amyloïdes par la Thioflavin T.

A. Structure moléculaire de la ThT (en haut) et représentation planaire de la ThT dont la rotation mutuelle définit la chiralité (en bas). B. Spectre d'émission de fluorescence de ThT caractéristique lors de la liaison avec les fibres amyloïdes suite à une excitation à 440 nm.

En résumé, pour qu'un assemblage protéique soit identifié comme une structure amyloïde, il doit afficher une morphologie fibrillaire non ramifiée, une structure

quaternaire β-croisée et des propriétés de liaison à des sondes/colorants caractéristiques.

1.2.2 Mécanisme de formation des fibres amyloïdes

Le processus de formation de fibre amyloïde est couramment suivi par la fluorescence de la sonde ThT. Une cinétique sigmoïdale peut alors être observée et celle-ci présente trois phases : (*i*) une phase de latence, (*ii*) une phase de croissance et (*iii*) une phase de saturation (Arosio *et al.*, 2015; Knowles *et al.*, 2014). Une multitude d'études ont suggéré plusieurs modèles décrivant le mécanisme d'amyloïdogénèse de peptides/protéines. Un de ces modèles consiste à la polymérisation nucléée. Ce mécanisme est dirigé par des monomères qui sont intrinsèquement, ou partiellement, désordonnés et qui forment des noyaux protéiques compétents, plus susceptibles de former des fibres par un processus thermodynamique défavorable qui a lieu lors de la phase de latence. Par la suite, les fibres se développent rapidement à partir de ces noyaux compétents grâce à l'addition de monomères ou d'oligomères (Figure 1.5). Dans ce modèle, le taux d'addition de monomères au noyau est plus rapide que celui de la libération des monomères. Il a été suggéré que ces noyaux étaient des espèces ayant une conformation relativement bien définie et capable de s'agréger rapidement (Morris *et al.*, 2013). Ce modèle de polymérisation nucléée a été utilisé pour décrire le mécanisme de formation des fibres formées des séquences poly-Q (Bhattacharyya *et al.*, 2005) ainsi que l'insuline (Pease *et al.*, 2010).

D'autres mécanismes de formation des fibres amyloïdes ont été proposés, dont la polymérisation nucléée par conversion conformationnelle (Chiti et Dobson, 2017). Ce modèle est de plus en plus accepté par la communauté scientifique pour décrire la formation de fibres amyloïdes pour de nombreuses protéines, comme Sup35 (Serio *et*

al., 2000) et IAPP (Wei *et al.*, 2011). Selon ce modèle, les monomères s'auto-assemblent rapidement en oligomères non structurés dont la conformation et le niveau d'assemblage demeurent difficiles à définir. Ces assemblages initiaux peuvent ensuite subir une réorganisation structurale pour générer des noyaux compétents pour la croissance des fibres, et sur lesquels d'autres oligomères et/ou monomères s'additionnent, conduisant éventuellement à la formation de fibres amyloïdes (Figure 1.5). Dans ce modèle, l'étape limitante est la conversion conformationnelle des oligomères non définis en noyaux compétents pour la croissance des fibres amyloïdes (Chiti et Dobson, 2017). Il est à noter que pour une protéine donnée, le mécanisme de formation des fibres pourrait être décrit par plus d'un modèle. Par exemple, la formation des fibres d'Aβ, d'α-synucléine et des protéines de Prion peuvent être décrites à la fois par la polymérisation nucléée (Jarrett *et al.*, 1993; Masel *et al.*, 1999; Uversky *et al.*, 2001) et par la polymérisation nucléée par conversion conformationnelle (Almstedt *et al.*, 2009; Cremades *et al.*, 2012 ; Fu *et al.*, 2015).

Dans le cas des protéines globulaires, il a été suggéré que l'agrégation des protéines débute par l'exposition au solvant de segments favorisant l'agrégation, et qui sont normalement enfouis dans la conformation native. La structure acquiert une certaine flexibilité et déclenche la formation d'agrégats de type quasi natif, qui se transforment ensuite en amyloïde (Chiti et Dobson, 2009; Chiti et Dobson, 2017). La formation des fibres amyloïdes de β2-microglobuline (Eakin *et al.*, 2004 ; Eakin *et al.*, 2006) et de la transthyrétine (Lim *et al.*, 2016; Olofsson *et al.*, 2004) sont des exemples de ce mécanisme d'agrégation.

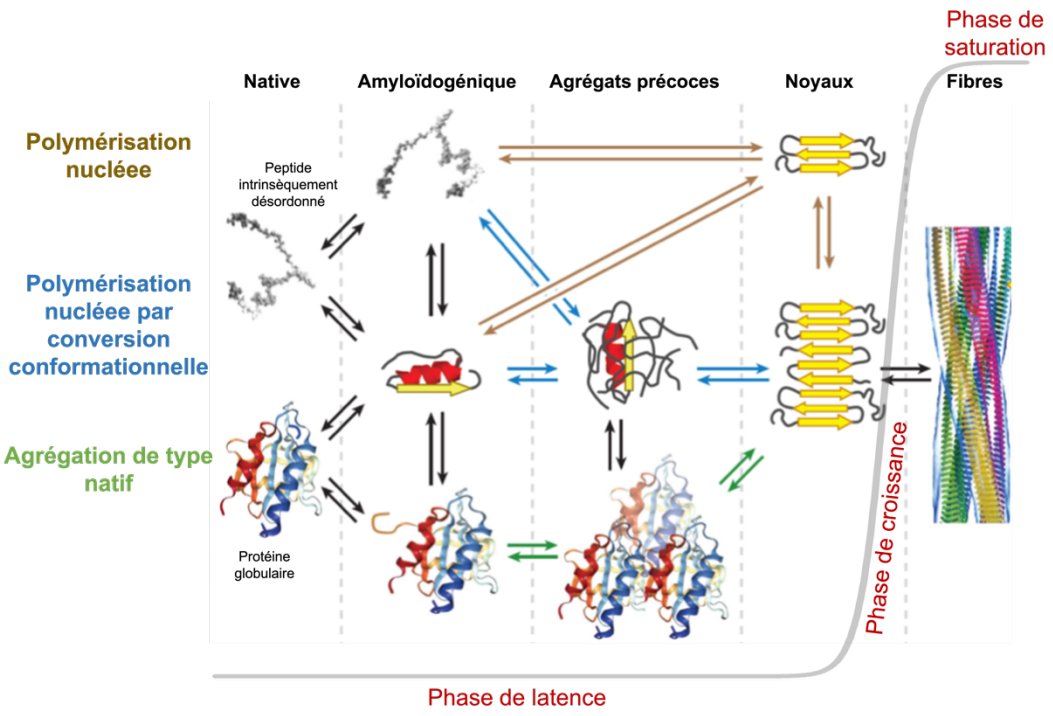


Figure 1.5 Mécanismes de formation des fibres amyloïdes.

Une cinétique sigmoïdale (courbe grise) est fréquemment observée et révèle trois phases : phase de latence, phase de croissance et phase de saturation. Trois voies de formation des fibres amyloïdes sont proposées : (1) Polymérisation nucléée (voie marron) ; (2) Polymérisation nucléée par conversion conformationnelle (voie bleue) et (3) Agrégation de type quasi natif (voie verte). Les flèches noires représentent la voie commune des trois mécanismes de formation des fibres. Figure adaptée de (Chiti et Dobson, 2017).

1.2.3 Facteurs qui modulent l'auto-assemblage amyloïde

Le mauvais repliement des protéines conduisant à la formation des fibres amyloïdes est fortement influencé par la séquence primaire du précurseur monomérique (Morris *et al.*, 2013). En outre, de nombreuses mutations ont été identifiées comme élément déclencheur du processus d'auto-assemblage amyloïde (Hunter et Brayne, 2018; Wu

et al., 2012). Par exemple, la mutation V30M de la transthyrétine, dont l'agrégation en fibres amyloïdes est responsable de la polyneuropathie familiale amyloïde, a été identifiée chez les patients dans les régions endémiques (Portugal, Suède, Japon) (Parman *et al.*, 2016; Ueda *et al.*, 2018; Zhen *et al.*, 2015). D'autres mutations de la protéine transthyrétine ont été aussi identifiées chez les patients de différentes régions, incluant la T60A dans la population d'origine irlandaise, la E89Q en Bulgarie, la S50R au Mexique, la F64L en Sicile, la S77Y et S77P en France et l'A97S à Taiwan (Adams *et al.*, 2019). Également, les fibres amyloïdes extraites du cœur d'un patient âgé avec une amyloïdose cardiaque étaient composées de TTR avec une substitution d'isoleucine par la valine en position 122 (V122I). En effet, l'ADN du sujet a démontré que cette substitution était due à une transition C → G. D'autres mutations associées aux autres types d'amyloïdoses sont présentées dans Tableau 1.3. L'agrégation et la formation de fibres amyloïdes dépendent également des conditions externes à la protéine. D'ailleurs, il a été rapporté que les ions métalliques peuvent moduler l'agrégation des polypeptides amyloïdogéniques, tels que le peptide Aβ et la protéine tau. Il a été démontré que des ions métalliques présents dans le milieu extracellulaire comme Zn^{2+}, Cu^{2+}, Fe^{3+}, Mn^{2+}, Pb^{2+}, Cd^{2+}, Hg^{2+} et Al^{3+} promeuvent la fibrillation de l'Aβ. En revanche, les ions Mg^{2+}, Fe^{2+} et Li^{+} réduisent la formation des fibres d'Aβ. En outre, l'agrégation de la protéine tau hyperphosphorylée en enchevêtrements neurofibrillaires est favorisée par les ions Zn^{2+}, Cu^{2+}, Fe^{3+}, Mn^{2+}, Pb^{2+}, Cd^{2+}, Hg^{2+} et Al^{3+}, alors que les ions Fe^{2+} et Li^{+} réduisent l'hyperphosphorylation de tau (Kim *et al.*, 2018).

La plupart des maladies associées aux dépôts amyloïdes apparaissent tard dans la vie. Le vieillissement semble favoriser la formation des fibres protéiques et jouer un rôle important dans les conditions pathologiques liées à l'agrégation protéique. Des données expérimentales ont montré le lien entre vieillissement et dépôt amyloïde dans les modèles animaux tels que C. elegans, les chiens, les souris et les chats (Cohen *et al.*, 2006 ; Head, 2013; Youssef *et al.*, 2016). Au cours de la vie humaine, une série d'altérations biologiques qui pourraient favoriser la formation de fibres se produisent.

Ces altérations incluent une baisse dans l'activité du protéasome, du lysosome et/ou des chaperonnes. Il est noté aussi qu'il y a une réduction, liée à l'âge, de l'efficacité de la machinerie cellulaire à répondre aux stress, tels que la dérégulation de l'homéostasie des ions métalliques, aux espèces oxygénées réactives, *etc*. (Annamalai *et al.*, 2017; Chiti et Dobson, 2017).

D'autre part, il a été observé que des modifications post-traductionnelles non-enzymatiques (NEPTMs) pourraient jouer un rôle clé dans la formation de fibres amyloïdes *in vitro* et *in vivo*. Ces modifications incluent la désamidation, l'oxydation, l'hyperphosporylation et la glycation (Tableau 1.3). Par exemple, il a été montré que la désamidation d'asparagine est impliquée dans la formation des fibres amyloïdes de protéines associées à la maladie d'Alzheimer et la formation de cataractes (Robinson et Robinson, 2001 ; Shimizu *et al.*, 2002 ; Shimizu *et al.*, 2005).

D'autres facteurs environnementaux peuvent moduler l'auto-assemblage de peptides amyloïdogéniques, tant *in vivo* qu'*in vitro*. Ceux-ci incluent une augmentation de la température, une modification du pH, l'agitation, une élévation du taux glycémique et/ou encore la présence d'agents oxydants (Tableau 1.3). Ces facteurs favoriseraient le mauvais repliement et/ou la dénaturation partielle des protéines, exposant ainsi au solvant les régions hydrophobes normalement enfouies dans la conformation native de la protéine (Knowles *et al.*, 2014). À cause des interactions défavorables avec le solvant, les protéines dénaturées ou partiellement repliées auraient tendance à se regrouper en formant des structures agrégées stables afin de minimiser les répulsions hydrophobiques, initiant ainsi la cascade amyloïdogénique (de Rosa *et al.*, 2014).

Tableau 1.3 Facteurs pouvant affectant la formation des fibres amyloïdes.

Facteur	Exemple de protéines impliquées	Référence
Mutations ; ΔE22 (Osaka), E22K (Italien), A21G et E22Q (Néerlandais), E22G (Arctique), D23N (Iowa), L34V (Italien)	Aβ	(Bugiani *et al.*, 2010; Hunter et Brayne, 2018; Nilsberth *et al.*, 2001; Tomiyama *et al.*, 2008 ; Wang *et al.*, 2000)
Mutations; A30P, E46K, H50Q, G51D, A53T, A53E	α-syn	(Flagmeier *et al.*, 2016; Ghosh *et al.*, 2014)
Mutation au codon-arrêt	Apolipoprotéine A-II	(Benson *et al.*, 2001; Yazaki *et al.*, 2003)
Mutation S20G (asiatique)	IAPP	(Meier *et al.*, 2016)
Hyperphosphorylation	Tau	(Gasparotto *et al.*, 2018; Owen *et al.*, 2019)
Glycation	Tau, Aβ	(Gasparotto *et al.*, 2018; Hsu *et al.*, 2019)
Oxydation	Aβ, Apolipoprotéine A-I, protéines globulaires	(Chan *et al.*, 2015 ; Gu et Viles, 2016 ; Marinelli *et al.*, 2018)
Désamidation	Crystalline, Aβ	(Sadakane et Kawahara, 2018; Srivastava *et al.*, 2017; Wang *et al.*, 2017)
Ions métalliques	Aβ, Tau, IAPP	(Ilitchev *et al.*, 2018; Kim *et al.*, 2018; Lee *et al.*, 2018)
Température	β-lactoglobuline	(Akkermans *et al.*, 2008; Zuniga *et al.*, 2010)
pH	α-syn, Aβ, IAPP	(Heneka *et al.*, 2015; Peduzzo *et al.*, 2020; Zhang *et al.*, 2020)
Agitation	β-microglobuline, IAPP	(Noji *et al.*, 2019; Sebastiao *et al.*, 2017)

1.2.4 Toxicité des assemblages

Tel que présenté à la figure 1.5, le processus de formation des fibres amyloïdes implique plusieurs conformations et la toxicité associée à ces différents assemblages demeure incomprise. Cependant, plusieurs mécanismes moléculaires toxiques dus aux assemblages (pré)amyloïdes ont été rapportés, notamment le dysfonctionnement mitochondrial (Winklhofer et Haass, 2010), la production d'espèces réactives d'oxygène (ROS) (Cheignon *et al.*, 2018; Han *et al.*, 2015 ; Uttara *et al.*, 2009), l'autophagie (Alvarez-Arellano *et al.*, 2018; Chiti et Dobson, 2017) et la perturbation de la membrane plasmique (Bauerlein *et al.*, 2017; De *et al.*, 2019 ; Ewald *et al.*, 2019; Goodchild *et al.*, 2014 ; Olzscha *et al.*, 2011).

Historiquement, les fibres amyloïdes ont été identifiées comme étant à l'origine de la mort cellulaire et de la dégénérescence des tissus atteints puisque celles-ci sont présentes uniquement chez les personnes malades (Glenner et Wong, 1984; Hardy et Allsop, 1991 ; Opie, 1901). Toutefois, de plus en plus d'évidences expérimentales et cliniques suggèrent que les espèces toxiques sont les intermédiaires oligomériques. Par exemple, la gravité du déclin cognitif chez les patients atteints de la maladie d'Alzheimer n'est pas en corrélation avec la présence de plaques amyloïdes (Nelson *et al.*, 2012), ce qui suggère que les agrégats pré-amyloïdes, voire oligomériques, sont la cause de la dégénérescence cellulaire. Conformément à ce point de vue, de nombreuses expériences *in vitro* ont montré la cytotoxicité des espèces oligomériques, y compris leur capacité intrinsèque à perturber la membrane plasmique. En effet, les oligomères du peptide amyloïde-β forment des pores affichant une structure en baril-β suite à leur insertion dans la membrane plasmique (Serra-Batiste *et al.*, 2016). De plus, une corrélation existe entre la présence d'oligomères de l'amyloïde-β liés à la membrane et l'afflux de Ca^{2+} à travers les membranes neuronales (Evangelisti *et al.*, 2016). Selon un mécanisme similaire, des oligomères d'α-synucléine entraînent également la formation

de pores perforant la bicouche lipidique (Fusco *et al.*, 2017; Tsigelny *et al.*, 2012). Cependant, les oligomères sont des assemblages protéiques transitoires, hautement hétérogènes en termes de poids moléculaire, de niveau de polymérisation et de structure, et quelques études ont rapporté une absence de toxicité. En outre, le processus de fibrillation de l'Aβ peut conduire à la formation de dimères et trimères stables qui ne sont pas toxiques pour les cellules neuronales (Chen et Glabe, 2006). Malheureusement, de par leur nature dynamique et hétérogène, les espèces oligomériques pré-fibrillaires représentent un énorme défi de caractérisation structurale et biologique. Des expériences récentes ont relancé le débat sur la question à savoir si les fibres amyloïdes contribuent à la maladie ou non (Tipping *et al.*, 2015). Notamment, des observations en cryo-TEM ont montré la présence d'inclusions intracellulaires formées à partir d'assemblage fibrillaire de poly-Q perturbant la fonction et la dynamique du réticulum endoplasmique (Bauerlein *et al.*, 2017). D'autres études employant des cellules en culture ont montré des assemblages extracellulaires de fibres du peptide Aβ interagissant avec les membranes, séquestrant les lipides et formant des inclusions tubulaires à la surface cellulaire (Han *et al.*, 2017). De plus, les études de Charidimou et *al.* ont rapporté que les fibres d'amyloïde-β induisent la mort des cellules neuronales (Charidimou *et al.*, 2017). Les effets nocifs des fibres amyloïdes sur les cellules peuvent être associés au fait que les fibres serviraient de réservoir à la libération d'oligomères (Cremades *et al.*, 2012; Lesne *et al.*, 2006 ; Martins *et al.*, 2008). En outre, les fibres matures pourraient agir comme puissants catalyseurs pour la génération des oligomères toxiques par nucléation secondaire (Arosio *et al.*, 2015 ; Cohen *et al.*, 2013 ; Gaspar *et al.*, 2017; Knowles *et al.*, 2009; Meisl *et al.*, 2014).

Malgré de nombreuses études élégantes, il demeure difficile d'identifier les espèces, parmi l'ensemble des assemblages protéiques, qui contribuent à la dégénérescence cellulaire et aux maladies associées à un gain de fonction toxique. L'élucidation progressive des propriétés conformationnelles et structurales des espèces cytotoxiques a commencé à révéler les déterminants moléculaires de ces espèces qui provoquent un

dysfonctionnement cellulaire. L'exposition de domaines hydrophobes à la surface des oligomères semble être un déterminant majeur de la toxicité induite par les oligomères. En effet, des espèces oligomères de tailles et de morphologies similaires, mais affichant des toxicités divergentes, ont été isolées et se sont révélées être différentes par leur hydrophobicité de surface, par exemple, le HypF-N (Campioni *et al.*, 2010), l'Aβ42 (Ladiwala *et al.*, 2012), l'α-syn (Cremades *et al.*, 2012) et le Sup35p (Krishnan *et al.*, 2012). De plus, des corrélations significatives ont été observées entre la toxicité de différentes formes oligomériques et l'exposition des domaines hydrophobes aux solvants, révélées grâce à l'interaction avec l'acide 8-anilino-1-naphtalènesulfonique (ANS) (Bolognesi *et al.*, 2010). De façon similaire, des protéines amyloïdogéniques exprimées dans les cellules humaines ont également induit une toxicité directement corrélée avec l'exposition des régions hydrophobes à la surface des agrégats (Olzscha *et al.*, 2011). Un autre déterminant important de la toxicité des oligomères semble être leur petite taille. Les résultats rapportés sur les assemblages de $A\beta_{(1-40)}$ et/ou $A\beta_{(1-42)}$ représentent une source importante d'informations. Notamment, différentes études ont indiqué (*i*) que les monomères, dimères et trimères de Aβ (4–14 kDa) présentent une faible toxicité (Chimon *et al.*, 2007; O'Nuallain *et al.*, 2010 ; Yang *et al.*, 2017) ; (*ii*) qu'une toxicité maximale est retrouvée avec les oligomères de petite taille (oligomères pré-fibrillaires (18–90 kDa) (Kayed *et al.*, 2007; Kayed *et al.*, 2009) ; (*iii*) que la toxicité diminue ensuite avec les oligomères de tailles élevées (oligomères fibrillaires (68-104 kDa)) (Stroud *et al.*, 2012), protofilaments annulaires (250–400 kDa) (Lasagna-Reeves *et al.*, 2011) et agrégats sphériques (670 kDa) (Hoshi *et al.*, 2003)) ; et (*iv*) que les structures fibrillaires affichent une faible toxicité (Ahmed *et al.*, 2010; Chimon *et al.*, 2007). Conformément aux caractéristiques des espèces oligomériques, une série d'oligomères d'HypF-N a été générée et étudiée. Notamment, la toxicité des oligomères corrèle de façon inversement proportionnelle à leur taille. À l'opposée, la toxicité est directement proportionnelle à leur hydrophobicité de surface (Campioni *et al.*, 2010). Une explication plausible de l'importance de la petite taille dans la toxicité des oligomères est leur coefficient de diffusion élevé, qui leur permet de diffuser plus

rapidement et d'interagir plus facilement avec les membranes cellulaires. Les espèces ayant une exposition importante de leurs régions hydrophobes afficheraient une forte capacité à altérer et s'insérer dans le milieu lipophile des membranes plasmiques (Chiti et Dobson, 2017; Fusco *et al.*, 2017).

Néanmoins, la grande variété d'espèces intermédiaires générées lors du processus d'amyloïdogenèse augmente la complexité de la caractérisation des structures cytotoxiques. En effet, des études récentes ont montré que les plus petits oligomères d'$A\beta_{(1-42)}$ sont ceux qui sont les plus puissants pour induire une perméabilité des membranes. En revanche, les oligomères de plus grande taille, mais solubles, sont ceux qui provoquent le plus efficacement une réponse inflammatoire dans les cellules gliales. Ces résultats suggéreraient qu'il pourrait exister différents mécanismes de cytotoxicité induits par différentes espèces oligomériques solubles du peptide Aβ(De *et al.*, 2019). Par ailleurs, l'équipe de recherche de Chiti a comparé six exemples d'oligomères préformés de protéines amyloïdogéniques (α-syn, Aβ, HypF-N) affichant une toxicité différente et ayant différentes compositions en feuillets-β. Les résultats ont montré l'absence de toute corrélation mesurable entre la nature de leur structure secondaire et leur toxicité cellulaire (Vivoli Vega *et al.*, 2019). En outre, il devient de plus en plus évident que la propagation des fibres ayant des caractères *prion-like* génère un certain nombre de dépôts fibrillaires qui amplifient la diversité et la complexité des dépôts amyloïdes (Aguzzi et Lakkaraju, 2016; Brettschneider *et al.*, 2015 ; Prusiner, 2013).

1.2.5 Fibres amyloïdes fonctionnelles

Bien que les fibres amyloïdes soient historiquement associées à diverses pathologies, de nombreuses protéines adoptent une conformation amyloïde afin de remplir des

fonctions biologiques essentielles, et ce, chez une grande variété d'organismes vivants. Ces assemblages protéiques sont connus en tant que fibres amyloïdes fonctionnelles (tableau 1.4). Chez l'humain, les fibres amyloïdes formées de la protéine prémélanosome-17 (PMEL17), de polypeptides dans le liquide séminal humain ou d'hormones peptidiques dans les vésicules de sécrétion constituent des exemples. La protéine PMEL17, sous conformation quaternaire amyloïde, participe au métabolisme de la mélanine. La formation des fibres de PMEL17 catalyse la formation de mélanine, la concentre et facilite son transport (Watt *et al.*, 2009 ; Watt *et al.*, 2013). Dans le liquide séminal, plusieurs fragments de la phosphatase acide prostatique (PAP, également connue sous le nom de ACPP) et des fragments de seménogéline 1 et 2 (SEM1 et SEM2) s'auto-assemblent pour former des fibres amyloïdes (Bergman *et al.*, 2016; Castellano et Shorter, 2012). Ces structures quaternaires affichent des propriétés anti-microbiennes et protègent les spermatozoïdes contre les infections. Elles servent aussi de filtre qui retient les spermatozoïdes de mauvaise qualité permettant uniquement aux plus robustes de s'échapper et fertiliser l'ovocyte (Bergman *et al.*, 2016 ; Castellano et Shorter, 2012 ; Easterhoff *et al.*, 2013 ; Roan *et al.*, 2017). En outre, il a été observé que les hormones peptidiques sont entreposées dans les granules sécrétoires à des concentrations élevées et ce, sous un état amyloïde, exposant ainsi le caractère réversible de l'amyloïdogénèse (Maji *et al.*, 2009).

Chez les bactéries, un réseau extracellulaire de fibres amyloïdes formées de protéines curli permet l'adhésion aux surfaces et l'invasion des cellules de l'hôte. Ces fibres amyloïdes fonctionnelles conduisent à l'activation du système immunitaire et échafaudent des communautés bactériennes appelées biofilms (Barnhart et Chapman, 2006; DePas et Chapman, 2012). Ces structures amyloïdes sont également associées à la virulence des infections agressives et sont, en conséquence, des cibles thérapeutiques attractives (Blanco *et al.*, 2012 ; Lo *et al.*, 2013). D'autres exemples de fibres amyloïdes fonctionnelles sont présentés dans le tableau 1.4.

Les amyloïdes fonctionnelles présentent un contraste avec les amyloïdes dites pathologiques. Nonobstant la production d'espèces potentiellement toxiques durant le processus d'assemblage des fibres amyloïdes, il est remarquable que les cellules puissent produire ces amyloïdes fonctionnelles sans souffrir des effets nocifs. Ainsi, les études sur les amyloïdes fonctionnelles peuvent ouvrir vers de nouvelles stratégies de prévention et de traitement pour les maladies associées aux dépôts d'agrégats protéiques insolubles.

Tableau 1.4 Exemples d'assemblages amyloïdes fonctionnels.

Protéine	**Fonction biologique associée**	**Organisme**	**Référence**
PMEL17	Métabolisme de la mélanine	Humain	(Chuang *et al.*, 2018 ; Watt *et al.*, 2009; Watt *et al.*, 2013)
PAP et SEM (1 et 2)	Protection des spermatozoïdes	Humain	(Bergman *et al.*, 2016; Castellano et Shorter, 2012)
Hormones peptidiques	Entreposage	Humain	(Chuang *et al.*, 2018; Maji *et al.*, 2009)
Protéines de liaison d'élément de polyadénylation cytoplasmique (CPEB3)	Contrôle la traduction des protéines	Humain	(Chuang *et al.*, 2018; Drisaldi *et al.*, 2015)
Ure2p	Régulation du catabolisme d'azote	*Saccharomyces cerevisiae*	(Baxa *et al.*, 2005)
Sup35p	Régulation de la lecture des codons d'arrêt	*S. cerevisiae*	(King *et al.*, 1997)

Curli	Formation de biofilms	*Escherichia coli, Salmonella spp.*	(Chapman *et al.*, 2002; Gebbink *et al.*, 2005)
Chaplin	Modulation de la tension de l'eau à la surface	*Streptomyces coelicolor*	(Claessen *et al.*, 2003; Gebbink *et al.*, 2005)

1.3 Islet Amyloid Polypeptide (IAPP)

1.3.1 Diabète de type II et dépôts amyloïdes d'IAPP

Le diabète est caractérisé par une hyperglycémie chronique et une altération du métabolisme des glucides. Cette élévation accrue de la glycémie est causée par une insuffisance totale ou partielle de la sécrétion d'insuline et/ou de l'action de cette hormone (Wu *et al.*, 2014). L'insuline est un peptide sécrété par les cellules-β pancréatiques et joue un rôle de régulateur du taux glycémique. Il existe deux formes de diabète, le diabète insulinodépendant (diabète de type 1, T1DM) et le diabète non insulinodépendant (diabète de type 2, T2DM). Le T1DM est une maladie métabolique caractérisée par la destruction auto-immune des cellules-β des îlots pancréatiques et de leurs fonctions sécrétoires, entraînant ainsi un déficit de production d'insuline. Quant au T2DM, la forme la plus courante du diabète (90 % à 95 % de tous les patients diabétiques) (Chen *et al.*, 2011), elle est causée principalement par la résistance à l'insuline (American Diabetes, 2015). Chez les personnes saines, lors de l'augmentation de la glycémie, l'insuline est alors sécrétée et stimule la consommation du glucose présent dans le sang par les cellules musculaires et hépatiques qui pourront ensuite l'utiliser comme source d'énergie. La sécrétion d'insuline inhibe également la

production de glucose endogène (DeFronzo, 2004; Westermark *et al.*, 2011). À l'opposé, chez les personnes atteintes du T2DM, une dérégulation de l'homéostasie du glucose est observée, ce qui mène à une hyperglycémie chronique (Thakarakkattil Narayanan Nair *et al.*, 2020). Cette dérégulation est induite par deux principaux facteurs : la résistance à l'insuline (non insulinodépendant) et la perturbation de la sécrétion d'insuline. En effet, l'hyperglycémie chronique induit la production de l'insuline en quantité importante menant à une inefficacité de l'insuline une fois liée à ses récepteurs, *c.-à-d*. la résistance à l'insuline (Kahn, 2003). Afin de compenser cette baisse d'activité de l'insuline, les cellules-β pancréatiques sécrètent davantage d'insuline et, par conséquent, cela aboutit à une surproduction d'insuline. Ce stress métabolique peut alors conduire au dysfonctionnement des cellules sécrétrices d'insuline, diminuant la sécrétion de cette dernière. Finalement, le taux de glucose dans le sang reste toujours élevé, *c.-à-d.* hyperglycémie chronique (Hebda et Miranker, 2009; Kahn, 2003 ; Roden et Shulman, 2019; Thakarakkattil Narayanan Nair *et al.*, 2020; Westermark *et al.*, 2011). Les personnes atteintes de T2DM souffrent également de complications diverses, telles que problèmes cardiovasculaires, neuropathie diabétique, néphropathie et rétinopathie (Chen *et al.*, 2011).

En 1901, une étude a décrit des dépôts fibrillaires présents dans les îlots de Langerhans du pancréas chez un patient atteint du diabète (Opie, 1901). Cependant, son importance dans cette physiopathologie a souvent été négligée, car les dépôts amyloïdes ne sont pas retrouvés chez l'ensemble des patients diabétiques (Ehrlich et Ratner, 1961; Westermark, 1972). D'autre part, la présence des dépôts protéiques pancréatiques n'est pas observée uniquement chez les diabétiques, mais l'est également chez quelques individus sains (Bell, 1959). En 1987, la principale composante protéique des dépôts amyloïdes dans les îlots pancréatiques est identifiée. La caractérisation du peptide isolé des îlots amyloïdes d'humains a conduit à l'identification d'un peptide à 37 acides aminés dont l'extrémité C-terminale est amidée, connu sous le nom d'*islet amyloïd polypeptide* (IAPP), ou amyline (Cooper *et al.*, 1987; Westermark *et al.*, 1987).

1.3.2 Biosynthèse de l'IAPP

Le gène codant pour l'IAPP est situé sur le bras court, plus précisément à la région p12.3, du chromosome 12 (Mosselman *et al.*, 1989 ; Mosselman *et al.*, 1988; Nishi *et al.*, 1989). Ce gène est composé de trois exons (104pb, 95pb et 1246pb) et deux introns (330pb et 4808pb). Le site d'initiation de la transcription a été identifié à environ 28 pb en aval d'une séquence TATAA, promoteur de type TATA. La transcription de l'exon1 mène à un ARN non codant qui sert de coiffe, alors que les exons 2 et 3 codent pour la prépro-hormone complète (Nishi *et al.*, 1989). La séquence d'IAPP mature se situe dans l'exon 3 (Höppener *et al.*, 1992) (Figure 1.6).

L'IAPP est initialement exprimé sous forme d'une prepro-hormone de 89 acides aminés, nommée preproIAPP. Ce segment inclus un peptide signal de 22 résidus qui est clivé suite à l'entrée du polypeptide dans le réticulum endoplasmique afin de former le proIAPP (Hutton, 1994) (Figure 1.6). Ce dernier subit différentes modifications post-traductionnelles dans l'appareil de Golgi et dans les vésicules sécrétoires de l'insuline (Marzban *et al.*, 2005). Le proIAPP est clivé au niveau de deux paires de résidus basiques (Lys-Arg), situées dans les domaines N-terminal et C-terminal, par les prohormones convertases PC2 et PC1/3. Des études ont démontré que, en utilisant des îlots de souris dépourvues de PC1/3 ou PC2, le proIAPP est clivé préférentiellement par la PC1/3 à son extrémité C-terminale et par la PC2 à son extrémité aminée (Marzban *et al.*, 2004; Wang *et al.*, 2001) (Figure 1.6). Après le clivage, les résidus basiques Lys et Arg subsistants en position C-terminale sont éliminés par l'action de la carboxypeptidase E (CPE). Dans le même temps, la glycine est enlevée et sert de donneur d'électrons pour l'amidation de l'extrémité C-terminale, effectuée par l'enzyme *peptidylglycine α-amidating mono-oxygenase* (PAM) (Marzban *et al.*, 2005). Le pont disulfure entre les cystéines 2 et 7 est ensuite formé afin de générer le polypeptide IAPP mature (Figure 1.6).

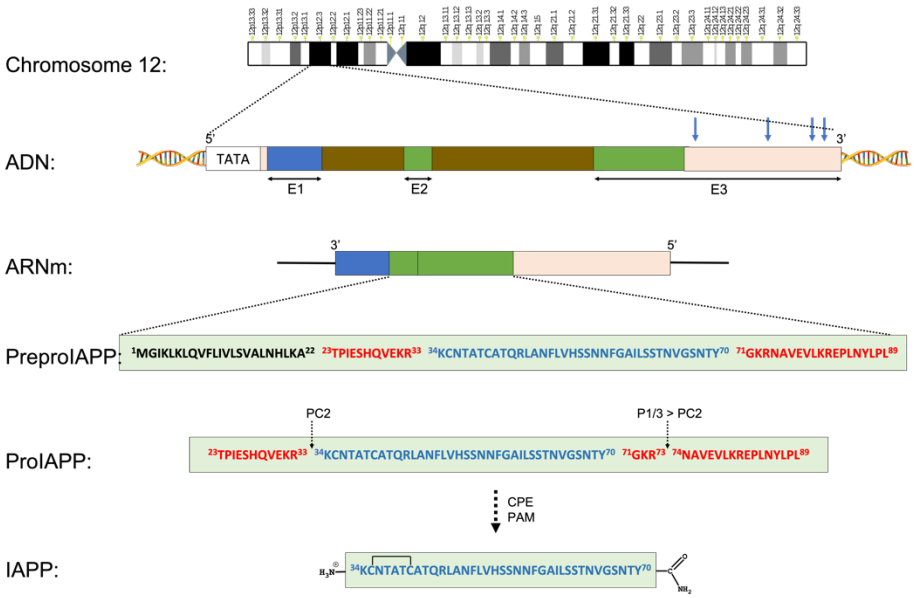


Figure 1.6 Biosynthèse et maturation de l'IAPP.

Les différents exons (E1, E2 et E3) sont identifiés sur la représentation du brin d'ADN. Les régions non codantes et les introns sont présentés en marron et en beige respectivement. Les flèches bleues indiquent les sites de polyadénylation. L'exon 1 qui sert de coiffe est en bleu. Le domaine du preproIAPP apparaît en vert. Les clivages enzymatiques sont représentés par les flèches pointillées.

Une mauvaise régulation de la synthèse et/ou des étapes de modifications post-traductionnelles durant la biosynthèse d'IAPP peut avoir un impact dans l'amyloïdogénèse de l'IAPP. Par exemple, les îlots pancréatiques murins exprimant le proIAPP, et dépourvus de l'enzyme PC2, ont activé leur programme de mort cellulaire, due à la présence d'amyloïdes, alors que le sauvetage de l'expression de la PC2, permettant la maturation de l'IAPP, a diminué significativement à la fois la formation d'amyloïde et le nombre de cellules apoptotiques (Marzban *et al.*, 2006; Marzban *et al.*, 2008). De plus, il a été récemment montré que l'hyperglycémie (glycémie > 16,9 mmol/l) est revenue chez 94 % des souris diabétiques immunodéficientes, receveuses d'une greffe d'îlots pancréatiques exprimant le proIAPP humain et

dépourvus de PC2, tandis que les receveurs d'îlots qui expriment le proIAPP humain et le PC2 sont restés normoglycémiques (retour à une glycémie normal) (Chen *et al.*, 2018; Courtade *et al.*, 2017). Ces études suggèrent qu'une altération de la maturation du proIAPP au site de clivage N-terminal peut entraîner une accumulation d'espèces toxiques et une perte et/ou un dysfonctionnement des cellules-β.

L'IAPP est co-exprimé, co-sécrété et co-entreposé avec l'insuline dans un rapport d'environ 1:100 (IAPP: insuline) par les cellules-β pancréatiques. Ce ratio peut atteindre 1:20 chez les patients atteints du diabète de type II (Owen *et al.*, 2019). Dans les vésicules sécrétoires, l'IAPP est entreposée à haute concentration, de l'ordre du millimolaire et doit donc être protégé contre son agrégation. En effet, l'IAPP s'agrège rapidement à cette concentration *in vitro*. Néanmoins, un faible pH dans les granules, qui favorise la forme imidazolium de l'His-18, et l'interaction avec l'insuline, maintiennent l'IAPP dans un état monomérique et empêchent la formation des fibres amyloïdes (Jaikaran *et al.*, 2004; Li *et al.*, 2013). De plus, les granules sécrétoires des cellules bêta des îlots pancréatiques de Langerhans, qui entreposent l'IAPP et l'insuline, se caractérisent par une concentration élevée en ions zinc, pouvant atteindre 10 à 25 μM (Foster *et al.*, 1993) (Brender *et al.*, 2010; Brender *et al.*, 2013). Il a été observé *in vitro* que ces concentrations physiologiques de Zn^{2+} ralentissent l'agrégation de l'IAPP, et ce, même à pH physiologique (Aspinwall *et al.*, 1997).

1.3.3 Rôles physiologiques de l'IAPP

L'IAPP est co-sécrété avec l'insuline par les cellules-β pancréatiques après l'apport de nutriments. Chez les rats, la concentration dans la circulation sanguine de l'IAPP passe de 3-5 picomolaires (pM) à 15-20 pM suite à une élévation de la glycémie (Lutz, 2010). Sur le plan physiologique, l'IAPP, après sa liaison avec le récepteur, agit en tant

qu'hormone glucorégulatrice agissant sur la sécrétion de glucagon et inductrice de satiété, protégeant contre l'hyperglycémie postprandiale (Bower et Hay, 2016; Hieronymus et Griffin, 2015). En effet, l'IAPP permet la réduction du taux de glucose dans le sang (*i*) en inhibant la sécrétion du glucagon, (*ii*) en ralentissant la vidange gastrique et (*iii*) en induisant la satiété (Hieronymus et Griffin, 2015) (Figure 1.7). Sous conditions diabétiques, l'expression, la maturation et la physiologie de l'IAPP deviennent dérégulées et cette hormone s'accumule alors sous forme de dépôts amyloïdes, dont l'implication dans la pathogenèse demeure encore aujourd'hui imprécise.

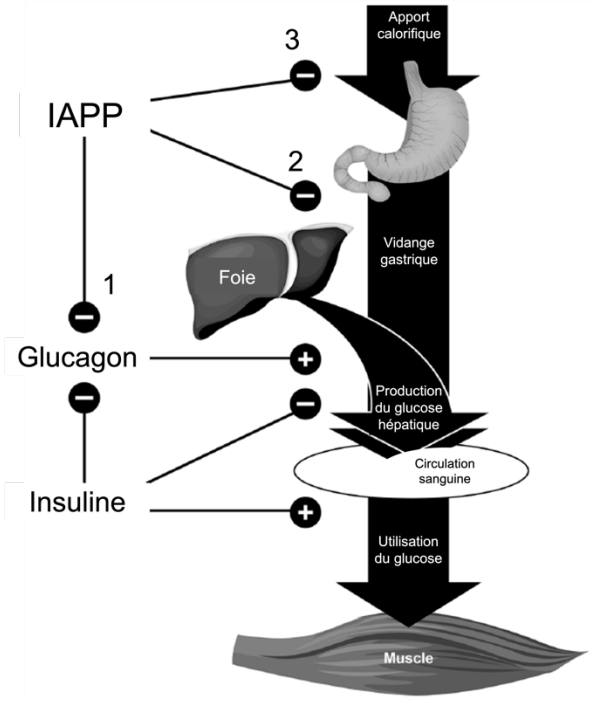


Figure 1.7 Rôles de l'IAPP sur l'homéostasie de glucose.

Les rôles physiologiques de l'IAPP sont : 1) inhiber la sécrétion de glucagon, 2) ralentir la vidange gastrique et 3) induire la satiété. Figure adaptée du (Hieronymus et Griffin, 2015).

L'IAPP est un membre de la famille des peptides de la calcitonine, qui comprend la calcitonine (CT), le peptide lié au gène de la calcitonine (*calcitonin-gene-related peptide*, CGRP) et l'adrénomédulline (Wimalawansa, 1997). De plus, l'IAPP partage 46 % d'identité de séquence primaire avec le CGRP (Tableau 1.5). Ces hormones peptidiques modulent leurs activités biologiques en interagissant et activant des récepteurs couplés aux protéines G (GPCR) de classe B (Chapter *et al.*, 2010).

Tableau 1.5 Séquence primaire des peptides de la famille de la calcitonine.

Peptides	Séquence primaire	% similitude avec IAPP
IAPP	K**C**-NTAT**C**AT QRLANFLVHS SNNFGAILSS TNVGSNTY--	--
α-CGPR	A**C**-DTAT**C**VT HRLAGLLSRS GGVVKNNFVP TNVGSKAF--	43%
β-CGPR	A**C**-NTAT**C**VT HRLAGLLSRS GGMVKSNFVP TNVGSKAF--	46%
CT	-**C**GNLST**C**ML GTYTQDFNKF HTF-----PQ TAIGVGAP--	14%
AM	YRQSMNNFQGLRSFG**C**-RFGT**C**TV QKLAHQIYQF TDKDKDNV-A PRSKISPQGY	<5%
IMD	TQAQLLRVG**C**-VLGT**C**QV QNLSHRLWQL MGPAGRQDSA PVDPSSPHSY	<5%

CGPR : Calcitonin-gene-related peptide, CT: Calcitonine, AM : Adrénomédulline, IMD : Intermédine. Les cystéines formant le pont disulfure sont en caractère gras. Les résidus différents de l'IAPP sont présentés en rouge.

Jusqu'à présent, aucun récepteur entièrement spécifique à l'IAPP n'a été identifié. En effet, l'IAPP partage, avec la calcitonine, les GPCRs CT, bien qu'il se lie à ces derniers avec une affinité relativement faible. La fonction, la pharmacologie et la sélectivité des récepteurs CT sont altérées par leur association avec des protéines modifiant l'activité des récepteurs, mieux connues sous le nom de *receptor activity-modifying proteins*, ou RAMPs. Ces dernières constituent une famille de protéines transmembranaires comprenant RAMP1, RAMP2 et RAMP3 (Hay *et al.*, 2006). L'association du récepteur CT avec une RAMP modifie la sélectivité du récepteur et augmente significativement

son affinité envers l'IAPP, formant ainsi les récepteurs AMY_1, AMY_2 et AMY_3 (Figure 1.6) (Bower et Hay, 2016; Christopoulos *et al.*, 1999). Le récepteur CT humain (hCTR) possède deux isotypes (hCTR1 et hCTR2) et ceci implique qu'il pourrait y avoir six différents sous-types de récepteurs de l'IAPP (Muff *et al.*, 1999). L'expression des CTRs et RAMPs a été initialement identifiée dans le cerveau et a ensuite été retrouvée dans plusieurs tissus périphériques, incluant ceux du cortex rénal et du pancréas (Cooper *et al.*, 1995 ; Martinez *et al.*, 2000; Paxinos *et al.*, 2004). Les RAMPs participent au transport du récepteur CT vers la surface membranaire et modulent l'interaction de ce dernier avec l'IAPP et la calcitonine (McLatchie *et al.*, 1998). Malgré l'importance de l'IAPP sur le plan physiologique, le rôle de ses récepteurs (CT et RAMPs) en relation avec leur activation spécifique par l'IAPP demeure peu caractérisé à ce jour (Westermark *et al.*, 2011). Des travaux de recherche sont donc requis afin de mieux comprendre l'implication physiologique de cette hormone peptidique et de ces récepteurs afin de développer des agonistes sélectifs et efficaces comme outils pharmacologiques et en conséquence, prévenir le développement du diabète de type II.

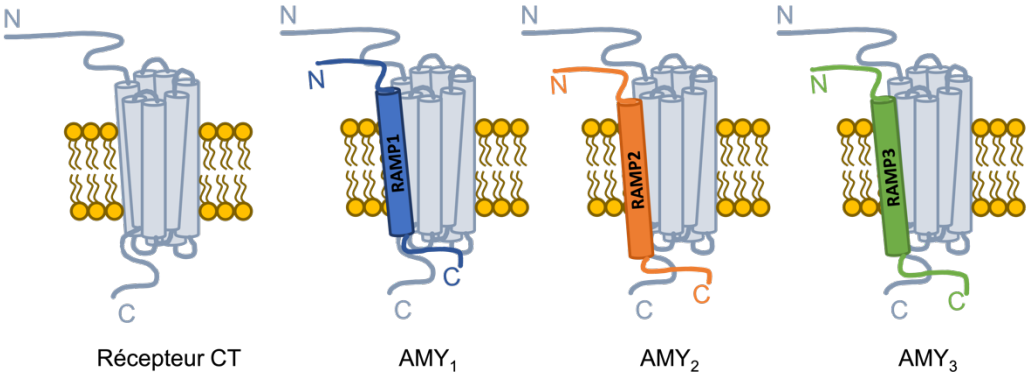


Figure 1.8 Représentation schématique du récepteur à calcitonine et des récepteurs de l'IAPP.

L'IAPP partage les récepteurs avec la calcitonine. Le récepteur CT s'associe avec des protéines RAMPs (receptor activity-modifying proteins) pour former des récepteurs de l'IAPP, AMY_1, AMY_2 et AMY_3. Figure adaptée de (Bower et Hay, 2016).

1.3.4 Phylogénie de l'IAPP

L'IAPP appartient à la famille des peptides apparentés à la calcitonine qui comprend l'adrénomédulline, les peptides associés aux gènes de la calcitonine (CGRP), l'intermédine et la calcitonine (Tableau 1.6) (Akter *et al.*, 2016). Ces peptides partagent des modifications post-traductionnelles clés : ils ont une extrémité C-terminale amidée et contiennent un pont disulfure intramoléculaire près de l'extrémité N-terminale. L'IAPP humain et les CGRPs partagent une haute similitude de séquence (43 % à 49 % de similitude) (Tableau 1.6). Cependant, l'IAPP humain est agressivement amyloïdogène *in vitro*, tandis que les CGRPs ne forment pas d'amyloïde (Akter *et al.*, 2016). La séquence primaire de l'IAPP a été déterminée chez plusieurs espèces de mammifères (Tableau 1.7). Les régions N-terminale et C-terminale, soient respectivement le segment 8-20 et 30-37, sont hautement conservées chez différentes espèces de mammifères et similaires à celles des CGRPs (Tableau 1.6 et Tableau 1.7). Cela suggère que ces régions sont importantes pour l'activité biologique de cette hormone. Au contraire, la région 20-29 présente beaucoup de variations (Tableau 1.6 et Tableau 1.7). Cette région variable est connue comme étant très amyloïdogénique et est importante dans l'auto-assemblage et l'agrégation de l'IAPP humaine (hIAPP). Notamment, cette région est hautement hydrophobe. De plus, le segment 20-29 de hIAPP isolé est suffisant pour induire la formation de structures fibrillaires stables (Glenner *et al.*, 1988 ; Griffiths *et al.*, 1995; Westermark *et al.*, 1990). Chez les primates, les félins et les chiens, la région 20-29 présente 1 à 2 substitutions par rapport à l'humain, dont une substitution d'une phénylalanine par une leucine. Cette

substitution n'affecte pas la capacité à former des amyloïdes d'IAPP puisque l'hydrophobicité est conservée (O'Brien *et al.*, 1990; Wong *et al.*, 2016). Ainsi, l'aspect hydrophobe dans une séquence peptidique est un des déterminants supportant la prédiction de la capacité d'agrégation d'un peptide (Família *et al.*, 2015). Tous les mammifères ne présentent pas de dépôts amyloïdes pancréatiques, notamment les souris et les rats (Betsholtz *et al.*, 1989; Westermark *et al.*, 1990). La comparaison de la séquence de l'IAPP du rat/souris (rIAPP) avec la séquence de l'IAPP humain ainsi que les premières expériences *in vitro* semblent confirmer l'hypothèse selon laquelle la capacité à former des amyloïdes est contrôlée par l'identité du segment 20-29 (Ashburn et Lansbury, 1993). En fait, le rIAPP contient six substitutions par rapport à la séquence retrouvée chez l'humain, dont cinq se trouvent dans le segment 20-29. Notamment, les résidus Ala25, Ser28 et Ser29 sont substitués par une proline (Betsholtz *et al.*, 1989). À l'opposé de l'IAPP humain, le rIAPP ne forme pas de fibres amyloïdes, bien qu'il ait été montré que l'IAPP de rat puisse s'auto-assembler et former des oligomères faiblement cytotoxiques (Abedini *et al.*, 2016) (Westermark *et al.*, 2011). Ainsi, le comportement différent de l'IAPP humain et du rat pourrait être dû aux différences dans la région 20-29 et/ou aux multiples résidus de proline, résidu connu pour être un perturbateur de feuillets-β et ainsi déstabiliser la structure fibrillaire (Moriarty et Raleigh, 1999; Westermark *et al.*, 1990). Deux facteurs font que les prolines défavorisent les structures secondaires : l'une est l'absence d'hydrogène sur l'amide, qui empêche la formation de pont hydrogène ; et l'autre est la restriction stérique imposée par la proline aux résidus voisins par le cycle pyrrolidine. Les angles phi (φ) et psi (ψ) stériquement accessibles par la proline (-75 º et 150 º respectivement) (Morgan et Rubenstein, 2013) sont incompatibles avec ceux des feuillets-β (parallèle : φ = -119 º et ψ = 113 º et anti-parallèle : φ = -139 º et ψ = 135 º) (McAllister et Floudas, 2009) et déforment ainsi considérablement les brins-β (Li *et al.*, 1996). Ainsi, la présence de trois prolines dans le rIAPP diminuent la stabilité des feuillets-β, qui est la structure secondaire majeure des fibres amyloïdes.

Ces premières études ont initialement conduit à penser que l'amyloïdogénèse de l'IAPP est strictement déterminée par la séquence primaire dans la région 20-29 (Abedini *et al.*, 2007; Westermark *et al.*, 1990). Cependant, la situation est plus complexe. D'autres fragments, en plus du segment 20-29 de l'IAPP, se sont ensuite révélés être suffisants pour former des fibres amyloïdes, soulignant que la région 20-29 n'est pas le seul segment amyloïdogène du polypeptide. Ceux-ci comprennent des peptides composés des résidus 30–37 (TNVGSNTY) (Nilsson et Raleigh, 1999), 8–20 (ATQRLANFLVHSS) (Jaikaran *et al.*, 2001) et 10–19, ainsi que des courts fragments de la région 10–19 (FLVHS et NFLVH) (Mazor *et al.*, 2002). De plus, afin d'identifier les résidus jouant un rôle clé dans la conversion structurale de l'IAPP, des études sur d'autres espèces animales ont été effectuées (Fortin et Benoit-Biancamano, 2015). Les analyses *in silico* et *in vitro* ont montré que la formation d'amyloïdes d'IAPP est inhibée lorsque le motif NFLVH (région 8-20) est remplacé par le motif DFLGR (tamarin-lion doré) ou le KFLIR (grand dauphin). L'amyloïdogénicité de l'IAPP est variable parmi les espèces. Parfois, chez certaines espèces, aucune cohérence n'existe dans les résultats *in vitro* et *in vivo*, ce qui rend la compréhension des mécanismes impliqués dans le processus d'amyloïdogénèse d'IAPP complexe. Par exemple, l'IAPP du furet peut former des fibres amyloïdes *in vitro* et cette formation réduit la viabilité des cellules-β. Toutefois, aucun dépôt d'amyloïde n'est détecté dans les îlots pancréatiques chez les furets sains ou chez les furets diabétiques (Paulsson *et al.*, 2011). L'étude de la variabilité de l'amyloïdogénicité d'IAPP chez différentes espèces informe sur les résidus et/ou des positions jouant un rôle clé dans la formation de fibres amyloïdes ainsi que la pathogénicité de l'IAPP.

Tableau 1.6 Séquence primaire d'IAPP de différentes espèces.

Espèce	Séquence primaire	% similitude avec hIAPP
Humain	KCNTATCAT QRLANFLVHS SNNFGAILSS TNVGSNTY	--
Rat	KCNTATCAT QRLANFLVRS SNNLGPVLPP TNVGSNTY	84%
Singe	KCNTATCAT QRLANFLVRS SNNFGTILSS TNVGSDTY	92%
Chien	KCNTATCAT QRLANFLVRT SNNLGAILSP TNVGSNTY	89%
Chat	KCNTATCAT QRLANFLIRS SNNLGAILSP TNVGSNTY	89%
Hamster	KCNTATCAT QRLANFLVHS NNNLGPVLSP TNVGSNTY	86%
Porc	KCNMATCAT QHLANFLDRS RNNLGTIFSP TKVGSNTY	73%
Furet	KCNTATCVT QRLANFLVRS SNNLGAILLP TDVGSNTY	84 %
Panda rouge	KCNTATCVT QRLANFLVRT SNNLGAILSP TNVGSNTY	89%
Raton-laveur	KCNTATCVT QRLANFLLRS SNNLGAILSP TNVGSNTY	86%
Tamarin-lion doré	KCNTATCSM HRLADFLGRS SNNFGAILSP TNVGSNTY	81 %
Éléphant africain	KCNTATCVR QHLANFYIIP ATVLNPSSLP TNVGSNTY	57 %
Grand dauphin	KCNTATCAT QRLAKFLIRS SNNLGAILSP TNVGSNTY	86%
Ours	KCNTATCAT QRLANFLVRS GNNLGAILSP TNVGSNTY	89%

Les résidus différents de l'IAPP sont présentés en rouge. Séquences tirées de (Fortin et Benoit-Biancamano, 2015).

1.3.5 Structures secondaires de l'IAPP

En solution aqueuse, l'IAPP affiche principalement une conformation désordonnée qui diverge d'une structure purement aléatoire (*random-coil*) par la formation transitoire de structures locales définies (Brender *et al.*, 2012; Williamson et Miranker, 2007; Yonemoto *et al.*, 2008). Certains solvants, tels que le trifluroéthanol (TFE) ou l'hexafluoroisopropanol (HFIP), sont connus pour induire la conformation en hélice-α de l'IAPP, révélant sa propension à former des hélices-α (Hubbard *et al.*, 1991; Wang *et al.*, 2014a). Des études effectuées par RMN en solution ont permis d'identifier des conformations hélicoïdales de l'IAPP. D'après ces études, il a été montré qu'en présence de micelles de dodécylsulfate de sodium (SDS) à pH acide (4,2), l'IAPP

adopte une structure en hélice-α qui couvre principalement le segment 5-28 (Figure 1.9A) (Patil *et al.*, 2009). Un modèle similaire, aussi en présence de micelles de SDS à pH physiologiques (7,3), a également été observé. Ce dernier consiste en la présence (*i*) d'une hélice-α pour le segment 7-17, (*ii*) d'une seconde hélice impliquant la région 21-28, (*iii*) d'un coude entre les hélices formant un angle de 30 ^{o} et (*iv*) d'une courte hélice 3_{10} comprenant les résidus 33-35 en C-terminal (Nanga *et al.*, 2011) (Figure 1.9B). Par ailleurs, les études de résonnance paramagnétique électronique (EPR) ont montré que la présence de larges vésicules unilamélaires (80 % de 1-palmitoyl-2-oleoyl-glycero-3-phospho-L-serine (POPS) et 20 % de 1-palmitoyl-2-oleoyl-glycero-3-phosphocholine (POPC)) mène à la formation d'une hélice-α dans la région 9-22 (Apostolidou *et al.*, 2008)

Par une combinaison d'études en spectrométrie de masse à mobilité ionique (IMS-MS) et en dynamique moléculaire avec échange de répliques (REMD), il a été suggéré que les monomères d'IAPP forment des structures en épingle à cheveux (*β-hairpin*) impliquant deux brins-β, *c.-à-d.* segments 9-17 et 23-33, reliés par un coude impliquant les positions 18 à 22 (Dupuis *et al.*, 2009 ; Wu et Shea, 2013) (Figure 1.9C). Cette structure en *β-hairpin* est topologiquement similaire à la conformation fibrillaire d'IAPP proposée par Tycko au moyen de la RMN à l'état solide (Luca *et al.*, 2007) (Figure 1.10). Hormis les liaisons hydrogènes du squelette peptidique, les interactions impliquées dans le *β-hairpin* d'IAPP sont dominées par des contacts non polaires entre les chaînes latérales des résidus hydrophobes (Mirecka *et al.*, 2016). De plus, selon les calculs de simulations thermodynamiques, la conformation *β-hairpin* est la plus stable parmi les autres conformations, *i.e* aléatoire et hélice-α (Reddy *et al.*, 2010). Ainsi, il est probable que la structure *β-hairpin* soit impliquée dans l'étape de l'auto-recognition de l'IAPP initiant le processus de la formation des fibres amyloïdes.

Tel que mentionné ci-dessus, l'IAPP adopte un large ensemble conformationnel en solution aqueuse, incluant une structure intrinsèquement désordonnée. Ceci indique

que ce peptide est susceptible de se replier en multiples conformations différentes dans les fluides physiologiques, impliquant une structure plus définie et précise lors (ou suite) à son interaction avec ses récepteurs ou à son agrégation. En outre, les études concernant la structure native de l'IAPP sont limitées dues à sa faible solubilité, sa forte capacité à s'auto-assembler et l'impossibilité de former des cristaux pour les analyses en diffraction des rayons X. En conséquence, la structure native de l'IAPP demeure hypothétique et seules des hypothèses par déduction, concernant sa conformation bioactive et les structures intermédiaires de son auto-assemblage, peuvent être tirées des données disponibles.

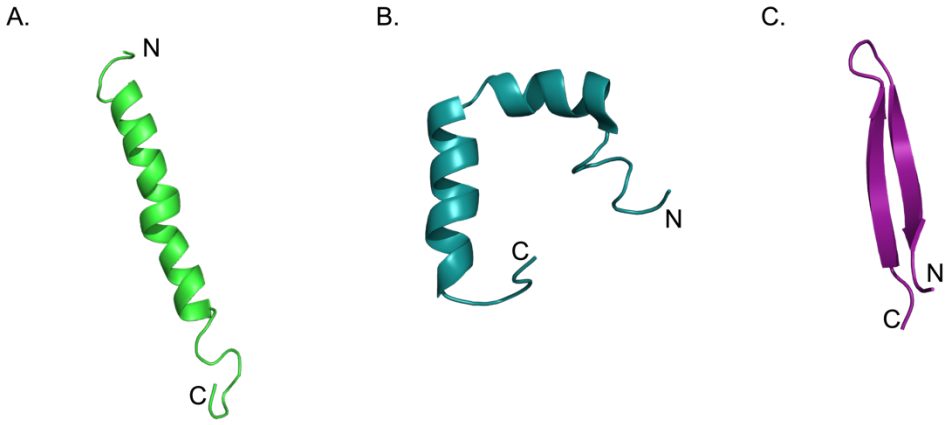


Figure 1.9 Exemples de structures secondaires de l'IAPP.

A. La conformation en hélice-α de l'IAPP en présence des micelles de SDS à pH 4,2, déterminée par RMN, PDB 2KB8. B. La structure en hélice-α de l'IAPP en présence du SDS à pH 7,3, déterminée par RMN, PDB 2L86. C. Représentation de la conformation en épingle à cheveux déterminée par la dynamique moléculaire.

1.4 Fibres amyloïdes d'IAPP

1.4.1 Structure (supra)moléculaire des fibres amyloïdes d'IAPP

La conformation de l'IAPP sous sa structure quaternaire amyloïde fibrillaire a été étudiée par de multitude d'approches, y compris la RMN à l'état solide, la diffraction des rayons X et l'EPR et différents modèles structuraux ont été proposés (Figure 1.10A). Les études de modélisation *in silico* suggèrent que les monomères d'IAPP adoptent un pli en forme de S avec trois brins β (segments 8-16, 20-27 et 30-37). Cette structure S est empilée de façon alignée, avec une élévation axiale de 0,47 nm, générant un réseau de trois feuillets β croisés, appelé structure *β-serpentin* (Kajava *et al.*, 2005). Ce modèle est peu connu et a été remplacé par le modèle déduit par la RMN à l'état solide (Luca *et al.*, 2007). Dans ce modèle, les fibres d'IAPP consistent en deux colonnes symétriques de monomères d'IAPP. Chaque monomère est sous forme de U et se superpose de façon perpendiculaire à l'axe de la fibre. Chaque colonne est formée de deux feuillets-β. Ces feuillets contiennent des brins β parallèles dans un empilement aligné (*in-register parallel β-sheets*) (Figure 1.10B). Dans ce modèle, les brins β en N- et C-terminal s'étendent des résidus 8 à 17 et 28 à 37, respectivement, et la boucle implique la région 18–27. Le segment 1-7 reste sous la forme aléatoire, et ce, probablement en raison des contraintes stériques imposées par le pont disulfure entre les cystéines aux positions 2 et 7. Deux différentes orientations des chaînes latérales ont été proposées impliquant différentes interactions entre les couches de feuillet-β. Dans la première proposition, les chaînes latérales des résidus Gln-10, Leu-12, Asn-14 et Leu-16 sont en interaction avec le feuillet-β (segment 28-37). Alors que les chaînes latérales des résidus Arg-11, Ala-13 et Phe-15 se trouvent vers l'extérieur de la fibre. Dans la deuxième proposition, les chaînes latérales de Arg-11, Ala-13 et Phe-15 se trouvent à l'intérieur de la fibre interagissant avec le feuillet-β formé par les résidus

28-37, tandis que les chaînes latérales de Gln-10, Leu-12, Asn-14 et Leu-16 sont dirigées vers l'extérieur du protofilament. En raison de l'organisation du brin-β, les orientations des chaînes latérales des résidus dans les brins sont alternées et sont prises en compte dans les deux propositions. Les fibres amyloïdes sont stabilisées par un ensemble d'interactions électrostatiques, d'interactions hydrophobes, et de liaisons hydrogènes.

Suite à la publication du modèle de Tycko, d'autres modèles ont été également proposés par l'équipe d'Eisenberg (Wiltzius *et al.*, 2008) pour la structure des fibres d'IAPP en utilisant différentes méthodes biophysiques. Les segments 21-27 (NNFGAIL) et 28-33 (SSTNVG) ont été cristallisés et ensuite analysés par diffraction aux rayons X. Les auteurs ont modélisé une structure des fibres amyloïdes avec l'IAPP complet grâce au programme *crystallographic object-oriented toolkit* en se basant sur les résultats de la cristallographie des segments 21-27 et 28-33. Ce modèle révèle une structure supramoléculaire similaire à celle proposée par Tycko, soit composée de 2 monomères espacés de 4.8 Å et organisés en 4 feuillets. La grande différence entre les deux modèles proposés par les deux groupes de recherche est la distance entre les deux feuillets-β intérieurs. En effet, le modèle du groupe de Tycko présente une distance inter-feuillets de 6 Å alors que celle dans le modèle d'Eisenberg est plus élevée, avec une distance de 12 Å (Luca *et al.*, 2007 ; Wiltzius *et al.*, 2008) (Figure 1.10A)

D'autres (supra)structures des assemblages amyloïdes de l'IAPP ont été proposées. Des études de EPR ont conduit à l'élaboration d'un modèle légèrement différent de ceux proposés par les groupes de Tycko et Eisenberg. En fait, les fibres sont toujours constituées d'empilements de monomères en forme de U, mais les plans des deux brins β sont décalés d'environ 15 Å (Bedrood *et al.*, 2012). Dans ces trois modèles (RMN, cristallographie et EPR), le segment amyloïdogénique 20-29 ne fait pas partie de la structure des feuillets-β ordonnés, mais il forme plutôt un coude qui relie les deux brins β.

Récemment, en 2020, Röder et al., Cao et al. et Gallardo et al. ont rapporté des structures cryo-EM des fibres amyloïdes d'IAPP à une résolution de 4.2 Å, 3.7 Å et 3.6 Å, respectivement (Figure 1.10C, D et E) (Röder *et al.*, 2020; Cao *et al.*, 2020; Gallardo *et al.*, 2020). Deux des groupes ont montré que les fibres d'IAPP sont constituées de deux protofilaments en forme de S qui sont composés de trois brins-β, formés par les segments 14-19 (ou 20), 26-30 (ou 32) et 35-36 (ou 37) qui sont lié par des boucles courtes (Figure 1.10C et E) (Gallardo *et al.*, 2020; Röder *et al.*, 2020). En revanche, le groupe de Cao propose plutôt des fibres constituées deux protofilaments plats en forme de I contenant de courts brins-β qui sont dans des segments similaires à ceux des plis en forme de S (Figure 1.10D) (Cao *et al.*, 2020). Les structures de cryo-EM en forme de S et de I diffèrent considérablement des modèles des fibres d'IAPP précédemment rapportés. Le polymorphisme des fibres amyloïdes et/ou différentes préparations d'IAPP peuvent expliquer ces différences.

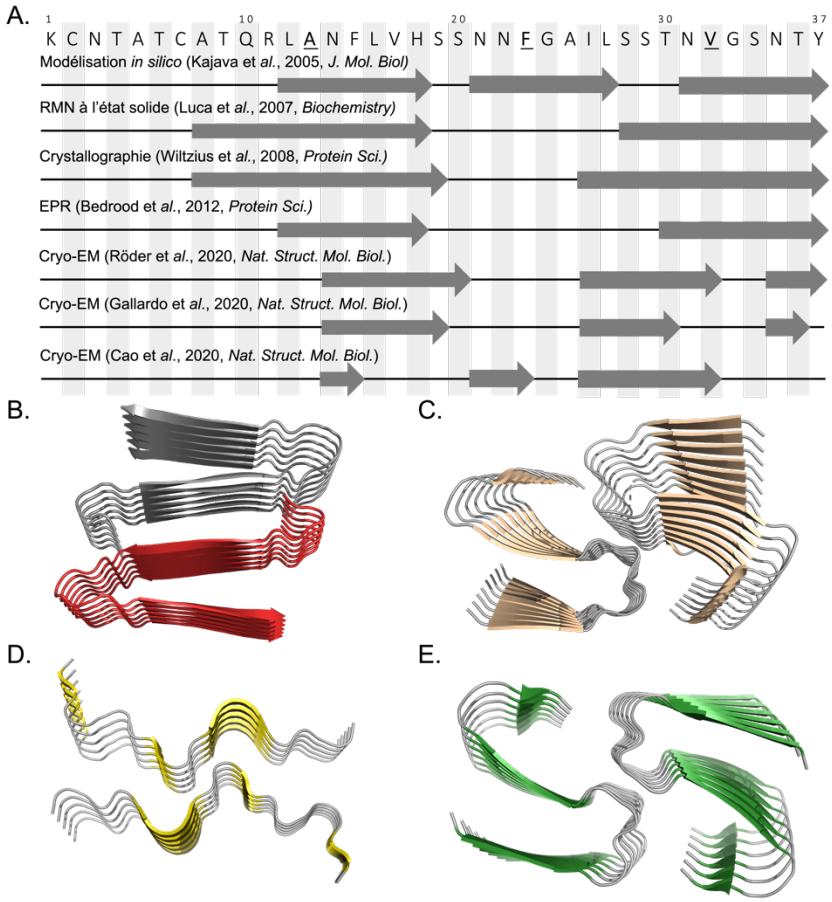


Figure 1.10 Structure (supra)moléculaire des fibres amyloïdes d'IAPP.

A. Comparaison de la structure des fibres d'IAPP étudiée par différentes approches. Les flèches indiquent les feuillets-β. Vue d'ensemble des structures des fibres d'IAPP proposées par : B. Luca et *al.* par la RMN à l'état solide (Luca *et al.*, 2007) ; C. Röder et *al.* par la cryo-EM (PDB 6Y1A) (Röder *et al.*, 2020) ; D. Cao et *al.* par la cryo-EM (PDB 6VW2) (Cao *et al.*, 2020) et D. Gallardo et *al.* par la cryo-EM (PDB 6ZRF) (Gallardo *et al.*, 2020).

1.4.2 Mécanismes de l'auto-assemblage amyloïde de l'IAPP

Le mécanisme par lequel les protéines s'auto-assemblent en fibres amyloïdes a été intensivement étudié, comme décrit dans la section 1.2.2. Afin de pouvoir former des fibres amyloïdes, l'IAPP doit subir des réarrangements conformationnels permettant la formation de (supra)structures localement ordonnées, appelées noyaux, qui initient le processus amyloïdogénique. À cet effet, l'étape limitante de ce processus est la conversion conformationnelle des monomères en oligomères et par la suite en noyaux précurseurs de la croissance des fibres amyloïdes. La cinétique de l'auto-assemblage de l'IAPP mesurée par la fluorescence de la ThT montre une courbe sigmoïdale représentative d'une polymérisation nucléée (Figure 1.5, courbe grise). Par ailleurs, des études ont montré la présence d'espèces intermédiaires oligomériques (section 1.4.2.1) précédant la formation du noyau compétent menant à la phase d'élongation, suggérant une polymérisation nucléée par conversion conformationnelle (Nagel-Steger *et al.*, 2016; Quittot *et al.*, 2018).

1.4.2.1 Hypothèse sur les intermédiaires oligomériques

Des études réalisées sur différents peptides amyloïdogéniques ont sugéré l'importance des espèces oligomériques dans la cascade de formation des fibres amyloïdes et, plus particulièrement, en lien avec la toxicité des amyloïdes (section 1.5) (Bemporad et Chiti, 2012; Kayed *et al.*, 2003). À cet effet, plusieurs études mécanistiques du processus de formation des fibres amyloïdes ont été menées en ciblant les premières étapes de l'auto-assemblage de l'IAPP. Deux principaux modèles ont été proposés : le modèle impliquant des intermédiaires hélicoïdaux (Abedini et Raleigh, 2009) et le modèle mettant en jeu des intermédiaires en épingle à cheveux (Dupuis *et al.*, 2009).

Pour le modèle impliquant les intermédiaires hélicoïdaux, les études en RMN en solution et les analyses *in silico* ont suggéré que l'IAPP monomérique adopte une structure secondaire caractérisée par la formation d'une conformation transitoire en hélice-α impliquant la région 5-19 et cette structure serait en passe de former des fibres amyloïdes (Williamson *et al.*, 2009 ; Williamson et Miranker, 2007). Selon ce modèle, la formation des espèces oligomériques d'IAPP serait favorisée par des associations hélice-hélice, de type *coiled-coil*. Cette oligomérisation initiale permettrait d'augmenter la concentration locale des segments amyloïdogéniques 20-29 et 30-37 de l'IAPP, favorisant ainsi des interactions intermoléculaires et la formation de feuillets-β. Cette structure en feuillet-β croît et forme ensuite des ultrastructures riches en feuillet-β (Abedini et Raleigh, 2009). Compte tenu de ce modèle, plusieurs molécules ont été conçues afin de cibler et stabiliser les intermédiaires hélicoïdaux dans le but d'inhiber la formation de fibres amyloïdes d'IAPP (Hassanpour *et al.*, 2014; Kumar *et al.*, 2014 ; Kumar et Miranker, 2013 ; Saraogi *et al.*, 2010).

Quant au deuxième mécanisme proposé, le groupe de Bowers a suggéré que l'assemblage de l'IAPP en fibres débutait par la formation de dimères riches en brin-β formant des espèces intermédiaires riches en *β-hairpin* (Dupuis *et al.*, 2009 ; Dupuis *et al.*, 2011). De plus, les travaux de notre laboratoire ont démontré que la conformation en hélice-α ne participe pas dans le processus de formation des fibres d'IAPP et est hors de la voie amyloïdogénique (*off-pathway*) (De Carufel *et al.*, 2015). Cela renforce l'hypothèse de l'importance des *β-hairpin* dans le mécanisme de formation des fibres amyloïdes. En outre, l'existence de ces deux mécanismes, très différents l'un de l'autre, indique que le mécanisme de formation de fibres ainsi que les détails conformationnels des espèces intermédiaires oligomériques demeurent un sujet important de recherche. Ce manque de compréhension demande des études mécanistiques additionnelles sur l'amyloïdogénèse de l'IAPP et plus spécifiquement sur l'implication de résidus spécifiques et des facteurs environnementaux modulant l'auto-assemblage amyloïde.

1.4.2.2 Facteurs modulant l'auto-assemblage amyloïde de l'IAPP

Mutations et substitutions de la séquence primaire. La principale mutation identifiée dans la séquence primaire d'IAPP chez l'humain est la mutation de Ser à Gly en position 20. Cette mutation, qui est principalement retrouvée chez certaines populations asiatiques, augmente les risques de développer le diabète (Akter *et al.*, 2016; Cho *et al.*, 2003 ; Lee *et al.*, 2001; Sakagashira *et al.*, 1996 ; Seino, 2001). Bien que cette mutation accélère la formation d'amyloïdes *in vitro*, le mécanisme moléculaire à la base de cet effet demeure inconnu (Sakagashira *et al.*, 2000). Afin d'avoir une meilleure compréhension de l'amyloïdogénèse de l'IAPP, de nombreuses études de substitutions/modifications de la séquence primaire d'IAPP ont été effectuées. En outre, il est connu que les interactions π-π et hydrophobes des résidus aromatiques sont importantes dans la formation d'amyloïdes (Gazit, 2002). Sachant que l'IAPP contient trois résidus aromatiques (Phe-15, Phe-23 et Tyr-37), quelques études ont ciblé le rôle mécanistique de ces résidus (Azriel et Gazit, 2001 ; Bakou *et al.*, 2017 ; Doran *et al.*, 2012). Par exemple, la substitution de ceux-ci par des résidus hydrophobes et non aromatiques, tels que la leucine, ralentit leur agrégation (Armstrong *et al.*, 2011; Marek *et al.*, 2007). Toutefois, ces substitutions n'empêchent ni la formation de fibres amyloïdes ni la toxicité sous-jacente (Marek *et al.*, 2007; Tu et Raleigh, 2013a). Cela indique que les acides aminés aromatiques ne sont pas essentiels à la formation des fibres d'IAPP. D'autre part, les substitutions de Phe-23 par des acides aminés non naturels hydrophobes et/ou non aromatiques tels que cyclohexylalanine (Cha), α-naphthylalanine (1- Nap) et β-naphthylalanine (2- Nap) (en ordre d'hydrophobicité) sur $IAPP_{20-29}$ (SNNFGAILSS) ont été effectuées afin de déterminer l'importance des résidus aromatiques dans la formation de fibres (Doran *et al.*, 2012). Le mutant F23Cha forme des fibres avec une cinétique atténuée. En revanche, les substitutions 1-Nap et 2-Nap accélèrent la formation des fibres. Ces résultats indiquent que la contribution amyloïdogène des acides aminés aromatiques de l'IAPP est fonction de leur

hydrophobicité, leur potentiel à former des feuillets-β, leur taille et leur forme planaire. Cependant, les interactions π-π des résidus aromatiques ne sont pas essentielles dans la formation de fibres amyloïdes de l'IAPP (Doran *et al.*, 2012; Marek *et al.*, 2007; Tracz *et al.*, 2004).

Une autre étude a été effectuée afin de définir le rôle de la chaîne latérale amidée des nombreux résidus asparagine de l'IAPP dans le mécanisme de formation de fibres amyloïdes (Koo *et al.*, 2008). Par exemple, les résidus Asn du segment l'$IAPP_{8-37}$ ont été successivement substitués par différents acides aminés, incluant N14L, N14A, N14S, N21L et N21S. La mutation de l'Asn-14 et 21 par une Leu ralentit fortement la formation de fibres, alors que la mutation des autres Asn de l'IAPP n'affecte pas la cinétique d'auto-assemblage du peptide. Les résultats ont montré que les Asn ne contribuent pas équitablement à l'auto-assemblage de l'IAPP. De plus, les effets drastiques des mutations successives aux positions 14 et 21 suggèrent que ces deux positions jouent un rôle clé dans l'agrégation de l'IAPP. Par conséquent, il serait intéressant d'étudier leur implication dans le processus de formation des fibres amyloïdes chez l'IAPP complet, et non le segment 8-37. Particulièrement, les études sur la position 21 pourraient être essentielles et nécessaires puisque cette position se situe à l'interface du segment en boucle (18-27) et de la région amyloïdogénique (20-29) dans la structure amyloïde (Figure 1.10). L'Asn-21 se situe aussi à l'interface entre la région N-terminale (5-19) qui a tendance à être en conformation hélice-α (Williamson et Miranker, 2007) et le segment 23-27 (FGAIL) qui pourrait se retrouver en brin-β au sein des oligomères avant de se transformer en boucle lors de la nucléation/élongation (Buchanan *et al.*, 2013).

D'autres études ciblant le résidu His18 ont aussi été réalisées. Par exemple, lorsque l'histidine est substituée par la glutamine, la proline ou la leucine, le processus de formation des fibres est accéléré de façon significative (Tu *et al.*, 2014a; Wang *et al.*, 2016). D'autre part, les substitutions de His-18 par des résidus chargés (Arg, Lys, Glu)

ralentissent le processus, *c.-à-d.* augmentation de la phase de latence, sans l'inhiber complètement (Khemtemourian *et al.*, 2017). Quant à la région amyloïdogénique 20-29 de l'IAPP, de simples substitutions dans cette région ont montré un grand impact sur la propension du peptide à s'auto-assembler. Par exemple, la substitution de l'Ile26 par un résidu Pro abolit la formation des fibres amyloïdes (Abedini *et al.*, 2007). Plusieurs autres substitutions dirigées ont été également effectuées afin de mieux comprendre les forces et les interactions qui contrôlent l'auto-assemblage. Le Tableau 1.6. présente les principales études répertoriées dans la littérature.

Tableau 1.7 Effets de substitutions de la séquence de l'IAPP sur l'auto-assemblage amyloïde.

Région	Substitution	Effet sur l'amyloïdogénécité	Référence
K1-C7 (désordonnée)	Réduction du pont disulfure	↑	(Wineman-Fisher *et al.*, 2016)
	Carboxylation C-terminal	↑	(Akter *et al.*, 2016)
A8-V17 (brin β1)	L12R L12P	↓Déstabilisation des hélices α)	(Louros *et al.*, 2015)
	F15L F15S F15A F15D	(formation des intermédiaires en hélice α)	(Tu et Raleigh, 2013a ; Wiltzius *et al.*, 2009)
	F15I F15K F15ILe F15NLe	↓	(Tu et Raleigh, 2013a ; Wiltzius *et al.*, 2009)
	V17C	↑	(Koo *et al.*, 2008)
	V17A	↑	(Wiltzius *et al.*, 2009)
	V17K	Pas d'effet	(Wiltzius *et al.*, 2009)
	A13C N14L N14A N14S	-	(Koo *et al.*, 2008)

	N21L N21S N22L L12N/N14L N14L/L16N		
H18-L27 (coude)	H18P H18Q H18L	↑	(Wang *et al.*, 2016), (Tu *et al.*, 2014a)
	H18R	Pas d'effet	(Wiltzius *et al.*, 2009)
	S20K	↓	(Cao *et al.*, 2012)
	S20G	↑↑	(Sakagashira *et al.*, 2000)
	F23L	↓	(Wiltzius *et al.*, 2008; Wiltzius *et al.*, 2009)
	G24P	-	(Abedini *et al.*, 2007; Meng *et al.*, 2010c)
	I26P	-	(Abedini *et al.*, 2007)
S28-Y37 (brin β2)	T30C N31L N35L	↑	(Koo *et al.*, 2008)
	T36C	Pas d'effet	(Koo *et al.*, 2008)
	Y37L	↓	(Fox *et al.*, 2010a)

↑: Accélération de la formation des fibres amyloïdes ; (: Ralentissement de la formation des fibres, - : Inhibition de la formation de fibres.

Nonobstant le nombre important d'études d'analyse structure -auto-assemblage effectuées, aucune analyse systématique de type *Ala-Scan* de toutes les positions de l'IAPP n'a été rapportée (Akter *et al.*, 2016; Cao *et al.*, 2013). Notamment, il est difficile de comparer ces différentes études, car différentes conditions ont été utilisées et le processus de formation des fibres amyloïdes d'IAPP est hautement sensible aux conditions expérimentales, telles que la composition du tampon, la température, le sel ajouté, le pH, l'agitation, la surface, le volume et même la pression. De plus, des travaux récents de notre laboratoire ont montré que la fréquence de la mesure de la

fluorescence de la ThT est un des facteurs expliquant la faible reproductibilité des études de cinétique de formation de fibres amyloïdes (Sebastiao *et al.*, 2017). Une autre complication vient du fait que certaines études ont utilisé le fragment tronqué d'IAPP ($IAPP_{8-37}$), qui ne contient pas les sept premiers résidus. Bien que ces résidus se trouvent à l'extérieur du corps rigide de la structure amyloïde, ceux-ci pourraient influencer le processus de formation et la stabilité des fibres amyloïdes.

Facteurs environnementaux. Il convient de mentionner que contrairement à une solution aqueuse homogène utilisée pour les expériences *in vitro* en laboratoire, les mécanismes de formation de dépôts amyloïdes *in vivo* sont fort probablement différents et pourraient impliquer des voies alternatives. Donc, les études mécanistiques sur l'amyloïdogenèse d'IAPP dans un environnement hétérogène mimant les conditions physiologiques, incluant la présence de macromolécules biologiques, sont importantes afin de mieux comprendre le mécanisme de formation des fibres. Par exemple, le pH pourrait être impliqué dans l'auto-assemblage de l'IAPP. En effet, lors de son expression, l'IAPP est entreposé dans des granules de sécrétion avec l'insuline. Le pH dans ces granules est de 5,5, alors que le pH du milieu extracellulaire est d'environ 7,4 (Khemtemourian *et al.*, 2011). Puisque l'IAPP ne s'agrège pas dans les granules de sécrétion, des hypothèses ont été proposées : *i*) l'insuline inhibe la formation des fibres d'IAPP en formant un complexe insuline-IAPP (Gilead *et al.*, 2006; Larson et Miranker, 2004; Westermark *et al.*, 1996) et *ii*) le pH influence la formation de fibres amyloïdes (Khemtemourian *et al.*, 2011). En fait, le pH acide (5,5) ralentit fortement la formation de fibres amyloïdes d'IAPP (Khemtemourian *et al.*, 2011). L'imidazole de la chaîne latérale de l'His devient protoné à pH 5,5 puisque le pKa de l'imidazolium est d'environ 6. En conséquence, le ralentissement de la fibrillisation à pH acide est possiblement dû à la charge positive de ce résidu, tel qu'observé pour les analogues H18K et H18R (Jha *et al.*, 2014; Khemtemourian *et al.*, 2017).

L'auto-assemblage de l'IAPP est fortement accéléré en présence de membranes lipidiques synthétiques (Knight et Miranker, 2004). De plus, les glycosaminoglycanes (GAGs) sont aussi reconnus comme des facteurs qui affectent la vitesse de formation de fibres amyloïdes (DeWitt *et al.*, 1993 ; Ohishi *et al.*, 1990; Young *et al.*, 1992). Les GAGs sont des polysaccharides non ramifiés retrouvés majoritairement dans la matrice extracellulaire et la membrane basale des cellules. Puisque ces polysaccharides sont intrinsèquement associés aux dépôts amyloïdes extraits de patients, les GAGs pourraient jouer un rôle dans la formation de fibres. En effet, des études de notre laboratoire ont montré que les GAGs accélèrent fortement la formation de fibres amyloïdes d'IAPP (De Carufel *et al.*, 2013).

1.5 Cytotoxicité de l'IAPP

La présence de dépôts fibrillaires dans les îlots pancréatiques de patients souffrant de diabète de type II a initialement conduit au postulat que les fibres amyloïdes participent directement à la dégénérescence des cellules-β pancréatiques. Cette hypothèse a ensuite été renforcée par les travaux de recherche du groupe de Lorenzo montrant la toxicité des fibres d'IAPP sur des cellules isolées d'îlots pancréatiques (Lorenzo *et al.*, 1994). Toutefois, au cours des dernières années, la majorité des études ont plutôt suggéré que les intermédiaires oligomériques d'IAPP constituent les espèces protéiques quaternaires les plus toxiques de la cascade amyloïdogénique (Figure 1.11). Par exemple, Bram et ses collègues ont rapporté que des anticorps isolés de patients diabétiques reconnaissent spécifiquement les oligomères d'IAPP. Ces anticorps neutralisent les effets pro-apoptotiques des oligomères toxiques sur des cellules pancréatiques (Bram *et al.*, 2014). Récemment, l'hypothèse de la toxicité des espèces oligomériques a été confirmée par l'étude d'Abedini et *al.* Dans cette étude, les assemblages prélevés durant la phase de latence étaient hautement cytotoxiques pour

les cellules-β pancréatiques. Ces assemblages intermédiaires étaient constitués de structures allant des monomères aux hexamères. En revanche, les échantillons prélevés plus tard dans l'assemblage, dans les phases d'élongation tardives et de saturation, affichaient une cytotoxicité limitée (Figure 1.11) (Abedini *et al.*, 2016; Young *et al.*, 2014).

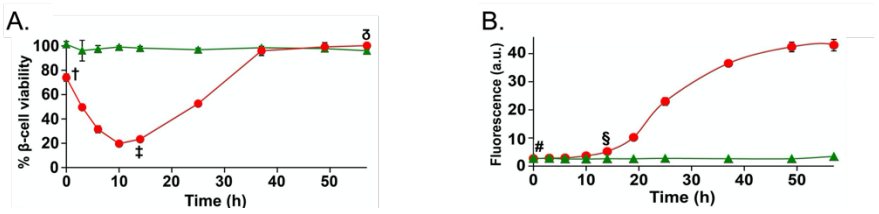


Figure 1.11 Toxicité de l'IAPP en fonction du temps d'auto-assemblage.

A. Viabilité cellulaire des cellules β-pancréatiques après traitement avec l'IAPP humain (courbe rouge) et de rat (courbe verte) préincubé de 0 h (monomère) à 60 h (fibrillaire). B. Cinétique d'auto-assemblage de l'IAPP humain (courbe rouge) ou de rat (courbe verte) mesurée par la fluorescence de la ThT. Figure adaptée de (Abedini *et al.*, 2016).

Il est maintenant acquis que la toxicité de l'IAPP est induite par la formation des espèces intermédiaires oligomériques. Il a été observé que la toxicité associée à l'agrégation de l'IAPP est souvent initiée par la perturbation de la membre plasmique (Janson *et al.*, 1999 ; Zhang *et al.*, 2017). La capacité de l'IAPP à perméabiliser les membranes dépend de la composition lipidique, du pH et de la force ionique. En effet, l'IAPP interagit fortement avec les membranes modèles qui contiennent souvent une fraction élevée de phospholipides anioniques et cette interaction membranaire est similaire en présence des vésicules membranaires des cellules-β isolées (Seeliger *et al.*, 2012). Cependant, les membranes synthétiques modèles utilisées dans les études biophysiques ne représentent pas réellement la rupture membranaire *in vivo*. En effet,

la membrane plasmique des cellules-β pancréatiques se compose de cholestérol, d'un faible pourcentage de lipides anioniques comparé aux membranes modèles (entre 2 % et 13 %) et elle est plutôt asymétrique (Abedini *et al.*, 2016; Trikha et Jeremic, 2011). Ainsi, l'IAPP extracellulaire fera face à une membrane avec un très faible pourcentage de lipides anioniques. De plus, le cholestérol est important pour l'absorption de l'IAPP *in vivo* (Trikha et Jeremic, 2011). En effet, certaines études biophysiques avec des membranes composées de cholestérol et des concentrations élevées de lipides anioniques (POPS) ont montré qu'avec une augmentation de la composition des POPS, le taux de fibrillogenèse augmente significativement (Zhang *et al.*, 2017).

De nos jours, il existe trois modèles de rupture membranaire dans lesquels les attractions électrostatiques entre le peptide cationique et les lipides anioniques permettent à la membrane de catalyser l'agrégation de l'IAPP (Knight et Miranker, 2004) (Figure 1.12). Le premier modèle propose que l'IAPP monomérique, et/ou les petits oligomères transitoires interagissent avec la membrane et s'insèrent dans la bicouche lipidique. Ensuite, l'intégrité de la membrane est perturbée par la croissance fibrillaire sur la membrane, entraînant un amincissement de cette dernière ainsi que sa fragmentation (Figure 1.12A) (Brender *et al.*, 2007; Owen *et al.*, 2019). Le deuxième modèle expliquant la perturbation membranaire consiste en la formation d'oligomères ayant une hydrophobicité élevée et perméables à la membrane, provoquant des destructions membranaires par l'extraction des lipides. Ce mécanisme est décrit comme un effet « détergent » puisque des vésicules lipidiques comprenant des agrégats protéiques sont formées (Figure 1.12B) (Domanov et Kinnunen, 2008; Iadanza *et al.*, 2018). Finalement, le troisième modèle de perturbation membranaire propose que les espèces intermédiaires oligomériques forment des pores à l'intérieur de la membrane, induisant la mort cellulaire (Figure 1.12C) (Birol *et al.*, 2018 ; Mirzabekov *et al.*, 1996; Raleigh *et al.*, 2017). Parallèlement à ce modèle, plusieurs études ont montré que des oligomères pré-formés, riches en feuillet-β et qui s'insèrent dans la membrane, forment des pores (Kayed *et al.*, 2009; Kayed *et al.*, 2004). Une autre étude a démontré que

l'IAPP, sous sa forme monomérique désordonnée, subit un réarrangement conformationnel, suite à sa liaison avec les lipides, en oligomère riche en hélice-α, menant à une destruction membranaire via la formation de canaux (Knight *et al.*, 2006). De plus, plusieurs évidences ont montré que la formation des pores et/ou la perturbation membranaire induite par l'oligomérisation de l'IAPP peut mener à une perte du contenu cellulaire et de l'osmolarité (Birol *et al.*, 2018; Last et Miranker, 2013). Des expériences sur des cellules traitées avec des préparations oligomériques d'IAPP ont permis d'identifier la formation des canaux membranaires potentiels comme site d'action. Ces formes oligomériques de l'IAPP humain sembleraient agir via le canal d'ion mécano-sensible, TRPV4, dans les membranes des cellules β afin d'augmenter l'influx calcique (Casas *et al.*, 2008) et de déréguler la voie de dégradation du protéasome intracellulaire (Casas *et al.*, 2007). L'internalisation des oligomères d'IAPP a été également observée dans les cellules-β INS-1E, suggérant que l'interaction externe du peptide avec la membrane pourrait conduire à l'internalisation du peptide, induisant de nombreux mécanismes en aval menant à la mort cellulaire (Abedini et Schmidt, 2013; Asthana *et al.*, 2018 ; Trikha et Jeremic, 2011).

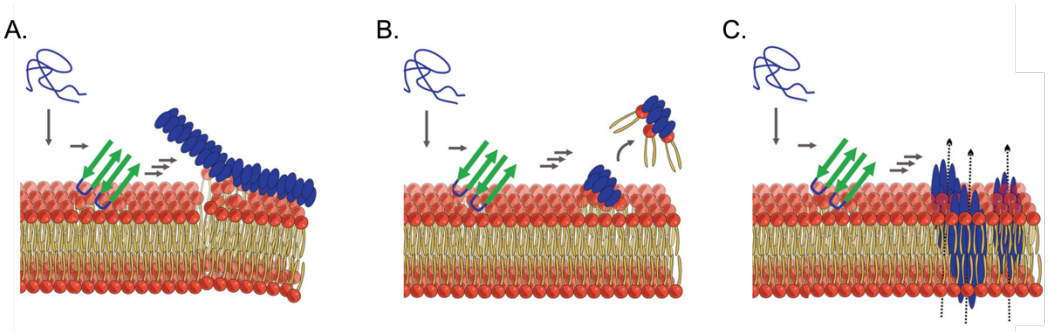


Figure 1.12 Mécanismes associés à la perturbation membranaire induite l'auto-assemblage de l'IAPP.

Les monomères interagissent avec la membrane lipidique. La formation d'oligomères conduit à la perturbation membranaire soit par A. la croissance des fibres, B.

l'extraction des lipides de la membrane de manière détergente, ou C. en formant des pores à l'intérieur des bicouches lipidiques. Figure adaptée de (Owen *et al.*, 2019).

La formation des fibres amyloïdes d'IAPP est associée à l'apoptose et un dysfonctionnement des cellules-β pancréatiques. Les voies apoptotiques extrinsèques peuvent être initiées via la liaison du ligand au récepteur FAS de la membrane cellulaire. Ceci initie à son tour l'activation de la caspase 8 et ensuite le clivage de la caspase 3 dans la cascade apoptotique. Il a été démontré que le traitement exogène de l'IAPP active cette voie pro-apoptotique. Également, la suppression du récepteur FAS, ou l'inhibition de la caspase 3 réduisent la cytotoxicité induite par l'IAPP (Law *et al.*, 2010; Park *et al.*, 2012; Zhang *et al.*, 2008). Des évidences ont montré que l'IAPP peut induire des réponses inflammatoires menant à la production de cytokines pro-inflammatoires, y compris l'interleukine 1α et l'interleukine 1β (Masters *et al.*, 2010 ; Westwell-Roper *et al.*, 2011). Par ailleurs, il a été observé que la voie pro-apoptotique impliquant des cJUN N-terminale kinases (JNK) est activée dans les îlots et dans les cellules-β suite aux traitements avec des concentrations élevées en IAPP. Il a également été démontré que cette voie (JNK) est activée en réponse aux amyloïdes générées à partir de l'IAPP endogène (Subramanian *et al.*, 2012).

Le stress du réticulum endoplasmique (RE) semble aussi jouer un rôle important dans la mort des cellules-β induite par l'IAPP (Eizirik *et al.*, 2008; Fonseca *et al.*, 2009). En effet, il a été montré qu'un stress important du RE chez les souris transgéniques qui surexpriment l'IAPP humain conduit à la mort cellulaire (Gurlo *et al.*, 2010). Toutefois, ce stress n'a pas été détecté dans les îlots pancréatiques en culture exprimant l'IAPP à des niveaux élevés (Hull *et al.*, 2009). L'autophagie pourrait également jouer un rôle dans la cytotoxicité induite par l'IAPP. La surexpression de l'IAPP humain dans les cellules-β a montré une diminution de l'activité autophagique par les lysosomes, induisant l'apoptose de ces cellules (Morita *et al.*, 2011; Rivera *et al.*, 2011). Dans des

conditions normales, les protéines extracellulaires sont synthétisées dans le RE et sont transportées vers l'appareil de Golgi, pour ensuite se retrouver dans des granules où elles sont entreposées avant leur sécrétion. En cas de repliement aberrant, les protéines mal-repliées/non-repliées (UPR) dans les granules sont ciblées par ubiquitination pour dégradation via les protéasomes. Certains granules fusionnent avec les lysosomes et sont détruits via le système lysosomal. L'IAPP humain est partiellement résistant aux protéases lysosomales. Chez les patients atteints de T2DM, la surexpression de l'IAPP affecte le trafic du RE, déclenchant une réponse UPR et créant un stress du RE qui peut conduire à la mort cellulaire. Des concentrations élevées d'IAPP s'accumulent dans les granules de sécrétion et/ou forment des agrégats dans le cytoplasme. Ceux-ci sont généralement retirés par l'autophagie et ciblés par le système lysosomal. Une surcharge de ce mécanisme de protection peut entraîner une apoptose (Raleigh *et al.*, 2017). À cet effet, Shigihara *et al.* ont observé que chez des souris transgéniques exprimant l'IAPP humain et *knock-down* pour l'*autophagy-related genes* 7 (*Atg7*), inhibant l'autophagie, la toxicité de l'IAPP est accrue (Shigihara *et al.*, 2014). En revanche, une stimulation de l'autophagie par traitement à la rifampicine sur les cellules-β en culture, protège contre la toxicité induite par l'IAPP (Rivera *et al.*, 2011).

Bien que l'implication de l'amyloïdogenèse de l'IAPP dans le T2DM reste à être précisée, plusieurs hypothèses ont été suggérées, comme résumé à la figure 1.13. Sous conditions prédiabétiques, il y a un début d'hyperglycémie et une résistance à l'insuline. Ces symptômes entraînent une augmentation du stress métabolique sur les cellules-β qui doivent produire davantage d'insuline et d'IAPP. La surproduction d'IAPP et d'insuline entraînerait à son tour une augmentation de la présence des peptides d'IAPP dans la matrice extracellulaire à des concentrations suffisamment élevées pour former les noyaux compétents qui déclenchent la fibrillisation de l'IAPP. Les interactions de l'IAPP avec les bicouches lipidiques membranaires (Jha *et al.*, 2009) et les GAGs de la matrice extracellulaire (Jha *et al.*, 2011) pourraient également augmenter la concentration locale d'IAPP. Le processus d'agrégation en amyloïde entraînerait la

dégénérescence des cellules-β pancréatiques par des mécanismes décrits ci-dessus. Ces dernières ne pourraient plus exprimer l'insuline et l'IAPP, aggravant l'hyperglycémie et le stress métabolique sur les cellules-β restantes, exacerbant ainsi davantage la progression du T2DM (DeFronzo, 2004; Montane *et al.*, 2012).

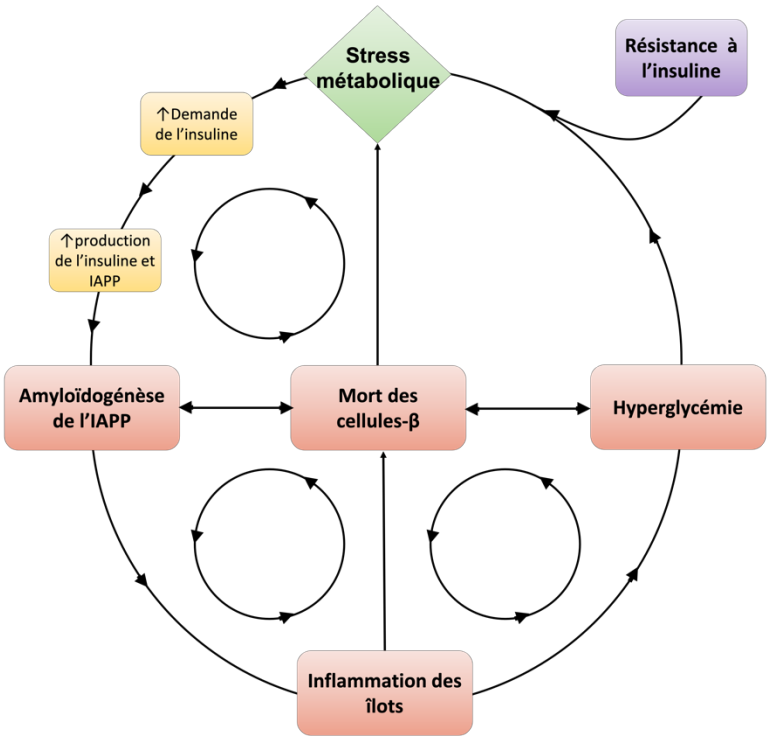


Figure 1.13 Représentation schématique de l'implication de la cascade de l'amyloïdogénèse de l'IAPP dans le diabète de type 2.

Des stress métaboliques sont provoqués par la résistance à l'insuline et l'hyperglycémie, exacerbant la formation d'amyloïdes et l'inflammation des îlots, ce qui entraînera un dysfonctionnement et la mort des cellules-β et, à son tour, aggraverait l'hyperglycémie et le stress métabolique des cellules-β restantes. Figure adaptée de (Montane *et al.*, 2012)

1.6 Inhibiteurs et modulateurs de l'amyloïdogénèse

Au XXIe siècle, le vieillissement de la population mondiale est un phénomène planétaire (Sninate et Bennana, 2018). Ainsi, l'incidence des amyloïdoses augmente rapidement avec l'augmentation de l'espérance de vie. Le développement de stratégies pour inhiber la formation de fibres amyloïdes est donc un domaine d'intérêt majeur et important. De nos jours, il existe 4 principales stratégies afin d'inhiber et/ou moduler l'amyloïdogénèse : (*i*) la stabilisation d'état(s) natif(s) et/ou non susceptible(s) de former des fibres amyloïdes ; (*ii*) l'inhibition de la croissance des fibres amyloïdes en déstabilisant et/ou en remodelant des fibres ; (*iii*) l'inhibition compétitive de l'oligomérisation incluant l'autoreconnaissance des protéines amyloïdogéniques et les interactions avec les cofacteurs de l'amyloïdogénèse ; (*iv*) le développement d'anticorps dirigés contre les espèces toxiques des protéines amyloïdogéniques (Asthana *et al.*, 2018; Soto, 2003).

1.6.1 Stabilisation des états non-amyloïdogéniques

Cette stratégie d'inhibition consiste à détourner les protéines amyloïdogéniques vers des structures moins susceptibles d'avoir un mauvais repliement. Puisque l'amyloïdogénèse est un processus thermodynamique contrôlé, un petit changement dans l'équilibre entre les conformations précurseurs et les conformations compétentes peut avoir un impact important sur la formation d'amyloïdes. Par exemple, avec cette stratégie de stabiliser l'état natif non-amyloïdogénique, le Tafamidis se lie à la conformation homo-tétramérique de la transthyrétine et inhibe sa dissociation en monomères, étape critique dans son processus amyloïdogénique. Le traitement de l'amyloïdose à la transthyrétine avec le Tafamidis est associé à une réduction

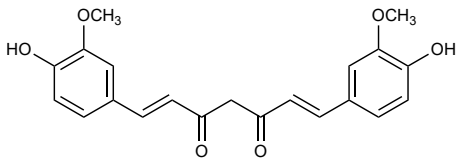
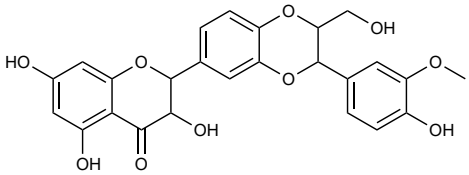
significative de la mortalité, à une baisse des hospitalisations et à une meilleure stabilisation de la transthyrétine par rapport au placebo (Park *et al.*, 2019). Le Tafamidis, connu sous d'autres noms, Vyndaqel ou Vyndamax, est la seule molécule qui est approuvée et utilisée en clinique pour traiter les patients atteints d'amyloïdose systémique sénile. Pour l'IAPP, qui est un peptide intrinsèquement désordonné, cette stratégie consiste à stabiliser les conformations moins amyloïdogéniques, notamment la structure en hélice-α. Des études ont permis de développer des polymères mimant l'hélice-α (Hassanpour *et al.*, 2014; Hebda *et al.*, 2009) et des foldamères oligoquinones chargées négativement (Kumar *et al.*, 2016), ayant pour but de stabiliser la conformation hélicoïdale. Par conséquent, l'agrégation de L'IAPP est inhibée. En outre, les penta- et hexa-peptides du segment 22-27 (NFGAIL) de la séquence de l'IAPP, chez qui l'acide aminé non naturel α, β-dihydroxyphénylalanine (DF) a été substitué aux résidus hydrophobes, ont montré une inhibition de la fibrillation et de la cytotoxicité (Mishra *et al.*, 2013). Dans une approche différente, il a été démontré que la protéine phycocyanine, complexée avec le sélénium, interfère avec la fibrillation de l'IAPP, en convertissant le peptide vers la formation de sphéroïdes non cytotoxiques qui empêchent l'apoptose des cellules-β (Li *et al.*, 2014).

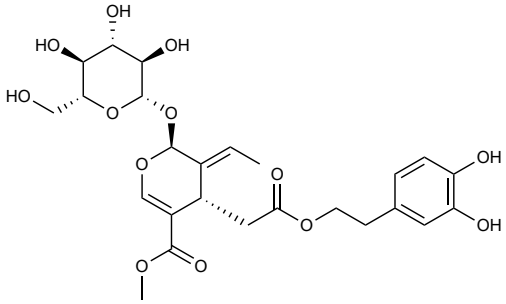
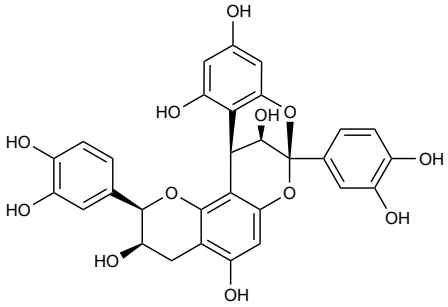
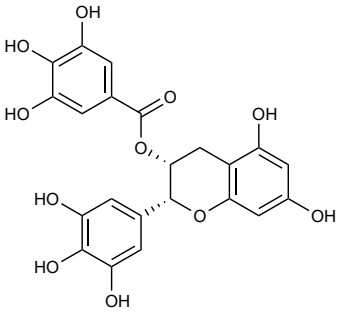
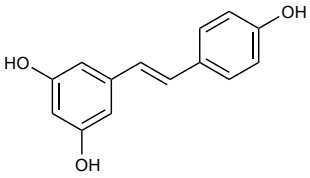
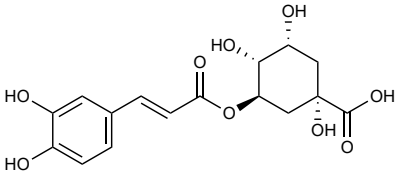
1.6.2 Inhibiteurs de la croissance des fibres amyloïdes

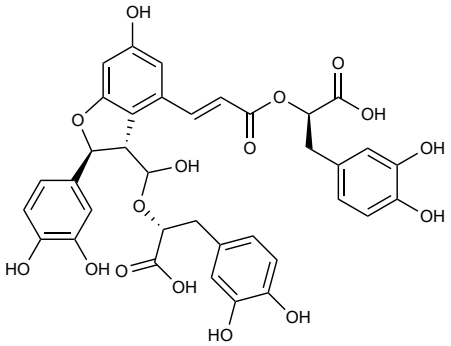
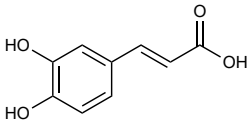
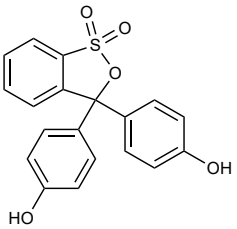
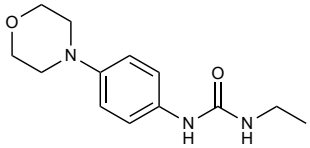
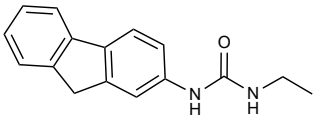
Il a été signalé qu'un certain nombre de petites molécules ont des effets inhibiteurs sur la formation des fibres d'IAPP (Tableau 1.9). Par exemple, le (-)-épigallocatéchine gallate (EGCG) extrait de fruits comme la framboise, le bleuet, la grenade et le raisin réduit considérablement la fibrillisation de l'IAPP (Kao *et al.*, 2015). Il a été démontré que l'EGCG inhibe l'ensemencement de la formation de fibres d'IAPP et protège les cellules-β INS-1 de rat contre la toxicité induite par l'IAPP (Meng *et al.*, 2010b). En plus de ses effets inhibiteurs, l'EGCG semble remodeler et perturber les fibres

amyloïdes d'IAPP une fois que celles-ci se sont formées (Cao et Raleigh, 2012). Les résidus qui interagissent avec l'EGCG comprennent Phe-23, Ala-25, Ile-26, Leu-27 et Tyr-37 (Wang *et al.*, 2014b). Une étude récente en dynamique moléculaire discrète (DMD) a indiqué que les composés polyphénols, la curcumine et le resvératrol interagissent avec l'IAPP via des liaisons hydrogène, des interactions π-π et des interactions hydrophobes, stabilisant ainsi les intermédiaires *off-pathway* (Ehrnhoefer *et al.*, 2008 ; Ladiwala *et al.*, 2011; Nedumpully-Govindan *et al.*, 2016). D'autre part, le resvératrol montre des effets inhibiteurs sur la formation de fibres de l'IAPP (Jiang *et al.*, 2011; Radovan *et al.*, 2009). En fait, le resvératrol se lie à l'His-18, inhibant la formation d'intermédiaires oligomères précoces lors de la fibrillisation de l'IAPP (Wei *et al.*, 2011). Dans une autre étude, de petites molécules dérivées du N-phényle-N'-(2-éthyle) urées (EU-362 et EU-418) ont montré une capacité à abroger l'oligomérisation de l'IAPP, protégeant les cellules (Fortin *et al.*, 2016). D'autres molécules ayant montré une capacité à inhiber l'amyloidogenèse de l'IAPP sont présentées au tableau 1.9.

Tableau 1.8 Exemples de molécules pouvant inhiber la formation de fibres amyloïdes d'IAPP.

Nom du composé	Structure moléculaire	Référence
Curcumine		(Nedumpully-Govindan *et al.*, 2016; Sparks *et al.*, 2012)
Silibinine		(Cheng *et al.*, 2012; Raimundo *et al.*, 2020)

Oleuropéine		(Rigacci *et al.*, 2010)
Proanthocyanidine A2		(Jiao *et al.*, 2013)
EGCG		(Bieschke *et al.*, 2010; Cao et Raleigh, 2012; Ehrnhoefer *et al.*, 2008; Jiao *et al.*, 2013; Wang *et al.*, 2014b; Young *et al.*, 2014)
Resvératrol		(Jiang *et al.*, 2011; Radovan *et al.*, 2009)
Acide clorogénique		(Cheng *et al.*, 2011)

Acide salvianolique B		(Cheng *et al.*, 2013)
Acide caféique		(Cheng *et al.*, 2011)
Rouge de phénol		(Porat *et al.*, 2004; Wu *et al.*, 2006)
EU-362		(Fortin *et al.*, 2016)
EU-418		(Fortin *et al.*, 2016)

En plus des petites molécules, un certain nombre d'analogues peptidiques de l'IAPP peuvent inhiber la croissance d'amyloïdes d'IAPP. Certaines mutations de la proline dans la région 20–29 convertissent l'IAPP en un puissant inhibiteur (Abedini *et al.*, 2007). Le fragment 13-18 (ANFLVH) de l'IAPP possède des pouvoirs inhibiteurs de la formation des fibres (Potter *et al.*, 2009). Également, le fragment $IAPP_{13-18}$ inhibe fortement la formation de fibres et diminue la cytotoxicité de la forme longue de l'IAPP (Obasse *et al.*, 2017). Une variante de l'IAPP N-méthylé s'est également révélée être un inhibiteur très efficace de la formation des fibres amyloïdes et de la cytotoxicité de

l'IAPP (Yan *et al.*, 2006). D'autre part, il a été montré récemment que les γ-peptides, similaires au fragment amyloïdogénique de l'Aβ (KLVFF), inhibent l'agrégation de l'IAPP (Bolarinwa *et al.*, 2020). Ces composés peptidiques pourraient fonctionner comme inhibiteur en ciblant des espèces intermédiaires oligomériques.

1.6.3 Inhibiteurs des interractions avec les cofacteurs de l'amyloïdogénèse

Comme mentionné dans la section 1.4.2.2, les dépôts amyloïdes sont associés à de nombreux co-facteurs tels que les GAGs. Ces composés peuvent moduler l'auto-assemblage amyloïde et, par conséquent, la cytotoxicité sous-jacente. Ainsi, l'inhibition des interactions entre l'IAPP et les GAGs serait une approche potentielle pour inhiber la cytotoxycité induite par les assemblages d'IAPP. De courts fragments d'héparine contenant de deux à huit monomères de saccharides ont protégé les cellules-β contre la toxicité de l'IAPP (Jha *et al.*, 2011). Les courts fragments d'héparine pourraient inhiber de manière compétitive la liaison de l'IAPP avec les GAGs endogènes (Saridaki *et al.*, 2012). Sur le même principe, des composés sulfatés, tels que l'acide fuchsine et le *fast green* FCF, qui miment les groupes sulfates des GAGs, inhibent à la fois la formation d'amyloïdes d'IAPP et l'effet accélérateur des GAGs (Meng et Raleigh, 2011). Ainsi, de petites molécules qui compétitionnent avec les GAGs pour la liaison aux protéines amyloïdogéniques pourraient servir d'inhibiteurs potentiels de l'amyloïdogenèse *in vivo*.

1.6.4 Les anticorps dirigés contre les assemblages amyloïdogéniques

Cette stratégie consiste en une immunisation contre les assemblages d'amyloïdes avec la génération d'anticorps dirigés contre les dépôts amyloïdes. L'immunisation du peptide Aβ associé à la maladie d'Alzheimer était initialement très prometteuse. Malheureusement, l'immunisation contre l'Aβ a entraîné des symptômes de méningo-encéphalite chez un sous-groupe de patients soumis à des essais cliniques, et les essais ont été interrompus (Schenk, 2002). D'autre part, le développement d'anticorps plus spécifiques contre les dépôts amyloïdes implique la génération d'anticorps conformationnels dirigés spécifiquement contre les oligomères ou les protofilaments, réduisant ainsi leur toxicité. Par exemple, l'anti-Aβ, mAb158, est capable de se lier sélectivement aux protofilaments de Aβ solubles, réduisant leur déposition dans le liquide céphalo-rachidien des souris transgéniques exprimant le mutant E22G de l'Aβ (Tucker *et al.*, 2015). Les essais cliniques de phase I ont montré qu'avec des anticorps BAN-2401, un mAb158 version humanisée, aucun effet secondaire n'a été observé (Logovinsky *et al.*, 2016). Une étude de phase II recrute actuellement des participants pour déterminer l'efficacité clinique du BAN-2401 sur les patients ayant des troubles cognitifs légers et des caractères AD légers. Quant à l'IAPP, des oligomères toxiques d'IAPP se forment chez des souris transgéniques exprimant l'IAPP humain, et les anticorps anti-oligomères toxiques n'empêchent pas l'apoptose des cellules-β induite par l'IAPP (Lin *et al.*, 2007). En conclusion, ceci suggère que les trois premières stratégies pourraient être plus utiles qu'une approche basée sur la vaccination dans le but de prévenir les maladies associées aux amyloïdes, notament, la prévention du diabète de type 2.

1.7 Problématique, hypothèse et objectifs

Au cours des dernières années, plusieurs études ont été effectuées afin de mieux comprendre la pathogénicité de l'IAPP et l'implication des dépôts amyloïdes dans le

diabète de type II. Les travaux de recherche concernant le développement d'agents anti-amyloïdogéniques doivent être supportés par des études mécanistiques du processus de formation des fibres amyloïdes et de toxicité afin de cibler précisément les espèces cytotoxiques de l'amyloïdogenèse. Cependant, l'élucidation des mécanismes de l'auto-assemblage amyloïde de l'IAPP s'avère difficile du fait que ce processus est hautement dynamique, difficilement contrôlable et fait intervenir de nombreuses conformations *off-* et *on-pathway*. De ce fait, l'identification des espèces toxiques formées lors de la formation des amyloïdes ainsi que leur mode d'action sur le dysfonctionnement cellulaire demeure un défi et une priorité. Le manque de compréhension dans le mécanisme de formation des fibres et des conformations causant la mort cellulaire empêche le développement d'agents anti-amyloïdogéniques. En conséquence, l'exploration de différents outils moléculaires demeure nécessaire afin d'augmenter les connaissances sur la pathogénicité de l'IAPP et de moduler et/ou d'abroger les dépôts d'amyloïdes pancréatiques.

1.7.1 Hypothèse

Nous supposons que les facteurs internes et externes, tels que les modifications post-traductionnelles non-enzymatiques, les substitutions ciblées d'acides aminés et des composés chimiques modulateurs de l'auto-assemblage amyloïde, contrôlent le processus d'amyloidogenèse et donc, la cytotoxicité sous-jacente. Par l'étude de ces effets mécanistiques, les déterminants physico-chimiques et conformationels de l'oligomérisation et de l'auto-assemblage pourront être élucidés. De plus, les études des relations auto-assemblage-toxicité pourraient également conduire à l'identification de chaînes latérales spécifiques qui modulent les voies d'agrégation et à la détection d'assemblages conformationnels distincts avec des mécanismes spécifiques de toxicité,

supportant ainsi la compréhensionde la pathogénicité de l'IAPP ainsi que son implication dans le diabète de type II.

1.7.2 Objectifs

L'objectif global de ce projet de thèse consiste à étudier les déterminants moléculaires modulant l'auto-assemblage amyloïde de l'IAPP afin de mieux comprendre les caractéristiques physicochimiques et conformationnelles de ce processus et des espèces quaternaires cytotoxiques. Pour ce faire, les trois objectifs spécifiques suivants seront ciblés :

1. Élucider le rôle de la désamidation des asparagines de l'IAPP sur le mécanisme moléculaire de formation des fibres amyloïdes et la cytotoxicité des espèces protéiques quaternaires.

2. Étudier les relations structure -auto-assemblage de l'IAPP en ciblant la position Asn-21 afin d'identifier les caractéristiques physicochimiques et conformationnelles associées à la cytotoxicité.

3. Évaluer la modulation de l'auto-assemblage et de la cytotoxicité de l'IAPP par des composés chimiques dendritiques multi-fonctionnalisés.

CHAPITRE II

ARTICLE I

ROLE OF SITE-SPECIFIC ASPARAGINE DEAMIDATION IN ISLET AMYLOID POLYPEPTIDE AMYLOIDOGENESIS: KEY CONTRIBUTIONS OF RESIDUES 14 AND 21

Phuong Trang Nguyen, Ximena Zottig, Mathew Sebastiao and Steve Bourgault

Manuscrit publié dans le journal *Biochemistry*, 56(29):3808-3817

doi: 10.1021/acs.biochem.7b00209.

Contribution des auteurs:

Phuong Trang Nguyen : Conception du projet, réalisation des expériences (synthèse et purification des peptides, assemblage des peptides *in vitro*, essais cinétiques par fluorescence de ThT, analyses des conformations secondaires par CD, analyses par

AFM, essais cellulaires, traitements des résultats, analyses statistiques des résultats, rédaction de l'article.

Ximena Zottig : Exécution des analyses en microscopie électronique.

Mathew Sebastiao : Exécution des analyses en microscopie électronique des expériences de co-assemblage des peptides.

Steve Bourgault : Supervision du projet, préparation des figures, correction de l'article.

NOTE : Les références de l'article sont incluses dans la bibliographie générale de la thèse

Role of Site-Specific Asparagine Deamidation in Islet Amyloid Polypeptide Amyloidogenesis: Key Contributions of Residues 14 and 21

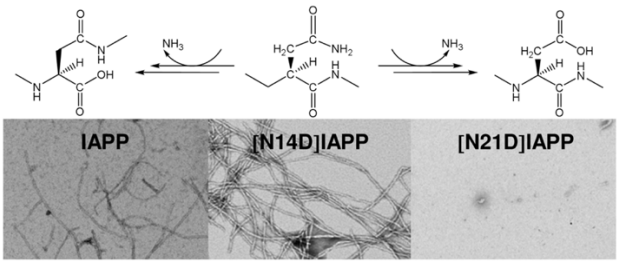
Phuong Trang Nguyen, Ximena Zottig, Mathew Sebastiao and Steve Bourgault*

Department of Chemistry, University of Québec in Montreal, Montreal, *C.P. 8888, Succursale Centre-Ville, Montreal, H3C 3P8, Canada*

Quebec Network for Research on Protein Function, Engineering, and Applications, PROTEO

*To whom correspondence should be addressed. E-mail: bourgault.steve@uqam.ca

Keywords: Amyloid / Asparagine Deamidation / Self-assembly / Islet Amyloid Polypeptide / Type II diabetes.



2.1 Résumé

La désamidation d'asparagine est une modification post-traductionnelle non-enzymatique spontanée qui se traduit par la conversion de l'asparagine en un mélange d'acide aspartique et d'acide isoaspartique. Cette conversion chimique module la conformation des protéines et les propriétés physicochimiques, ce qui pourrait entraîner un mauvais repliement et l'agrégation des protéines. Dans cette étude, nous avons étudié les effets de la désamidation d'asparagine sur l'amyloïdogénicité d'un peptide amyloïdogénique, l'*islet amyloïd polypeptide* (IAPP). Ce dernier est une hormone peptidique à 37 résidus dont la déposition sous forme de fibres amyloïdes insolubles est étroitement associée au diabète de type 2. Les résidus Asn ont été successivement remplacés par un Asp ou un isoAsp, et la formation d'amyloïdes a été évaluée par un test de fluorescence de la thioflavine T, la spectroscopie de dichroïsme circulaire, la microscopie à force atomique et la microscopie électronique à transmission. Alors que la désamidation d'asparagine en position 21 inhibait la conversion conformationnelle de l'IAPP et la formation d'amyloïdes, la mutation N14D accélérait l'auto-assemblage et conduisait à la formation de fibres amyloïdes longues et épaisses. En revanche, l'IAPP était tolérant à la désamidation successive des résidus Asn 22, 31 et 35. La présence d'un faible rapport molaire d'IAPP désamidé en position 14 favorisait la formation de noyaux et l'élongation à partir de l'IAPP sauvage. En outre, en utilisant la lignée cellulaire β-pancréatique INS-1E, nous avons observé que la désamidation d'asparagine ne modifiait pas significativement la toxicité induite par l'IAPP. Ces données indiquent d'une part que la désamidation d'asparagine peut moduler la formation de fibres amyloïdes d'IAPP et la morphologie des fibres, mais pas la cytotoxicité, et d'autre part que le site de modification joue un rôle critique sur l'améloïdogénèse du peptide. Globalement, cette étude renforce la notion que l'amyloïdogenèse de l'IAPP est gouvernée par des interactions intermoléculaires précises impliquant des chaînes latérales d'asparagine.

2.2 Abstract

Deamidation of asparagine residue is a spontaneous non-enzymatic post-translational modification that results in the conversion of asparagine into a mixture of aspartic acid and iso-aspartic acid. This chemical conversion modulates protein conformation and physicochemical properties, which could lead to protein misfolding and aggregation. In this study, we investigated the effects of site-specific Asn deamidation on the amyloidogenecity of the aggregation-prone peptide islet amyloid polypeptide (IAPP). IAPP is a 37-residue peptidic hormone whose deposition as insoluble amyloid fibrils is closely associated with type-2 diabetes. Asn residues were successively substituted by an Asp or isoAsp and amyloid formation was evaluated by thioflavin T fluorescence assay, circular dichroism spectroscopy, atomic force microscopy and transmission electron microscopy. Whereas deamidation at position 21 inhibited IAPP conformational conversion and amyloid formation, the mutation N14D hastened self-assembly and led to the formation of long and thick amyloid fibrils. In contrast, IAPP was somewhat tolerant to the successive deamidation of Asn residues 22, 31 and 35. Interestingly, a small molar ratio of IAPP deamidated at position 14 promoted the formation of nucleating species and the elongation from unmodified IAPP. Besides, using the rat pancreatic beta cell line INS-1E, we observed that site-specific deamidation did not significantly alter IAPP-induced toxicity. These data indicate that Asn deamidation can modulate IAPP amyloid formation and fibrils morphology and that the site of modification plays a critical role. Above all, this study reinforces the notion that IAPP amyloidogenesis is governed by precise intermolecular interactions involving specific Asn side chains.

2.3 Introduction

Non-enzymatic post-translational modifications (PTMs) of proteins are spontaneous covalent alterations, often irreversible, of residue side chains and/or polypeptide backbone. These PTMs, including glycation, nitration and deamidation, can alter dramatically the structure, stability, dynamics and/or aggregation propensity of proteins and can have profound biological implication (Augner *et al.*, 2014; Carrell et Lomas, 1997; Kelly, 1998). Accumulated experimental evidence has highlighted the contributions of spontaneous PTMs in protein misfolding diseases associated with polypeptide aggregation and amyloid deposition (Nilsson, 2008). Glutamine and asparagine deamidation, the most common non-enzymatic PTM, is associated with amyloid assembly of many aggregation-prone polypeptides, including γD-crystallin related to cataracts (Flaugh *et al.*, 2006), the amyloid-β (Aβ) peptide associated with the Alzheimer's disease (Roher *et al.*, 1993; Shimizu *et al.*, 2002), the α-synuclein related to Parkinson's disease (Robinson *et al.*, 2009) as well as immunoglobulin light chain associated with AL amyloidosis (Murphy *et al.*, 2011). For instance, significant levels of Gln-3, Asn-7 (Tottori-Japanese mutant) and Asn-23 (Iowa mutant) deamidation were identified in *ex vivo* fibrils of Alzheimer's disease patients (Harigaya *et al.*, 2000; Shimizu *et al.*, 2002; Shimizu *et al.*, 2005). Similarly, β2-microglobulin amyloid deposits isolated from patients afflicted with haemodialysis-related amyloidosis were shown to be deamidated at positions 17 and 42 (Odani *et al.*, 1990). By proteomic profiling it was recently reported that brain amyloid plaques extracted from patients afflicted with dementia-linked amyloidosis are enriched in various deamidated proteins (Adav *et al.*, 2016). These studies highlight that deamidation plays a key role in the etiology of amyloid-related diseases by initiating and/or enhancing protein self-assembly, although mechanistic details remain sparse. Besides,

deamidation can also occur upon protein deposition, uncovering the long-lived nature of amyloids.

Asn deamidation is a spontaneous PTM that consists of the conversion of an Asn residue to a mixture of Asp/isoAsp (Aswad *et al.*, 2000). This reaction is initiated by the nucleophilic attack of the α-amino of the C-neighboring residue on the carbonyl Asn side chain, leading to the formation of a cyclic succinimidyl intermediate (Figure 2.1A). This 5-member cyclic imide rapidly hydrolyzes into either aspartic acid or isoaspartic acid. Generally, a mixture composed of 60 to 85% of the L-iso-Asp and 15 to 40% of L-Asp with low amounts of D-Asp and D-isoAsp is obtained (Aswad *et al.*, 2000; Geiger et Clarke, 1987). The rate at which Asn deamidates varies depending on the primary sequence and tridimensional conformation of protein (Robinson et Robinson, 1991). For instance, the presence of a small and unbranched amino acid, such as Gly, Ala or Ser, at the C-terminal side of Asn enhances the rate of deamidation, whereas bulkier and branched residues decrease the rate of the reaction (Robinson et Robinson, 1991; Shi *et al.*, 2013). When an isoAsp is generated, deamidation reaction introduces a non-native CH_2 group into the polypeptide backbone and leads to the formation of a rotatable bond in the backbone (Dunkelberger *et al.*, 2012; Geiger et Clarke, 1987). This PTM introduces a negative charge within the protein sequence. Thus, Asn deamidation leads to perturbations of both the conformation and the physico-chemical properties of a protein and, accordingly, can modulate its propensity to self-assemble.

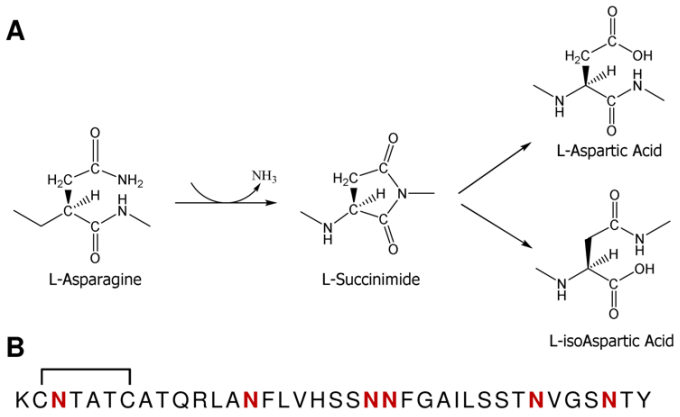


Figure 2.1 (A) Asn deamidation via the hydrolysis of the succinimide intermediate. (B) Sequence of human IAPP with Asn residues in red bold. IAPP has a disulfide bond between Cys-2 and Cys-7 and a C-α-amidated C-terminus.

The gluco-modulatory pancreatic hormone islet amyloid polypeptide (IAPP), or amylin, is a 37-residue peptide encompassing 6 Asn residues (Figure 2.1B) and several of these residues can be readily deamidated under physiological conditions (Dunkelberger *et al.*, 2012; Hekman *et al.*, 1998; Hekman *et al.*, 1999; Nilsson *et al.*, 2002). IAPP is an unusual aggregation-prone peptide whose deposition in the forms of amyloid fibrils in the islets of Langerhans is associated with type-II diabetes (Westermark *et al.*, 2011). The presence of insoluble IAPP deposits observed in the pancreas is known to accelerate type-II diabetes pathogenesis by exacerbating β-cell degeneration and, ultimately, compromising insulin secretion (Westermark *et al.*, 2011). IAPP rarely deposits in the pancreas of healthy individuals, although it is stored in the insulin secretory granule in non-diabetic subjects at a local concentration sufficiently high to form amyloid fibrils (Westermark, 2011). This suggests that other factors, such non-enzymatic PTMs could trigger IAPP amyloidogenesis in diabetic patients (Cao *et al.*, 2013; Jeong et An, 2015; Nguyen *et al.*, 2015). It was reported that IAPP deamidation under physiological conditions accelerates amyloid formation and that non-uniformly deamidated fibrils contain reduced amounts of β-sheet compared to

those assembled from wild-type sequence (Dunkelberger *et al.*, 2012). Moreover, low levels of Asn deamidation of a non-amyloidogenic 10-residue variant of $IAPP_{20-29}$ (SNNFPAILSS) led to the formation of aggregates that have amyloid-like characteristics (Nilsson *et al.*, 2002). IAPP is a positively charged C-α-amidated peptide that displays no negative charge and 3 positive charges (Figure 2.1B). Considering that deamidation introduces a negative charge in the peptide sequence and that aggregation is usually favored when the net charge of the protein is closer to zero (Chiti *et al.*, 2002; Nilsson, 2008), Asn deamidation is anticipated to have an effect on IAPP self-assembly.

Whereas the effect of untargeted Asn deamidation has been reported for IAPP (Dunkelberger *et al.*, 2012) and its non-amyloidogenic variant segment 20-29 (Nilsson *et al.*, 2002), no study has precisely addressed the contributions of each Asn to Asp/isoAsp substitutions. The specific Asn residue subjected to deamidation likely dictates the effects on amyloid assembly and different deamidation sites could result in opposite effect on IAPP self-assembly. In this context, we investigated the roles of site-specific Asn deamidation on IAPP amyloid formation by successively substituting Asn residues by an Asp and isoAsp. According to the deamidation site, divergent effects were observed on the kinetics of self-assembly and on the morphology of the resulting amyloid fibrils. We observed key contributions of positions 14 and 21 in the nucleation and elongation phases of IAPP amyloidogenesis. Although studies have revealed that deamidation prompts the aggregation of amyloidogenic polypeptides, this study reinforces the notion that the site of Asn deamidation plays a critical role in this effect.

2.4 Materials and Methods

2.4.1 Peptide Synthesis and Purification

All peptides were synthesized on a Tribute peptide synthesizer (Protein Technologies) using Fmoc chemistry and a 2-(6-chloro-1-H-benzotriazole-1-yl)-1,1,3,3-tetramethylaminium hexafluorophosphate (HCTU) coupling strategy, as previously described (De Carufel *et al.*, 2013). According to the strategy previously developed by Raleigh, oxazolidine pseudoproline dipeptide derivatives were incorporated to facilitate the synthesis (Abedini et Raleigh, 2005). Asn residues were subsequently substituted by Asp or isoAsp. Peptides were cleaved from the resin using a mixture of trifluoroacetic acid (TFA), ethanedithiol (EDT), phenol and water. After filtration and evaporation of the cleavage mixture, peptides were precipitated and washed with diethylether. Crude peptides were purified by reverse-phase high performance liquid chromatography (RP-HPLC). To increase solubility, crude peptides were dissolved in 35% acetic acid (v/v) before being injected on a preparative C_{18} column (Phenomenex) using a linear gradient of acetonitrile (ACN) in H_2O/TFA (at 0.6% v/v). Collected fractions were analyzed by analytical RP-HPLC using an Aeris peptide XB C_{18} column (Phenomenex) and by 'time of flight' mass spectrometry using a LC/MS-TOF (Agilent). Fractions corresponding to the desired peptide with purity higher than 95% were pooled and lyophilized. Disulfide bond formation between Cys-2 and Cys-7 was achieved by dimethyl sulfoxide (DMSO) oxidation under mild agitation overnight. Peptides were repurified by RP-HPLC as described above. The formation of disulfide bond was confirmed by treating, or not, peptide with a mixture of dithiothreitol and β-mercaptoethanol and by comparative analyses of the treated and nontreated samples with analytical RP-HPLC.

2.4.2 IAPP Sample Preparation

Aliquots of monomerized IAPP were prepared by dissolving the lyophilized and purified peptide in 100% hexafluoro-2-propanol (HFIP) to a concentration of 1 mg/mL. The solution was sonicated for 30 min and filtered through a 0.22 μm hydrophilic PVDF filter before being lyophilized. The resulting peptide powder was solubilized for a second time in HFIP, sonicated for 30 min and the solution was aliquoted (500 to 100 μg aliquots) and lyophilized. Peptide concentrations were validated by measuring absorbance at 280 nm using a theoretical molar extinction coefficient of 1490 M^{-1} cm^{-1} Monomerized IAPP samples were kept dried at -80°C until used, but not for longer than 4 weeks.

2.4.3 Kinetics of Amyloid Formation

Peptide solutions were prepared by dissolving the lyophilized and monomerized peptides at a concentration of 50 μM in 20 mM Tris, pH 7.4 containing 40 μM thioflavin T (ThT). Assays were performed at 25°C without stirring in sealed black-wall, clear-bottom 96-well non-binding surface plates (Corning) with a total volume of 100 μL per well. Final peptide concentrations varied between 1 to 50 μM and ThT concentrations was constant at 40 μM. Fluorescence was measured every 10 min over the course of 20 h, using an Infinite M1000pro fluorescence plate reader (TECAN). The fluorescence, with excitation at 440 nm and emission at 485 nm, was measured from the bottom of the well. For each experiment, control reactions (without IAPP) were carried. Data obtained from triplicate wells were averaged, corrected by subtracting the corresponding control reaction, and plotted as fluorescence *vs* time.

Data of time-dependence of ThT fluorescence were fitted to a sigmoidal Boltzmann model where T_{50} is the time required to reach half of the fluorescence intensity, *k* is the apparent first-order constant and Y_{max} and Y_0 are, respectively, the maximum and initial fluorescence values:

$$Y = \frac{Y_0 + (Y_{max} - Y_0)}{1 + e^{-(T - T_{50})/k}}$$

The lag time (the time before detectable amyloid formation occurs), as predicted by means of the nucleation dependent polymerization model, is described as $T_{50} - 2/k$. Data (lag time and final ThT) of at least four different lots of peptides were averaged and were expressed as the mean ± S.D.. Evaluation of the results was made using the Student's t-test and statistical difference (between wild-type IAPP and deamidated IAPP) was established at $P < 0.05$.

2.4.4 Circular Dichroism Spectroscopy

Lyophilized aliquots of monomerized IAPP and its deamidates derivatives were dissolved in 20 mM Tris-HCl, pH 7.4 at 50 μM and incubated at 25°C without agitation. At the desired time of incubation, samples were incorporated into a 2 mm path length quartz cell. Far-UV CD spectra were recorded from 190 to 260 nm using a J-815 CD spectropolarimeter (Jasco) at 25°C. The wavelength step was set at 0.5 nm with an average time of 10 s per scan at each wavelength step. Each collected spectrum was background subtracted with peptide-free buffer. The raw data was converted to mean residue ellipticity (MRE) using the following formula:

$$MRE\ (deg.cm^2.dmol^{-1}) = \frac{Mean\ residue\ weight\ (g.mol^{-1}) \times CD\ signal\ (\text{deg})}{10\ \times pathlength\ (cm) \times peptide\ cencentration\ (g.mL^{-1})}$$

2.4.5 Transmission electron microscopy

Lyophilized and monomerized IAPP peptides were solubilized in 20 mM Tris-HCl, pH 7.4, at a final concentration of 50 μM. The solution was incubated for 24 hours at 25°C without agitation before being diluted to 5 μM in deionized water. Solutions were immediately applied to glow-discharged carbon films on 300 mesh copper grids. After adsorption for 1 min and air-blotting, samples were negatively stained with 1.5% uranyl formate for 1 min and air-dried for 15 minutes. Images were recorded using a FEI Tecnai 12 BioTwin microscope operating at 120 kV and equipped with an AMT XR80C CCD camera system.

2.4.6 Atomic force microscopy

Lyophilized and monomerized IAPP peptides were solubilized in 20 mM Tris-HCl, pH 7.4 at a final concentration of 50 μM. Solution was incubated for 24 hours at 25°C without agitation before being diluted to 5 μM in 1% acetic acid and immediately applied to freshly cleaved mica, as previously reported (Nguyen *et al.*, 2016). The mica was washed twice with deionized water and air-dried for 24 hours after blotting. Images were acquired on a Veeco/Bruker Multimode AFM using tapping mode with a silicon tip (2-12 nm tip radius, 0.4 N/m force constant) on a nitride lever. Images were taken at 0.2 Hz and 1024 scan/minute. For quantification analysis, the width and length of at

least 50 individual fibrils per experiments were determined and plotted as a frequency distribution using the Prism 6.0 software. Data (height and length) of at least three individual experiments performed with different lots of peptides were averaged and were expressed as the mean ± S.E.M.

2.4.7 Cytotoxicity Assay

Rat INS-1E (pancreatic β-cell line) cells were seeded in black wall clear bottom 96-well plates (Tissue culture treated) at a density of 30 000 cells/well (100 µl/well) in RPMI-1640 medium supplemented with 10% FBS, 2 mM L-glutamine, 100 U/ml penicillin, 100 mg/ml streptomycin, 10 mM HEPES, 1 mM sodium pyruvate, 50 mM β-mercaptoethanol. After 48 h incubation at 37°C in a 5% CO_2, cells were treated by adding 50 µl of IAPP derivatives solutions at 3× of final concentrations (50 µM to 3 µM) solubilized in 20 mM Tris, pH 7.4. Cells were incubated for specific time (4 h to 120 h) and cellular viability was measured by the resazurin reduction assay. Cell viability (in %) was calculated from the ratio of the fluorescence of the treated sample to the control cells (non-treated). Data (in %) of at least four lots of peptides were averaged and were expressed as the mean ± S.D. Results were analyzed using the Student's t-test and statistical difference (between IAPP and deamidated derivatives) was established at $P < 0.05$. Statistical analysis was performed using Prism 6.0 software.

2.5 Results

2.5.1 Effect of Asn Deamidation on the Kinetics of Self-Assembly

IAPP is a positively charged peptide that encompasses six Asn residues. Asn deamidation leads to the substitution of a neutral residue by a negatively charged residue (Asp/isoAsp) and reduces IAPP net charge and, perhaps, solubility. Moreover, incorporation of a CH_2 group into the backbone affects the conformation and backbone flexibility of peptides. Thus, we initially probed the effects of the successive substitutions of residues Asn-14, Asn-21, Asn-22, Asn-31 and Asn-35 by an Asp and isoAsp on the kinetics of self-assembly. We did not study the effect of Asn-3 deamidation since the segment 1-7 is not part of the amyloid core (Luca *et al.*, 2007) and that the segment 8-37 exhibits similar fibrillization kinetics of that full length IAPP (Koo *et al.*, 2008; Koo et Miranker, 2005). Amyloid formation was monitored by measuring the fluorescence of the amyloid-specific dye ThT, a small molecule that exhibits an increase of its fluorescence upon specific binding to the amyloid cross-β-sheet quaternary structure (Naiki *et al.*, 1989). Under the conditions of our fibrillization assay, *i.e.* pH 7.4, 25°C, non-binding surface microplates and quiescent conditions, IAPP at 12.5 μM showed a lag phase of 5.8 h and a T_{50} of 9.5 h (Figure 2.2 and Figure S2.1). The lag time corresponds to the time before detectable amyloid formation occurs whereas the T_{50} is the time required to reach half of the maximum ThT fluorescence. Asn deamidation modulated IAPP amyloid formation and these effects varied according to the deamidation site (Figure 2.2). For instance, substitution of Asn14 by Asp accelerated amyloid formation and led to a significantly higher ThT fluorescence after 20 hours incubation. Thus, incorporation of a negatively charged residue at position 14 with an equivalent chain length, *i.e.* Asn→Asp mutation, enhances IAPP

amyloidogenicity. Reducing Asp14 chain length and/or introducing a CH_2 surrogate into the polypeptide backbone counteracted these effects as observed from the kinetics of [N14isoD] IAPP. Sequential incorporations of an Asp or an isoAsp residue at positions 22, 31 and 35 affected modestly the kinetics of IAPP assembly, with the mutants N22D, N31isoD and N35isoD showing a slightly significant lower ThT fluorescence after 20 h incubation (Figure 2.2C). In sharp contrast, incorporation of a negative charge at position 21, *i.e.* N21D and N21isoD mutations, inhibited amyloid assembly. The striking difference in the kinetics of IAPP amyloidogenesis between N21D and N22D strengthens the notion that the self-association of IAPP is driven by highly specific interactions. Concurrent substitutions of the 6 Asn residues by Asp and isoAsp led to derivatives, [NXD] IAPP and [NXisoD] IAPP, which do not form ThT-positive proteospecies, owing the incorporation of 6 negative charges on the peptide (Figure S2.2).

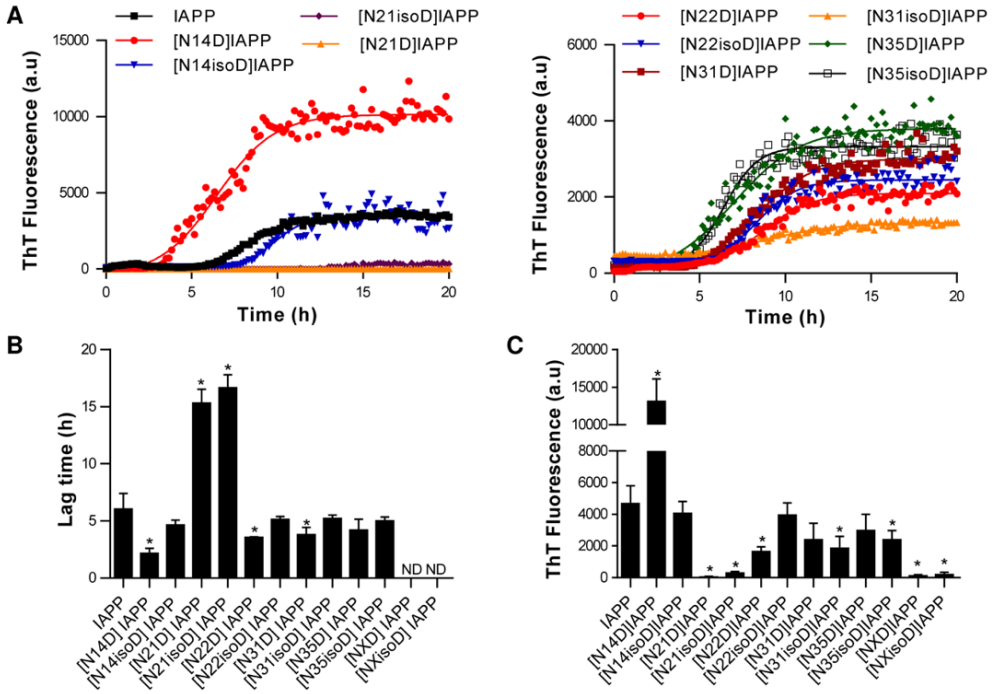


Figure 2.2 Effect of site-specific Asn deamidation on the kinetics of IAPP amyloid formation.

(A) Representative kinetics of amyloid assembly of IAPP (■, left panel) and its deamidated derivatives monitored by ThT fluorescence. Peptides were incubated at 12.5 μM under quiescent conditions at 25°C in 10 mM Tris-HCl buffer, pH 7.4 and the fluorescence of ThT (40 μM) was measured every 10 min with excitation at 440 nm and emission at 485 nm. The curves represent the best fit from the sigmoidal growth model. (B) Lag time and (C) final ThT fluorescence of the kinetics of fibril formation. (B, C) Data represent mean ± S.E.M. of at least four experiments performed in triplicate. [NXD] and [NXisoD]; substitutions of the 6 Asn residues by Asp and isoAsp, respectively.

2.5.2 Effect of Asn Deamidation on the conformational transition

In its monomeric state in aqueous solution, IAPP exhibits mainly a random coil structure characterized by the presence of transient helical motif (Williamson et Miranker, 2007). As observed in Figure 2.3, the CD spectra of freshly solubilized IAPP displayed a single minimum at around 201 nm, indicating a random coil conformation. Upon incubation under the conditions of the ThT fibrillization assay, *i.e.* no agitation, 25°C and pH 7.4, a conformational conversion into a β-sheet secondary structure was observed by CD spectroscopy. In their monomeric and soluble conformation, all N→D and N→isoD derivatives displayed a random coil conformation with CD spectra almost identical to native IAPP (Figure 2.3 and Figure S2.3). Peptide conformation was then evaluated after 24 h incubation under quiescent conditions. As expected from the results of the ThT assay, the CD spectra of most of the deamidated assemblies exhibited a single minimum at around 218 nm, indicating a secondary structure rich in β-sheets (Figure 2.3 and Figure S2.3). The CD spectrum of [N14D] displayed a negative signal of ellipticity at 218 nm more intense than the WT. Substitutions of residue Asn-21 with Asp and isoAsp inhibited the random coil-to-β-sheets conformational conversion of IAPP observed after 24 h incubation. Thus, Tht assay and CD spectroscopy revealed that positions 14 and 21 play determinant roles in IAPP self-assembly, as previously reported with successive mutation of Asn14 and Asn21 with a Leu residue (Koo *et al.*, 2008).

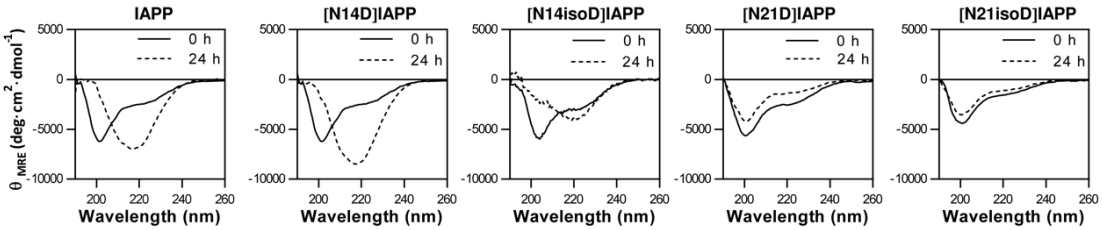


Figure 2.3 Effect of site-specific Asn deamidation on the conformational transition of IAPP.

Far UV circular dichroism spectra of IAPP and its deamidated derivatives. Peptides were incubated under quiescent conditions at 25°C in 10 mM Tris-HCl buffer, pH 7.4 and the analysis was performed after 0 and 24 h incubation.

2.5.3 Effect of Asn Deamidation on the supramolecular architecture of amyloids

The morphology of the assemblies formed after 24 h incubation under quiescent conditions was evaluated by TEM and representative images are shown in Figure 2.4. [N14D] IAPP assemblies were longer and a higher density of fibrils was observed compared to WT IAPP. By AFM, an average length of 0.98 ± 0.35 μm was evaluated for [N14D] IAPP fibrils in contrast to 0.42 ± 0.21 μm for IAPP (Figure S2.4). Strikingly, the amyloid fibrils formed by [N14isoD] IAPP were also very long and appeared rather twisted. Thus, incorporation of a negatively charged residue at position 14 favors amyloid elongation, even with the addition of a CH_2 surrogate within the peptide backbone. Moreover, AFM analysis revealed that the [N14D] IAPP fibrils were significantly thicker than those obtained from unmodified IAPP with an average of height of 4.99 ± 0.83 nm compared to 3.45 ± 1.29 nm (Figure S2.4). In sharp contrast, no fibril was observed for the N21D and N21isoD analogs, in agreement with the random coil conformation observed by CD spectroscopy and the low ThT fluorescence (Figure 2.4). Nonetheless, some small aggregates could be observed by TEM. Thus,

substitution of the amide group at position 21 with a carboxylate group induces the formation of amorphous aggregates characterized by a random coil conformation. Deamidation of Asn-22 led to the formation of fibrils with morphologies that are distinct from those of unmodified IAPP, *i.e.* shorter, thinner and clumpier. Substitution of Asn-31 with an Asp favored the formation a dense network of thin fibrils whereas incorporation of an isoAsp at position 31 led to amyloid fibrils similar to unmodified IAPP fibrils. Similarly, deamidation at the C-terminal domain, *i.e.* [N35D] and [N35isoD] IAPP, led to amyloids with comparable morphology to WT IAPP. Finally, no fibrils were observed for the fully deamidated IAPPs.

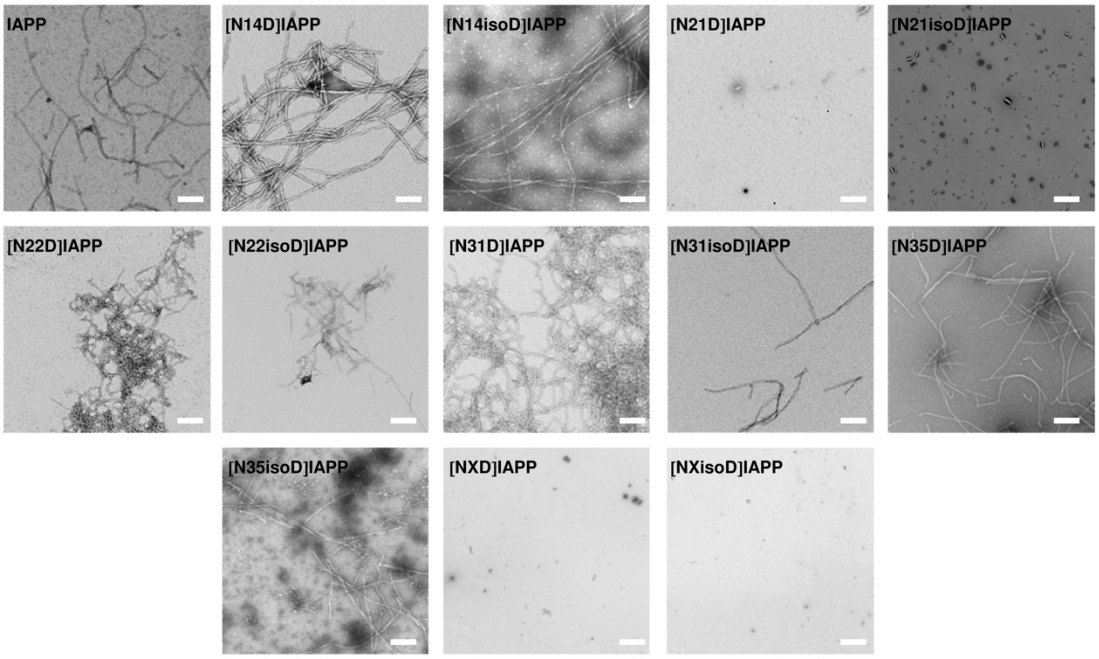


Figure 2.4 Effect of site-specific Asn deamidation on the morphology of IAPP assemblies.

Representatives TEM images of assemblies of IAPP and its deamidated derivatives. Peptides were incubated for 24 h under quiescent conditions before TEM analysis. Scale bar: 100 nm.

2.5.4 Deamidation of Asn-14 triggers amyloidogenesis by unmodified IAPP

As described above, deamidation of residue Asn-14 into Asp accelerates the nucleation phase and promotes amyloid elongation into long fibrils. Accordingly, we investigated if the presence of a small amount of pre-febrillar IAPP deamidated at position 14 can trigger WT IAPP amyloid formation, *i.e.* a co-assembly experiment. IAPP was incubated with monomeric [N14D] IAPP at different molar ratio; from 95:5 to 99:1 (IAPP: [N14D] IAPP) and amyloid assembly was followed by ThT fluorescence. In all conditions, the final concentration of IAPP (WT and N14D mutant) was 12.5 μM. Interestingly, the kinetics of self-assembly for the 95:5, 97.5:2.5 and 98:2 mixtures were nearly identical to the one observed for [N14D] IAPP (Figure 2.5A). The lag-times of these mixtures were slightly longer than the lag time of a [N14D] IAPP solution whereas the final ThT fluorescence measured during the saturation phase were statistically similar (Figures 2.5B and 2.5C). At 1% molar ratio (0.125 μM of [N14D] IAPP), the deamidated mutant did not have any significant effect on the assembly of unmodified IAPP (12.375 μM). It is worth mentioning, that [N14D] IAPP incubated alone at concentrations ranging between 0.625 μM (95:5 molar ratio) and 0.125 μM (99:1 molar ratio) did not led to the formation of amyloids detectable by ThT fluorescence (data not shown). Therefore, [N14D] IAPP interacts with its WT counterpart, hastening the formation of the nucleus and amyloid elongation. By TEM, the assemblies formed by mixing IAPP with a small fraction (5 to 2%) of the deamidated peptide N14D were long (Figure 2.5D) and morphologically similar to the one formed by [N14D] IAPP alone (Figure 2.4). These data indicate that a small amount of specifically deamidated IAPP at position 14 can considerably promotes the aggregation of non-deamidated IAPP and could have important pathophysiological implication.

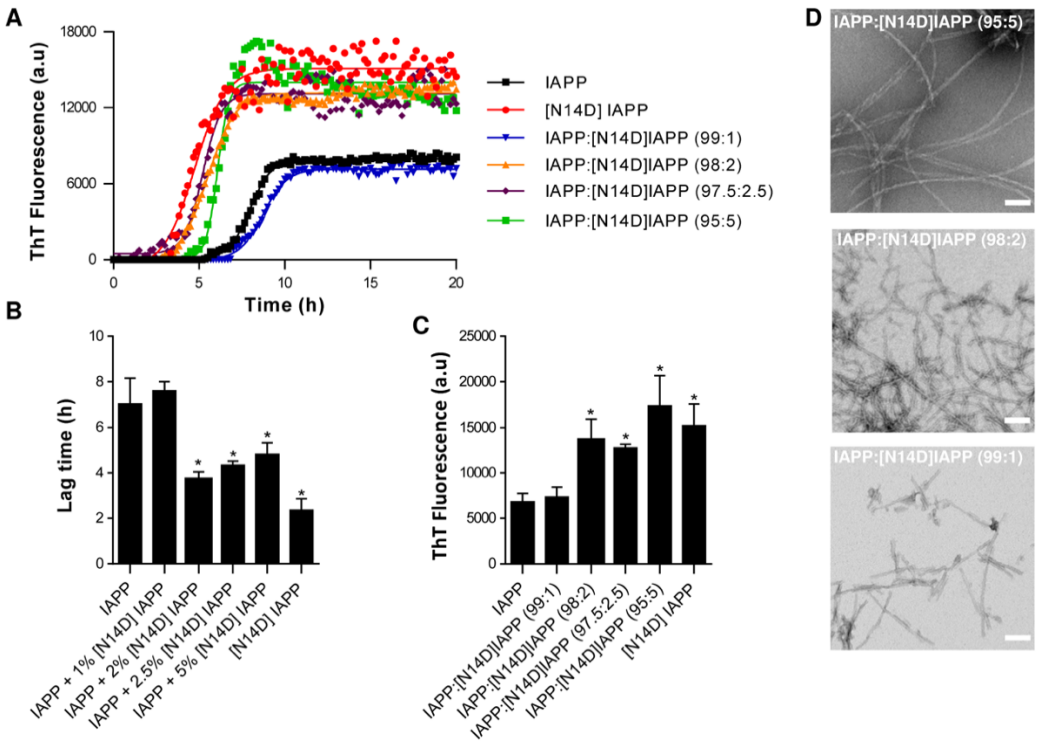


Figure 2.5 [N14D] IAPP accelerates unmodified IAPP amyloid formation.

(A) Representative kinetics of amyloid assembly of IAPP, [N14D] IAPP and mixtures of IAPP:IAPP[N14D] monitored by ThT fluorescence. Monomerized pre-fibrilar peptides were incubated at a final total concentration of 12.5 μM under quiescent conditions at 25°C and the fluorescence of ThT (40 μM) was measured every 10 min. The curves represent the best fit from the sigmoidal growth model. (B) Lag time and (C) final ThT fluorescence of the kinetics of fibril formation. (D) Representative TEM images of IAPP:[N14D] mixtures after 24 h incubation under quiescent conditions

2.5.5 IAPP deamidated at position 21 co-assembles into amyloid fibrils with WT-IAPP

Considering that deamidation of residue Asn-14 precludes amyloid formation, we evaluated if [N21D] IAPP could inhibit or slow down WT IAPP self-assembly. Monomerized pre-fibrillar IAPP (12.5 μM final concentration) was incubated with

increasing concentrations of N21D (0.25 to 6.25 μM) and amyloid formation was monitored by ThT fluorescence and TEM. At a low concentration, N21D delayed the nucleation step of IAPP whereas at high concentrations, deamidated IAPP at position 21 accelerated amyloid formation and increased final ThT fluorescence (Figure 2.6). The kinetics of amyloid assembly of a mixture of IAPP:[N21D] IAPP (12.5 μM:6.25 μM), total peptide concentration of 18.75 μM, was similar to a kinetics obtained with 18.75 μM WT IAPP (Figure S2.5). This observation indicates that IAPP deamidated at position 21 co-assembles with unmodified IAPP into amyloid fibrils, although the N21D peptide alone displays a weak 86myloidogenicity. By TEM, we observed that co-incubation of 12.5 μM WT IAPP with 6.25 μM N21D led to the formation of a dense network of fibrils (Figure 2.6D). In sharp contrast, when IAPP is incubated with rIAPP, which is also poorly amyloidogenic, the formation of amyloids is hindered (Figure S2.6). Thus, position Asn-21 is definitively playing a critical role in the nucleation step and, in contrast to rIAPP, the mutant N21D is not an inhibitor of WT IAPP fibril formation.

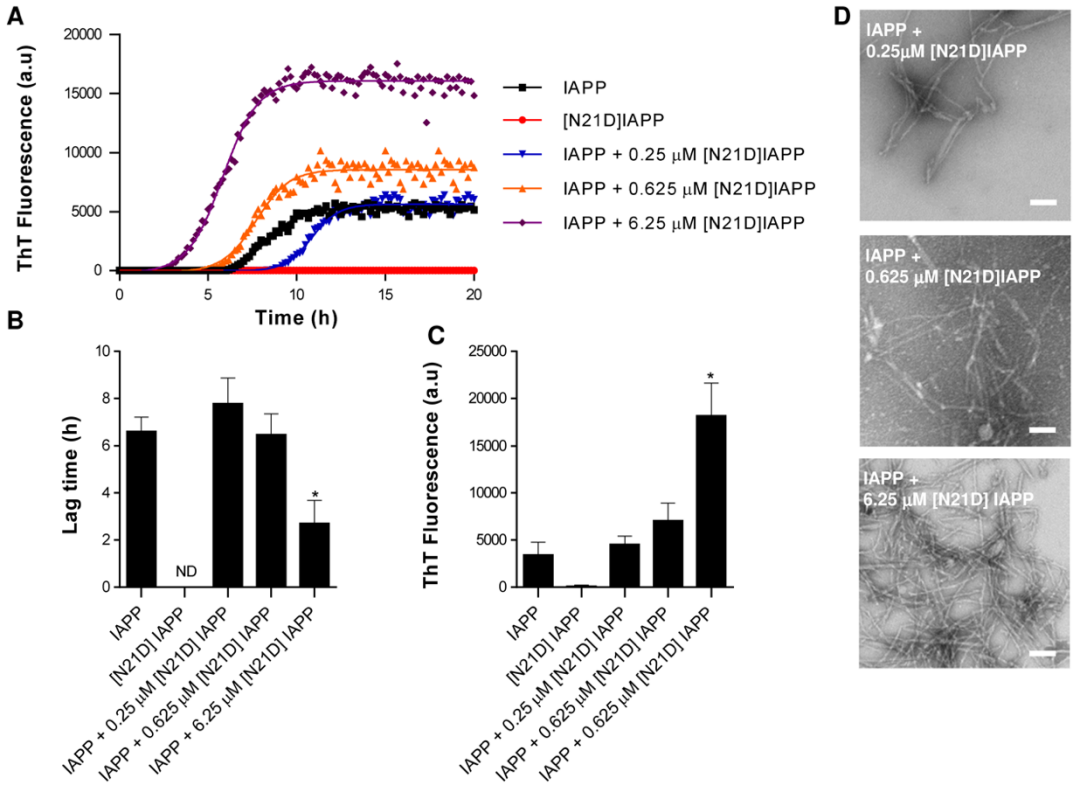


Figure 2.6 Effect of [N21D] IAPP on unmodified IAPP amyloid formation.

(A) Representative kinetics of amyloid assembly of IAPP (12.5 μM), [N21D] IAPP (12.5 μM) and mixtures of IAPP:[N21D] IAPP monitored by ThT fluorescence. Monomerized pre-fibrilar peptides were incubated under quiescent conditions at 25°C and the fluorescence of ThT was measured every 10 min. The curves represent the best fit from the sigmoidal growth model. (B) Lag time and (C) final ThT fluorescence of the kinetics of fibril formation. (D) Representative TEM images of IAPP:[N21D] mixtures after 24 h incubation under quiescent conditions.

2.5.6 Effect of Asn Deamidation on IAPP-mediated cytotoxicity

As previously reported, IAPP induced a concentration-dependent decrease of cellular viability (Cao *et al.*, 2013; De Carufel *et al.*, 2013; Nguyen *et al.*, 2015). In contrast,

mature amyloid fibrils as well as IAPP sequence from rodent (rIAPP), which is not prone to amyloid assembly owing to the presence of Pro residues, are known to be poorly cytotoxic (Cao *et al.*, 2013; De Carufel *et al.*, 2015). These studies have suggested that pre-fibrillar intermediates and/or the process of amyloid formation are the main mediators of cell death. As observed by ThT fluorescence, CD spectroscopy and TEM, Asn deamidation at given positions modulates the kinetics of IAPP self-assembly as well as the morphology of the resulting amyloid fibrils and, accordingly, could modulate IAPP cytotoxicity. We initially evaluated the cytotoxicity of IAPP and its deamidated derivatives using a pancreatic β-cell line (INS-1E) under two paradigms: (*i*) an acute treatment (50 to 12.5 μM for 24 h) and a chronic exposure (3 μM for up to 120 h). Strikingly, no statistically significant differences between IAPP and site-specific deamidated derivatives were observed under these two conditions (Figure 2.7A, Figure 2.7B and Figure S2.7). For instance, [N14D] IAPP and [N21D] IAPP, which exhibit opposite self-assembly properties, are both equivalents for their cytotoxic potential. These data are somewhat surprising and indicate that the *in vitro* propensity of IAPP derivatives to self-assemble into amyloid fibrils in homogenous conditions does not necessarily correlate to their cytotoxicity. Nonetheless, [NXD] IAPP and [NxisoD] IAPP, which do not aggregate, were non-toxic to INS-1E cells. We then evaluated the viability of cells that were exposed to IAPP and the [N14D] and [N21D] mutants for shorter period of time. Interestingly, the amyloidogenic prone [N14D] IAPP derivative reduced the viability of INS-1E cells after 6 h treatment whereas unmodified IAPP and [N21D]IAPP showed cytotoxicity after 8 h incubation (Figure 2.7C). This result might replicate the increased 88myloidogenicity induced by deamidation at position 14.

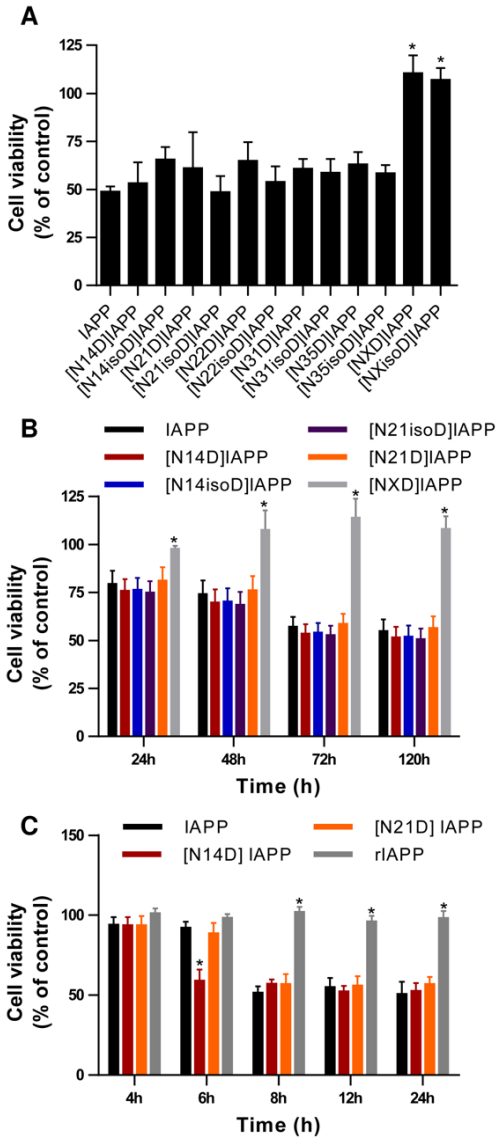


Figure 2.7 Effect of site-specific Asn deamidation on IAPP-induced cytotoxicity.

(A) INS-1 pancreatic β-cells were treated with 50 μM IAPP or its deamidated derivatives for 24h before cell viability was measured. (B) INS-1 cells were treated with 3 μM IAPP and its deamidated derivatives and cell viability was measured after 24, 48, 72 and 120 hours. (C) INS-1 cells were treated with 50 μM IAPP, its deamidated derivatives and rIAPP and cell viability was measured after 4, 6, 8 and 24 hours. (A, B, C). Cell viability was measured by means of the resazurin reduction assay and compared to cells treated with vehicle (100% cell viability). Data represent the mean ± S.E.M. of at least three experiments performed in triplicate. *Statistically significant difference between IAPP and derivatives ($P < 0.05$).

2.6 Discussion

Whereas the correlation between the deposition of IAPP amyloid fibrils and the pathogenesis of type-II diabetes is well documented (Westermark *et al.*, 2011), many uncertainties regarding the mechanism of IAPP self-assembly and induced cytotoxicity remain. Particularly, the initial interactions between IAPP monomers that drive self-assembly as well as the chemical and structural features of the peptide that allow it to be amyloidogenic prone still remain the subject of active research. Over the last two decades, a number of studies have investigated the consequence of mutations on the amyloidogenicity of IAPP to better understand the forces that drive self-assembly (Abedini *et al.*, 2007; Cao *et al.*, 2013; Koo *et al.*, 2008; Tu et Raleigh, 2013b; Wiltzius *et al.*, 2008; Wiltzius *et al.*, 2009). Early studies as well as sequence difference between rodents and human IAPP have initially suggested that the aggregation propensity of IAPP is somewhat tolerant to site specific substitutions, excepted for mutations within the 20-29 segment (Cao *et al.*, 2013; Westermark *et al.*, 1990). Nonetheless, numerous mutations outside the 20-29 amyloidogenic region, including A13E (Fox *et al.*, 2010b), Y37L (Tu et Raleigh, 2013b) and F15K (Wiltzius *et al.*, 2009) were shown to abolish or to slow down significantly amyloid formation. Interestingly, IAPP encompasses 6 amide Asn residues that span over the peptide primary structure. It was observed that the substitution of Asn-14 and Asn-21 by the hydrophobic residue Leu, which occupies a similar steric volume, abolish IAPP amyloid formation (Koo *et al.*, 2008). In contrast, the mutants N22L, N31L and N35L show a similar capacity to their WT IAPP(8-37) counterpart to self-assemble (Koo *et al.*, 2008). These previous studies have exposed that specific residues govern IAPP fibrillar assembly while some regions are somewhat less critical. The present study reinforces the notion that precise physicochemical properties of specific residue side chains are critical for nucleation and/or elongation processes. Our data confirm the key contributions of Asn side chain at positions 14 and

21 in amyloid formation and reveal that Asn deamidation sites have inequivalent effect on self-assembly.

One of the most drastic effect of Asn deamidation is observed when a carboxylate group is introduced at position 14, the N14D mutant shows a short nucleation phase and forms a dense network of long fibrils. This result is surprising considering that the mutations N14L, N14S and N14A are known to inhibit amyloid formation (Koo *et al.*, 2008). Moreover, incorporation of a negatively charged residue (Glu) at the neighboring A13 residue was shown to disrupt amyloid formation (Fox *et al.*, 2010b). Clearly, the nucleation and elongation steps of IAPP amyloidogenesis are governed by precise intermolecular interactions that are mediated by specific side chains. While the conformation(s) of the nucleating species is still the matter of active debate, two main models have been proposed for the initial oligomerization steps on-pathway to amyloid growth: the helical intermediates model (Abedini et Raleigh, 2009; Wiltzius *et al.*, 2009) and the *β*-hairpins model (Dupuis *et al.*, 2011). The helical intermediates model proposes that IAPP self-association is thermodynamically linked to helix formation within the 5–20 segment, in a similar way of the driven forces of coiled-coil motif formation. Accordingly, side chain of residue Asn-14 would project on the same face of the α-helix as Arg-11 and His-18 (positions ©, © + 3 and © + 7). Thus, the mutation N14D could favor the formation of a transient α-helix and/or of helical oligomers through electrostatic stabilization. Alternatively, position 14 could be involved in a critical hydrogen bond network within the nucleating species; requiring that the side chain has concurrently two hydrogen-bond acceptor groups, as for Asn and Asp. This could explain why IAPP self-assembly is non-tolerant to the N14L, N14S and N14A mutations whereas the N14D mutation as a pro-amyloidogenic effect.

The structure of IAPP fibrils solved by solid state NMR consists of two columns of related monomers packed against each other (Luca *et al.*, 2007). Each polypeptide

monomer adopts a U-shaped structure and contains two β-strands (residues 8-17 and residues 28-37) connected by a bend-loop (residues 18-27). In this model, the Asn14 side chain is in close proximity to the β-sheet formed by the residues 28-37 and projects between the two β-sheet layers in a hydrophobic environment. In the amyloid fibrils, the Asn-14 side chains are organized in parallel arrays along the fibril axis and are, most likely, making interactions between their equivalent residues in adjacent monomers. Accordingly, carboxylic acids are known for their ability to self-associate as dimeric pair in hydrophobic environment and this could explain the propensity of [N14D] IAPP to elongate into long and thick amyloid fibrils with high ThT-binding properties.

The concept of positional specificity in IAPP self-assembly (Koo *et al.*, 2008) is particularly noticeable by the effects of deamidation at positions 21 and 22. Whereas amyloid assembly is hindered by the N21D and N21isoD mutations, substitution of the adjacent N22 to Asp or isoAsp altered very modestly IAPP assembly. These observations are in agreement with a previous study showing that the N21L and N21S mutations disrupt IAPP amyloid assembly whereas the N22L substitution does not affect the nucleation and the elongation phases (Koo *et al.*, 2008). Obviously, the amide group at position 21 appears to be critical for the formation of the nucleating species. Finally, deamidation at positions 31 and 35 did not affect the time necessary to reach the high-energy nucleus, the rate of amyloid growth as well as the morphology of the assemblies. These data reinforce the concept that the 11-25 segment mediates the initial intermolecular interactions leading to amyloid assembly (Liu *et al.*, 2010; Liu *et al.*, 2012).

It was previously reported that non-targeted and spontaneous (*aging*) Asn deamidation accelerates IAPP self-assembly and alters fibrils structure (Dunkelberger *et al.*, 2012). However, the Asn residues subjected to deamidation were not identified. In this study,

we show that the deamidation sites play critical roles, perhaps divergent, in IAPP fibrilization. Such positional specificity in the effect of deamidation on amyloid assembly has been reported for the Aβ peptide with position 23 enhancing aggregation while position 7 having a limited effect (Shimizu *et al.*, 2002). Therefore, assessing the contributions of Asn deamidation on peptide self-assembly also requires targeted residue-specific modifications to obtain mechanistic details at the molecular level. Using pramlintide, a synthetic IAPP derivative used in the clinics, it was reported that 5 of the 6 Asn residues are prone to deamidation; Asn-21 and Asn-35 are the most deamidated whereas Asn-31 is not converted to either aspartic acid or isoaspartic acid (Hekman *et al.*, 1998; Hekman *et al.*, 1999). Herein, we find that modification at position 21 precludes IAPP amyloid assembly whereas deamidation of residue 35 has no significant effect on the kinetics of assembly and fibril morphology. It would be interesting to probe how different combinations of deamidation sites, such as the concurrent mutations N14D and N21D, modulate amyloid formation. Especially, we observe that a low molar ratio (≅ 2%) of IAPP specifically deamidated at position 14 triggers unmodified IAPP assembly and hastens fibril elongation. Thus, this non-enzymatic PTM could play an initiating role in IAPP amyloid deposition associated with type II diabetes. In contrast to the N14D mutant, [N21D] IAPP, at low concentrations, elongates the nucleation phase of WT IAPP and acts as a partial amyloid formation inhibitor, as observed for rIAPP. Strikingly, at higher concentrations, the N21 analog hastens WT IAPP amyloidogenesis and co-assembles with its WT counterpart into a dense network of fibrils. While the introduction of a carboxylate group at position 21 prevents the formation of the nucleating conformation(s) in a homogenous peptide solution, the presence of WT IAPP, bearing an amide group at position 21, allows the N21D mutant to undergo amyloid assembly.

The cytotoxicity of site-specific deamidated IAPP derivatives was evaluated using the INS-1E cell line. The fully deamidated IAPP analogs (NXD and NxisoD) and rIAPP

were not cytotoxic at concentrations of 50 μM and lower, indicating a correlation between the 94myloidogenicity measured in vitro (ThT fluorescence, CD spectroscopy, TEM) and the toxicity in cellular model. Similarly, the N14D mutant, which displayed a short nucleation phase, showed toxicity after 6 h incubation whereas for WT IAPP, the initial decrease of cellular viability was observed after 8 h. The cytotoxic effects of the N14IAPP observed at 6 h most likely replicate its high 94myloidogenicity observed in vitro. On the other hand, regarding the N21D mutant, no one-to-one relationship between the amyloid formation propensity in vitro and toxicity on INS-1E cells was observed. These data highlight that it remains challenging to predict the resulting toxicity of an amyloidogenic polypeptide, such as IAPP, solely based on its propensity to self-assemble into amyloid fibrils in vitro under homogenous conditions. Overall, this study emphasizes the importance of addressing the individual contribution of deamidation sites in amyloid formation and provides novel insights regarding the molecular interactions that drive self-assembly.

2.7 Supporting Information

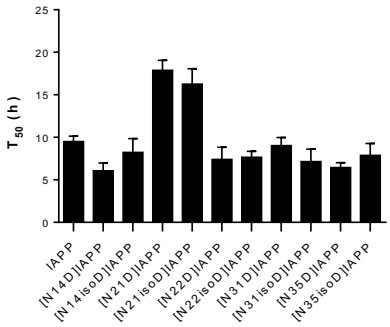


Figure S2.1 Kinetics (T_{50}) of amyloid assembly of IAPP and its deamidated derivatives.

The T_{50} of amyloid formation for each peptide was determined as described in the Materials and Methods.

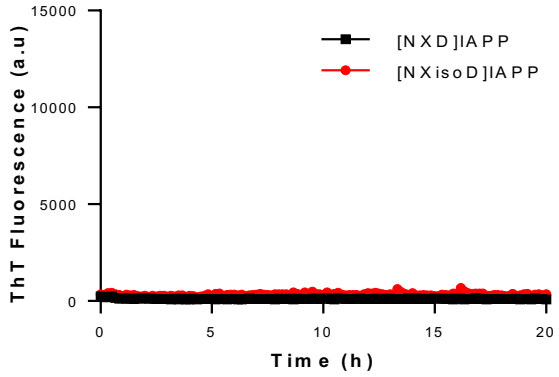


Figure S2.2 Kinetics of amyloid formation of fully deamidated IAPP derivatives monitored by ThT fluorescence.

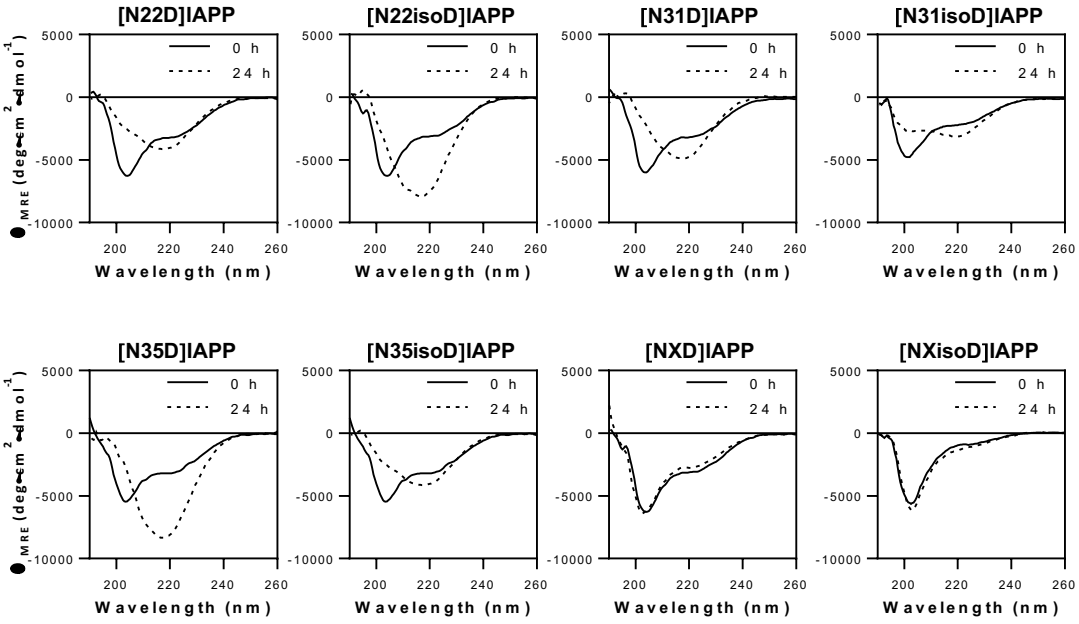


Figure S2.3 Effect of site-specific Asn deamidation on the conformational transition of IAPP.

Far UV circular dichroism spectra of IAPP and deamidated derivatives. Peptides were incubated under quiescent conditions at 25°C in 10 mM Tris-HCl buffer, pH 7.4 and the analysis was performed after 0 and 24 h incubation.

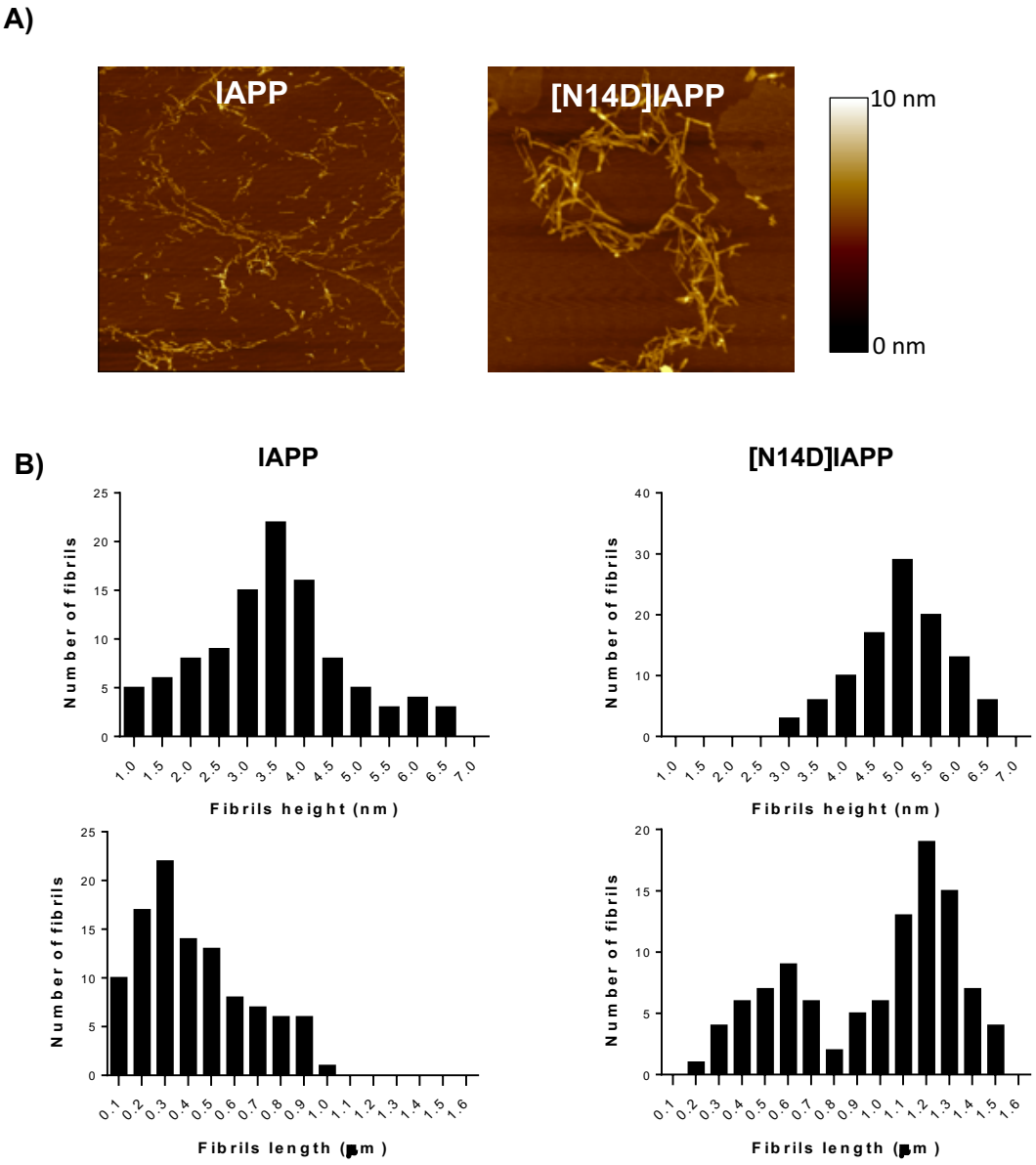


Figure S2.4 Effect of Asn-14 deamidation on the morphology of amyloid fibrils.

(A) Representative atomic force microscopy (AFM) images of IAPP and its N14D mutant incubated for 24 hours. Images are 5 μm × 5 μm. (B) Distribution of height and length of IAPP and [N14D]IAPP amyloid fibrils.

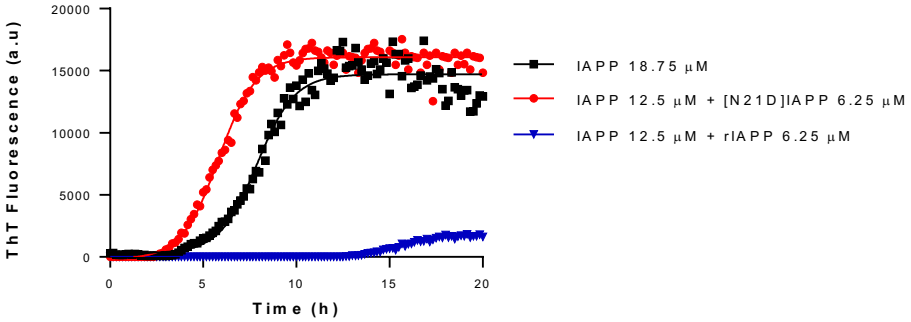


Figure S2.5 Effect of [N21D] IAPP and rIAPP on IAPP amyloid formation.

Kinetics of amyloid formation of IAPP at 18.75 µM, or at 12.5 µM in presence of 6.25 µM of [N21D]derivatives monitored by Tht fluorescence.

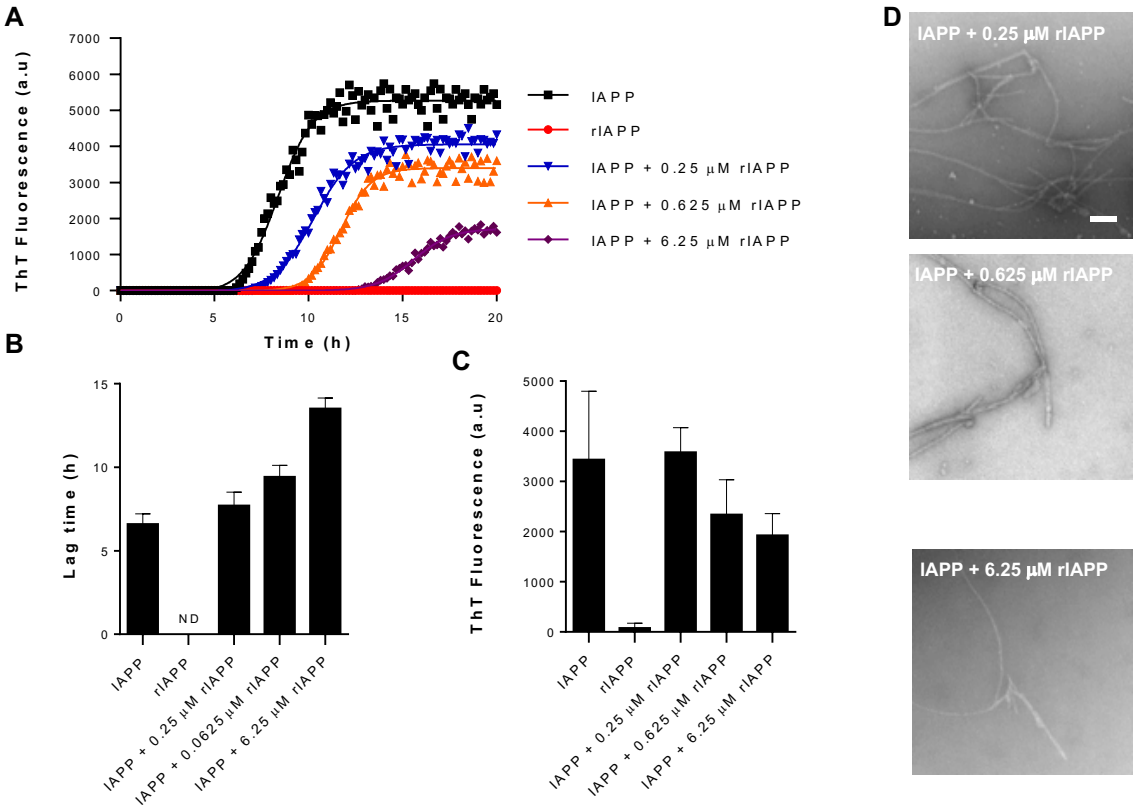


Figure S2.6 rIAPP inhibits hIAPP amyloid formation.

(A) Representative kinetics of amyloid assembly of IAPP (12.5 µM), rIAPP (12.5 µM) and mixtures of IAPP:rIAPP monitored by ThT fluorescence. Monomerized pre-fibrilar peptides were incubated under quiescent conditions at 25°C and the fluorescence of ThT (40 µM) was measured every 10 min. The curves represent the best fit from the sigmoidal growth model. (B) Lag time and (C) final ThT fluorescence of the kinetics of fibril formation. (D) Representative TEM images of IAPP:rIAPP mixtures after 24 h incubation under quiescent conditions.

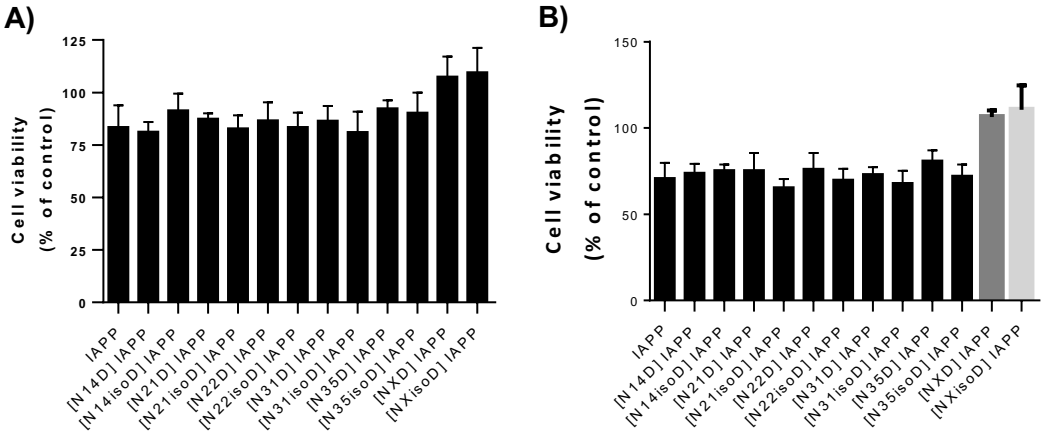


Figure S2.7 Effect of Asn deamidation on IAPP-induced cytotoxicity.

Cytotoxic effects of deamidated IAPP on INS-1 cells at 12.5 μM (A) and 25 μM (B). (A,B) INS-1 cells were treated with IAPP and its derivatives at 12.5 and 25 μM for 24h. Cell viability was measured by the resazurin reduction assay and compared to cells treated with buffer only (100% cell viability).

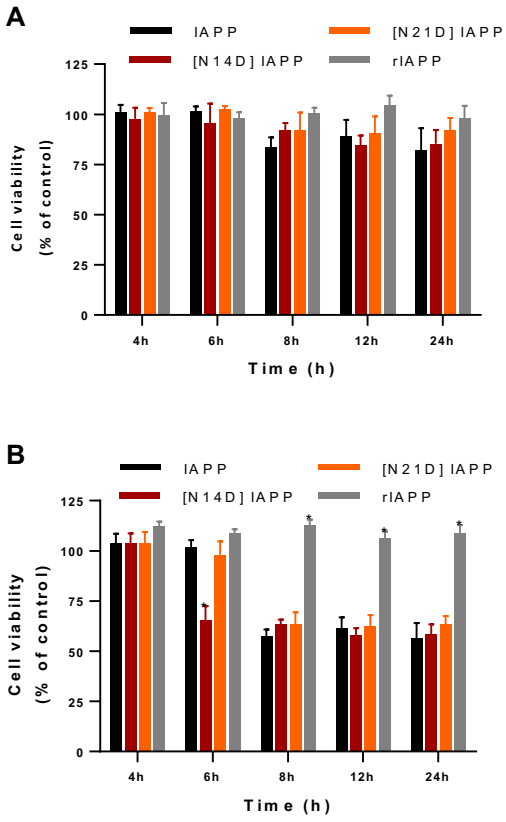


Figure S2.8 Effect of Asn deamidation on the kinetics of IAPP-induced cytotoxicity.

Cytotoxic effects of IAPP, deamidated IAPP at position 14 and 21 and rIAPP on INS-1 cells at 12.5 µM (A) and 25 µM (B). (A,B) INS-1 cells were treated with IAPP and its derivatives at 12.5 and 25 µM for 4h, 6h, 8h, 12h and 24h. Cell viability was measured by the resazurin reduction assay and compared to cells treated with buffer only (100% cell viability).

CHAPITRE III

ARTICLE II

OLIGOMER-LIKE FIBRILS: TRANSMISSIBLE PROTEOTOXIC SPECIES EXPANDING THE DIVERSITY OF AMYLOID ASSEMBLIES

Phuong Trang Nguyen, Ximena Zottig, Mathew Sebastiao, Alexandre Arnold, Isabelle Marcotte and Steve Bourgault

Manuscrit soumis à *Communications Biology* en novembre 2020.

Contribution des auteurs :

Phuong Trang Nguyen : Conception du projet, réalisation des expériences (Synthèse et purification des peptides, assemblage des peptides *in vitro*, essais cinétiques par fluorescence de ThT, analyses des conformations secondaire par CD, analyses par AFM, essais biologiques, microscopie confocale), traitements des résultats, analyses statistiques, rédaction de l'article.

Ximena Zottig : Exécution des analyses de FTIR, XRD, microscopie électronique en tranmission et cryo-EM.

Mathew Sebastiao : Exécution des mesures et des analyses de RMN à l'état solide.

Alexandre Anold : Conception expérimentale pour les expériences en RMN à l'état solide.

Isabelle Marcotte : Supervision des études en RMN à l'état solide.

Steve Bourgault : Supervision du projet, préparation des figures, correction de l'article.

NOTE : Les références de l'article sont incluses dans la bibliographie générale de la thèse

AVANT-PROPOS DU CHAPITRE III

Les études de la désamidation d'asparagine (Chapitre II) suggèrent que l'Asn-21 joue un rôle crucial dans l'auto-assemblage *in vitro* de l'IAPP. Nous avons poursuivi ce projet en étudiant les relations structure-auto-assemblage en se focalisant sur la position 21 afin d'obtenir des informations sur le mécanisme moléculaire de l'auto-assemblage de l'IAPP et d'étudier la nature conformationnelle des assemblages toxiques associés à la mort des cellules-β. Cette étude a conduit à la publication d'un article scientifique, dont ma collègue Élizabeth Godin et moi-même sommes co-premières auteures. Cet article, *Identification of a hinge residue controlling islet aymloid polypeptide self-assembly and cytotoxicity*, a été publié dans *Journal of Biological Chemistry* (JBC) et est disponible en Annexe II.

En résumé, les études biophysiques ont révélé que la chaîne latérale amide de l'Asn-21 n'est pas essentielle pour la nucléation et l'élongation en fibres amyloïdes, puisque les analogues N21A et N21G se sont assemblés en fibres prototypiques. À l'opposé, la substitution de l'Asn-21 par une proline, qui est conformationnellement contrainte et induit une structure en boucle, accélère l'auto-assemblage de l'IAPP. Les substitutions successives par des résidus hydrophobes (N21L et N21F) ont mené à la formation d'agrégats riches en feuillets-β, ThT-négatifs et ayant une forte hydrophobicité de surface. Des essais cellulaires ont révélé qu'il n'y a pas de corrélation directe entre l'amyloïdogénicité *in vitro* de ces analogues et leur toxicité. En revanche, la perturbation de vésicules de lipides anioniques révèle que la disruption membranaire est fortement associée avec la cytotoxicité observée. L'analogue N21F s'auto-assemble en agrégats *worm-like*, et ceux-ci causent la perte de l'intégrité structurale de la membrane lipidique et induit l'apoptose des cellules-β. Ces résultats indiquent que des interactions intra et intermoléculaires spécifiques impliquant l'Asn-21 favorisent la nucléation primaire de l'IAPP en modulant la conversion conformationnelle des

intermédiaires oligomériques en fibres amyloïdes. Cette étude indique que la position 21 joue un rôle de charnière moléculaire qui module l'amyloïdogénicité et la cytotoxicité de l'IAPP.

L'analogue N21Q a initialement fait partie de cette étude. L'étude étendue sur cet analogue a mené à la préparation de l'article intitulé *Oligomer-like fibrils : novel proteotoxic species expanding the diversity of amyloid assemblies,* qui consiste au Chapitre III de cette thèse.

Oligomer-like fibrils: transmissible proteotoxic species expanding the diversity of amyloid assemblies

Phuong Trang Nguyen[1,2], Ximena Zottig[1,2], Mathew Sebastiao[1,2], Alexandre Arnold[1,2], Isabelle Marcotte[1,2] and Steve Bourgault*[1,2]

[1]Department of Chemistry, Université du Québec à Montréal, Montreal, Canada, H3C 3P8,

[2]Quebec Network for Research on Protein Function, Engineering, and Applications, PROTEO, Quebec, Canada

*Corresponding author: Prof. Steve Bourgault, Canada Research Chair in Chemistry of Biological Nanoassemblies, Department of Chemistry, Université du Québec à Montréal, C.P. 8888, Succursale Centre-Ville, Montréal (Québec), H3C 3P8, Canada, Telephone: (514) 987-3000 (5161); e-mail: bourgault.steve@uqam.ca

3.1 Résumé

Le mauvais repliement des protéines et le dépôt tissulaire des assemblages amyloïdes en feuillets-β croisés sont associés à de nombreuses maladies. Alors que des preuves biochimiques convaincantes ont révélé que les espèces cytotoxiques de la cascade amyloïde sont les intermédiaires préfibrillaires, la toxicité des fibres amyloïdes matures et hautement ordonnées a également été démontrée. La divergence concernant la cytotoxicité des oligomères et des fibres amyloïdes est associée à la diversité (supra)structurelle et au polymorphisme, complexifiant leur caractérisation. Dans la présente étude, en exploitant l'*islet amyloid polypeptide* (IAPP) dont le dépôt dans les îlots pancréatiques est associé au diabète de type II, nous décrivons la formation de fibres amyloïdes hautement toxiques affichant des caractéristiques d'oligomères. Ces fibres ressemblant aux oligomères sont assemblées à partir d'un dérivé de l'IAPP contenant une substitution d'Asn par Gln en position 21 (N21Q). Les fibres cytotoxiques de N21Q partagent des propriétés (supra)moléculaires structurelles avec les fibres amyloïdes non toxiques formées à partir de l'homologue sauvage, y compris une distance inter-brin prototypique de 4.7 Å, une conformation riche en feuillet-β et la reconnaissance par des anticorps anti-amyloïdes. Parallèlement, les fibres cytotoxiques de N21Q ont des caractéristiques biophysiques des oligomères toxiques; faible capacité à se lier à la thioflavine-T, hydrophobicité élevée à la surface, grande flexibilité et reconnaissance par l'anticorps anti-oligomère A11. Ces caractéristiques d'oligomères sont associées à une capacité élevée des fibres de N21Q à perturber les membranes lipidiques et à provoquer un dysfonctionnement cellulaire. En particulier, la conformation toxique de type oligomère des fibres N21Q, qui est préservée lors de l'allongement en fibres, est transmissible à l'IAPP sauvage. L'identification de fibres cytotoxiques matures avec des caractéristiques oligomériques/préfibrillaires élargit la diversité des amyloïdes et ces assemblages stables de type oligomère représentent une

occasion unique d'élucider les caractéristiques structurales des pathologies associées aux amyloïdes.

3.2 Abstract

Protein misfolding and amyloid deposition are associated with numerous diseases. The detailed characterization of the proteospecies mediating cell and tissue degeneration still remains elusive owing to the (supra)structural polymorphism and dynamic conformational nature of the assemblies populating the amyloid pathway. Here, by using the islet amyloid polypeptide (IAPP) whose pancreatic deposition is associated with type II diabetes, we describe the formation of highly toxic amyloid fibrils with oligomer characteristics. These prototypical filaments are assembled from an IAPP derivative containing an apparently trivial Asn-to-Gln substitution at position 21 (N21Q). N21Q fibrils share structural properties with cytocompatible amyloid fibrils, including long and linear morphology, 4.7 Å inter-strand distance and β-sheet-rich conformation. Concurrently, N21Q fibrils have characteristics of soluble oligomers, such as low binding to thioflavin-T, high surface hydrophobicity, solvent exposure of F23 and recognition by the anti-oligomer A11 antibody, leading to high potency to cause plasma membrane disruption and cellular dysfunction. Predominantly, the toxic oligomer conformation of N21Q fibrils, which is preserved upon elongation, is transmissible to naïve IAPP. The identification of well-defined fibrils with cytotoxic oligomer properties expands the conformational diversity of amyloids and these thermodynamically stable assemblies represent a unique opportunity to elucidate the structural basis of amyloid disorders.

3.3 Introduction

Misfolding and aggregation of proteins into ordered cross-β amyloid assemblies are associated with over fifty human diseases, including the Alzheimer's disease (AD), type II diabetes mellitus and systemic amyloidosis (Chiti et Dobson, 2017). Amyloid fibril formation and tissue deposition are initiated by the self-recognition of (partially) unfolded proteins and implicate a infinite array of off- and on-pathway prefibrillar intermediates (Knowles *et al.*, 2014). The close association between the deposition of insoluble protein aggregates and localized tissue degeneration has initially led to the hypothesis that amyloid fibrils are causing cell death. However, compelling biochemical and pharmacological evidences have indicated that the most cytotoxic proteospecies of the amyloid cascade are the oligomeric intermediates and that fibrils are generally non-toxic (Benilova *et al.*, 2012; Chiti et Dobson, 2017). For instance, the amyloid-β (Aβ) peptide impairs synaptic plasticity in absence of fibrillar assemblies, through the formation of oligomeric intermediates(Shankar *et al.*, 2008), while the influx of Ca^{2+} across neuronal membranes correlates closely with binding of Aβ oligomers to the plasma membrane(Evangelisti *et al.*, 2016). Cytotoxicity, including persistent ability to disrupt cellular membranes, has been reported for transient oligomers assembled from numerous proteins associated with amyloid disorders, including the islet amyloid polypeptide (IAPP)(Abedini *et al.*, 2016; Birol *et al.*, 2018), α-synuclein(Fusco *et al.*, 2017; Winner *et al.*, 2011) and transthyretin(Bourgault *et al.*, 2011a; Reixach *et al.*, 2004). Strikingly, cytotoxic oligomers have been generated from proteins that do not spontaneously self-assemble and that are not associated with amyloid diseases (Bucciantini *et al.*, 2004; Bucciantini *et al.*, 2002), suggesting that prefibrillar aggregates share physicochemical and/or structural properties mediating toxicity.

Although these studies have supported the oligomer hypothesis, *i.e.* that soluble aggregates are the main causative agents of amyloid-associated diseases, prefibrillar assemblies are dynamic, transient, and heterogeneous in size and conformation, leading to major challenges for characterizing their structure(s) and elucidating their mechanisms of toxicity. Furthermore, thorough studies have periodically reported the cytotoxicity of well-defined fibrils (Tipping *et al.*, 2015) including those assembled from IAPP (Krotee *et al.*, 2017), huntington protein(Nekooki-Machida *et al.*, 2009), β2-microglobulin(Goodchild *et al.*, 2014; Milanesi *et al.*, 2012) and α-synuclein(Pieri *et al.*, 2012). Discrepancies among the relationships between toxicity and (supra)molecular architecture of amyloid proteospecies originate from their high structural diversity at the atomistic and mesoscopic levels. A given amyloidogenic protein can misfold and aggregate into multiple populations of oligomers and fibrils, and each of these quaternary conformers can display divergent cytotoxicity. For instance, Aβ peptide oligomerization can lead either to stable non-toxic dimers/trimers (Chen et Glabe, 2006) and to pentamers that are very toxic to neuronal cells (Ahmed *et al.*, 2010). By varying self-assembly conditions, two populations of stabilized α-synuclein oligomers with similar sizes and morphologies were obtained; one type being benign to cells and the other population avidly perforating lipid bilayers (Chen *et al.*, 2015; Fusco *et al.*, 2017). Similarly, under different temperatures, the huntington protein with extended polyglutamine misfolds into distinct amyloid fibrils with dissimilar conformations associated with divergent neurotoxicity (Nekooki-Machida *et al.*, 2009). While some supramolecular organizations mediating toxicity have been proposed, including the β-barrel structure of Aβ peptide oligomers (Serra-Batiste *et al.*, 2016), the annular conformation of α-synuclein oligomers (Fusco *et al.*, 2017) and the pairs of β-sheets mated by a dry interface for IAPP fibrils (Krotee *et al.*, 2017), it has also been proposed that cytotoxicity of could be independent of a given structure(Vivoli Vega *et al.*, 2019). Thus, the elucidation of the toxic conformation(s) of the amyloid

cascade is still the matter of active debates, owing to the large ensemble of on- and off-pathway transient proteospecies assembled along the aggregation pathway.

Studies have exploited site-directed mutagenesis to define the chemical determinants of amyloid self-assembly and to elucidate the conformational rearrangements triggering oligomerization, nucleation and/or fibril elongation. Structure-self-assembly relationship studies often lead to the identification of residues modulating aggregation and to the detection of distinct assemblies with unique underlying mechanisms of toxicity (Abedini *et al.*, 2007; Hatami *et al.*, 2017). Using such approach, we recently reported that N21 of IAPP behaves as a molecular hinge controlling secondary and quaternary conformational conversion, as well as toxicity toward β-cells (Godin *et al.*, 2019). IAPP is a 37-residue peptide hormone whose deposition as insoluble amyloids in the pancreatic islets is associated with type II diabetes (Westermark *et al.*, 2011). Substitution of N21 by a hydrophobic residue has been shown to reshape IAPP aggregation landscape and to lead to toxic worm-like aggregates (Godin *et al.*, 2019). In the present study, we report that the apparently trivial Asn-to-Gln substitution at position 21 of IAPP, *i.e.* the addition of a single methyl group into a 4 kDa peptide, led to the formation of amyloid fibrils with high cytotoxicity. These defined prototypical fibrils displayed oligomer-like properties, such as exposition of hydrophobic clusters, recognition by the conformational A11 antibody, and high capacity to perturb plasma membrane. These thermodynamically stable oligomer-like fibrils reveal that the oligomer conformation can be transmissible and represent a unique opportunity to elucidate the structural features of toxic amyloid proteospecies.

3.4 Materials and Methods

3.4.1 Synthesis, Purification and Sample preparation

Peptides were synthesized on solid support using Fmoc-chemistry and 2-(6-chloro-1-H-benzotriazole-1-yl)-1,1,3,3-tetramethylaminium hexafluorophosphate (HCTU) coupling strategy with the incorporation of oxazolidine pseudoproline derivatives, as previously described.(De Carufel *et al.*, 2013) After cleavage, crude peptides were purified by RP-HPLC and collected fractions were analyzed by LC/MS-TOF. Disulfide bond formation between Cys-2 and Cys-7 was achieved by dimethyl sulfoxide oxidation under mild agitation. Cyclized peptides were purified by RP-HPLC and fractions corresponding to the desired product with purity higher than 95% were pooled and lyophilized. Peptides labelled with Alexa488 NHS ester were prepared as previously described.(Birol *et al.*, 2018) Aliquots of monomerized peptides were prepared by dissolving the lyophilized peptide in hexafluoro-2-propanol (HFIP). The solution was sonicated for 30 min, filtered through a 0.22 μm hydrophilic filter and lyophilized. The resulting peptide powder was solubilized for a second time in HFIP to 1 mg/ml, sonicated for 30 min and lyophilized. Dried samples were stored at -80°C, but not for longer than 4 weeks.

3.4.2 Preparation of oligomers and fibrils

Prefibrillar species and fibrils were prepared by incubating freshly dissolved monomerized peptides under quiescent conditions at 150 μM in 20 mM Tris-HCl buffer, pH 7.4 for 15 min and 48 h, respectively, unless otherwise stipulated. Labelled

peptide oligomers and fibrils were prepared by incubating non-labelled peptides and labelled peptides (99.5:0.5, molar ratio) under quiescent conditions at a final concentration of 150 μM.

3.4.3 Kinetics of amyloid formation

Solutions were prepared by dissolving the monomerized peptide in 20 mM Tris-HCl, pH 7.4. Assays were performed at 25°C without stirring in sealed black-wall clear-bottom 96-well non-binding surface plates with a total volume of 100 μL per well. Final peptide concentrations were 12.5 or 25 μM in presence of ThT (40 μM), ANS (50 μM) or FlAsH (0.5 μM). Fluorescence of ThT (Ex. 440 nm, Em. 485 nm), ANS (Ex. 355 nm, Em. 480 nm) or FlAsH (Ex. 508 nm, Em. 533 nm) were measured every 10 min. over the course of 20 h. Data obtained from triplicate wells were averaged, corrected by subtracting the corresponding control reaction and plotted as fluorescence *vs* time. Data of time-dependence of fluorescence were fitted to a sigmoidal Boltzmann model where T_{50} is the time required to reach half of the fluorescence intensity, k is the apparent first-order constant and Y_{max} and Y_0 are, respectively, the maximum and initial fluorescence values:

$$Y = \frac{Y_0 + (Y_{max} - Y_0)}{1 + e^{-(T - T_{50})/k}}$$

The lag time is described as $T_{50} - 2/k$. Data (lag time and final fluorescence) of at least four different lots of peptides were averaged and were expressed as the mean ± S.D.

3.4.4 Seeding experiments

Fibrils assembled as described above were collected and sonicated for 20 min. All seeding experiments were performed with 0.5% - 5.0% of freshly prepared seeds and appropriate percentage of soluble peptide monomer, resulting in a final concentration of 150 μM.

3.4.5 Fluorescence spectroscopy (ThT and ANS)

At the indicated incubation time, samples were diluted to a final concentration of 50 μM, in presence of a final concentration of 40 μM of ThT or 100 μM ANS. Fluorescence was measured in a quartz ultra-micro cells 10 mm length using a PTI QuantaMaster 400 spectrofluorometer. For ThT, excitation was set at 440 nm and emission from 450 nm to 550 nm was recorded. For ANS, the excitation was set at 355 nm and emission was recorded from 385 nm to 585 nm. Data are the average of at least four individual experiments.

3.4.6 Circular dichroism spectroscopy

Peptide samples were diluted to a final concentration of 50 μM and incorporated into a 1 mm path length quartz cell. Far-UV CD spectra were recorded from 190 to 260 nm using a Jasco J-815 CD spectropolarimeter at 25°C. The wavelength step was set at 0.5 nm with an average time of 10 s per scan at each wavelength step. Spectrum was background subtracted with peptide-free buffer. Raw data was converted to mean

residue ellipticity (MRE). Thermal unfolding transitions were monitored by the variation of CD signal at 222 nm between 25 °C and 104 °C with a heating rate of 1.0 °C min^{-1}. Transitions were evaluated using a nonlinear least square fit assuming a two-state model, *i.e.* assembled and unassembled.

3.4.7 Attenuated Total Reflectance-Fourier Transform Infrared Spectroscopy

ATR-FTIR spectra were recorded using a Nicolet Magna 560 spectrometer equipped with a nitrogen-cooled MCT detector. Each spectrum was an average of 128 scans recorded at a resolution of 2 cm^{-1} using a Happ–Genzel apodization. Data analysis was performed using Grams/AI 8.0 software.

3.4.8 Powder X-Ray Diffraction

Fibrils were deposited on an X-ray diffraction lamella and dried overnight. Powder XRD was performed using a Bruker D8 Advance X-ray diffractometer. The current and the voltage were 40 mA and 40 mV, respectively, with a step size of 0.112° s−1 in the 2θ range of 5–50°. Interplanar distances were determined from powder raw pattern (2θ), satisfying Bragg's condition.(Zottig *et al.*, 2019).

3.4.9 Transmission electron microscopy

Fibrils were diluted to 10 μM in deionized water and immediately applied to glow-discharged carbon films on 300 mesh copper grids. After adsorption and air-blotting, samples were negatively stained with 1.5% uranyl formate. Images were recorded using a FEI Tecnai 12 BioTwin microscope operating at 120 kV and equipped with an AMT XR80C CCD camera system. For immunogold labelling, grids with adsorbed fibrils were floated on droplets of 4% of Tween in PBS to block non-specific binding for 30 min and washed with droplets of PBS 0.05% Tween. After incubation with primary antibodies (A11, LOC and/or 4G8) in PBS 0.05% Tween for 90 min, grids were washed before being incubated with droplets of gold-conjugated secondary antibody (goat anti-mouse IgG for 4G8, and goat anti-rabbit IgG for LOC and A11) for 1 h. Grids were washed and stained with 1.5% (w/v) uranyl formate.

3.4.10 Atomic force microscopy

Prefibrillar species and fibrils were diluted to 10 μM in 1% acetic acid, and immediately applied to freshly cleaved mica. The mica was washed twice with deionized water and air-dried. Images were acquired on a Veeco/Bruker Multimode AFM using tapping mode with a silicon tip (2-12 nm tip radius, 0.4 N/m force constant) on a nitride lever. Images were taken at 0.2 Hz and 1024 scan/minute.

3.4.11 Solid-state nuclear magnetic resonance

Fibrils for SS-NMR were prepared using uniformly labelled ^{13}C, ^{15}N peptides at positions Ala13, Phe23 and Val22. Fibrils assembled at 750 μM were concentrated by ultracentrifugation at 100 000g for 45 min at 4 °C. The supernatant was discarded and

the pellet was resuspended in water and lyophilized. The lyophilized fibrils were then packed dry into NMR rotors, with a final recovery ranging between 50-80% of the mass of the initial peptide. NMR spectra were recorded on a 400 MHz wide-bore Bruker Avance III-HD using a triple-resonance 1.9 mm magic-angle spinning (MAS) probe operating in double resonance. MAS speed was set at 26 kHz for 2D DARR experiments with a 200 ms mixing time and the ^{13}C and ^{1}H radiofrequency fields were 83 kHz and 100 kHz, respectively. Cross-polarization was used (1.3 ms) during acquisition with a 70 to 100% intensity ramp on the ^{1}H radiofrequency channel, and protons were decoupled using the spinal-64 sequence. All experiments were recorded at 277 K and spectra were referenced to TMS by the ^{13}C (38.43 ppm) shift in adamantane. Data was acquired and processed using Topspin and Mestrenova.

3.4.12 Dot Blot

Ten µl of peptide sample (150 µM) was applied to a nitrocellulose membrane. The membranes were allowed to air dry and were blocked in 5% non-fat dried milk in TBS-T for 30 min at room temperature. The membranes were then incubated with different primary antibodies (A11, LOC, 4G8) for 2h at room temperature with agitation. After three washes in TBS-T, the membranes were incubated with the appropriate secondary antibody (goat anti-mouse IgG for 4G8, goat anti-rabbit IgG for LOC and A11 antibodies) for 1 h at room temperature with agitation. The secondary antibodies were diluted 1:10 000 in 5% non-fat dried milk in TBS-T. Blots were washed three times with TBS-T, and secondary antibody reactivity was revealed by enhanced chemiluminescence.

3.4.13 Cell viability

Rat INS-1E (pancreatic β-cell line) cells were plated in black wall clear bottom 96-well plates at a density of 20 000 cells/well (100 µl/well) in RPMI-1640 medium supplemented with 10% FBS, 2 mM L-glutamine, 100 U/ml penicillin, 100 mg/ml streptomycin, 10 mM HEPES, 1 mM sodium pyruvate, 50 mM β-mercaptoethanol. After 48 h incubation at 37°C in a 5% CO_2, cells were treated by the addition of 50 µl of peptides (monomers, prefibrillar or fibrils) at 3× of final concentrations (50 µM to 1 µM) solubilized in 20 mM Tris, pH 7.4. Cells were incubated for 5h (time-resolved assay) or 24h and cellular viability was measured by the resazurin reduction assay. Cell viability (in %) was calculated from the ratio of the fluorescence of the treated sample to the control cells (non-treated). Data (in %) of at least four lots of peptides were averaged and were expressed as the mean ± S.D. Results were analyzed using the Student's t-test and statistical difference was established at $P < 0.05$. For CHO-K1, cells were plated at a density of 20 000 cells/well (100 µl/well) in Ham F-12 medium supplemented with 10% FBS, 2 mM L-glutamine, 100 U/ml penicillin, 100 mg/ml streptomycin.

3.4.14 Caspase-3 activity assay

Rat INS-1 β-cells were cultured in 12-well plates at a density of 400 000 cells/well in complete RPMI-1640 medium. After 48 h incubation, cells were treated with peptide solutions for different time (0-24h), at final peptide concentration of 50 µM. β-cells were lysed on ice for 30 minutes followed by a centrifugation at 16 000g for 20 min. Caspase-3 activity in the supernatant was measured by a colorimetric assay. Caspase-3 activity after 2h reaction was evaluated at 37°C by measuring absorbance at 405 nm. The caspase-3 activity in µmol pNA released per min per ml of cell lysate based on the formula:

$$Caspase\ 3\ activity\ (^{\mu M}/_{min}) = \frac{\mu\text{mol pNA}}{\text{t} \times \text{v}}$$

where µmol pNA (p-nitoaniline) is calculated from pNA calibration curve, t is the reaction time in min and v is the volume of sample in L. Data of at least four experiments were averaged and were expressed as the mean ± S.D. The same procedure was done for CHO-K1 cells.

3.4.15 Lactate Dehydrogenase (LDH) release assay

Rat INS-1 β-cells or CHO-K1 cells were cultured in 96-well plates (tissue culture treated) at a density of 30 000 cells/well. After 48 h incubation at 37°C in a 5% CO_2, cells were treated with peptide solutions. 50 µf of media was collected at different times (0h to 12h) and incubated with the reaction mixture from the Pierce LDH Cytotoxicity Detection Kit for 30 min at room temperature. Reaction was stopped and absorbance was measured from 490 nm to 680 nm. To determine LDH activity, the 680 nm absorbance value (background) was subtracted from the 490 nm absorbance before calculation. Percentage of LDH leakage was calculated using the following equation:

$$\%\ LDH\ leakage = \frac{LDH\ activity_{peptide-treated} - LDH\ activity_0}{\text{LDH activity}_{max} - LDH\ activity_0} \times 100$$

where LDH $activity_0$ is the absorbance measured in absence of peptide and LDH $activity_{max}$ is the absorbance measured for cells treated with lysis buffer. Data of at least

four individual experiments performed with different lot of peptides were averaged and were expressed as the mean ± S.E.M.

3.4.16 Preparation of large unilamellar vesicles

Lipids DOPC/DOPG (7:3, molar ratio) were solubilized in chloroform in a glass tube and solvent was evaporated with a nitrogen stream. Lipid film was then rehydrated in 20 mM Tris-HCl pH 7.4 for at least 30 minutes. The solution was freeze-thawed 5 times before being extruded with a 100 nm polycarbonate membrane for 20 cycles. For membrane leakage assays, the lipid film was rehydrated in a 20 mM Tris-HCl pH 7.4 buffer containing 70 mM calcein. Free calcein was separated from the calcein-filled LUVs using size-exclusion chromatography (Sephadex G25-fine) and elution with 20 mM Tris-HCl, 150 mM NaCl (pH 7.4). Lipid concentration was determined by a colorimetric assay whereas size distribution of LUVs was evaluated by dynamic light scattering.

3.4.17 Calcein leakage assay

Peptides (monomers, prefibrillar and fibrils) were prepared as described above and used at a final concentration of 50 μM. Calcein-LUVs were used at a final concentration of 500 μM. Fluorescence was monitored in sealed black-wall, clear-bottom 96 well non-binding surface plates with a total volume of 100 μL per well. Measurements were performed every 15 min using an excitation wavelength of 495 nm and emission at 517 nm. The control used to determine 100% leakage (F_{max}) was calcein-LUVs with 0.1% of Triton X-100. Dye leakage was reported using the following equation:

$$\%\ membrane\ leakage = \frac{\mathrm{F} - F_0}{\mathrm{F}_{max} - F_0} \times 100$$

where F_0 is the fluorescence of the LUVs in absence of peptide. Data of at least four individual experiments performed with different lot of peptides were averaged and were expressed as the mean ± S.E.M.

3.4.18 Confocal microscopy

CHO-K1 ells were cultured in 8-well cell culture chamber at a density of 15 000 cells/well for 48 h before treatment. Alexa488-labeled oligomers or fibrils were added to cells and incubated at 37 °C or 4 °C for 3h. After incubation, cells were washed three times with PBS. Membrane was stained with 0.2 μg/ml of Cell mask 0.1 μg / mL DAPI (4′,6-Diamidino-2-phenylindole dihydrochloride). Cells were then washed three times with PBS, fixed with 4% paraformaldehyde and washed three times with PBS and stored in glycerol: Tris-HCl buffer (50% v/v). Fluorescence was analyzed with a confocal Nikon microscope equipped with a 60x oil immersion objective. All images were analyzed using ImageJ software.

3.4.19 Proteinase K digestion

Freshly dissolved peptides and fibrils were incubated with 120 U/mL of Proteinase K for 1h at 37℃. Solutions were mixed with an equal volume of a-cyano-4-hydroxycinnamic acid matrix and analyzed by MALDI-TOF mass spectrometry.

3.4.20 Statistical analysis

Statistical analyses were performed using the Student's t-test and statistically significance statistical difference (between IAPP and N21Q, otherwise stated) was established at $p < 0.001$ (*); $p < 0.0001$ (**); $p < 0.00001$ (***). Statistical analyses were carried out using GraphPad Prism 8.0 software.

3.4.21 Data availability

The data supporting the findings of this manuscript are available from the corresponding authors upon reasonable request.

3.5 Results

3.5.1 Shifting the toxicity of amyloid fibrils with a single N-to-Q substitution.

IAPP is known for its high propensity to self-assemble into cross-β amyloid structures, which are associated with the pathogenesis of type II diabetes. As reported by solid-state NMR, each monomeric units of the amyloid fibrils are composed of two β-strands connected by a disordered loop involving positions H18 to L27(Luca *et al.*, 2007). Recent cryo-EM studies have revealed conformational polymorphism of IAPP fibrils, with monomers composed of three β-sheets of variable lengths connected by disordered loops (Cao *et al.*, 2020; Gallardo *et al.*, 2020; Röder *et al.*, 2020). Cryo-EM study has

indicated that the around 90% of fibrils are composed of two S-shaped and intertwined protofilaments with the β-sheets composed of N14-S20, I26-V32 and N35-Y37(Röder *et al.*, 2020). Notwithstanding the models of IAPP fibrils, residue N21, which is critical for self-assembly and toxicity (Godin *et al.*, 2019; Koo *et al.*, 2008; Nguyen *et al.*, 2017), is located in a disordered loop joining β-strands and its side chain projects outward into protofilament interface and participates in protofilament packing (Fig. 1a). As reported for amyloidogenic proteins, amyloid fibrils assembled from IAPP are usually poorly cytotoxic, whereas oligomers and prefibrillar species damage cells (Abedini *et al.*, 2016; De Carufel *et al.*, 2015). Strikingly, the modest substitution of Asn at position 21 by a Gln (N21Q), which corresponds to displacement of the amide group away from the peptide backbone by approximatively 1.5 Å, led to the formation of fibrils that are highly toxic to β-pancreatic cells (Fig. 3.1). Fibrils were prepared by incubating the monomerized peptide in 20 mM Tris-HCl, pH 7.4 for 48 h at 150 μM under quiescent conditions at room temperature. Under these conditions, N21Q derivative self-assembled into prototypical twisted filaments (Fig. 3.1b), showing a concentration-dependent cytotoxicity. Viability measured by the metabolic activity of pancreatic INS-1E cells, a cell line commonly used to study IAPP, decreased below 20% of control at 25 μM N21Q, whereas IAPP fibrils showed no toxicity under all concentrations (Fig. 3.1c). IAPP-mediated toxicity is associated with numerous cellular events, including oxidative stress, mitochondrial dysfunction, plasma membrane disruption and apoptosis (Raleigh *et al.*, 2017). Considering that caspase-3 activation is an upstream event to viability measured by the metabolic activity, INS-1E cells were incubated for 1 to 6 h with fibrils before measuring caspase-3 activity. N21Q fibrils induced a significant increase of caspase-3 activation, with roughly a 3-fold increase compared to IAPP fibrils after 150 min incubation (Fig. 3.1d). Cytotoxicity of N21Q fibrils was further validated using the Live/Dead assay and INS-1E β-cells treated with IAPP fibrils showed a similar green/red ratio to the cells treated with the control (Fig. 3.1e, Fig. S3.1). The red fluorescence correlates with loss of plasma membrane

integrity and the green fluorescence is associated with intracellular esterase activity. In sharp contrast, cells treated with N21Q fibrils were all red-positive, indicative of perturbation of the plasma membrane.

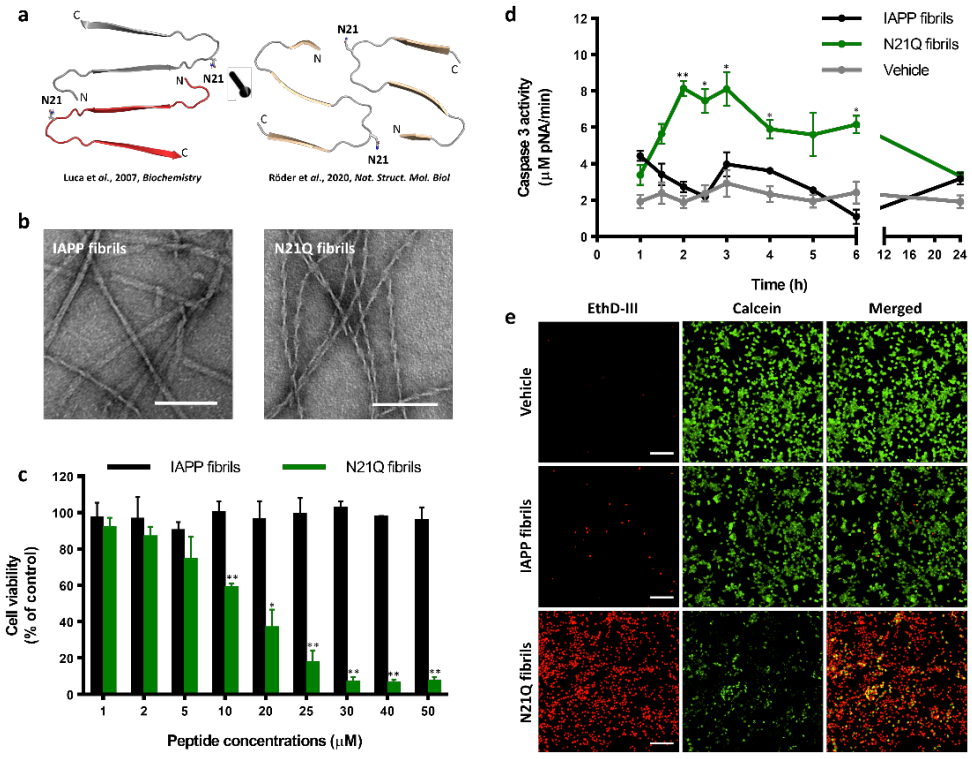


Fig. 3.1 Modulating the cytotoxicity of IAPP fibrils with an N-to-Q substitution at position 21.

a SS-NMR and cryo-EM models of IAPP secondary structure in amyloid fibrils showing the side chain of Asn21(Luca *et al.*, 2007; Röder *et al.*, 2020). b Representative TEM images of IAPP and N21Q fibrils. Scale bar: 100 nm. c INS-1E cells were incubated for 24 h with pre-assembled fibrils. d Caspase-3 activation over treatment time of INS-1E cells incubated with 50 μM fibrils. c-d Data represent mean ± S.E.M. of at least four experiments performed in triplicate. e Representative fluorescence microscopy images showing the distribution of live (green) and dead (red) INS-1E cells after treatment with 50 μM fibrils for 24 h. Scale bar: 50 μm. b-e Fibrils were assembled from freshly dissolved monomerized peptides incubated under quiescent conditions for 48 h at a concentration of 150 μM in 20 mM Tris-HCl buffer, pH 7.4.

We investigated if the unexpected toxicity of N21Q fibrils could result from the presence of soluble oligomers associated with an incomplete fibrillization and/or breakage of fibrils into oligomers. First, peptides were assembled for up to 5 days and cytotoxicity of the aggregation mixtures was periodically evaluated. Prolonging self-assembly did not modify the divergent toxicity observed between WT and N21Q fibrils (Fig. S3.2). Secondly, fibrils were isolated by centrifugation to remove any remaining soluble species that could cause cell death. Fibrils were subjected, or not, to a 30 min sonication, before being centrifuged at 35 000 g for 45 min. Pellets were washed, sonicated or not, and centrifuged a second time. First supernatants and final pellets were analyzed by transmission electron microscopy (TEM) and cytotoxicity was evaluated. N21Q fibrils isolated in the final pellet, with or without sonication, remained toxic to pancreatic cells (Fig. S3.3). Thirdly, as amyloid formation is a dynamic process and fibrils can disassemble and release toxic oligomers (Chuang *et al.*, 2018), we evaluated thermodynamic stability by thermal denaturation monitored by circular dichroism (CD) spectroscopy. According to the β-sheet signal at 218 nm, IAPP and N21Q fibrils in presence of 4 M urea showed a similar thermal unfolding midpoint (T_m); 58.1 ± 0.2°C for IAPP and 61.3 ± 0.5°C for N21Q (Fig. S3.4). Fourthly, stability against proteolysis was assessed by subjecting the assemblies to 120 U/mL of proteinase K (PK) for 1 h and digestion was evaluated by MALDI-TOF mass spectrometry. N21Q and WT fibrils showed an equivalent stability against PK proteolysis, suggesting a similar degree of fibril compactness and/or undetectable dissociation of soluble species (Fig. S3.5). These observations indicate that the cytotoxicity of N21Q assemblies is mediated by defined fibrils and is not associated with lower stability or the presence of soluble oligomers.

3.5.2 Supramolecular characterization of cytotoxic fibrils

To obtain insights into the molecular basis of the discrepancy in toxicity between IAPP and N21Q fibrils, their (supra)molecular properties were compared. As observed by TEM and atomic force microscopy (AFM), both peptides assembled into two major distinctive fibril morphologies: flat ribbons, and twisted filaments with varied pitches (Fig. 3.2a, b). Morphological heterogeneity of IAPP fibrils prepared *in vitro* is well-known (Luca *et al.*, 2007). Quantification of over 3000 fibrils per peptide using AFM images revealed that the prevalence of twisted fibrils in the N21Q samples was significantly higher (Fig. 3.2c). N21Q fibrils were somewhat shorter, with an average length of 1.08 ± 0.17 μm, compared to 1.42 ± 0.36 μm (Fig. 3.2c, Fig. S3.6). The average height of N21Q fibrils was approximatively half of the diameter measured for IAPP fibrils, *i.e.* 3.12 ± 1.24 nm *vs* 5.98 ± 2.62 nm (3.07 *vs* 6.11 nm, considering the median), suggesting that the number of protofilaments composing the fibrils and/or their compactness diverge. Measurement of Young's modulus revealed that N21Q fibrils displayed lower stiffness. Structural organization was probed by attenuated total reflectance Fourier transform infrared (ATR-FTIR) and far-UV CD spectroscopy. The amide I region of IAPP and N21Q spectra (1700 –1600 cm^{-1}) were practically identical with three characteristic amide peaks (Fig. 3.2d). The first pic at 1685 cm^{-1} suggests an anti-parallel β-sheet, in agreement with the molecular organization of IAPP fibrils (Luca *et al.*, 2007; Röder *et al.*, 2020). Signal at 1645 cm^{-1} represents turn structure, whereas the peak at 1616 cm^{-1} is indicative of β-sheets under the amyloid fold (Zandomeneghi *et al.*, 2004). CD spectra of IAPP and N21Q fibrils displayed a single minimum at 218 nm, corresponding to a β-sheet-rich secondary structure (Fig. 3.2e). The amyloid architecture was probed by measuring the fluorescence of thioflavin T (ThT), whose emission increases sharply upon binding to cross-β quaternary structure (Sebastiao *et al.*, 2017). Whereas fibrils assembled from the IAPP presented a sharp

ThT signal, N21Q fibrils led to a modest increase in ThT fluorescence (Fig. 3.2f), suggestive of less defined ThT binding sites. Although low-ThT binding is generally ascribed to prefibrillar assemblies, this characteristic has been reported for fibrils assembled from different peptides, including pufferfish IAPP (Wong *et al.*, 2016) and the Japanese mutant of Aβ (ΔE22) (Cloe *et al.*, 2011). Accessibility of hydrophobic clusters was evaluated using the 8-anilino-1-naphtalenesulfonic acid (ANS) that binds to solvent-exposed hydrophobic domains, leading to an increase and blue shift of fluorescence emission. In comparison to WT fibrils, the N21Q fibrils led to a strong increase of ANS fluorescence, indicative of higher surface hydrophobicity (Fig. 3.2g). Powder X-ray diffraction (XRD) of both fibrils revealed a diffraction pattern characterized with two sharp peaks and Bragg reflections corresponding to 4.7 Å and 8.9 Å periodic spacing were measured (Fig. 3.2h). The 4.7 Å meridional reflection corresponds to the prototypical signature of amyloids arising from the β-strand spacing. While the 8.9 Å inter-sheet distance is rather short for amyloids, which is typically around 10 Å, the inter-sheet spacing is shorter in dry interface (Nelson *et al.*, 2005), as for powder XRD. Overall, these results indicate that IAPP and N21Q fibrils exhibit a similar structural organization, although dissimilarities were observed at the mesoscopic level (morphology, height) and in the ability to interact with environment sensitive dyes.

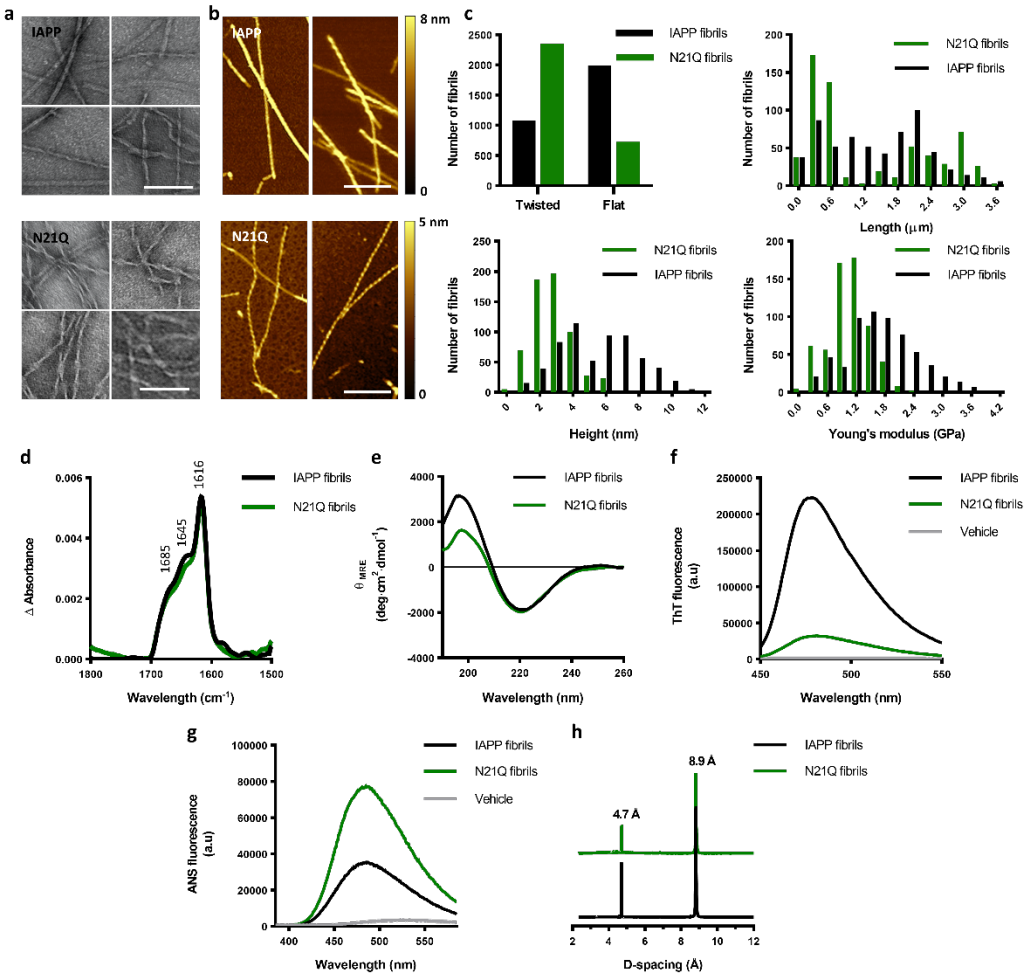


Fig. 3.2 Characterization of N21Q cytotoxic fibrils.

a,b Representative images of flat and twisted IAPP and N21Q fibrils revealed by (a) TEM and (b) AFM. Scale bar: 100 nm. c Distributions of mesoscopic morphology and stiffness of over 3 000 fibrils per peptide imaged by AFM. d ATR-FTIR absorbance spectra of the amide I region (1500-1800 cm^{-1}) of IAPP and N21Q fibrils. e Far-UV circular dichroism spectra of IAPP and N21Q fibrils. f ThT fluorescence of fibrils. Emission spectra of ThT (40 μM) with an excitation at 440 nm. g Surface hydrophobicity measured by ANS fluorescence. Emission spectra of ANS (100 μM) with an excitation at 355 nm. h Powder XRD diffraction spectra revealing a periodic amyloid packing for IAPP and N21Q fibrils. a-h Fibrils were assembled from freshly dissolved monomerized peptides incubated under quiescent conditions for 48 h at 150 μM in 20 mM Tris-HCl buffer, pH 7.4. Assemblies were diluted to 10 μM (a,b,c) and 50 μM (e,f,g), immediately before analysis.

SS-NMR was used to evaluate changes in the microenvironment of specific residues induced by the N-to-Q substitution that could expose molecular fingerprints of toxicity. Peptides with uniformly labelled ^{13}C and ^{15}N residues at positions A13, F23, and V32 were assembled at 750 μM and fibrils were recovered by centrifugation and lyophilized. Fibrils conserved their distinctive biophysical properties and cytotoxicity (Fig. 3.7). Labelled residues were selected to comprise the different segments of the peptide according to SS-NMR and cryo-EM models of fibrils (Fig. 3.3a) (Luca *et al.*, 2007; Röder *et al.*, 2020). Cross-polarization (CP) dipolar assisted rotational resonance (DARR) spectra of IAPP (black) and N21Q (green) fibrils were overlaid (Fig. 3.3b). Assignments of residue chemical shifts were established based on the connectivity pattern and the typical ranges for each carbon. Secondary ^{13}C chemical shifts (Δδ) for Cα, Cβ, and CO of labelled residues were calculated as $\Delta\delta = \delta_{obs} - \delta_{RC}$ (Fig. S3.8). Chemical shifts indicated that the cross-β-sheet structure is largely retained in both fibril preparations, as indicated by Δδ of Cβ being positive, and CO and Cα being negative. Spectra obtained from both fibrils were similar in the aliphatic and aromatic regions, with two minor changes regarding A13 Cβ and V32 Cγ. Pronounced changes were observed in the carbonyl region of the spectra. N21Q fibrils carbonyl resonances were deshielded compared to IAPP, indicative of either a change in structure or local environment (Fig. 3.3c, Fig. S3.8). F23 exhibited the largest change in CO shift, from 169.8 ppm in IAPP to 173.4 ppm in N21Q fibrils, leading to alteration of F23 CO secondary shift, from strongly negative (-3.3 ppm) in IAPP to 0.3 ppm in N21Q. Considering the lack of changes in the Cα and Cβ secondary shifts of F23, this is not related to alteration in secondary structure but may instead be a result of local increase in hydrophobicity (Mallamace *et al.*, 2018). Change in V32 CO secondary shifts, from negative value towards zero, suggested a similar effect affecting the C-terminal region.

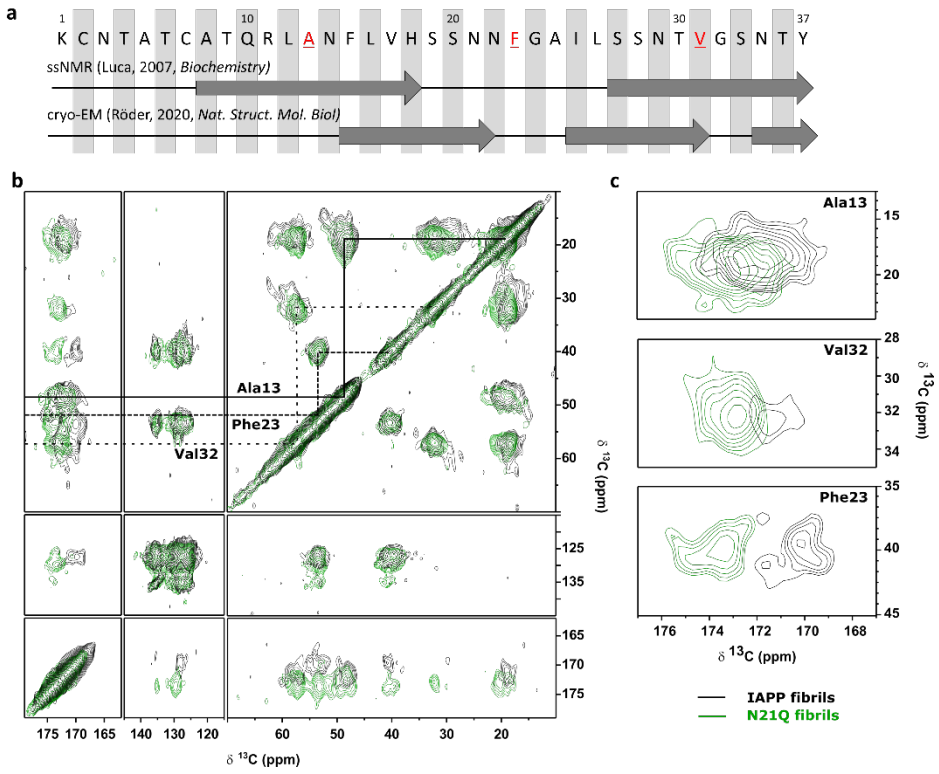


Fig. 3.3 SS-NMR spectra of N21Q and WT IAPP fibrils.

a Sequence of IAPP showing the ^{13}C and ^{15}N uniformally labelled residues (red underlined) and the secondary structures under the amyloid fold. b CP-DARR spectra of IAPP and N21Q fibrils. c Carbonyl region of the spectrum showing changes in Ala13, Val32 and Phe23 chemical shifts. b-c Fibrils were assembled from monomerized peptides incubated under quiescent conditions for 48 h at 750 µM in 20 mM Tris-HCl buffer, pH 7.4. Fibrils were recovered by ultracentrifugation at 100 000g for 45 min, 4 °C. Pellet was re-suspended in water and lyophilized before SS-NMR analysis.

3.5.3 Kinetics of self-assembly and time-resolved analysis of cytotoxicity

The observed distinct biological properties, *i.e.* cytocompatible *vs* toxic, from fibrils assembled from closely related peptides, *i.e.* IAPP *vs* N21Q, could arise from divergent

aggregation pathways. Accordingly, we evaluated the kinetics of self-assembly by ThT and ANS fluorescence, as well as using an assay based on fluorescein arsenical hairpin (FlAsH). Although a weak ThT signal was measured for N21Q, typical sigmoidal traces characterized with three distinct phases (lag, elongation, saturation) were observed, suggestive of a nucleation-dependent polymerization (Fig. 3.4a, Fig. S3.9). Lag-times of 9.9 ± 2.0 h and 7.0 ± 1.5 h were extracted respectively from IAPP and N21Q ThT kinetics, indicating that the N21Q substitution hastens nucleation. Considering the low ThT-signal of N21Q, the fluorogenic probe FlAsH was used. FlAsH, which fluorescence quantum yield dramatically increases upon its binding to a tetracysteic tag (Luedtke *et al.*, 2007), has been recently used to detect IAPP self-assembly through the formation of a non-contiguous tetra-Cys binding motif involving the N-terminal C2 and C7(Quittot *et al.*, 2018). This method is well-suited to detect ThT-negative fibrils (Quittot *et al.*, 2018), as those assembled from N21Q. Self-assembly monitored by FlAsH and performed under reducing conditions, revealed a typical sigmoidal growth with lag-time of 7.3 ± 1.4 h and 2.6 ± 1.9 h for IAPP and N21Q, respectively (Fig. 3.4b, Fig. 3.9). Kinetics of aggregation monitored by ANS fluorescence confirmed that the N21Q substitution accelerates nucleation (Fig. 3.4c).

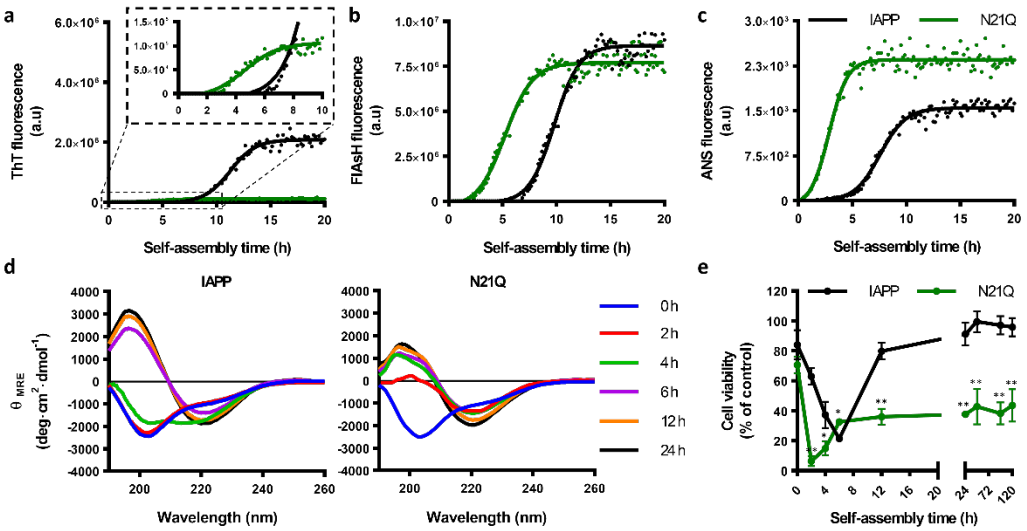


Fig. 3.4 Kinetics of self-assembly and time-resolved analysis of cytotoxicity.

a-c Kinetics of self-assembly monitored by (a) ThT, (b) FlAsH, and (c) ANS fluorescence. Monomerized peptides were incubated at 12.5 µM under quiescent conditions in 20 mM Tris-HCl buffer, pH 7.4 in the presence of ThT (40 µM), FlAsH (0.5 µM) or ANS (50 µM). Fluorescence of ThT (Ex 440 nm, Em 485 nm), FlAsH (Ex 508 nm, Em 533 nm) and ANS (Ex 355 nm, Em 480 nm) was measured every 10 min. Data from triplicates were averaged and fitted with a Boltzmann sigmoidal curve. d Time-resolved secondary conformational conversion of IAPP and N21Q monitored by CD spectroscopy. e Time-resolved cytotoxicity of proteospecies evaluated by measuring the metabolic activity of INS-1E upon 5 h incubation with 50 µM pre-assembled peptides. d-e Freshly dissolved monomerized peptides were incubated under quiescent conditions at 150 µM in 20 mM Tris-HCl buffer, pH 7.4.

Next, the toxicity of the proteospecies assembled along the aggregation pathway was evaluated. When freshly dissolved monomerized peptides (0 h) were immediately applied to INS-1E cells, a concentration-dependant toxicity is observed for both peptides, albeit N21Q was significantly more toxic (Fig. S3.10). The higher toxicity of monomeric N21Q correlated with a hastened capacity to induce caspase-3 activation and to perturb synthetic large unilamellar vesicles (LUVs) composed of phosphocholine/phosphoglycerol (DOPC/DOPG) (Fig. S3.10). For time-resolved

toxicity, peptides were incubated at 150 μM and after different incubation times, the conformational shift was observed by CD spectroscopy and toxicity was evaluated. Cellular viability was measured after 5 h incubation with 50 μM proteospecies by measuring metabolic activity. In agreement with self-assembly kinetics, the random coil→β-sheet secondary structural conversion occurred after 2 h for N21Q and after 6 h for IAPP (Fig. 3.4d). As previously reported (Abedini *et al.*, 2016), IAPP cytotoxicity correlated with self-assembly time, with the proteospecies populating the lag phase decreasing cell viability and the fibrils, *i.e.* over 24 h self-assembly time, being non-cytotoxic (Fig. 3.4e). In sharp contrast, N21Q species of the elongation and saturation phases remained cytotoxic, although their toxicity was less compared to the one induced by the assemblies of the lag phase. Taken together, these data suggest that N21Q substitution hastens IAPP self-assembly into fibrillar assemblies that conserve biological properties of soluble toxic oligomers.

3.5.4 N21Q fibrils share conformational characteristics with prefibrillar toxic oligomers.

Time-resolved analysis suggested that the toxic oligomer-like properties of N21Q are maintained upon fibril elongation. This hypothesis was evaluated using conformational antibodies that specifically recognize distinct supramolecular structures (Kayed *et al.*, 2007). As revealed by dot blot analysis, isolated IAPP and N21Q fibrils were recognized by the anti-amyloid LOC and 4G8 antibodies (Fig. 3.5a). The oligomer-specific A11 antibody recognized oligomers, which were prepared by incubating the peptides at 150 μM for 15 min (Fig. S3.11). Strikingly, the A11 antibody recognized N21Q fibrils (Fig. 5a). ELISA (Fig. S3.12) confirmed these results. In contrast to IAPP fibrils, immunogold EM images revealed that N21Q fibrils were simultaneously

recognized by the anti-amyloid 4G8 (10 nm gold-particles, white arrows) and the anti-oligomer A11 (20 nm gold-particles, yellow arrows) antibodies (Fig. 3.5b). IAPP and N21Q fibrils separately incubated with A11, LOC and 4GB primary antibodies confirmed the orthogonality of the double labelling approach (Fig. S3.13). Thus, N21Q peptide preserves the A11-specific oligomer epitope upon elongation into fibrils. Several conformational models have been proposed for IAPP oligomers, including α-helix coiled-coil (Abedini et Raleigh, 2009), β-hairpin assemblies (Dupuis *et al.*, 2009) and parallel β-sheets involving the 20-29 segment (Buchanan *et al.*, 2013). The latter model proposes that the 20-29 segment of IAPP mediates initial self-recognition and that the oligomers contain stacks of solvent-exposed β-sheets involving the ^{23}FGAIL^{27} region. Considering that N21Q fibrils exhibit oligomeric characteristics, exposure of the 20-29 region during self-assembly was evaluated by replacing F23 by a p-cyano-phenylalanine (F_{CN}) whose fluorescence quantum yield is modulated by solvent exposure. As previously reported (Marek *et al.*, 2010), fluorescence of F23F_{CN} IAPP decreased over self-assembly time, indicating that position 23 is being buried from the solvent with fibril growth (Fig. 3.5c). In sharp contrast, high fluorescence final persisted during F23F_{CN} N21Q self-assembly. This observation suggests that the ^{23}FGAIL^{27} region remains solvent-exposed in the fibrils, in agreement with the SS-NMR data showing alterations of the chemical shifts of F23 in N21Q fibrils (Fig. 3.3). Solvent-exposure of residue F15, which would be buried inside IAPP fibrils according to the SS-NMR (Luca *et al.*, 2007) and cryo-EM (Röder *et al.*, 2020) models, was also evaluated by incorporating a F_{CN}. Strikingly, fluorescence intensity of both F15$_{CN}$ peptides decreased over incubation time, indicating that this region is buried in N21Q and IAPP fibrils (Fig. 3.5c). These data indicate that the oligomer conformation of N21Q is preserved upon fibril elongation and that the exposure of the FGAIL hydrophobic region could contribute to the toxicity of N21Q fibrils.

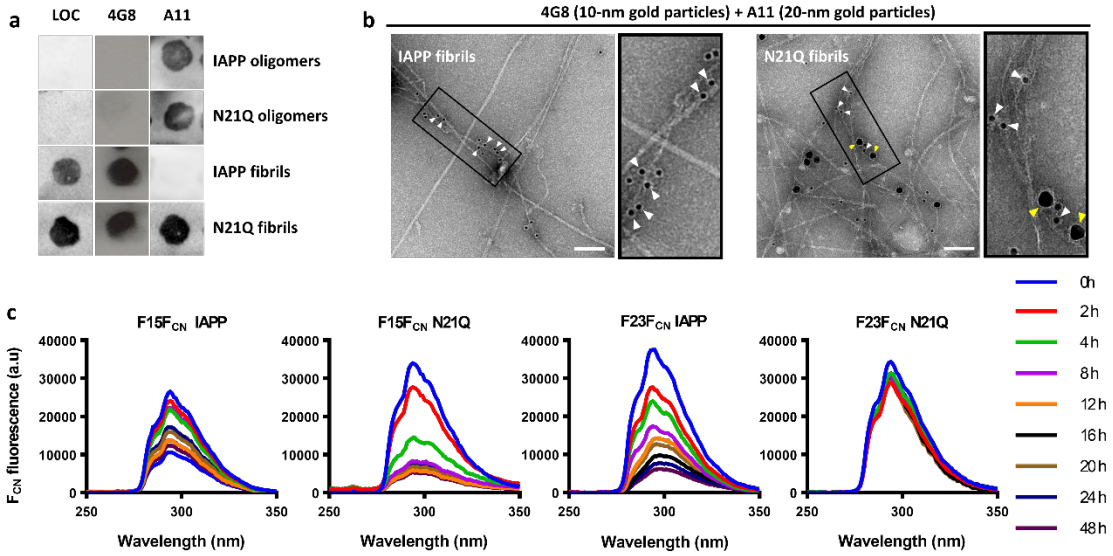


Fig. 3.5 N21Q fibrils exhibit oligomer-like conformation and expose residue F23 on the surface.

a Dot-blot analysis of IAPP and N21Q oligomers and fibrils. b Immunogold labelling electron microscopy images of IAPP and N21Q fibrils, scale bar: 100 nm. 3 × zoom image of the region indicated by the rectangle. a-b Peptides were incubated under quiescent conditions for 15 min (oligomers) and 48 h (fibrils) at 150 µM in 20 mM Tris-HCl buffer, pH 7.4. c F_{CN} fluorescence emission spectra over self-assembly time. Peptides were incubated under quiescent conditions for 48 h at 150 µM in 20 mM Tris-HCl buffer, pH 7.4.

3.5.5 N21Q fibrils disrupt plasma membrane

Several mechanisms mediating the toxicity of oligomers have been proposed, and plasma membrane disruption remains the most abundantly described (Brender *et al.*, 2012). The capacity of N21Q fibrils to disrupt lipid membranes was compared to the one of IAPP oligomers. Disruption of lipid bilayer was first evaluated using DOPC:DOPG (7:3) LUVs loaded with self-quenched calcein. WT oligomers (Fig. S3.11) and N21Q fibrils induced high permeabilization of LUVs with leakage of 40 to

60% after 3 h incubation, whereas IAPP fibrils induced below 10% of leakage after 5 h incubation (Fig. 3.6a). Plasma membrane disruption of β-cells was evaluated by measuring the release of the cytoplasmic enzyme lactate dehydrogenase (LDH). As anticipated, IAPP fibrils did not led to a significant release of LDH, whereas N21Q fibrils and WT oligomers induced high LDH activity in the media, with activity around 60% of the cells treated with the lysis buffer (Fig. 3.6b). Moreover, IAPP oligomer mixture and N21Q fibrils induced a similar time-dependant activation of caspase-3, suggestive of a similar mechanism of toxicity (Fig. 3.6c). Interaction of N21Q fibrils with the plasma membrane was evaluated by confocal microscopy and compared with toxic oligomers and cytocompatible fibrils. Fluorescent quaternary species were prepared by co-assembling Alexa Fluor 488-labelled monomers with unlabeled monomerized peptides at a molar ratio of 0.5:100, allowing the formation of fluorescent fibrils and oligomers with equivalent (supra)structural and biological properties to unlabelled peptides. CHO cells were used, since INS-1E cells detached promptly in presence of N21Q fibrils, precluding the washing steps necessary for microscopy analyses. CHO cells showed similar susceptibility towards concentration-dependant membrane disruption and toxicity induced by the proteospecies (Fig. S3.14). Z-stack reconstruction images revealed that IAPP fibrils gather at the cell surface and do not incorporate avidly within the plasma membrane (Fig. 3.6d). In sharp contrast, IAPP oligomers colocalized with lipids and extracted them from the membrane. Strikingly, N21Q fibrils damaged plasma membrane by pulling-out lipids, as observed with the formation of large yellow puncta containing the fluorescent fibrils in green and lipid vesicles in red (Fig. 3.6d). These data revealed that the N21Q fibrils mediate plasma membrane disassembly and permabilization, perhaps an upstream event to cell death, as observed for toxic oligomers.

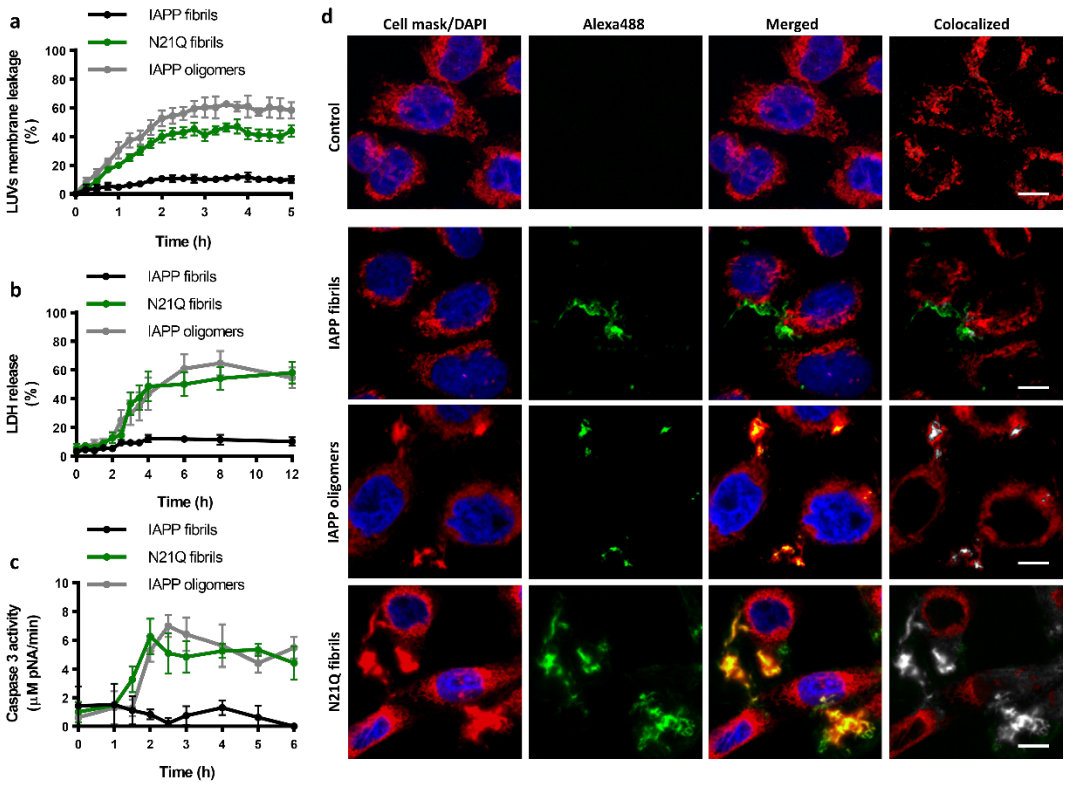


Fig. 3.6 N21Q fibrils disrupt lipid vesicles and plasma membrane.

a Membrane leakage of 500 μM DOPC:DOPG LUVs (7:3) by 50 μM oligomers and fibrils. b LDH release from INS-1E cells incubated with 50 μM fibrils and oligomers for different times. c Caspase-3 activation upon incubation of INS-1E cells with 50 μM fibrils and oligomers for different treatment times. d Representative fluorescent confocal images of CHO-K1 cells treated with Alexa Fluor-488 labelled (green) fibrils and oligomers. Cell nuclei and plasma membrane were stained in blue and red, respectively. Scale bar: 10 μm. a-b Oligomers and fibrils were assembled from monomerized peptides incubated under quiescent conditions for 15 min (oligomers) and 48 h (fibrils) at 150 μM in 20 mM Tris-HCl buffer, pH 7.4.

3.5.6 The oligomer-like toxic conformation of N21Q fibrils propagates to WT IAPP

Secondary nucleation, which corresponds to formation of nucleus catalyzed through interactions of pre-existing fibrils with monomers, or oligomers, plays a critical in amyloid formation (Tornquist *et al.*, 2018). By this mechanism, the conformation of an aggregate can propagate to a naïve polypeptide building block, whose assemblies will acquire the properties of pre-formed aggregates, as prion propagation. Accordingly, we evaluated the cross-seeding properties of N21Q and IAPP fibrils, *i.e.* how fibrils can propagate their properties to monomeric counterparts. First, isolated N21Q fibrils were used to seed amyloid formation of WT IAPP. Interestingly, increasing the molar ratio of N21Q seeds, from 0.5 to 5% (molar equivalent), in IAPP self-assembly induced a progressive decrease of ThT fluorescence, an increase in surface hydrophobicity, and the formation of a conformational epitope that is recognized by the anti-oligomer A11 antibody (Fig. 3.7a,b). Appropriate controls validated that up to 2.5 μM N21Q seeds (5 mol%) do not contribute to A11 binding and ANS signal (Fig. S3.15). Moreover, incubating monomeric F23F_{CN} IAPP in presence of N21Q seeds led to the formation of F23F_{CN} IAPP fibrils with high solvent exposure of F23 side chain, indicating that the N21Q conformation propagates to WT peptide (Fig. 3.7c). TEM images revealed that the presence of N21Q seeds within IAPP self-assembly mixture led to the formation of a mixture of twisted fibrils and flat ribbons, with twisted morphology being progressively more prevalent with increasing N21Q seeds (Fig. S3.16). Predominantly, IAPP fibrils grown in presence of over 2% of N21Q seeds were toxic to pancreatic β-cells (Fig. 3.7d). As control, INS-1E cells were treated with the respective concentrations of N21Q seeds (0.25 to 2.5 μM), and no decrease of cell viability was measured under these concentrations (Fig. S3.17). The inverse seeding experiment was also performed, *i.e.* N21Q self-assembly was seeded with IAPP fibrils. Under these conditions, N21Q assemblies progressively acquired conformational and biological properties of IAPP fibrils; low toxicity, high ThT-binding, low

hydrophobicity, progressive burying of Phe23, low recognition by the A11 antibody, and higher prevalence of ribbon morphology (Fig. S3.18). Overall, these results indicate that the oligomer-like conformation of N21Q fibrils is transmissible to the WT peptide, which suggests that the cytotoxic motif constitutes an organized supramolecular architecture.

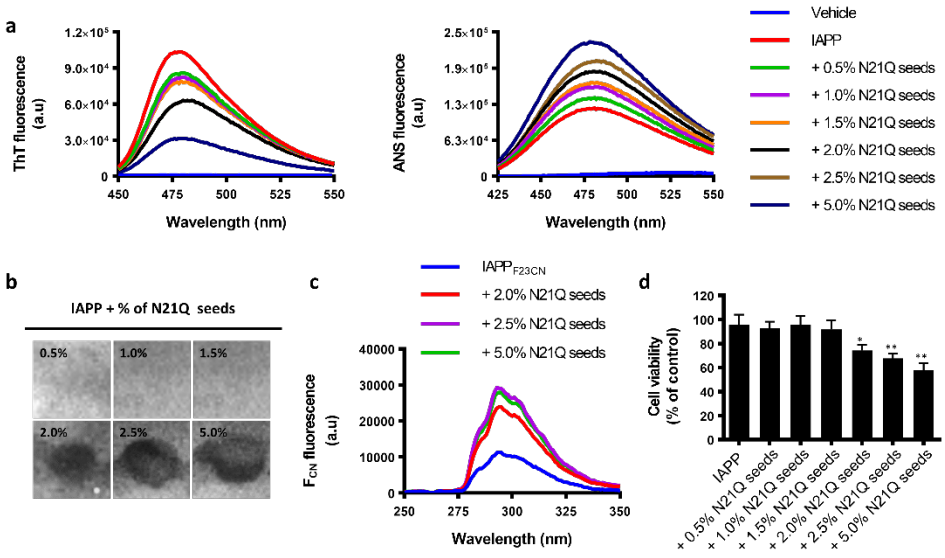


Fig. 3.7 The oligomer conformation of N21Q fibrils propagates to IAPP.

a-c Self-assembly of IAPP seeded with N21Q pre-assembled fibrils (0.5 to 5 mol%) was characterized by (a) ThT fluorescence and ANS fluorescence, (b) dot-blot analysis with the anti-oligomer A11 antibody and (c) F_{CN} fluorescence of the F23F_{CN} IAPP. (d) Cell viability of INS-1E treated with 50 µM IAPP fibrils seeded with N21Q pre-assembled fibrils. (a-d) N21Q fibrillar seeds were grown for 48h (quiescent conditions, 150 µM in 20 mM Tris-HCl buffer, pH 7.4) before being isolated and used to seed the amyloid formation of IAPP under quiescent conditions for 48 h.

3.6 Discussion

Inconsistency among the reported toxicity of the proteospecies of the amyloid cascade has been associated with their atomistic/mesoscopic structural polymorphism and dynamic nature, which could ultimately modulate progression of amyloid-related disorders (Fändrich *et al.*, 2018; Tycko, 2015). It is known that the self-assembly of a given protein under different conditions leads to the formation of assemblies with discrete morphologies, and each of these structures can exert distinct functionalities. Similarly, site-specific mutagenesis can result in diverse supramolecular structures with divergent toxicity. Herein, we took advantage of an apparently trivial N-to-Q substitution to identify a novel fibrillar nanostructure with oligomer properties and high cytotoxicity, underlining the high susceptibility of amyloid self-assembly to point mutation. Toxicity of defined amyloid assemblies has been ascribed to fibril breakage into short protofilaments and leakage of soluble oligomers. This is not the case for N21Q fibrils, as these assemblies showed comparable thermodynamic and enzymatic stability with IAPP fibrils and, perhaps, represent an energetic dead-end of aggregation. Interestingly, the oligomer properties of N21Q assemblies are preserved during fibril elongation and are transmissible to its WT counterpart. On the one hand, N21Q fibrils share prototypical amyloid characteristics with IAPP fibrils, including a 4.7 Å distance between stacked β-strands, a conformation rich in β-sheet, low solvent-exposition of F15, recognition by anti-amyloid antibodies, and long and linear morphology. One the other hand, cytotoxic N21Q fibrils diverge from IAPP fibrils by low ThT-binding, high surface hydrophobicity, solvent exposure of F23, recognition by oligomer-specific antibody, short thickness and higher proportion of twisted filaments. These divergent properties, which arise from the minor incorporation of a methyl group within N21 side chain, are associated with high ability to disrupt lipid membranes and to cause cellular dysfunction.

Studies regarding the molecular basis of amyloid-related pathogenicity have proposed determinants of prefibrillar species associated with cytotoxicity, including size, hydrophobicity, compactness, rigidity and morphology. For the Aβ peptide, it has been shown that toxicity correlates inversely to the size of aggregates (Chimon *et al.*, 2007; De *et al.*, 2019; Kayed *et al.*, 2009; Stroud *et al.*, 2012; Yang *et al.*, 2017). It has been proposed that low molecular weight oligomers, with a high diffusion coefficient, diffuse rapidly within biological environment, favoring aberrant interactions with cellular components. Herein, we showed that cytotoxicity is mediated by defined fibrils with microscale length, indicating that toxicity does not necessarily correlate with oligomerization state, suggestive of conformational-dependent toxicity. Studies with oligomers assembled from diverse polypeptides, including Sup35(Krishnan *et al.*, 2012), HypF-N (Campioni *et al.*, 2010), Aβ (Ladiwala *et al.*, 2012; Okada *et al.*, 2019) and α-synuclein(Fusco *et al.*, 2017), have exposed that oligomers of similar size and morphology can exposed divergent toxicity, which correlates closely with exposure of hydrophobic clusters and capacity to disrupt plasma membranes(Stefani, 2010). Poorly toxic oligomers have compact structures with the hydrophobic region buried inside, as observed for mature amyloid fibrils. Conversely, loose oligomers with high degree of hydrophobic exposure tend to be more cytotoxic (Campioni *et al.*, 2010; Stefani, 2012). In the present study, N21Q fibrils exhibited high hydrophobicity and these hydrophobic clusters likely involve organized stacks of the ^{23}FGAIL^{27} segment. Surface hydrophobicity of N21Q assemblies promoted its insertion within plasma membrane, resulting in disassembly of lipid bilayers and plasma membrane permeabilization. Although both fibril preparations showed high polymorphism, the prevalence of twisted fibrils was significantly more important for N21Q, which can be transposed to different organization/packaging of protofilaments. It has been reported for Aβ, that twisted fibrils are more toxic to their striated ribbon counterpart (Petkova *et al.*, 2005), and twisted morphology has been observed for fibrils extracted from Alzheimer patients (Qiang *et al.*, 2017). The capacity of N21Q fibrils to perturb lipid membranes could be associated with twisted supramolecular organization, which could increase

surface hydrophobicity. Twisted morphology, either from twisting of protofilament(s) around a central axis or wrapping of protofilaments around an internal axis, emerges early during elongation. While stacking of monomers, or oligomers, onto growing fibrils is driven by hydrophobic contacts, protofilament twisting and wrapping are modulated by a fine balance of specific interactions, including steric repulsions and hydrogen bonding, both being highly dependent of residue side chains (Auer *et al.*, 2008). According to the cryo-EM model of IAPP fibrils, N21 side chain of an S-shaped protofilament connects the opposite protofilament with a long and weak hydrogen bond involving the amidated C-terminus (Röder *et al.*, 2020). As observed by AFM, the N-to-Q substitution affects twisting and/or wrapping of protofilaments, and the width and stiffness of the resulting fibrils, likely by modulating the strength, the stability and/or the positioning of inter-protofilament H-bond.

IAPP self-assembly is ascribed to a nucleated conformational conversion of oligomers, in which hydrophobic collapse of IAPP monomers leads to rapid oligomerization into large ensemble of aggregates followed by the slow conversion of competent oligomers into protofilaments (Quittot *et al.*, 2018). The 20-29 segment has been proposed to drive self-recognition into on-pathway oligomers, which could be composed of stacks of ^{23}FGAIL^{27} β-sheets (Buchanan *et al.*, 2013; Serrano *et al.*, 2017). Accordingly, nucleation is kinetically controlled by an energy barrier involving the conversion of this segment from a β-sheet into a loop, which allows formation of the hairpin (Luca *et al.*, 2007), or S-shaped(Gallardo *et al.*, 2020; Röder *et al.*, 2020), structure within monomers of the growing protofilament. Not only N21 acts as a molecular hinge modulating IAPP primary nucleation (Godin *et al.*, 2019), it forms extensive interlayer hydrogen-bonding interactions within protofilament, known as polar ladder(Gallardo *et al.*, 2020; Röder *et al.*, 2020). As observed by time-resolved ThT, ANS and FlAsH fluorescence, CD spectroscopy, and solvent exposition of F_{CN}15, N21Q substitution reduced the lag phase, indicating that the amide group at position 21 is a key player in nucleation and, perhaps, elongation. Particularly, the oligomer conformation

recognized by the A11 antibody is preserved during elongation. As observed by the solvent-exposure of $F_{CN}23$ and SS-NMR analysis, this conformational epitope likely made of repeating arrays of ^{23}FGAIL^{27} remains exposed in N21Q mature fibrils. Seeding experiments revealed that the oligomer-like conformation of N21Q fibrils is structurally defined at the quaternary level. Overall, these observations suggest that the N21Q substitution unlocks an alternative self-assembly pathway emerging concurrently to primary nucleation, leading to cytotoxic fibrils.

In contrast to soluble oligomers, N21Q fibrils avidly seeded self-assembly and the resulting IAPP assemblies comprise cytotoxic properties. This ability to seed amyloid formation indicates that the oligomer-like conformation of N21Q is organized into a repeating display of monomers, wherein all monomers share identical conformation. The transmissible and exposed lattice of monomers recognized by the A11 antibody and likely involving the 20-29 domain could represent the toxic quaternary epitope. The capacity of prefibrillar intermediates to cause cellular dysfunction has been associated with their intrinsic ability to induce disassembly of plasma membrane, modulating downstream events leading to cell death. Nonetheless, the dynamics and structural heterogeneity of oligomers constitute major challenges for their structural and biological characterization. Considering that N21Q fibrils share conformational and biological characteristics with toxic oligomers, including a persistent ability to pull-out lipids from plasma membrane and disassemble lipid bilayers, these thermodynamically stable fibrils offer a unique opportunity to define the structural determinants of oligomer-induced cell death. The present study showed for the first time that the oligomer conformation can be preserved upon fibril elongation and can propagate through prion-like spreading. The identification of these novel defined filaments with concomitant fibrillar and oligomeric properties expands the diversity of amyloid assemblies and increases the complexity of quaternary structures associated with amyloid-related disorders.

3.7 Supporting Information

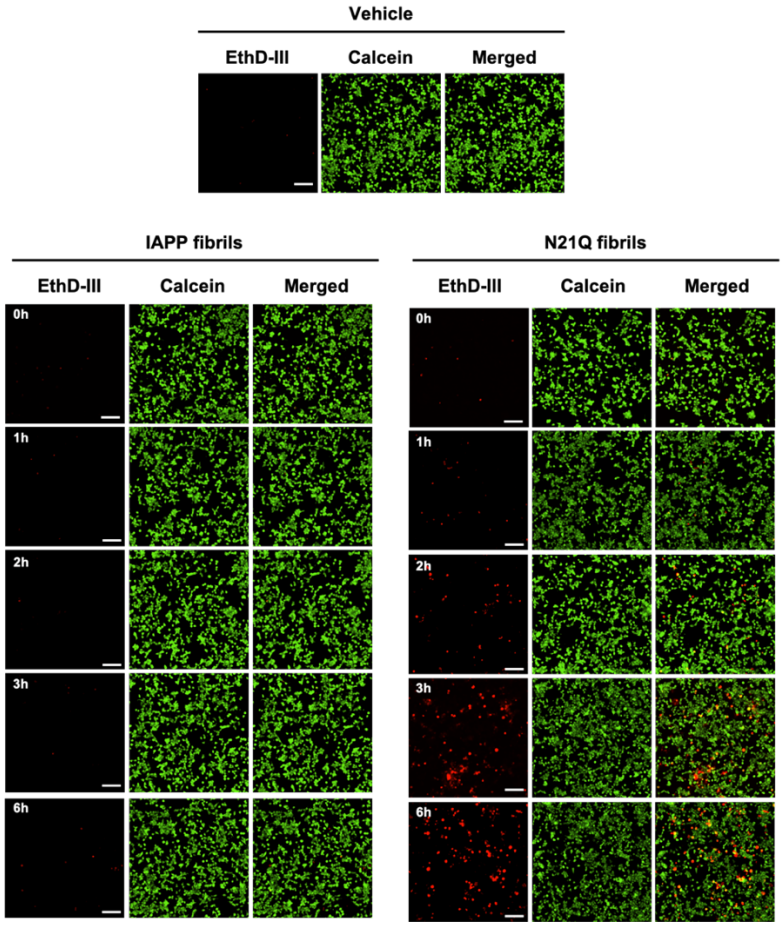


Fig. S3.1 Cytotoxicity of IAPP and N21Q fibrils measured by the LIVE/DEAD assay.

Representative fluorescence microscopy images showing the distribution of lived (green) and dead (red) INS-1E cells after treatment with 50 μM fibrils for 0 h to 6 h. Scale bar: 100 μm. Fibrils were assembled from freshly dissolved monomerized peptides incubated under quiescent conditions for 48 h at a concentration of 150 μM in 20 mM Tris-HCl buffer, pH 7.4.

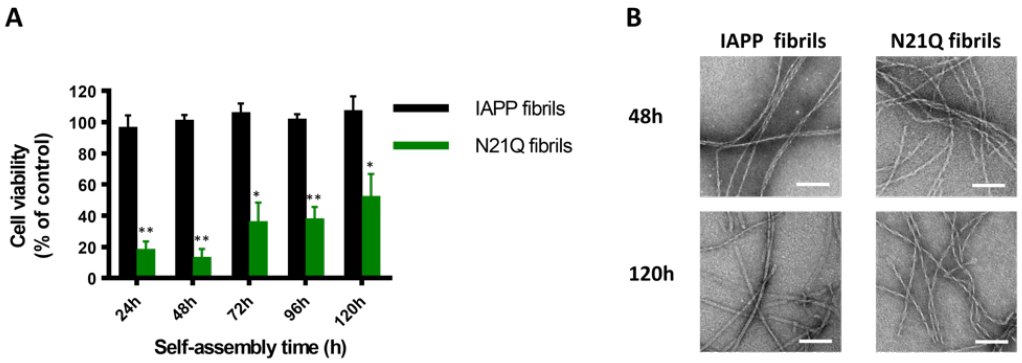


Fig. S3.2 Fibril toxicity over extended self-assembly periods.

(A) Cell viability of INS-1E treated with 50 μM of WT and N21Q fibrils assembled for different time, ranging between 24 h and 120 h. Data represent mean ± S.E.M of at least four individual experiments performed in triplicate. (B) TEM images of IAPP and N21Q fibrils after 48 h and 120 h of self-assembly time. Scale bar: 100 nm. (A,B) Fibrils were assembled from freshly dissolved monomerized peptides incubated under quiescent conditions at a concentration of 150 μM in 20 mM Tris-HCl buffer, pH 7.4.

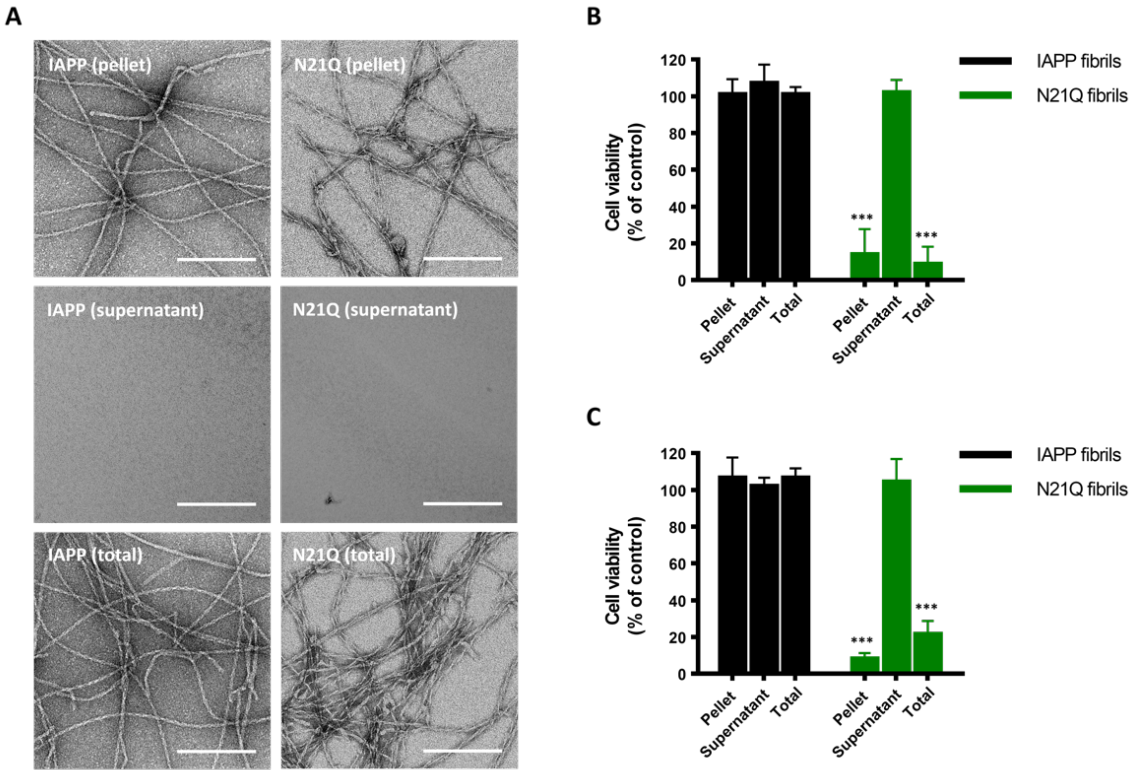


Fig. S3.3 Cytotoxicity of isolated IAPP and N21Q fibrils.

(A) Assemblies recovered after centrifugation were imaged by TEM. (B,C) Cytotoxicity of isolated fibrils (B) without sonication and with (C) 30 min sonication. Data represent mean ± S.E.M of at least four individual experiments performed in triplicate. INS-1E cells were incubated with 50 µM fibrils. (A,B,C) Fibrils were assembled from freshly dissolved monomerized peptides incubated under quiescent conditions for 48 h at a concentration of 150 µM in 20 mM Tris-HCl buffer, pH 7.4. Fibrils were isolated by two successive centrifugations at 35 000g for 45 min at 4 °C.

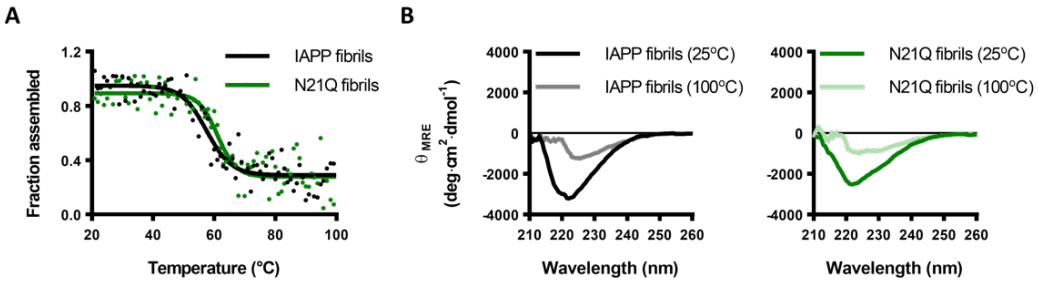


Fig. S3.4 Thermodynamic stability of IAPP and N21Q fibrils.

(A) Representative thermal denaturation curve of IAPP and N21Q fibrils monitored by CD spectroscopy with ellipticity at 218 nm. IAPP fibrils showed a T_m of 58.1 ± 0.2 °C and N21Q fibrils showed a T_m of 61.3 ± 0.5°C. (B) Representative CD spectra of IAPP and N21Q fibrils at 25 °C and 100 °C in presence of 4 M urea. (A,B) Fibrils were assembled from freshly dissolved monomerized peptides incubated under quiescent conditions for 48 h at a concentration of 150 μM in 20 mM Tris-HCl buffer, pH 7.4. Fibrils were diluted to 50 μM immediately before analysis.

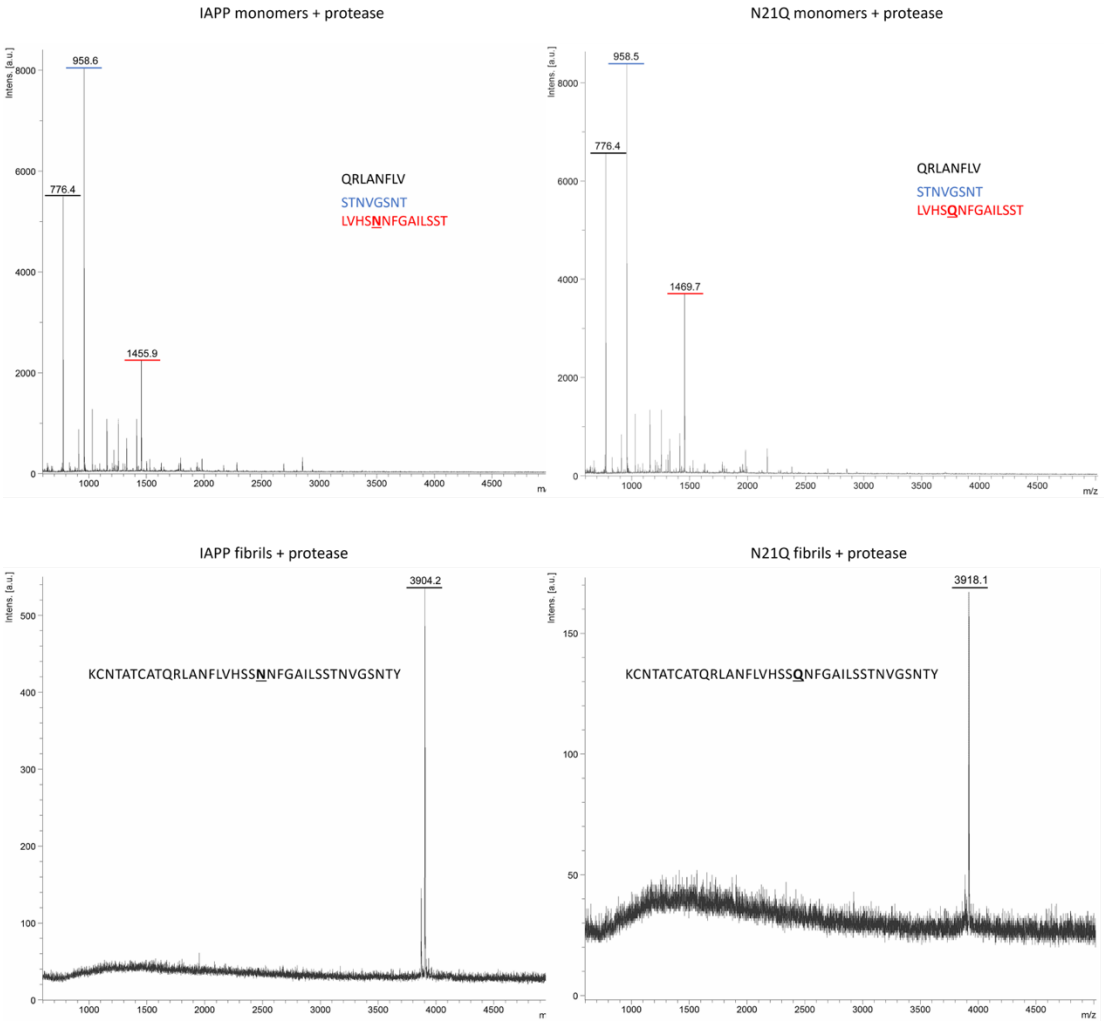


Fig. S3.5 Stability of IAPP and N21Q fibrils against proteinase K proteolysis.

MALDI-TOF mass spectrometry analysis of monomers and fibrils after treatment with proteinase K. Fibrils were assembled from freshly dissolved monomerized peptides incubated under quiescent conditions for 48 h at a concentration of 150 µM in 20 mM Tris-HCl buffer, pH 7.4. The assemblies were incubated with 120 U/ml of proteinase K for 1 h before MALDI-TOF analysis.

	Average		Median	
	IAPP	N21Q	IAPP	N21Q
Fibril length	1.42 ± 0.36 µm	1.08 ± 0.17 µm	2.55 µm	1.76 µm
Fibril height	5.98 ± 2.62 nm	3.12 ± 1.24 nm	6.11 nm	3.07 nm
Young's modulus	1.47 ± 0.78 GPa	1.21 ± 0.39 GPa	2.16 GPa	1.20 GPa

Fig. S3.6 Mean and median values of length, height and Young's modulus of IAPP and N21Q fibrils.

Peptide were assembled from freshly dissolved monomerized peptides and incubated for 48h at 150 µM in 20 mM Tris-HCl buffer, pH 7.4, under quiescent conditions before analysis of by AFM. At least 3000 fibrils per peptide were quantified.

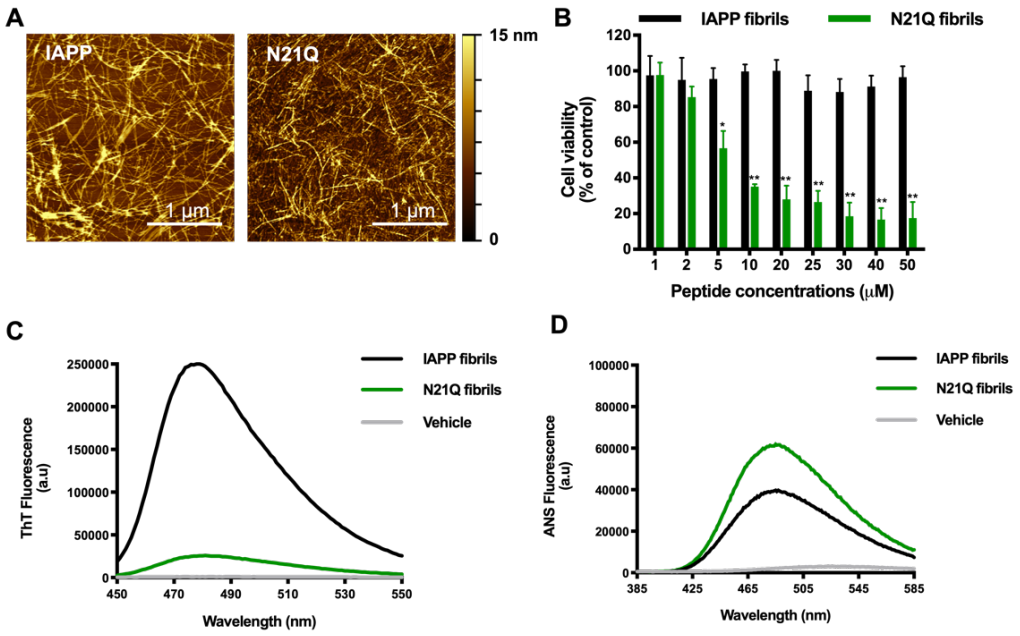


Fig. S3.7 Characterization of IAPP and N21Q fibrils after lyophilization.

(A) Representative AFM images of IAPP and N21Q fibrils resuspended in water after lyophilization. (B) INS-1E cells were incubated for 24 h with reconstituted fibrils, with concentrations ranging between 1 to 50 µM. Data represent mean ± S.E.M of at least four experiments performed in triplicate. (C) ThT fluorescence of reconstituted fibrils. The emission spectra of ThT (40 µM) was recorded from 450 nm to 550 nm with excitation at 440 nm. (D) Surface hydrophobicity of reconstituted fibrils measured by ANS fluorescence. The emission spectra of ANS (100 µM) was recorded from 385 nm to 585 nm with excitation at 355 nm. (A-D) Fibrils were assembled at 750 µM in 20 mM Tris-HCl, pH 7.4 for 48 h at room temperature under quiescent conditions. The resulting fibrils were recovered by ultracentrifugation at 100 000 g for 45 min at 4 °C. The pellet was re-suspended in nanopure water and lyophilized. Lyophilized aliquot were reconstituted in water to reach a concentration of 50 µM or 150 µM before analysis.

A

Residue	Carbon	δ IAPP (ppm)	δ N21Q (ppm)	δ RC (ppm)	Δδ IAPP (ppm)	Δδ N21Q (ppm)
Ala13	CO	171.8	173.0	175.1	-3.3	-2.1
	Cα	48.1	48.5	49.8	-1.7	-1.3
	Cβ	19.1	20.0	16.4	2.7	3.6
Phe23	CO	169.8	173.4	173.1	-3.3	0.3
	Cα	53.2	53.4	55.0	-1.8	-1.6
	Cβ	40.2	40.3	36.9	3.3	3.4
Val32	CO	170.9	173.0	173.6	-2.7	-0.6
	Cα	57.8	57.2	59.5	-1.7	-2.3
	Cβ	31.9	32.0	30.2	1.7	1.8
	Cγ	18.0	18.9	18.4	-	-

B

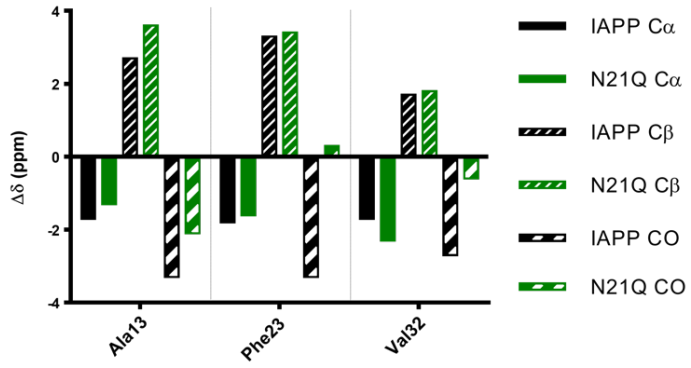
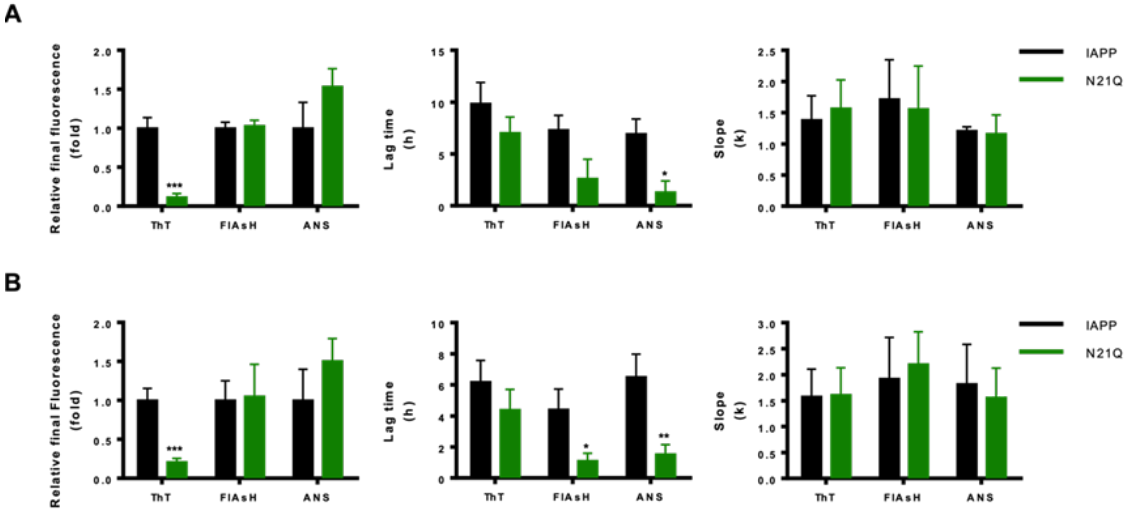


Fig. S3.8 Secondary ^{13}C chemical shifts of Ala13, Phe23 and Val32.

(A) Table of ^{13}C chemical shifts (Δδ) for Cα, Cβ, and CO of labelled residues calculated as $\Delta\delta = \delta_{obs} - \delta_{RC.}$ (B) Summarized of ^{13}C chemical shifts (Δδ) of Ala13, Phe23 and Val32 in IAPP and N21Q fibrils. (A,B) Fibrils were assembled at 750 μM in 20 mM Tris-HCl, pH 7.4 for 48 h at room temperature under quiescent conditions. The resulting fibrils were recovered by ultracentrifugation at 100 000 g for 45 min at 4 °C. Supernatant was removed and the fibril pellet was re-suspended in nanopure water and lyophilized.



C

		Relative fluorescence (x fold)		Lag time (h)		Slope (k)	
		IAPP	N21Q	IAPP	N21Q	IAPP	N21Q
12.5 µM	ThT	1.00 ± 0.14	0.12 ± 0.05	9.87 ± 2.02	7.05 ± 1.53	1.38 ± 0.39	1.57 ± 0.46
	FlAsH	1.00 ± 0.08	1.03 ± 0.07	7.33 ± 1.40	2.61 ± 1.89	1.72 ± 0.63	1.56 ± 1.41
	ANS	1.00 ± 0.33	1.54 ± 0.23	6.95 ± 1.43	1.32 ± 1.09	1.21 ± 0.06	1.16 ± 0.31
25 µM	ThT	1.00 ± 0.15	0.21 ± 0.05	6.19 ± 1.39	4.39 ± 1.32	1.58 ± 0.52	1.61 ± 0.52
	FlAsH	1.00 ± 0.25	1.05 ± 0.41	4.41 ± 1.32	1.11 ± 0.49	1.92 ± 0.79	2.20 ± 0.62
	ANS	1.00 ± 0.40	1.51 ± 0.29	6.51 ± 1.46	1.54 ± 0.62	1.82 ± 0.76	1.56 ± 0.57

Fig. S3.9 Kinetics of amyloid formation.

Relative final fluorescence, lag time and slope determined by fitted sigmoidal curve at (A) 12.5 µM and (B) 25 µM peptide using ThT, FlAsH and ANS fluorescence. (C) Kinetic parameters monitored by ThT, FlAsH and ANS. (A,B,C) Peptides were incubated at 12.5 µM or 25 µM under quiescent conditions in 20 mM Tris-HCl buffer, pH 7.4 in the presence of ThT (40 µM) or FlAsH (0.5 µM) or ANS (50 µM). Fluorescence of ThT (Ex 440 nm, Em 485 nm), FlAsH (Ex 508 nm, Em 533 nm) or ANS (Ex 355 nm, Em 480 nm) was measured every 10 min. Data represent mean ± S.D. of at least four experiments performed in triplicate.

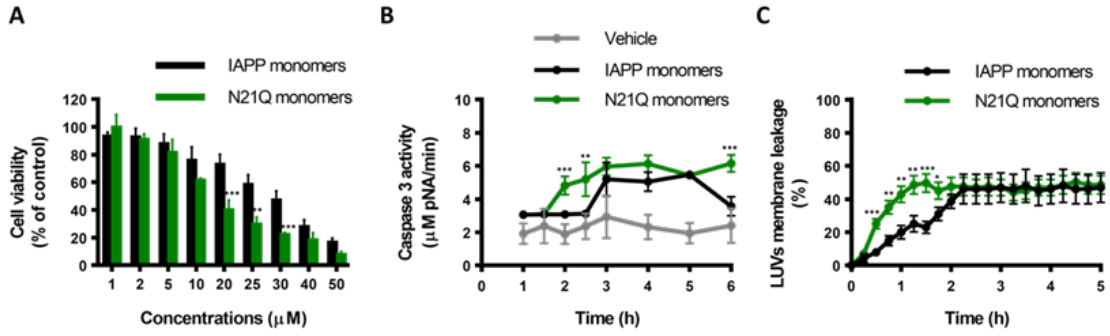


Fig. S3.10 Cytotoxicity and lipid membrane perturbation induced by monomers.

(A) Cytotoxicity of IAPP and N21Q monomers evaluated by measuring metabolic activity and compared to that of cells treated with the vehicle. INS-1E cells were treated for 24 h with different concentrations (0-50 µM) of IAPP and N21Q monomers. Data represent mean ± S.E.M of at least four experiments performed in triplicate. (B) Caspase-3 activation upon different incubation periods (1 to 6 h) with 50 µM IAPP and N21Q monomers. (C) Membrane leakage of 500 µM DOPC:DOPG LUVs (7:3) by 50 µM monomeric peptides.

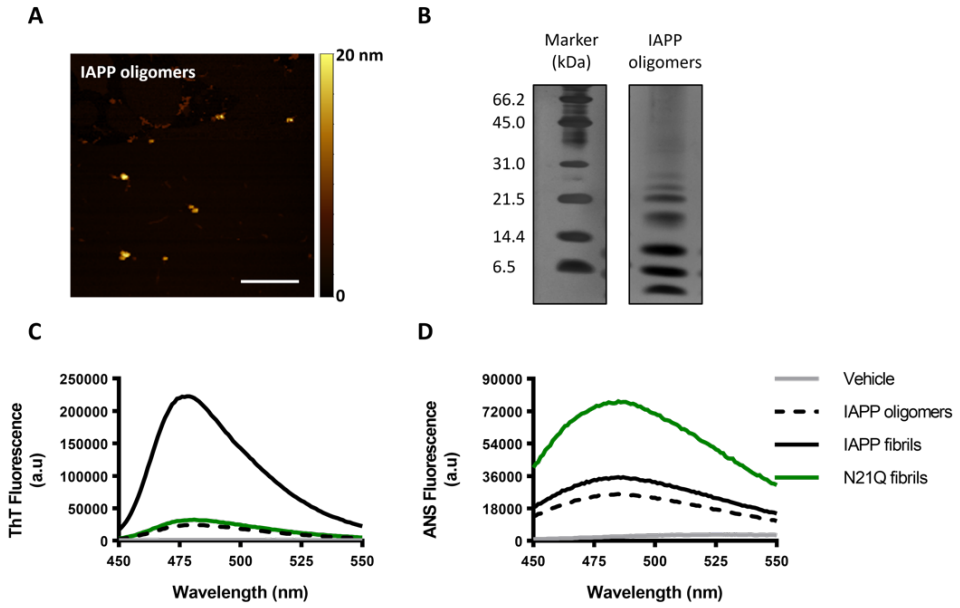


Fig. S3.11 Characterization of IAPP oligomers.

(A) AFM image of IAPP oligomers, scale bar: 500 nm. (B) Representative SDS-PAGE of photochemically cross-linked (PICUP) prefibrillar species. (C) ThT fluorescence of IAPP oligomers compared to IAPP and N21Q fibrils. The emission spectra of ThT (40 μM) was recorded from 450 nm to 550 nm with an excitation set at 440 nm. (D) Surface hydrophobicity of IAPP oligomers compared to IAPP and N21Q fibrils measured by ANS fluorescence. The emission spectra of ANS (100 μM) was recorded from 385 nm to 585 nm with an excitation set at 355 nm. (A-D) Oligomers and fibrils were prepared from freshly dissolved monomerized peptides and incubated for 15 min (oligomers) and 48h (fibrils) at 150 μM in 20 mM Tris-HCl buffer, pH 7.4, under quiescent conditions. Assemblies were diluted to 50 μM immediately before analysis.

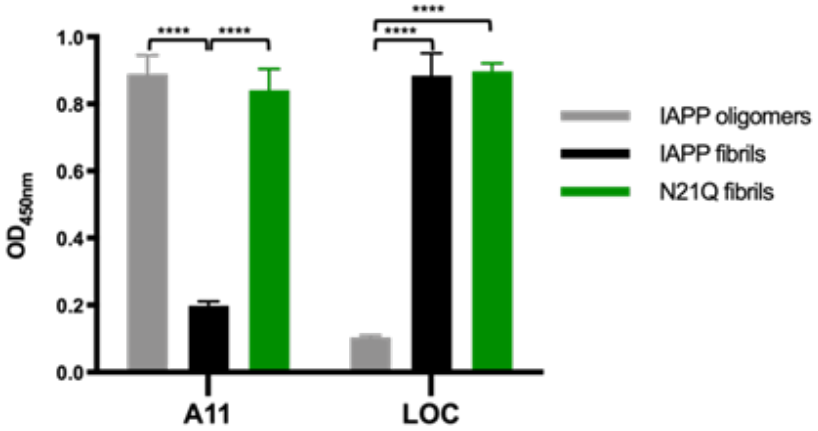


Fig. S3.12 ELISA analysis of IAPP and N21Q proteospecies.

Assemblies were obtained from freshly dissolved monomerized peptides incubated under quiescent conditions for 15 min (oligomers) and 48 h (fibrils) at a concentration of 150 μM in 20 mM Tris-HCl buffer, pH 7.4. High-binding ELISA plates were coated with 1.5 μM of peptide assemblies (oligomers or fibrils) overnight at 4°C. Wells were washed three times and blocked with PBS 0.05% tween-20. Coated plates were treated with conformational antibodies (1:1000; A11: anti-oligomers or LOC: anti-amyloid) for 3h at room temperature. Plates were washed and incubated with peroxidase-conjugated goat anti-rabbit IgG (1:10 000). Peroxidase signal was detected using 3,3'-5,5'-tetramethyl benzedine (TMB) and by measuring absorbance at 450 nm. Data represent mean ± S.E.M of at least four experiments performed in triplicate.

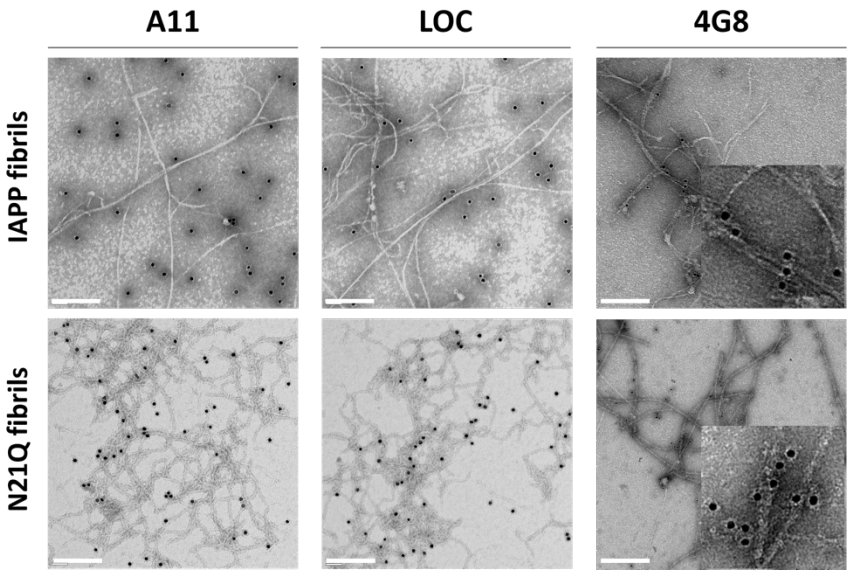


Fig. S3.13 TEM-immunogold labelling of IAPP and N21Q fibrils.

Immunogold electron microscopy images of IAPP and N21Q fibrils, scale bar: 500 nm. Assemblies were incubated with anti-amyloid 4G8, anti-amyloid LOC or the anti-oligomer A11. Fibrils were assembled from freshly dissolved monomerized peptides incubated under quiescent conditions for 48h at a concentration of 150 μM in 20 mM Tris-HCl buffer, pH 7.4.

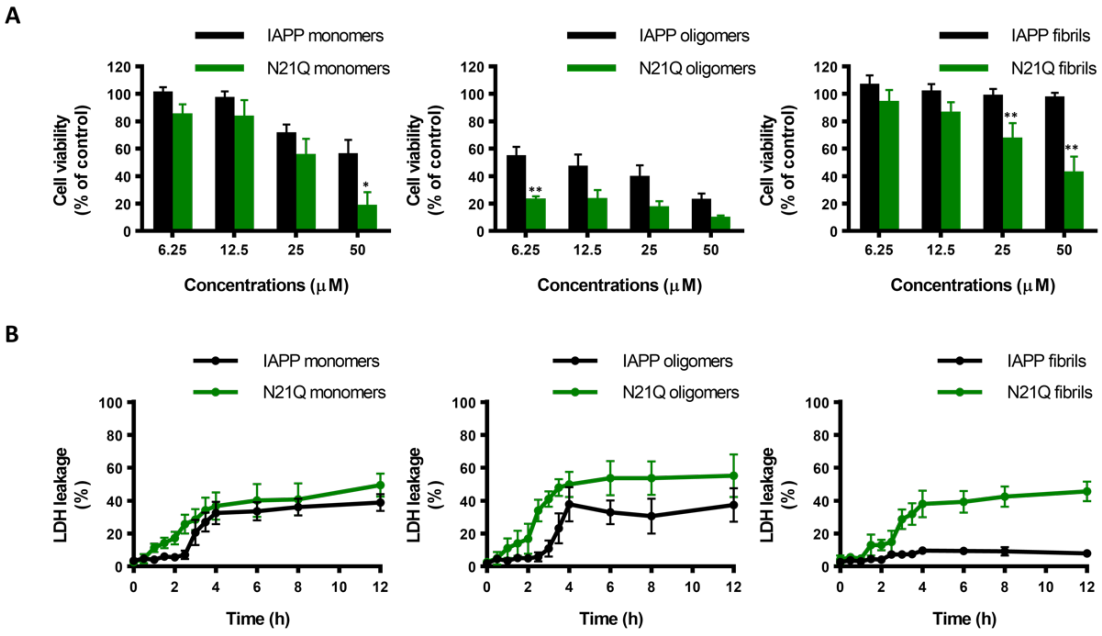


Fig. S3.14 Toxicity of IAPP and N21Q assemblies on CHO K1 cells.

(A) Cell viability of CHO K1 cells upon treatment with increasing peptide concentrations (6.25 to 50 μM) of WT and N21Q monomers, oligomers and fibrils. Data represent mean ± S.D. of at least four individual experiments performed in triplicate. (B) LDH release from CHO K1 cells treated with 50 μM IAPP and N21Q monomers, oligomers or fibrils for different times (0 h -12 h). (A, B) Peptide monomers, oligomers and fibrils were prepared from freshly dissolved monomerized peptides and incubated for 0 h (monomers), 15 min (oligomers) and 48 h (fibrils) at 150 μM in 20 mM Tris-HCl buffer, pH 7.4, under quiescent conditions.

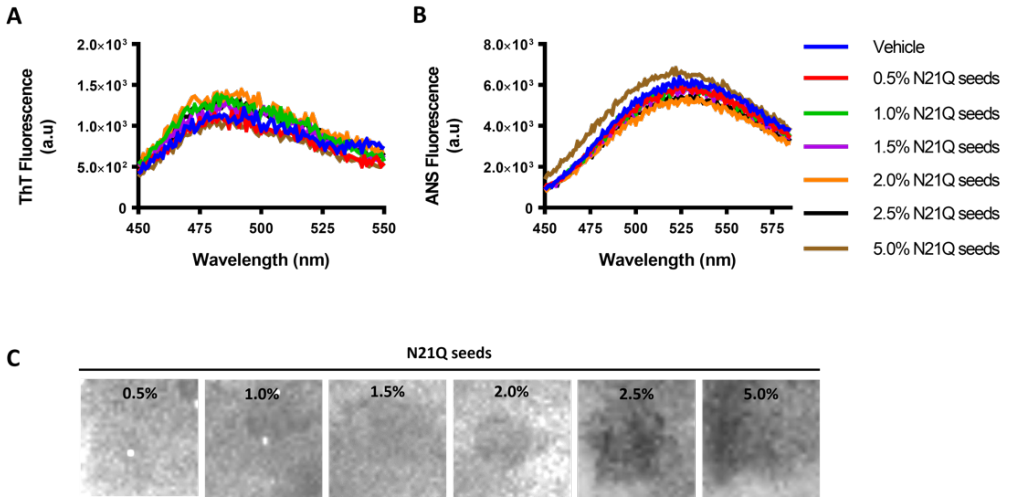


Fig. S3.15 Characterization of N21Q seeds.

N21Q seeds (0.25 - 2.5 µM; *i.e.* equivalent to 0.5 - 5.0 %) were characterized by (A) ThT fluorescence (Ex: 440 nm, Em: 450-550 nm), (B) ANS fluorescence (Ex: 355 nm, Em: 385-585 nm), (C) dot-blot with the anti-oligomer A11 antibody. (A-C) N21Q seeds were assembled from freshly dissolved monomerized peptide incubated under quiescent conditions for 48 h at 150 µM in 20 mM Tris-HCl buffer, pH 7.4. Seeds were diluted to reach concentrations ranging between 0.25 to 2.5 µM (0.5% to 5.0% in the seeding experiment) before analysis.

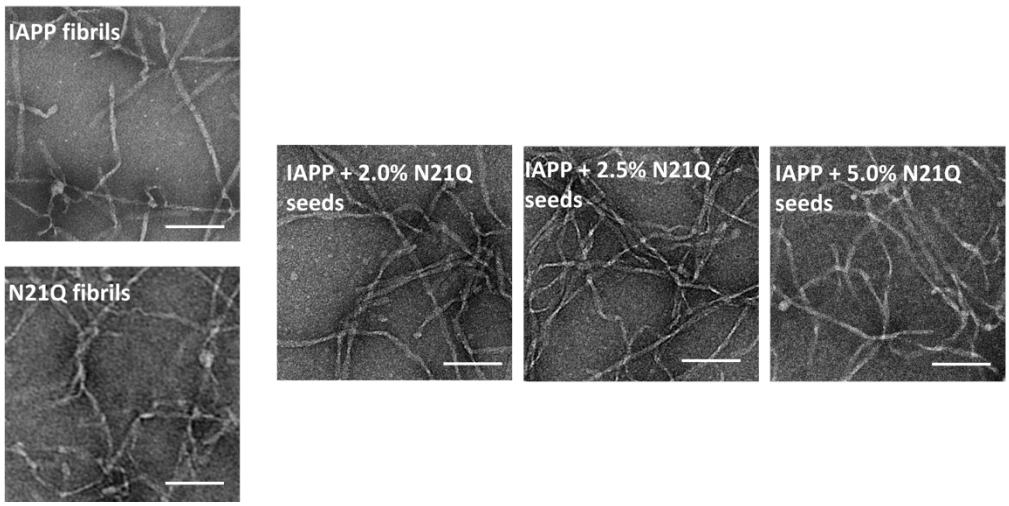


Fig. S3.16 Electron microscopy images of IAPP assemblies seeded with N21Q fibrils.

TEM images of WT IAPP seeded with N21Q seeds (2% - 5 mol%), scale bar: 100 nm. N21Q seeds were grown for 48 h (quiescent conditions, 150 μM in 20 mM Tris-HCl buffer, pH 7.4) before being isolated and used to seed amyloid formation of IAPP under quiescent conditions for 48 h at 150 μM in 20 mM Tris-HCl buffer, pH 7.4. Assemblies were diluted to 50 μM immediately before TEM analysis.

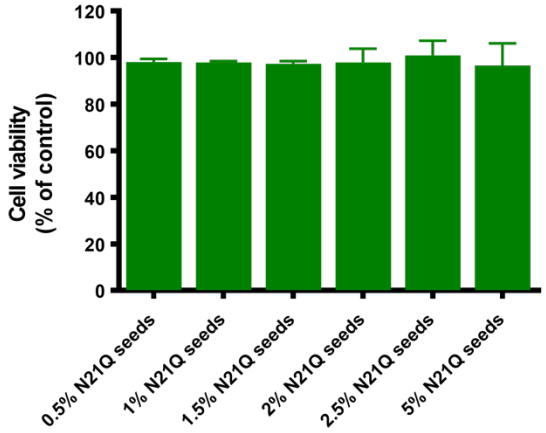


Fig. S3.17 Cytotoxicity of N21Q fibrillar seeds at low concentrations.

Toxicity of N21Q seeds alone (0.5% - 5.0%; 0.25 to 2.5 μM) was evaluated by measuring the metabolic activity of INS-1E cells. Data represent mean ± S.E.M of at least four experiments performed in triplicate. Fibrils were assembled from freshly dissolved monomerized N21Q peptide incubated under quiescent conditions for 48 h at a concentration of 150 μM in 20 mM Tris-HCl buffer, pH 7.4. Seeds were diluted to 0.25 to 2.5 μM (0.5% to 5.0 mol%) before evaluating cell viability.

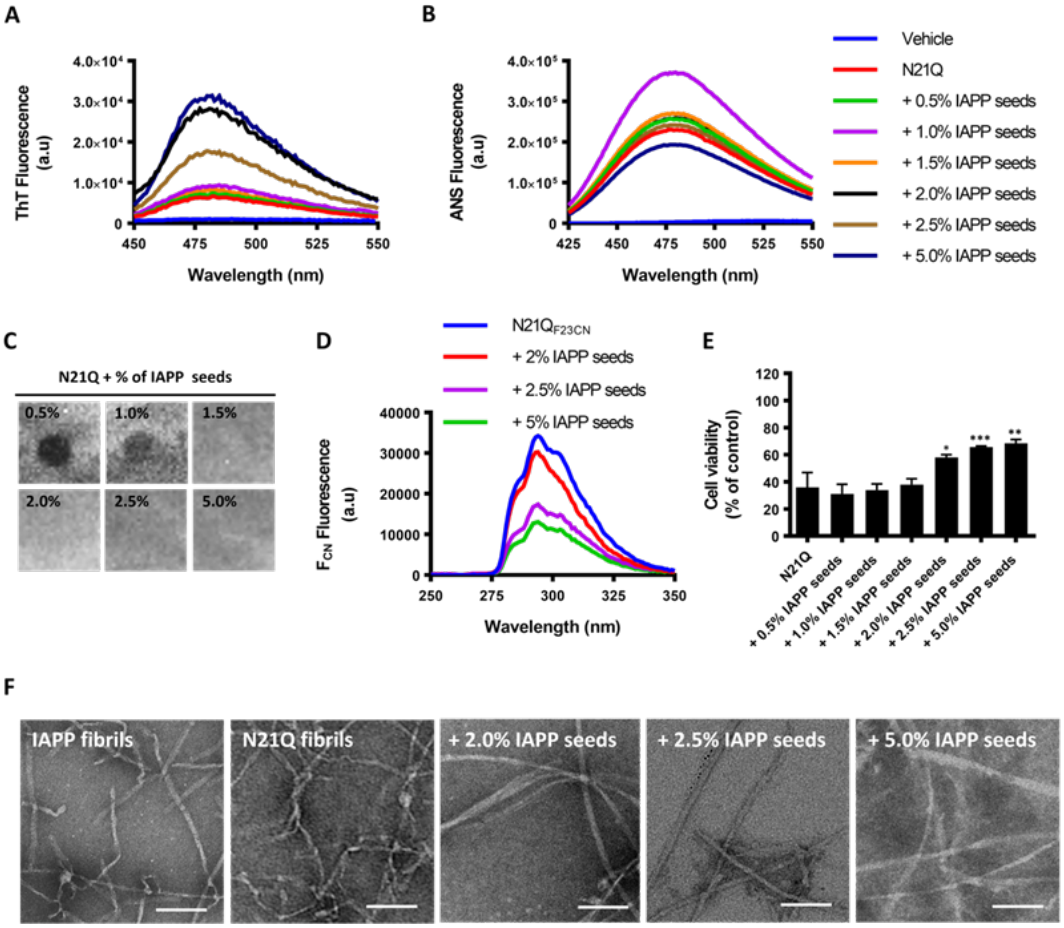


Fig. S3.18 Seeding of N21Q self-assembly with IAPP amyloid fibrils.

Self-assembly of N21Q seeded with WT IAPP fibrils (0.5-5.0 mol%) was characterized by (A) ThT fluorescence, (B) ANS fluorescence, (C) dot-blot analysis with the conformational anti-oligomer A11 antibody and (D) F_{CN} fluorescence of the N21Q F23F_{CN} derivative. (E) Cell viability of INS-1E treated with N21Q fibrils seeded with WT IAPP pre-assembled fibrils. (F) TEM images of N21Q fibrils seeded with IAPP seeds (2 – 5 mol%), scale bar: 100 nm. (A-F) IAPP seeds were grown for 48 h (quiescent conditions, 150 µM in 20 mM Tris-HCl buffer, pH 7.4) before being isolated and used to seed the self-assembly of N21Q under quiescent conditions for 48 h at 150 µM in 20 mM Tris-HCl buffer, pH 7.4.

CHAPITRE IV

ARTICLE III

LOW GENERATION ANIONIC DENDRIMERS MODULATE ISLET AMYLOID POLYPEPTIDE SELF-ASSEMBLY AND INHIBIT PANCREATIC β-CELL TOXICITY

Phuong Trang Nguyen, Rishi Sharma, Rabindra Reja, Carol Anne De Carufel, René Roy and Steve Bourgault

Manuscrit publié dans *RSC advances*, 80(6):76360-76369.

doi: 10.1039/C6RA15373A

Contribution des auteurs :

Phuong Trang Nguyen : Conception du projet de recherche, réalisation des expériences (Synthèse et purification des peptides, assemblage des peptides in vitro, essais cinétiques par fluorescence de ThT, analyses des conformations secondaire par CD, analyses par AFM, essais cellulaires), traitements des résultats, analyses statistiques des résultats, rédaction de l'article.

Rishi Sharma : Synthèse et purification des dendrimères.

Rabindra Reja : Synthèse et purification des dendrimères.

Carol Anne De Carufel : Début des essais cinétiques par fluorescence de ThT, analyses des conformations secondaire par CD..

René Roy : Supervision du projet en lien avec la synthèse des dendrimères.

Steve Bourgault : Supervision du projet, préparation des figures, correction de l'article.

NOTE : Les références de l'article sont incluses dans la bibliographie générale de la thèse

Low generation anionic dendrimers modulate islet amyloid polypeptide self-assembly and inhibit pancreatic β-cell toxicity†

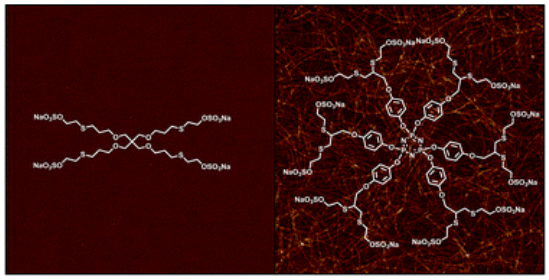
Phuong T. Nguyen[a,b,c], Rishi Sharma[a], Rabindra Reja[a], Carole Anne De Carufel[a,b,c], René Roy*[a] and Steve Bourgault*[a,b,c]

* Corresponding authors

[a]Department of Chemistry, Pharmaqam, University of Québec in Montreal, C.P. 8888, Succursale Centre-Ville, Montreal, Quebec, Canada
E-mail: roy.rene@uqam.ca
Tel: +1-514-987-3000 ext. 2546

[b]Department of Chemistry, Pharmaqam, University of Québec in Montreal, C.P. 8888, Succursale Centre-Ville, Montreal, Quebec, Canada
E-mail: bourgault.steve@uqam.ca
Tel: +1-514-987-3000 ext. 5161

[c]Quebec Network for Research on Protein Function, Engineering and Applications, PROTEO, Canada



4.1 Résumé

Le dépôt de l'islet amyloid polypeptide (IAPP) sous forme de fibres amyloïdes insolubles dans les îlots pancréatiques est associé au diabète de type II. Des études récentes ont révélé que les fibres amyloïdes n'interviennent pas dans la dégénérescence des cellules-β, mais que les espèces pré-fibrillaires et/ou le processus de formation de fibres eux-mêmes sont cytotoxiques. Ainsi, les stratégies thérapeutiques visant à prévenir la mort des cellules-β associées aux dépôts amyloïdes devraient séquestrer les espèces pré-fibrillaires et/ou moduler les étapes initiales de la fibrillation. Dans cette vue, des structures dendritiques flexibles contenant 4 à 16 groupes fonctionnels (hydroxyle, amine, carboxylate ou sulfate) ont été conçus et évalués pour leurs effets sur l'auto-assemblage et la cytotoxicité de l'IAPP. Les dendrimères carboxylés ont accéléré la fibrillation de l'IAPP proportionnellement à la densité du groupe de surface, alors que les dendrimères polyhydroxylés neutres et polycationiques n'ont pas affecté la cinétique de l'auto-assemblage amyloïde. De plus, comme l'ont révélé la fluorescence de la thioflavine T, la spectroscopie circulaire par dichroïsme et la microscopie à force atomique, le dendrimère sulfaté G_0 a inhibé la formation d'amyloïde en conservant le peptide dans sa conformation aléatoire. En revanche, les dendrimères sulfatés G_1 ont accéléré l'auto-assemblage de l'IAPP en longues fibres amyloïdes par un mécanisme d'échafaudage. Quant aux dendrimères anioniques, la toxicité induite par l'IAPP sur les cellules-β pancréatiques a été atténuée. Nos résultats indiquent que les dendrimères sulfatés peuvent modifier la voie de fibrillisation de l'IAPP et inhiber sa protéotoxicité, soit en accélérant la formation d'amyloïde, soit en séquestrant le peptide dans un état non-agrégé et non-toxique. Cette étude offre de nouvelles perspectives mécanistiques pour la conception d'échafaudages nanomoléculaires afin de manipuler l'auto-assemblage de peptides amyloïdogéniques nativement désordonnés.

4.2 Abstract

The deposition of the islet amyloid polypeptide (IAPP) as insoluble amyloid fibrils in the pancreatic islets is associated with type II diabetes. Recent studies have revealed that pre-fibrillar proteospecies and/or the amyloidogenic process mediate β-cell degeneration whereas amyloid fibrils are poorly cytotoxic. Thus, therapeutic strategies that aim at preventing β-cell death associated with amyloid deposition should either sequester prefibrillar species and/or modulate the initial steps of fibrillization. In this view, low generation flexible dendritic scaffolds harboring 4 to 16 hydroxyl, amine, carboxylate or sulfate functional groups were designed and evaluated for their effects on IAPP self-assembly and cytotoxicity. Whereas neutral polyhydroxylated and polycationic dendrimers did not affect the kinetics of amyloid assembly, carboxylated dendrimers accelerated IAPP fibrillization proportionally to surface group density. Interestingly, as revealed by thioflavin T fluorescence, circular dichroism spectroscopy and atomic force microscopy, the G_0 sulfated dendrimer inhibited amyloid formation by maintaining the peptide in a random coil conformation. In contrast, G_1 sulfated dendrimers potentiated IAPP self-assembly into long amyloid fibrils by a scaffold-based mechanism. Anionic dendrimers attenuated IAPP-induced toxicity on pancreatic β-cells. Our results indicate that sulfated dendrimers can alter the fibrillization pathway of IAPP and inhibit its proteotoxicity, either by accelerating amyloid formation or by trapping the peptide in a non-aggregating and non-toxic state. This study offers novel mechanistic insights for the design of a nanomolecular scaffold to manipulate the self-assembly of natively disordered amyloidogenic peptides.

4.3 Introduction

Numerous human diseases are associated with the deposition and accumulation of insoluble protein aggregates within the extracellular space, including the Alzheimer's diseases and several amyloidoses(Cohen et Kelly, 2003). Protein aggregation is a consequence of the self-assembly of a polypeptide, often into a quaternary structure rich in cross-β-sheets, known as amyloids fibrils. Over 30 endogenous proteins have been identified as precursors of amyloids whose depositions are linked to cellular degeneration (Chiti et Dobson, 2006). Owing to the causative link between amyloid deposition and the pathological states, the identification of molecules that can interfere with the amyloidogenic process is an area of extensive research (Cohen et Kelly, 2003). Therapeutic strategies to arrest protein aggregation include; (*i*) stabilization of the protein in its native state, (*ii*) destabilization of amyloid cross-β-sheets quaternary structure and (*iii*) inhibition of oligomerization (Soto, 2003). For instance, stabilization of transthyretin (TTR) quaternary native state led to the discovery of the first molecule used in the clinics to treat an amyloid disease (Bulawa *et al.*, 2012). However, this rational approach is challenging to apply to intrinsically disordered polypeptides (IDPs), such as the β-amyloid peptide (Aβ), the islet amyloid poplypeptide (IAPP) and α-synuclein, as the amyloidogenic precursors exhibit a wide conformational ensemble (Abedini et Raleigh, 2009). Nonetheless, molecules harboring several hydrophilic and/or charged chemical groups at their surface have been reported to modulate IDP self-assembly. For example, the green tea polyphenol (-)-epigallocatechin gallate (EGCG), which is known to inhibit the aggregation of Aβ (Ehrnhoefer *et al.*, 2008), α-synuclein (Bieschke *et al.*, 2010), IAPP (Meng *et al.*, 2010b) and the tau protein (Wobst *et al.*, 2014), exhibits a high density of hydroxyl groups. Besides, sulfated glycosaminoglycans (GAGs) are known to accelerate fibril formation and to inhibit the toxicity of several amyloidogenic IDPs, including Aβ (McLaurin *et al.*, 1999) and

IAPP (De Carufel *et al.*, 2013; Jha *et al.*, 2011). Nonetheless, the relationships between the nature and density of hydrophilic functional groups with the effects on IDPs self-assembly have been poorly addressed so far.

Over the last decade, a few studies have reported that dendrimers can modulate amyloid formation from amyloidogenic IDPs, such as Aβ-peptide derivatives, prion protein fragments and IAPP, by either accelerating or preventing self-assembly (Benseny-Cases *et al.*, 2012; Gurzov *et al.*, 2016). Dendrimers consist of globular polymers built on a central core scaffold surrounded by layers of branched monomers (Roy et Shiao, 2015). These scaffolds, which represent a unique class of nanostructures that can be designed with various sizes, shapes and surface chemistries, have recently received attention as potential anti-amyloidogenic agents (Benseny-Cases *et al.*, 2012; Heegaard *et al.*, 2007). For instance, cationic poly(propyleneimine) dendrimers decorated with maltose were shown to convert toxic Aβ species into nonfibrillar aggregates and to reduce amyloid cytotoxicity on PC12 and SH-SY5Y cells (Klementieva *et al.*, 2011). Similarly, gallic acid-triethylene glycol dendrimers decorated with morpholine groups have been shown to reduce the toxicity of Aβ peptide fragment by accelerating the conversion of cytotoxic oligomeric species into fibrils (Klajnert *et al.*, 2012). Particularly, owing to their flexible nature and to the high density of chemical functionalities that can be attached to the dendritic core, these nanostructures are perfectly suited to target natively unfolded polypeptides.

IAPP is a 37-residue glucomodulatory hormone (Figure 4.1A) that is co-expressed and co-secreted with insulin by the pancreatic β-cells (Westermark *et al.*, 2011). In patients afflicted with type-2 diabetes (DM-2), this unusual aggregation-prone peptide forms amyloids that deposit in the pancreas, leading to the degeneration of the islets of Langerhans (Westermark *et al.*, 2011). IAPP amyloidogenesis observed in the pancreas is known to exacerbate pancreatic β-cells death; accelerating the progression

of the physiopathology. When applied to isolated pancreatic cells in culture, non-fibrillar IAPP induces cell death (Abedini et Schmidt, 2013; Kapurniotu *et al.*, 2002; Nguyen *et al.*, 2015), although clear mechanistic details remain elusive. Interestingly, amyloid fibrils show low toxicity and as for other amyloidogenic polypeptides, oligomeric species are considered as the most proteotoxic species of the self-assembly cascade (Cao *et al.*, 2013; De Carufel *et al.*, 2013). There is currently no therapeutic strategy to prevent amyloid deposition observed in pancreatic islets of diabetic patients. Thus, the discovery of compounds that modulate IAPP amyloidogenesis and prevent β-pancreatic cells death represents an important research goal. However, targeting an IDP amyloidogenic peptide that exhibits a wide conformational ensemble, such as IAPP, is challenging and requires the design of novel and flexible molecular scaffolds.

Whereas the effects of large neutral or cationic dendrimers on IDPs self-assembly have been recently reported, nothing is known about how low generation anionic dendrimers can modulate fibrillization of amyloidogenic IDPs. Moreover, although derivatives densely functionalized with hydrophilic and/or charged groups are known to modulate the amyloidogenic process, mechanistic insights about the relationship between the chemical nature, orientation and density of functional units are still scarce. In this context, we investigated the structure-activity relationships (SAR) of low generation polyhydroxylated, polyaminated, polycarboxylated and polysulfated dendrimers harboring 4 to 16 peripheral groups. The present study shows a unique effect of sulfated dendrimers on amyloidogenesis that reside in the charge density and indicates that IAPP-induced cytotoxicity can be efficiently inhibited with anionic dendrimers. Our results offer key indications regarding the nature of the proteotoxic species and expose novel mechanistic insights for the design of molecular identities to manipulate the self-assembly of amyloidogenic IDPs.

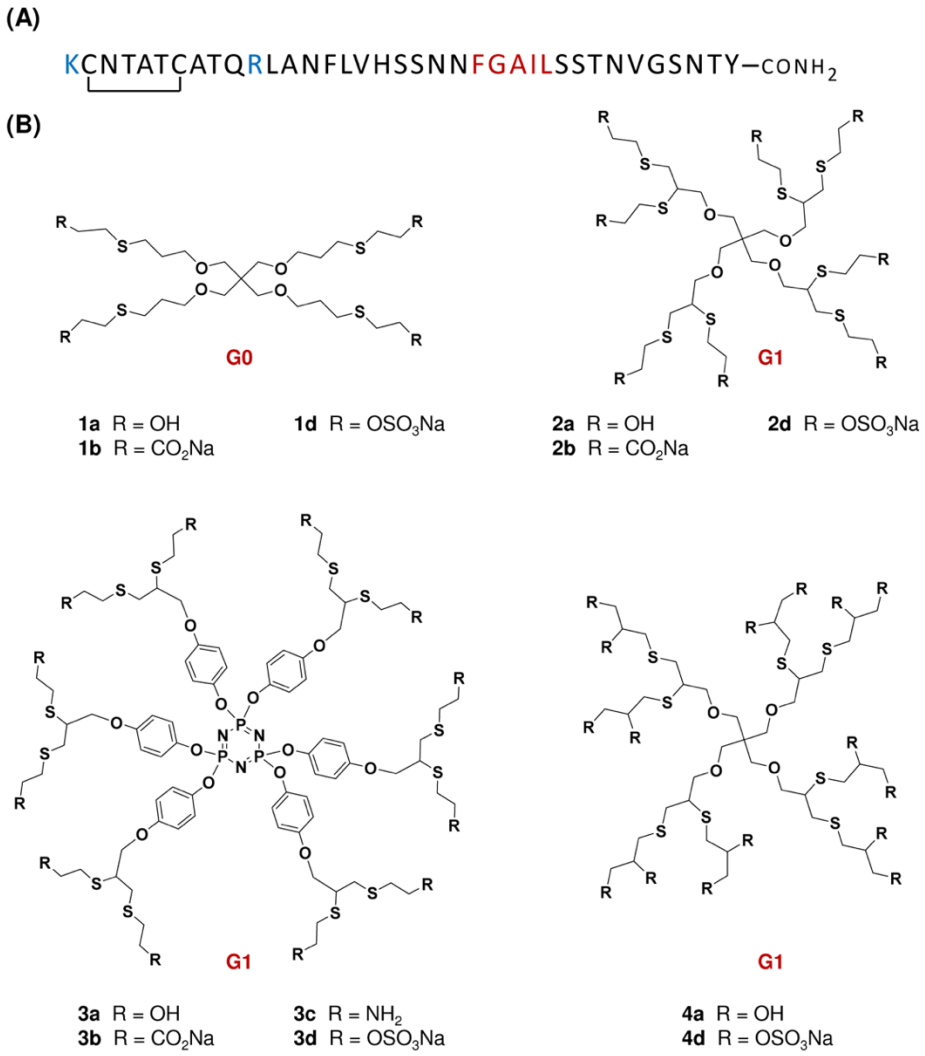


Figure 4.1 Primary structure of human IAPP and chemical structures of surface low generation dendrimers used in the present study.

(A) Primary structure of human IAPP. Positively charged residues are indicated in blue whereas the amyloidogenic domain is represented in red. IAPP contains a disulfide bond between Cys-2 and Cys-7 and a C-α-amidated C-terminus. (B) Chemical structures of surface low generation dendrimers used in the present study. The generation level (G) is indicated in red.

4.4 Materials and Methods

4.4.1 Dendrimers synthesis, purification and characterization

Synthetic routes towards low generation flexible dendrimer scaffolds and approaches for their purification and characterization are described in detail in Annexe I.

4.4.2 Peptide synthesis and IAPP sample preparation

IAPP was synthesised by solid phase peptide synthesis based on Fmoc chemistry and 2-(6-Chloro-1-H-benzotriazole-1-yl)-1,1,3,3-tetramethylaminium hexafluorophosphate (HCTU) coupling strategy using a tribute infrared (IR) synthesizer. Two oxazolidine pseudoproline dipeptide derivatives were incorporated: Fmoc-Ser-Ser($\psi^{Me,Me}$pro)-OH was incorporated at positions Ser-19 and Ser-20 whereas Fmoc-Leu-Ser($\psi^{Me,Me}$pro)-)-OH was inserted at positions Leu-27 and Ser-28(Abedini et Raleigh, 2005). Cleavage from the resin was achieved with a mixture of TFA/ethanedithiol/phenol/water (92/2.5/3/2.5) and after TFA evaporation, the peptide was precipitated with diethylether, washed several times with diethylether, solubilized in 20% acetic acid (v/v) before being lyophilized. Crude IAPP was purified by preparative reversed-phase high performance liquid chromatography (RP-HPLC) using a linear gradient of ACN in H_2O/TFA (0.06% v/v) To increase the solubility, crude IAPP was dissolved in 35% acetic acid (v/v) before being injected on a C18 (5 μm, 100 Å) column (250 x 21.2 mm). Collected fractions were analyzed by analytical RP-HPLC using a C18 (3.6 μm) column (250 mm x 4.6 mm) and a linear gradient of

ACN in H_2O/TFA (0.06% v/v). Fractions were also analysed by 'time of flight' mass spectrometry using a LC/MS-TOF (Agilent) to confirm the identity of the peptide. Fractions corresponding to the desired peptide were pooled and lyophilized before cyclisation was performed. Disulfide bond formation between Cys-2 and Cys-7 was achieved by dimethyl sulfoxide (DMSO) oxidation (Abedini *et al.*, 2006). Purified IAPP was dissolved in 100% DMSO at a final concentration of 2 mg/mL and the sample was gently stirred for 20 hours at room temperature. After incubation, 50% acetic acid (v/v) was added to the peptide mixture to a final ratio of 9:1 (50% acetic acid:DMSO) and IAPP was re-purified by RP-HPLC as above-described. Fractions corresponding to the desired product and with purity higher than 95%, confirmed by analytical RP-HPLC, were finally pooled and lyophilized.

4.4.3 Amyloid formation monitored by thioflavin T fluorescence

IAPP solutions were prepared by dissolving monomerized IAPP at a concentration of 25 μM (2× of final concentration) in 20 mM Tris, pH 7.4, containing 40 μM ThT immediately before final dilution and measurement. Dendrimers were solubilized in either 20 mM Tris buffer (polycarboxylate, polysulfate and polyamine) or in MeOH (polyhydroxyl) at 10× and 100×, respectively. For studies with OH-substituted dendrimers, MeOH concentration was kept below 1% (v/v) and control reaction contained the same percentage of MeOH. Assays were performed at 37°C without stirring in sealed black-wall, clear-bottom 96-well non-binding surface plates (Corning) with a total volume of 100 μL per well. ThT fluorescence was measured every 10 min over the course of 20 h, using an Infinite M1000 fluorescence plate reader (TECAN). The fluorescence, with excitation at 440 nm and emission at 485 nm, was measured from the bottom of the well. For each experiment, control reactions (without

IAPP) were carried. Data obtained from triplicate wells were averaged, corrected by subtracting the corresponding control reaction and plotted as fluorescence vs time. Data of time-dependence of ThT fluorescence were fitted to a sigmoidal growth model where T_{50} is the time required to reach half of the fluorescence intensity, k is the apparent first-order constant and Y_{max} and Y_0 are, respectively, the maximum and initial fluorescence values:

$$Y = \frac{Y_0 + (Y_{max} - Y_0)}{1 + e^{-(T - T_{50})/k}}$$

The lag time, the time before detectable amyloid formation occurs, as predicted by means of the nucleation dependent polymerization model, is described as $T_{50} - 2/k$. Data represents the average of at least two independent experiments performed in triplicate.

4.4.4 Circular dichroism spectroscopy

IAPP was dissolved in 20 mM Tris, pH 7.4 and mixed with an equivalent volume of 2× of dendrimers prepared in the corresponding buffer, and the samples were incorporated into a 2 mm path length quartz cell. Far-UV CD spectra were recorded from 189 to 260 nm using a J-815 CD spectropolarimeter (Jasco) at 25°C. The wavelength step was set at 0.5 nm with an average time of 10 s per scan at each wavelength step. Each collected spectrum was background subtracted with the corresponding IAPP-free sample. Each spectrum represents the average of at least two independent experiments.

4.4.5 Atomic force microscopy

AFM was performed with a MultiMode 8 atomic force microscope controlled by Nanoscope V electronics (Bruker, Billerica, MA) equipped with a 100-µm scanner (J-scanner). IAPP (50 µM) was solubilized in absence or in presence of functionalized dendrimers in 20 mM Tris-HCl pH 7.4. The solution was incubated for 20 h at 25°C before being diluted by a factor of 10 in acetic acid 1%. 20 µl of IAPP sample were deposited onto a freshly cleaved mica and incubated for 2 min at room temperature. The mica was washed twice with deionized water and air-dried for 24 h. AFM images were recorded in tapping mode using silicon probes (Bruker). Line scan frequency was set at 0.2 Hz. For quantification analysis, the width and length of at least 50 individual fibrils per experiment were determined and plotted as a frequency distribution using the Prism 6.0 software. Data (height and length) of at least three individual experiments were averaged and were expressed as the mean ± standard deviation.

4.4.6 Cell toxicity assay

Rat INS-1 β-pancreatic cells were seeded in black wall clear bottom 96-well plates (TC treated) at a density of 30 000 cells/well (100 µl/well) in RPMI-1640 medium supplemented with 10% FBS, 2mM L-glutamine, 100 U/mL penicillin, 100 µg/mL streptomycin, 10 mM HEPES, 1 mM sodium pyruvate, 50 µM β-mercaptoethanol. INS-1 cells were provided by Pr Alain Fournier, INRS-Institut-Armand, Canada. After 48 h incubation at 37°C in a 5% CO_2 incubator, cells were treated by directly adding 50 µl of IAPP solutions at 3× of final concentration in 20 mM Tris, pH 7,4, (with or without dendrimers) that have been pre-incubated, or not, for 16 h at room temperature. The cells were incubated for 24 h and cell viability was measured by the resazurin reduction assay. Cell viability (in % of control) was calculated from the ratio of the

fluorescence of the treated sample to the control cells (non-treated). All compounds were individually tested using the above protocol for their cytotoxicity at concentrations of 5 and 50 μM. Data (in %) of at least three individual experiments performed in triplicate were averaged and were expressed as the mean ± S.E.M. Evaluation of the results was made using the Student's t-test and statistical difference (between control and dendrimers-treated or between IAPP-treated and IAPP-treated + dendrimers) was established at $P < 0.05$. Statistical analysis was performed using Prism 6.0 software.

4.5 Results and discussion

4.5.1 Synthesis of low generation dendrimers

To address the effect of dendrimers on IAPP amyloidogenesis and to obtain key SAR information regarding the nature and density of surface groups and the molecular scaffold, a small library of flexible low generation (G0, G1) neutral, cationic and anionic dendrimers were prepared (Figure 4.1B). A divergent synthesis was designed for the construction of polyhydroxylated, polyaminated, polycarboxylated and polysulfated dendrimers harboring 4 to 16 peripheral groups. These molecules were readily synthesized using either thiol-ene or thiol-yne reactions around tetravalent and hexavalent core molecules (Sharma *et al.*, 2014; Sharma *et al.*, 2015; Sharma *et al.*, 2016). Experimental details regarding the synthesis of these compounds are included in Annexe I.

4.5.2 Effect of low generation dendrimers on IAPP amyloid formation

We initially evaluated the effect of low generation functionalized dendrimers on the kinetics of fibril formation by measuring the fluorescence of the amyloid-specific dye thioflavin T (ThT). ThT is a small compound that exhibits a strong increase of its fluorescence quantum yield upon its specific binding to the cross-β-sheet quaternary structure of amyloid fibrils (Naiki *et al.*, 1989). IAPP amyloidogenesis is often described as a nucleation-dependent polymerization process that is characterized by a ThT-negative phase (lag-phase), in which the high-energy nucleus is formed, followed by a thermodynamically favorable elongation phase that is characterized by the rapid growth of the fibrils(Hebda et Miranker, 2009) (Figure 4.2A). In absence of dendrimers, the sigmoidal time course of IAPP fibrillization (12.5 μM; pH 7.4; quiescent condition; non-binding surface) displayed a lag time of 7.72 h and a T_{50} of 9.36 h (Table 4.1). The T_{50} corresponds to the time required to reach half of the maximum ThT fluorescence whereas the lag time is ascribed to the time before detectable amyloid formation occurs. In presence of 1 eq. of neutral polyhydroxylated dendrimers (compounds 1a to 4a) no significant changes in the rate of amyloid formation and final ThT fluorescence were detected (Table 4.1; Figure S4.1). This result suggests that the inhibitor effect of polyhydroxylated compounds on IAPP aggregation, such as EGCG (Meng *et al.*, 2010b) and glucopyranosylgenistein(Jesus *et al.*, 2014), reside in their polyphenolic nature and/or in the spatial distribution of their hydroxyl groups rather than simply in their high density of hydroxyl groups. Similar results were observed for the cationic dendrimer decorated with 12 amine functions (compound 3c; Table 4.1; Figure S4.2). As cationic dendrimers are known for their inherent cell toxicity (Benseny-Cases *et al.*, 2012), we evaluated only one amine-functionalized dendrimer in this study.

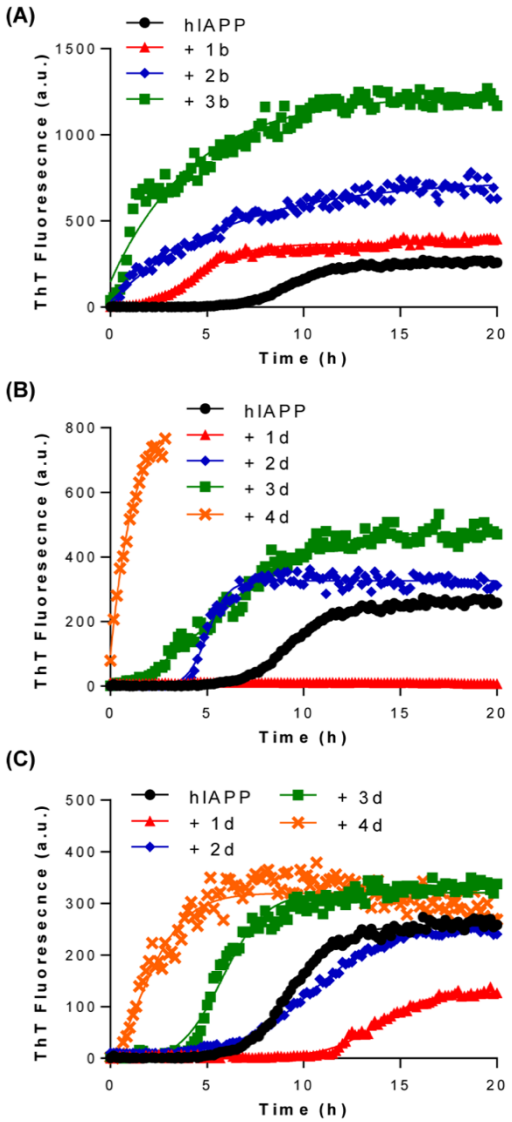


Figure 4.2 Effects of low generation dendrimers on IAPP amyloid fibril formation monitored by ThT fluorescence.

IAPP (12.5 μM) was incubated in 20 mM Tris, pH 7.4, at 25°C without agitation in the absence or in the presence of (A) 1 eq. of compounds 1b to 3b, (B) 1 eq. of compounds 1d to 4d or (C) 0.1 eq. of compounds 1d to 4d. (A, B, C) ThT fluorescence was measured every 10 min over the course of 20 h, with excitation at 440 nm and emission at 485 nm.

Table 4.1 Effects of low generation G0 and G1 dendrimers on IAPP amyloid formation.

Compound[a]	R[b]	Lag time[c] (h)	T_{50}[d] (h)	Maximum intensity[e] (% of IAPP control)
hIAPP	-	7.72	9.36	100
1a	OH (4)	7.58	9.06	109
2a	OH (8)	8.30	10.50	112
3a	OH (12)	6.68	7.95	102
4a	OH (16)	7.70	8.79	103
1b	COOH (4)	2.83	4.22	144
2b	COOH (8)	< 1	< 1	287
3b	COOH (12)	N.D.	N.D.	480
3c	NH_2 (12)	8.06	9.84	1.12
1d	OSO_3H (4)	> 20	> 20	N.D.
2d	OSO_3H (8)	4.38	5.01	127
3d	OSO_3H (12)	4.03	5.39	186
4d	OSO_3H (16)	N.D.	< 0.5	> 800
1d (0.1 eq)	OSO_3H (4)	12.18	13.77	49
2d (0.1 eq)	OSO_3H (8)	8.78	10.4	95
3d (0.1 eq)	OSO_3H (12)	3.98	5.78	125
4d (0.1 eq)	OSO_3H (16)	< 1	1.36	126
Eprodisate	SO_3H (2)	8.17	9.98	102
Eprodisate (5 eq.)	SO_3H (2)	8.08	9.61	103

[a]Concentration of IAPP was 12.5 μM and all compounds were tested at 1 eq. (12.5 μM), otherwise stated. Each data represents the mean from at least two individual experiments performed in triplicate. [b]Number in ( ) corresponds to the number of surface groups attached on the dendrimer. [c]Lag time corresponds to the time before detectable amyloid formation occurs, as predicted by means of the nucleation dependent polymerization model. [d]T50 corresponds to the time required to reach half

of the maximum ThT fluorescence. [e]The maximum fluorescence of IAPP in absence of compound was set as 100.

In contrast, dendrimers functionalized with carboxylate units showed strong accelerating effects on IAPP self-assembly. Incubation of IAPP in presence of 1 eq. of compounds 1b and 2b reduced the lag-phase to 2.83 h. and to less than 1h., respectively (Table 4.1; Figure 4.2A). Dendrimer decorated with 12 carboxylate groups (3b) hastened IAPP fibrillogenesis to such an extent that the lag phase was abolished. As inferred from the observed final ThT fluorescence intensity, polycarboxylated G1 dendrimers (2b, 3b) increased the amount of fibrils formed and/or favor the formation of amyloids with better defined cross-β-sheets structure. We observed a direct correlation between the increase of fibrilization and the number of carboxylic units attached to the dendrimeric core. IAPP is a cationic peptide displaying a net charge of +3 at physiological pH (Figure 4.1; N-terminus amine, Lys^{1} and Arg^{11}), favoring its binding through electrostatic interactions to anionic groups. Accordingly, our results suggest that G1 carboxylated dendrimers potentiate IAPP amyloidogenesis by a scaffold-based mechanism, in which the carboxylate groups interact with the positively charged N-terminal domain of IAPP, increasing the local peptide concentration and favoring self-association of the 20-27 amyloidogenic domain into β-sheet-rich assemblies. This scaffold-based mechanism has been previously proposed for the accelerating effect of sulfated GAGs on the assembly of several amyloidogenic polypeptides (Bourgault *et al.*, 2011b; Motamedi-Shad *et al.*, 2009; Solomon *et al.*, 2011). the acceleration effect on IAPP fibrillization observed for carboxylated dendrimers was not detected for their sulfated counterparts. In fact, when 1 eq. of G0 sulfated dendrimer (1d) was incubated with IAPP, no ThT positive signal was measured over the course of a 20h. assay (Figure 4.2B), suggesting a total inhibition of the formation of cross-β-sheet rich assemblies. Thus, substituting the 4 carboxylate groups on the G0 dendritic scaffold by 4 sulfate units led to a compound (1d) that

instead of potentiating amyloid assembly inhibits amyloid formation. As both groups are deprotonated under the conditions of the fibrillization assay (pH 7.4), this discrepancy is not related to the charge state of the G0 dendrimer, but most likely resides in their distinctive solubilization capacity. This result reinforces the notion that the sulfate group constitutes a key molecular identity for the design of amyloid assembly inhibitors (Meng *et al.*, 2010a). Anionic dendrimers decorated with 8, 12 or 16 sulfate units (2d, 3d, 4d, respectively) enhanced amyloid formation in a charge density dependent manner. Nonetheless, these effects were less pronounced compared to their carboxylated equivalents. As the sulfated dendrimers displayed interesting amyloid modulating properties when employed at 1 eq., *i.e.* acceleration or inhibition of IAPP amyloid formation, we evaluated the effects of compounds 1d to 4d at 0.1 eq (1.25 μM). When used at 0.1 eq to IAPP, compound 1d harboring 4 sulfate units still delayed the formation of ThT-positive species with a lag phase of over 12 hours (Figure 4.2C). Similarly, the accelerating effects of compounds 2d, 3d and 4d on IAPP amyloid assembly were significantly reduced.

To assess the importance of the clustered nature of sulfated dendrimers, we evaluated the effects of eprodisate (propane-1,3-disulfonate) on IAPP amyloid formation. It has been reported that eprodisate, which was developed and tested into the clinics as an amyloid inhibitor (Aisen *et al.*, 2007), had no effect on proIAPP(1-48) aggregation (Meng et Raleigh, 2011). However, the effect of this compound on IAPP self-assembly has never been described in the literature. We observed that this disulfonated GAGs mimetic had no significant effects on IAPP amyloidogenesis when employed at 1 and 5 eq. (Table 4.1; Figure S4.3). Considering that 62.5 μM of eprodisate (5 eq.) correspond to a concentration of 125 μM sulfonate units whereas 12.5 μM of compound 1d (1 eq.) correspond to a concentration of 50 μM sulfate groups, this indicates that the inhibitory effect of compound 1d most likely resides in its multivalency rather than in the concentration of anionic groups in solution. Moreover,

the high flexibility of the G0 dendrimeric scaffold as well as the distance between sulfated units could also make a key contribution to this anti-assembly effect. Interestingly, the sulfonated triphenyl methane derivative acid fuchsin, harboring 3 sulfonate groups, has been reported to be a potent inhibitor of IAPP fibrillization (Meng *et al.*, 2010a), supporting the key role of this chemical group for the inhibition of amyloid formation.

4.5.3 Modulation of amyloid assembly by low generation sulfated dendrimers monitored by atomic force microscopy

ThT fluorescence reports the formation of protein aggregates rich in cross-β-sheets quaternary structure and not the formation of amorphous aggregates and/or non-fibrillar species. Moreover, the strong inhibitory effect of compound 1d at 1 eq. on amyloid formation observed by ThT fluorescence could be related to the inhibition of dye binding to the amyloids, rather to a real effect on IAPP amyloidogenesis. For instance, it has been observed that the previously reported inhibitory effect of aspirin and ketoprofen on IAPP assembly resides in the interference with Congo Red binding and that these compounds have no effects on amyloid formation (Tu *et al.*, 2014b). Thus, we validated the results obtained with the ThT kinetics assays by monitoring the fibrillization process by atomic force microscopy (AFM). AFM analysis revealed the formation of amyloid fibrils with an average length of 476.5 ± 192.7 nm and an average diameter of 3.52. ± 1.15 nm when IAPP was incubated in absence of dendrimers for 20 hours (Figure 4.3A). This result is consistent with previous studies showing that IAPP forms fibrils of around 300 to 1000 nm length and 3 to 10 nm height, when incubated in aqueous buffer at room temperature without agitation(De Carufel *et al.*, 2015; Luca *et al.*, 2007; Meng et Raleigh, 2011; Radovan *et al.*, 2008). When IAPP

was incubated in presence of 1 eq. compound 1d, no fibrils were found on the mica (Figure 4.3B). This data supports the inhibition of amyloid formation reported with the ThT assay. In sharp contrast, the presence of compound 3d in the aggregation mixture led to the massive formation of very long (1143.7 ± 252.7 μm) fibrils with an average height of around 5.85 ± 1.66 nm (Figure 4.3C). This result shows that the dendrimer decorated with 12 sulfate units not only accelerated amyloid fibrils formation but favored the formation of significantly longer fibrils. All controls (buffer alone, compounds 1d and 3d alone) did not show any aggregates after 20 hours incubation under the same conditions. AFM analysis performed with representative sulfated G0 and G1 dendrimers confirmed the results obtained with the ThT fluorescence assays and indicated that compound 1d does not only inhibit cross-β-sheets assembly, but it also prevents amorphous aggregation of IAPP.

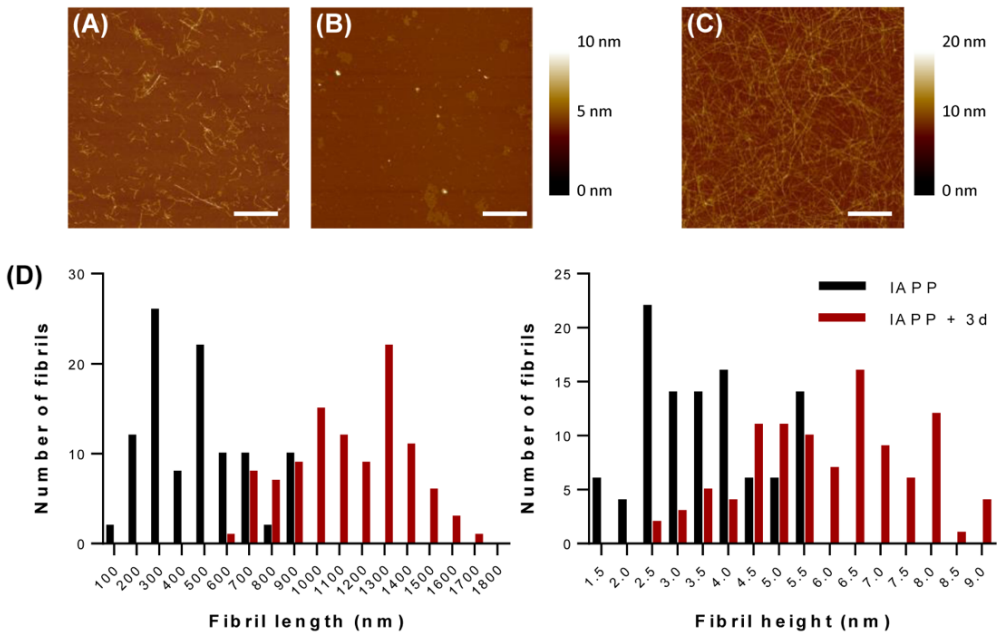


Figure 4.3 Low generation sulfated dendrimers modulate IAPP amyloid fibril formation.

Representative atomic force microscopy (AFM) images of IAPP incubated for 20 hours in absence (A) or in presence of (B) 1 eq. of compound 1d or (C) 1 eq. of compound 3d. Images are 5 μm × 5 μm and scale bar represents 1 μm. (D) Distribution of height and length of IAPP amyloid fibrils prepared in absence and in presence of 1 eq. of compound 3d. All experiments were performed in 20 mM Tris, pH 7.4, at 25°C without agitation in presence of 50 μM IAPP.

4.5.4 Modulation of IAPP conformational transition by low generation sulfated dendrimers

In its monomeric soluble structure, IAPP mainly adopts a random coil conformation, although it diverges from a pure disordered peptide by the transient appearance of helical segments (Williamson et Miranker, 2007). Amyloid formation of natively disordered peptide is usually accompanied by a transition of the polypeptide secondary structure from a random coil to a β-sheet-rich conformation, involving different conformational intermediates that could be either on- or off-pathway (De Carufel *et al.*, 2015; Williamson *et al.*, 2009). Considering the promising results (ThT assay, AFM) obtained with the polysulfated dendrimers, we evaluated the capacity of these compounds to modulate IAPP conformational transition. The CD spectrum of freshly dissolved IAPP was characteristic of a random coil conformation with a single minimum around 202 nm (Figure 4.4A). After 20 h incubation in absence of dendrimers, IAPP exhibited a CD spectrum with a single minimum at around 220 nm, characteristic of a β-sheets-rich secondary structure (Figure 4.4C). Strikingly, when IAPP was incubated with the dendritic scaffold functionalized with 4 sulfate groups (1d), this conformational transition was inhibited and IAPP remained in a random coil conformation upon 20 h incubation. As anticipated from AFM analysis and ThT assay, incubation of IAPP in presence of compound 3d accelerated its conformational transition from a random coil to a β-sheet rich structure, supporting the pro-

amyloidogenic effect of densely sulfated dendrimers. Moreover, this data shows that although the fibrils obtained without or with compound 3d are morphologically different, as observed by AFM, both amyloid preparations have a secondary structure rich in β-sheets.

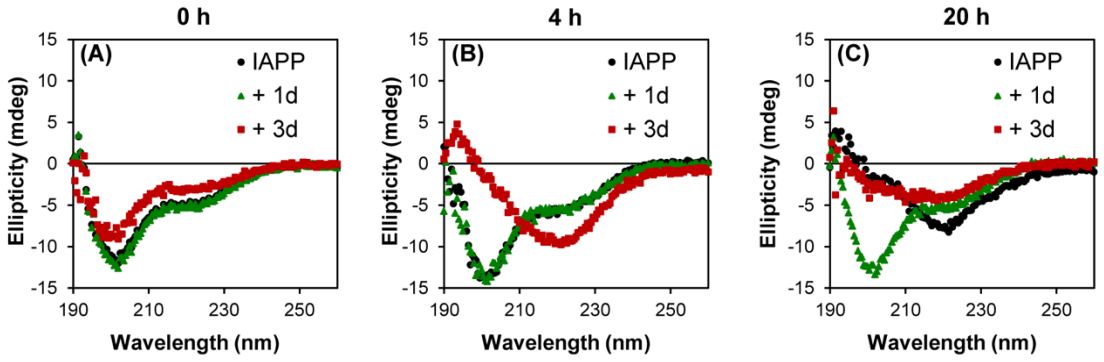


Figure 4.4 Conformational transition of IAPP modulated by low generation sulfonated dendrimers.

Representative far-UV circular dichroism spectra of 50 μM IAPP incubated in absence (black) or in presence of 1 eq. of compound 1d (green) or 1 eq of compound 3d (red) at time (A) 0 h, (B) 4 h and (C) 20 h. All experiments were performed in 20 mM Tris, pH 7.4, at 25°C without agitation.

4.5.5 Anionic low generation dendrimers inhibit IAPP-induced pancreatic β-cells toxicity.

All dendritic compounds were initially evaluated for their cytotoxicity towards pancreatic β-cells by means of the resazurin cell viability assay. Among all derivatives, only the cationic dendrimer decorated with amine units (3c), showed potent cytotoxicity at 5 and 50 μM, with cellular viability of 40 and 5% of control, respectively (Figure 4.5A). All neutral and anionic G0 and G1 dendrimers did not affect the viability

of pancreatic β-cells. Next, compounds were tested for their capacity to inhibit cell death induced by IAPP. It is known that IAPP induces death of pancreatic β-cells, although the exact molecular mechanisms of toxicity are still the matter of active debate (Abedini et Schmidt, 2013; Nguyen *et al.*, 2015). When cells were treated with freshly dissolved monomerized IAPP, a decrease of cellular viability upon 24 hours treatment was observed in a concentration-dependent manner, with cellular viability of approximatively 40% of non-treated cells at 50 μM (Figure S4.4). This cytotoxic effect is related to the aggregation propensity, as it has been shown that the non-amyloidogenic rodent IAPP is not cytotoxic at concentrations lower than 50 μM(De Carufel *et al.*, 2015). We evaluated the toxicity of IAPP proteospecies generated upon 20 h incubation at 25°C in absence or in presence of 0.1 (5 μM) and 1 eq. (50 μM) of functionalized dendritic scaffolds. As compound 3c was cytotoxic, it was not tested for its ability to protect pancreatic cells against IAPP toxicity. As anticipated from their absence of effects on IAPP amyloidogenesis, neutral polyhydroxylated dendrimers did not reduce, nor increase, the cytotoxicity of 50 μM IAPP on β-pancreatic cells (Figure 4.5B). In contrast, polycarboxylated G1 dendrimers attenuated IAPP-induced cell death proportionally to the number of carboxylate units attached to the dendritic core. Actually, the protecting effect of polycarboxylated dendrimers was not dependent to the concentration of carboxylate groups present in solution but was rather proportional to the density of substitution. For instance, 50 μM compound 1b, i.e. 200 μM of carboxylate groups, did not protect cells against IAPP effect whereas compound 3b at 5 μM, i.e. 60 μM of carboxylate units, totally inhibited the cytotoxic effect of IAPP. This observation is consistent with the results obtained with the ThT assay and suggests that compound 3b is protecting pancreatic cells by accelerating amyloid formation and/or by converting proteotoxic species (monomer, oligomer, and pre-fibrillar) into non-culprit fibrillary aggregates. A similar trend was observed for the polysulfated derivatives (Figure 4.5B), whereas compound 3d (12 sulfate units) and 4d (16 sulfate units) increased the viability of IAPP-treated cells. Interestingly, compound 1b at a

concentration 50 μM, which showed a clear inhibition of amyloid formation, as measured by ThT-fluorescence, AFM as well as CD spectroscopy, partially inhibited the toxicity of IAPP.

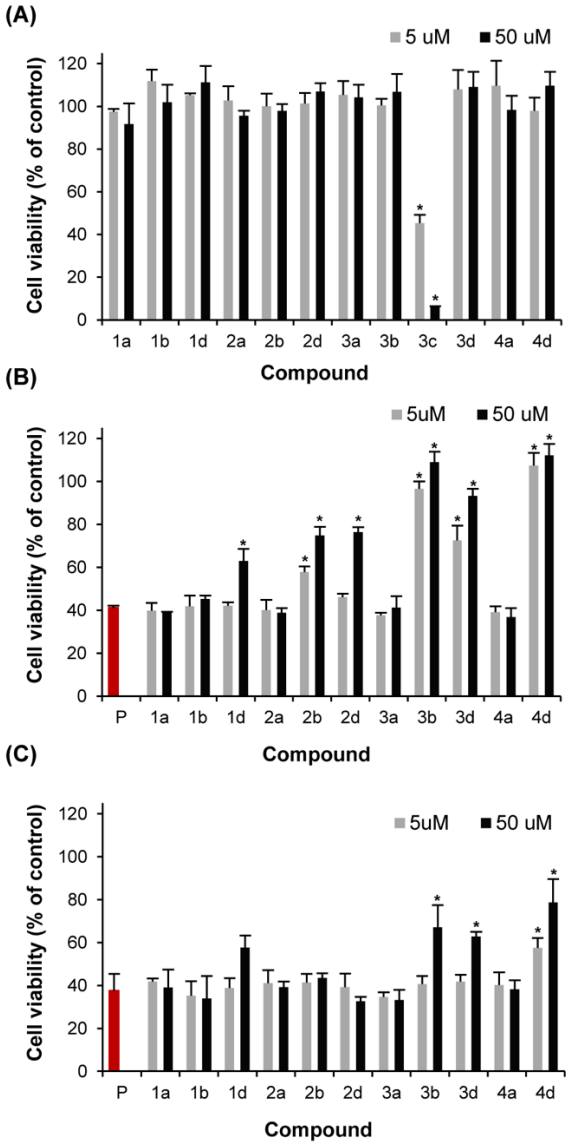


Figure 4.5 Inhibition of IAPP-induced cytotoxicity on β-pancreatic cells by low generation dendrimers.

(A) Viability of INS-1 cells incubated for 24 h with 5 or 50 μM dendrimers. (B) Viability of INS-1 cells treated for 24 h with IAPP (50 μM; P) that has been pre-incubated for 20 h in absence (red) or in presence of 5 or 50 μM dendrimers. (C) Viability of INS-1 cells treated for 24 h with freshly dissolved IAPP (50 μM) in absence (red) or in presence of 5 or 50 μM dendrimers. *Statistically significant difference between (A) control vs dendrimer treated or (B,C) IAPP-treated vs dendrimer IAPP-treated ($P < 0.05$).

Next, we evaluated the effect of these dendritic scaffolds on IAPP-toxicity when they were co-applied with the peptide to the media of pancreatic cells, *i.e.* without 20 h. pre-incubation. Under these conditions, only compounds 3b, 3c and 4b at 50 μM showed a significant reduction of IAPP-induced cell death (Figure 4.5C). Taking into account that these compounds drastically accelerated IAPP assembly *in vitro*, they most likely reduced IAPP toxicity by sequestering IAPP proteospecies and/or by accelerating the amyloidogenic cascade to such an extent that the toxicity is reduced. Compound 1d appeared to protect partially pancreatic cells when added simultaneously to IAPP in the cell media at 50 μM, although this effect was not statistically significant. This result illustrates that a potent inhibitory effect on amyloid formation in a homogenous *in vitro* environment does not necessarily correlate with a strong capacity of this compound to protect cells against the toxicity of an amyloidogenic polypeptide. Accordingly, it is particularly important that the identification of amyloid modulators *in vitro* is also performed *in milieu* that recapitulates, as much as possible, the complex biological environment in which IAPP aggregation and toxicity occur (Nguyen *et al.*, 2015), an avenue that we are currently exploring.

4.6 Conclusion

The self-assembly of the peptidic hormone IAPP in the pancreatic islets is associated with DM-2. While the correlation between amyloid deposition and the severity and progression of DM-2 has been well-established (Westermark, 2011), there is currently no therapeutic approaches targeting this amyloidogenic cascade. Over the last two decades, several compounds, including aromatic-rich small molecules (Cheng *et al.*, 2013; Hassanpour *et al.*, 2014; Jesus *et al.*, 2014; Meng *et al.*, 2010a; Meng *et al.*, 2010b; Tomiyama *et al.*, 1997), N-methylated peptide derivatives(Yan *et al.*, 2006), phosphonated molecular tweezers (Lopes *et al.*, 2015) and sulfated glycosaminoglycans (De Carufel *et al.*, 2013; Jha *et al.*, 2011), were shown to modulate IAPP self-assembly *in vitro* and to reduce its cytotoxicity. Strikingly, although their scaffolds are structurally divergent, the majority of these molecules are densely functionalized with hydrophilic and/or charged groups on their surface. Nonetheless, the relationships between the nature/density of the chemical function and the effect on IAPP amyloid formation have never been explicitly addressed. This lack of knowledge particularly precludes the identification and optimization of amyloid modulators. Moreover, IAPP is a natively disordered polypeptide and needs to undergo transient secondary and quaternary conformational rearrangements to self-assemble intro fibrillary aggregates. These complex structural conversions are not completely understood and are still the matter of active research. Therefore, the rational design of compounds targeting pre-amyloid transient structural states is extremely challenging and molecular scaffolds with high conformational flexibility could demonstrate unique anti-amyloid assembly properties.

In this study, we evaluated the effects of low generation dendrimers decorated with 4 to 16 functional groups on IAPP amyloidogenesis and IAPP-induced pancreatic β-

cells toxicity. These dendritic scaffolds are perfectly suited to probe how multi-homofunctionalized molecular templates can modulate the self-assembly of amyloidogenic IDPs. Particularly, these dendrimers were designed to be highly flexible in order to accommodate the wide conformational ensemble of native IAPP and its numerous transient conformations during the assembly process. Moreover, whereas the anti-amyloidogenic potential of large dendrimers was recently recognized for polypeptides related to Alzheimer and prion diseases (Benseny-Cases *et al.*, 2012; Heegaard *et al.*, 2007; Klajnert *et al.*, 2012; Klementieva *et al.*, 2013; Wasiak *et al.*, 2012), the effects of low generation dendrimers on IDP self-assembly and toxicity have never been assessed so far. We identified a G0 dendrimer decorated with 4 sulfate groups (1d) that efficiently inhibit IAPP amyloid assembly. Interestingly, compound 1d not only prevented fibrillization, but also inhibited IAPP conformational conversion. This indicates that compound 1d interacts with IAPP in its natively disordered secondary structure, preventing its aggregation and its conformational transition into β-sheets competent nucleus. The high flexibility of the G0 scaffold most likely accommodates the large ensemble of distances between the two positively charged residue side chains (Lys^{1}, Arg^{11}). In turn, this electrostatic-mediated binding of IAPP to compound 1d prevents the interpeptide interactions that are driving amyloid assembly.

Increasing the number of sulfated units from 8 to 16 led to an acceleration of amyloid formation, most likely by a scaffold-based mechanism, as previously reported for highly sulfated GAGs (Bourgault *et al.*, 2011b; De Carufel *et al.*, 2013; Jha *et al.*, 2011). Whereas the sulfated G0 dendrimer decorated with 4 units (compound 1d) inhibited fibrillization, the G1 2d dendrimer (8 sulfate groups) potentiated IAPP self-assembly. These results offer a novel perspective regarding the relation between the number of sulfate groups on a flexible molecular scaffold and the effects on self-assembly. Over the last fifteen years, several studies have shown that pre-fibrillar

intermediates are the most toxic species and that well-defined amyloid fibrils are poorly cytotoxic (Bourgault *et al.*, 2011a; Kayed *et al.*, 2003). The protective effect observed for polysulfated G1 dendrimers against IAPP-induced toxicity highlights that sequestering proteotoxic species of the amyloidogenic cascade through the acceleration of fibrillization constitute a therapeutic strategy to reduce β-cell loss that deserves further investigation.

4.7 Supporting Information

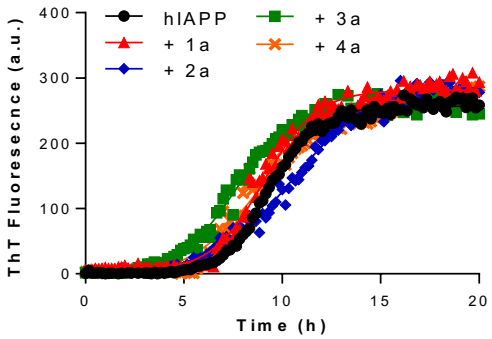


Figure S4.1 Effects of polyhydroxyl low generation dendrimers on IAPP amyloid fibril formation monitored by ThT fluorescence.

IAPP (12.5 μM) was incubated in 20 mM Tris, pH 7.4, at 25°C without agitation in the absence (●) or in the presence of 1 eq. of compound 1a (▲), compound 2a (♦), compound 3a (■) or compound 4a (×). ThT fluorescence was measured every 10 min over the course of 20 h, with excitation at 440 nm and emission at 485 nm.

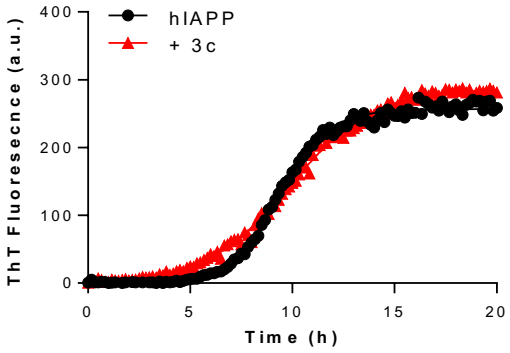
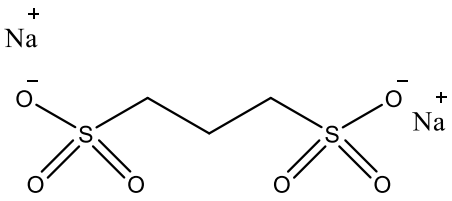


Figure S4.2 Effect of polyamine G1 dendrimer on IAPP amyloid fibril formation monitored by ThT fluorescence.

IAPP (12.5 μM) was incubated in 20 mM Tris, pH 7.4, at 25°C without agitation in the absence (•) or in the presence of 1 eq. of compound 3c (▲). ThT fluorescence was measured every 10 min over the course of 20 h, with excitation at 440 nm and emission at 485 nm.

(A)



(B)

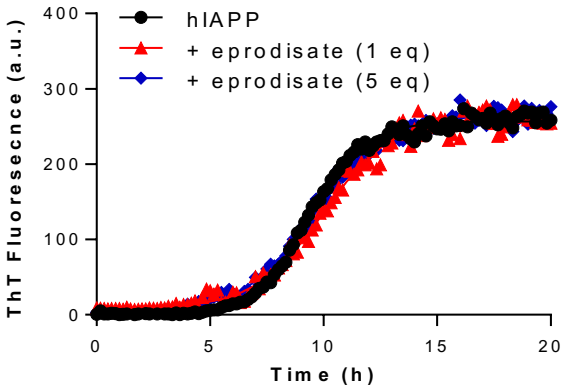


Figure S4.3 Effect of the glycosaminoglycan mimetic, eprodisate (sodium propane-1,3-disulfonate) on IAPP amyloid fibril formation monitored by ThT fluorescence.

(A) Chemical structure of eprodisate. (B) IAPP (12.5 μM) was incubated in 20 mM Tris, pH 7.4, at 25°C without agitation in the absence (•) or in the presence of 12.5 μM (▲) or 62.5 μM (♦) of eprodisate. ThT fluorescence was measured every 10 min over the course of 20 h, with excitation at 440 nm and emission at 485 nm.

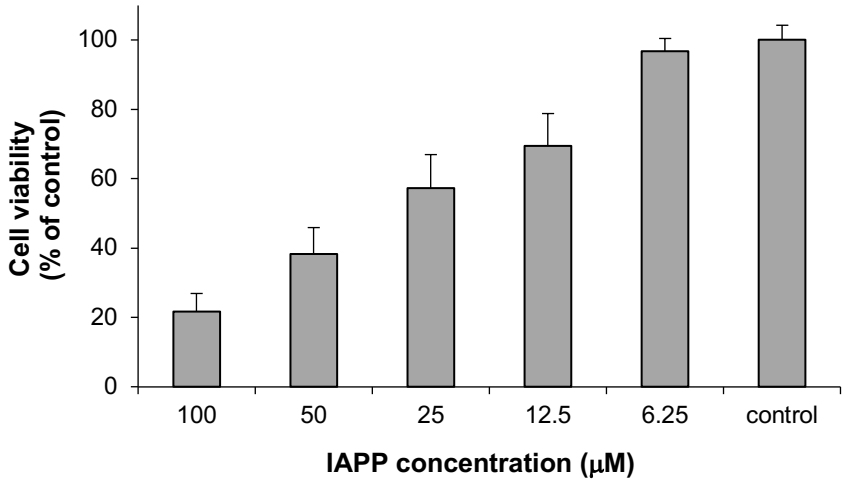


Figure S4.4 Concentration-effect of IAPP on the viability of INS-1 pancreatic β-cells.

INS-1 cells were treated with concentrations of IAPP ranging from 100 to 6.25 μM for 24 h. and cell viability was measured by the resazurin reduction assay and compared to cells treated with vehicle only (100% cell viability).

CHAPITRE V

DISCUSSION GÉNÉRALE

Nonobstant que de nombreuses études ciblant la pathogénicité de l'IAPP et son implication dans le diabète de type II aient été récemment publiées, l'élucidation des mécanismes de l'auto-assemblage amyloïde de l'IAPP s'avère difficile par le fait que ce processus est hautement dynamique, difficilement contrôlable et fait intervenir de nombreuses conformations *off* - et *on-pathway*. Particulièrement, les interactions initiales entre les monomères d'IAPP qui conduisent à l'oligomérisation ainsi que les caractéristiques physicochimiques et structurales des espèces protéotoxiques de l'IAPP restent toujours l'objet d'actives recherches. Dans le but de mieux comprendre les caractéristiques physicochimiques et conformationnels de ce processus et d'identifier les espèces quaternaires cytotoxiques, nous avons étudié les déterminants moléculaires modulant l'auto-assemblage amyloïde de l'IAPP. Plus précisément, les effets de facteurs internes (la désamidation d'asparagine, les substitutions ciblées d'acides aminés) et externes (composés chimiques multi-fonctionnalisés) sur le processus d'amyloïdogénèse et la cytotoxicité sous-jacente de l'IAPP ont été ciblés.

La désamidation d'asparagine affecte l'amyloïdogénèse de l'IAPP mais pas sa cytotoxicité

Les protéines/peptides amyloïdogéniques sont particulièrement sensibles aux modifications post-traductionnelles non enzymatiques causées par divers facteurs de stress, y compris les oxydants, les sucres réducteurs et les aldéhydes réactifs, et ce en raison de leur longue durée de vie (Soskic *et al.*, 2008; Trougakos *et al.*, 2013). De telles modifications post-traductionnelles non enzymatiques sont connues pour provoquer des altérations structurales dans de nombreuses protéines amyloïdogéniques (Sadakane et Kawahara, 2018). Notamment, la désamidation des résidus Asn est une réaction chimique hautement répandue qui se produit pendant le vieillissement des protéines (Lam *et al.*, 2018; Sadakane et Kawahara, 2018). En outre, une étude computationnelle ciblant plus de 170 000 résidus Asn dans 13 300 protéines, a permis d'apprécier l'importance de cette modification post-traductionnelle. Les résultats ont révélé qu'au moins un résidu Asn dans 17 % des protéines analysées était soumis à une désamidation d'au moins 10 % et ce, en cinq jours sous conditions physiologiques (Robinson, 2002). La désamidation d'Asn se produit par réarrangement intramoléculaire et implique un intermédiaire succinimide (Figure 2.1A). Ce dernier est rapidement hydrolysé dans les conditions physiologiques et un mélange d'acide aspartique (Asp) et d'iso-aspartique (isoAsp) est généré. Cette conversion d'Asn en Asp/isoAsp entraîne un changement au niveau la charge locale de la protéine, ce qui peut conduire à divers phénomènes biologiques, y compris la formation de fibres amyloïdes. Des études antérieures ont montré que la désamidation module la formation des fibres amyloïdes, notamment l'amyloïdogénèse du peptide Aβ associé à la maladie d'Alzheimer (Fossati *et al.*, 2013; Sargaeva *et al.*, 2011; Shimizu *et al.*, 2002). En outre, l'agrégation de la protéine microglobuline-β 2 (Kad *et al.*, 2001) et de la cristalline s'est également avérée être affecté par la désamidation d'Asn (Gupta et Srivastava, 2004 ; Takata *et al.*, 2008). De plus, il a été également montré *in vitro* que la désamidation d'Asn accélère l'auto-assemblage de l'IAPP et altère la structure des fibres amyloïdes obtenues (Dunkelberger *et al.*, 2012). Toutefois, l'IAPP contient six résidus Asn, et les résidus soumis à cette désamidation n'ont pas été spécifiquement identifiés.

À cet effet, l'évaluation de la contribution spécifique de la désamidation Asn sur l'auto-assemblage des peptides nécessite des modifications ciblées sur des résidus Asn particuliers afin d'obtenir des détails mécanistiques à l'échelle (supra) moléculaire. Des études antérieures ont montré que l'Asn-21, l'Asn-22 et l'Asn-35 sont les résidus les plus susceptible à la désamidation (Hekman *et al.*, 1998; Lam *et al.*, 2018). Selon les résultats présentés au chapitre 2, les sites de désamidation affectent différemment la fibrillisation de l'IAPP. D'une part, les modifications en positions 14 et 21 ont un effet drastique sur la cinétique d'auto-assemblage en fibres amyloïdes. D'autre part, la désamidation successive des autres résidus Asn n'a pas eu d'effet significatif sur la cinétique d'assemblage et la morphologie des fibres obtenues (Figures 2.2A et 2.4). Une telle spécificité concernant la position de désamidation sur l'impact sur l'assemblage des amyloïdes a été également rapportée pour le peptide Aβ. En effet, la désamidation en position 23 résulte en une accélération de la formation des fibres amyloïdes alors que celle en position 7 a un effet inhibiteur sur l'amyloïdogenèse (Sadakane et Kawahara, 2018; Shimizu *et al.*, 2002). Il serait intéressant d'étudier comment différentes combinaisons de sites de désamidation, telles que les mutations simultanées N14D et N21D, modulent la formation d'amyloïde afin de mieux comprendre les implications biologiques sous-jacentes. Notamment, nous avons observé qu'un faible rapport molaire (1 % à 5 %) d'IAPP désamidé en position 14 promeut l'assemblage de l'IAPP non-modifié et accélère l'allongement des fibres. Contrairement à l'analogue N14D, le N21D, à une faible concentration de 250 nM, prolonge la phase de nucléation de l'IAPP sauvage et agit comme un inhibiteur de la formation de fibres amyloïdes (Figure 2.6) et ce comme observé pour l'isoforme rIAPP (Figure S2.6). Toutefois, à des concentrations plus élevées, l'analogue N21D accélère l'amyloïdogenèse de l'IAPP sauvage et le co-assemblage résulte en un dense réseau de filaments (Figure 2.6). Alors que l'introduction d'un groupement carboxylate en position 21 inhibe la formation de fibres amyloïdes, la présence de l'IAPP sauvage, portant un groupe amide en position 21, permet à l'analogue N21D de subir un réarrangement secondaire et quaternaire en fibres amyloïdes. Il a été observé que la

formation d'intermédiaire succinimide des résidus Asn est très rapide et que cet intermédiaire, sous conditions physiologiques, a un court temps de demi-vie de l'ordre de l'heure avant son hydrolyse pour générer un mélange d'Asp et d'isoAsp (Sadakane et Kawahara, 2018). De plus, des études ont suggéré que les résidus Asn/Asp sont sujets au clivage de liaisons peptidiques des protéines et que la séquence His-Asp constituait un signal de dégradation protéique au sein des cellules (Brennan et Clarke, 1995; Geiger et Clarke, 1987). Or, la séquence primaire de l'IAPP n'affiche pas le motif His-Asp (avant ou après la désamidation). Ceci indique que, sous conditions physiologiques, que l'IAPP désamidé ne pourrait être éliminé rapidement et pourrait s'accumuler dans les tissus et par la suite pourrait jouer un rôle d'initiateur (l'analogue N14D) ou de co-assembleur avec l'IAPP sauvage (l'analogue N21D) dans les dépôts amyloïdes associés au diabète de type II.

La cytotoxicité des dérivés désamidés a été évaluée en utilisant la lignée cellulaire INS-1E. Les analogues d'IAPP entièrement désamidés (NXD et NXisoD) et l'isoforme rIAPP n'étaient pas cytotoxiques, ce qui suggère une certaine corrélation entre l'amyloïdogénécité mesurée *in vitro* (fluorescence ThT, spectroscopie CD, TEM) et la toxicité dans un modèle cellulaire. L'analogue N14D, qui présentait une très courte phase de nucléation, a montré une toxicité après 6 h d'incubation alors que pour l'IAPP sauvage, la diminution de la viabilité cellulaire n'a été observée qu'après 8 h. Les effets cytotoxiques du [N14D] IAPP observés à 6 h sont probablement associés à sa forte amyloïdogénécité observée *in vitro*. Concernant l'analogue N21D, aucune relation entre la capacité de former des fibres amyloïdes *in vitro* et la cytotoxicité sur les cellules INS-1E n'a été observée. Ces résultats soulignent qu'il demeure difficile de prédire la toxicité résultante d'un polypeptide amyloïdogénique, tel que l'IAPP, en se basant simplement sur sa capacité à s'auto-assembler en fibres amyloïdes *in vitro*. Dans l'ensemble, cette étude souligne que la désamidation ciblée d'asparagine module l'amyloïdogénèse de l'IAPP sans affecter la cytotoxicité sous-jacente de l'IAPP, et

suggère de potentielles implications biologiques de la désamidation dans la formation de fibres amyloïdes.

Rôles de chaînes latérales de résidus spécifiques dans les processus de nucléation et d'élongation amyloïde

Au cours des dernières années, plusieurs études ont évalué les impacts de substitutions spécifiques d'acides aminés sur l'amyloïdogénécité de l'IAPP afin de mieux comprendre les forces qui gouvernent son auto-assemblage en fibres amyloïdes (Abedini *et al.*, 2007 ; Cao *et al.*, 2013 ; Tu et Raleigh, 2013b ; Wiltzius *et al.*, 2008 ; Wiltzius *et al.*, 2009). Les premières études ont été réalisées en se basant sur la différence observée entre la séquence primaire de l'IAPP humain et celle retrouvée chez les rongeurs (Tableau 1.7). Ces études ont initialement suggéré que la propension à l'agrégation de l'IAPP est tolérante à différentes substitutions spécifiques sur les acides aminés, à l'exception des substitutions effectuées au niveau du segment 20-29 de l'IAPP (Cao *et al.*, 2013 ; Westermark *et al.*, 1990). Néanmoins, de récentes études ont révélé que de nombreuses substitutions en dehors de la région amyloïdogénique 20-29, y compris A13E, Y37L et F15K, abolissaient ou ralentissaient considérablement la formation des fibres amyloïdes d'IAPP (Fox *et al.*, 2010b ; Tu et Raleigh, 2013b ; Wiltzius *et al.*, 2008). De plus, nos données montrent que lorsqu'un groupe carboxylate est introduit en position 14, la phase de nucléation est raccourcie et un dense réseau de longues fibres est observé (Figure 2.2 et Figure 2.4). Ce résultat est surprenant puisque les substitutions N14L, N14S et N14A sont connues pour inhiber la formation des fibres amyloïdes (Koo *et al.*, 2008). D'autre part, il a été montré que la substitution d'Ala-13, voisin de l'Asn-14, par un résidu Gln, perturbe la formation d'amyloïde (Fox *et al.*, 2010b). L'ensemble de ces résultats suggère que les phases de nucléation et d'élongation de l'amyloïdogénèse de l'IAPP sont médiées par des interactions intra et/ou intermoléculaires précises impliquant des chaînes latérales spécifiques.

En ce qui concerne les réarrangements conformationnels nécessaires à la nucléation, ceux-ci font toujours l'objet de recherches actives. Deux principaux modèles ont été proposés pour les étapes d'oligomérisation de la phase de latence : le modèle des intermédiaires hélicoïdaux et le modèle des épingles à cheveux (Abedini et Raleigh, 2009; Dupuis *et al.*, 2009; Wiltzius *et al.*, 2009). Le modèle des intermédiaires hélicoïdaux propose que l'auto-association de l'IAPP est thermodynamiquement associée à la formation d'hélice au niveau du segment 5-28 (PDB 2KB8) (Figure 1.7). Sous cette conformation, la chaîne latérale du résidu Asn-14 se projetterait sur la même face de l'hélice que celles de l'Arg-11 et His-18 (positions *i*, *i* + *3* et *i* + *7*). Ainsi, la mutation N14D pourrait favoriser la formation de cette conformation transitoire en hélice par des stabilisations électrostatiques (Figure 5.1).

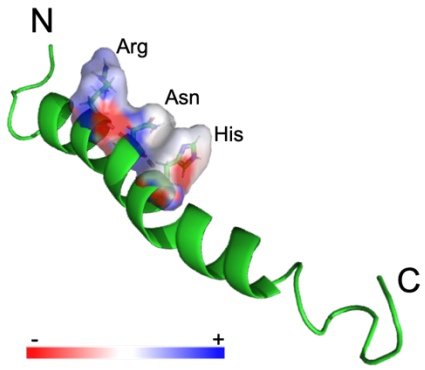


Figure 5.1 Distribution électrostatique impliquant les résidus Arg-11, Ans-14 et His-18 lorsque l'IAPP adopte sa conformation secondaire en hélice-α.

De plus, le résidu Asn en position 14 pourrait être impliqué dans un réseau de liaisons hydrogènes qui serait critique pour la formation d'espèces intermédiaires nucléantes. Cela pourrait nécessiter que la chaîne latérale du résidu en position 14 soit susceptible d'agir simultanément comme accepteur et donneur de ponts hydrogène, comme pour Asn et Asp. Cela pourrait donc expliquer pourquoi l'auto-assemblage de l'IAPP n'est

pas tolérant aux mutations N14L et N14A (Koo *et al.*, 2008), alors que la substitution N14D a un effet accélérateur sur la formation des fibres amyloïdes. De plus, malgré sa capacité de former des ponts hydrogène, le variant N14S inhibe également la formation de fibres amyloïdes (Koo *et al.*, 2008). En effet, la Ser ne possède qu'un groupement hydroxyle, elle forme donc qu'une seule liaison hydrogène comparée à l'Asn qui peut en former deux. En considérant la structure amyloïde de l'IAPP obtenue au moyen de la RMN à l'état solide (Figure 1.8), la chaîne latérale de l'Asn-14 se projette entre les deux couches de feuillet-β et ce, dans un environnement très probablement hydrophobe. De plus, dans les fibres amyloïdes, les chaînes latérales Asn-14 sont organisées en un réseau parallèle le long de l'axe des fibres et interagissent fort probablement avec les Asn-14 des monomères adjacents. En outre, les acides carboxyliques sont reconnus pour leur capacité à s'auto-associer dans un environnement hydrophobe et non-polaire (Di Tommaso, 2013), ce qui pourrait expliquer la forte amyloïdogénécité de l'analogue N14D, dont les fibres amyloïdes sont longues et épaisses. Un autre effet drastique sur la formation des fibres a été observé pour l'analogue N21D. Cette substitution inhibe complètement l'auto-assemblage amyloïde et cet analogue affiche des effets inhibiteurs sur l'auto-assemblage de l'IAPP sauvage, et ce, à de faibles concentrations. Selon notre étude, le site de déamidation est crucial pour l'impact sur l'auto-assemblage de l'IAPP. Ce concept de spécificité de site de substitution est particulièrement notable au niveau des mutations N21D/N21isoD qui empêchent la formation des fibres, alors que la substitution du N22 adjacent en Asp ou isoAsp modifie que légèrement l'auto-assemblage de l'IAPP. D'autre part, la mutation S20G, mutation familiale chez les populations asiatiques, est connue pour augmenter l'amyloïdogénique et la cytotoxicité de l'IAPP sur les îlots murins (Meier *et al.*, 2016). Nos observations sont en accord avec des études de Koo et ses collègues montrant que les mutations N21L et N21S perturbent l'assemblage en fibres amyloïdes d'IAPP, alors que la substitution N22L n'affecte ni la phase de nucléation ni celle d'élongation (Koo *et al.*, 2008). De toute évidence, le groupe amide en position 14 ou 21 est critique pour la formation des espèces intermédiaires durant la phase de

nucléation. Puisque nos résultats ont montré que les substitutions aux positions 31 et 35 n'ont pas affecté la polymérisation nucléée de l'IAPP, ces données renforcent l'hypothèse selon laquelle la région 11-25 initie la formation des intermédiaires transitoires stabilisés par des interactions intermoléculaires conduisant à l'assemblage en fibres amyloïdes (Liu *et al.*, 2010 ; Liu *et al.*, 2012). Globalement, nos données révèlent des contributions clés impliquant des propriétés physicochimiques précises des chaînes latérales aux positions 14 et 21, qui se révèlent essentielles pour les processus de nucléation et/ou d'élongation.

Les interactions intra et intermoléculaires impliquant Asn-21 modulent la conversion conformationnelle des intermédiaires oligomériques en fibres amyloïdes.

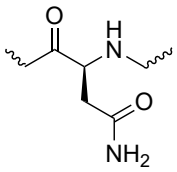
L'Asn en position 21 se retrouve dans la région amyloïdogénique 20-29. De plus, lorsque le peptide se retrouve en structure amyloïde, l'Asn-21 se situe dans la région en boucle (18-27) qui relie les deux brins β (Luca *et al.*, 2007). L'Asn-21 se retrouve aussi très proche de la région hydrophobe FGAIL (23-27) qui pourrait se retrouver en brin-β au sein des oligomères, avant de se transformer en boucle lors de la nucléation/élongation (Buchanan *et al.*, 2013; Williamson et Miranker, 2007). Ces observations combinées à nos résultats concernant la désamidation de l'Asn-21 suggèrent que l'Asn-21, incluant sa chaîne latérale et son squelette peptidique, est critique dans l'amyloïdogénèse de l'IAPP. Ainsi, une meilleure compréhension des forces impliquant le résidu en position 21 dans l'amyloïdogénèse et la toxicité de l'IAPP permettrait de mieux comprendre les relations auto-assemblage/cytotoxicité de l'IAPP. Dans ce contexte, plusieurs substitutions sur l'Asn-21, avec des acides aminés naturels et non naturels (Figure 5.2), ont été effectuées afin de comprendre l'importance de la taille (N21A, N21Q), de l'hydrophobicité (N21L, N21F) et de la polarité de la chaîne latérale (N21D, N21isoD, N21Dab) ainsi que l'impact de la flexibilité du squelette peptidique (N21Aib, N21P, N21G, N21n) (Annexe II et avant-propos du Chapitre III). Dans cette étude publiée dans JBC, nous avons révélé que la

chaîne latérale amide de l'Asn-21 n'est pas requise pour la nucléation et l'élongation en fibres amyloïdes, puisque les analogues N21A et N21G peuvent s'auto-assembler en filaments prototypiques. Cependant, la cinétique de formation des fibres amyloïdes observée pour ces deux analogues était ralentie, incluant une phase de nucléation allongée. Quels que soient les contacts initiaux entre les monomères, un réarrangement structural à haute énergie au sein du segment 20-29 est nécessaire pour la conversion des oligomères en fibres amyloïdes. Dans le modèle des oligomères en feuillet-β, impliquant la région ^{23}FGAIL^{27}, cette barrière énergétique ralentirait la formation des fibres amyloïdes et serait à l'origine de la phase de latence (Buchanan *et al.*, 2013 ; Serrano *et al.*, 2017) (Figure 5.3). Ainsi, la suppression du groupement amide (N21A, N21G), qui est à la fois un donneur et un accepteur de ponts hydrogène, pourrait augmenter la barrière énergétique, ralentissant l'auto-assemblage amyloïde (Figure 5.3).

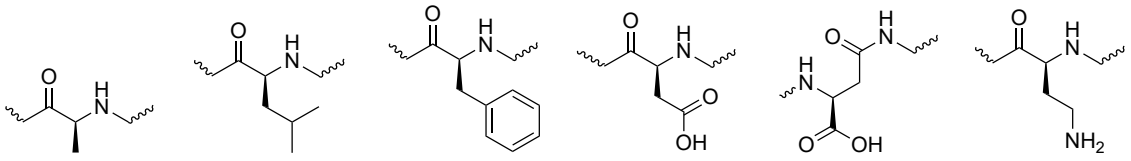
L'Asn-21 a aussi été substitué par une proline, qui est connue comme étant un puissant déstabilisateur de feuillet-β, et qui, par conséquent, devrait inhiber la formation des fibres (Jiang *et al.*, 2009). De façon surprenante, l'analogue N21P accélère plutôt l'auto-assemblage de l'IAPP. Ces mêmes effets ont été observés lorsque l'énantiomère D-Asn a été inséré à cette position. Les énantiomères de configuration D sont souvent utilisés afin de déstabiliser les hélices α et peuvent favoriser les structures en boucles (Hruby, 2002; Martin *et al.*, 2017; Mehrazma *et al.*, 2018). Alors, en favorisant la conformation en boucle par les substitutions Pro et D-Asn (N21P, N21n), la barrière énergétique de la nucléation pourrait être grandement diminuée et le processus de formation des fibres ainsi accéléré (Figure 5.3).

L'analogue N21Aib se retrouve principalement en conformation désordonnée et ne forme pas efficacement des fibres amyloïdes. L'acide aminé non-naturel Aib est connu pour induire la conformation en hélice-α (Karle, 2001) et pour augmenter l'encombrement au niveau du squelette peptidique. Ainsi, le dérivé N21Aib reste

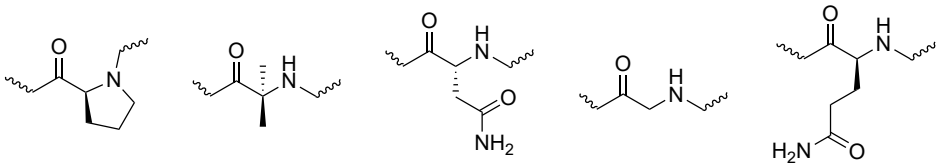
emprisonné dans une conformation principalement aléatoire, et se replie difficilement dans la conformation favorisant la nucléation.



Asn (N)



Ala (A) Leu (L) Phe (F) Asp (D) isoAsp (isoD) Dab



Pro (P) Aib D-Asn (n) Gly (G) Gln (Q)

Figure 5.2 Acides aminés (naturels et non naturels) ainsi que leur chaîne latérale utilisée dans notre étude.

Représentation des substitutions de l'Asn par différents acides aminés naturels et non-naturels utilisées dans cette thèse. Dab : acide 2,4-diaminobutrique; Aib : acide aminoisobutyrique.

Des charges positives et négatives ont été introduites à la position 21 (N21Dab, N21D, N21isoD). L'introduction de charges à la position 21 a complètement inhibé la formation de fibres. Les charges pourraient induire des répulsions entre les monomères au niveau de la région amyloïdogénique 20-29, lors de l'initiation de l'auto-assemblage, ce qui ralentit considérablement la nucléation (Figure 5.3).

Les substitutions de l'Asn-21 par des résidus hydrophobes (N21F et N21L) ont mené à la formation d'agrégats *worm-like* riches en feuillets-β et affichant une forte hydrophobicité de surface. Étonnamment, la simple substitution N21Q, soit l'ajout d'un carbone à la chaîne latérale, accélère la formation des fibres amyloïdes (Figure 3.4 et S3.7). Comme l'Asn, le résidu Gln contient le groupement amide qui peut accepter ou donner des protons. Avec la chaîne latérale plus longue et la présence de l'amide de Gln, les interactions intermoléculaires, stabilisées par les ponts hydrogènes, semblent hautement favorisées.

Les résultats de viabilité cellulaire montrent que la cytotoxicité induite par les différentes espèces quaternaires de ces analogues, à l'exception de N21F et N21Q, ne diffère pas de celle de l'IAPP sauvage, *i. e* les espèces intermédiaires sont toxiques et les fibres matures sont non-toxiques. L'auto-assemblage de l'analogue N21F mène à la formation d'agrégats *worm-like* hautement cytotoxiques et induisant la perturbation membranaire. L'analogue N21Q forme des nanofilaments hautement toxiques. Cette toxicité inattendue des fibres de N21Q a été confirmée en isolant les fibres et en évaluant la stabilité et la conformation des assemblages fibrillaires (Chapitre 3). Ainsi, la toxicité pourrait être conservée tout au long du processus d'auto-assemblage, incluant la formation des agrégats *worm-like* (N21F) et des fibres matures (N21Q). Ces résultats suggèrent qu'il n'y a pas une association simple et directe entre l'auto-assemblage amyloïde et la cytotoxicité des peptides et que les analogues N21F et N21Q pourraient emprunter des voies d'agrégation alternatives qui conduisent à la formation de conformations nocives (Figure 5.3). Ces résultats suggèrent que non seulement les interactions intra et intermoléculaires spécifiques de l'Asn-21 jouent un rôle crucial dans l'auto-assemblage en initiant la nucléation primaire de l'IAPP, mais que cette position 21 pourrait également moduler la conversion conformationnelle des intermédiaires oligomériques en fibres amyloïdes.

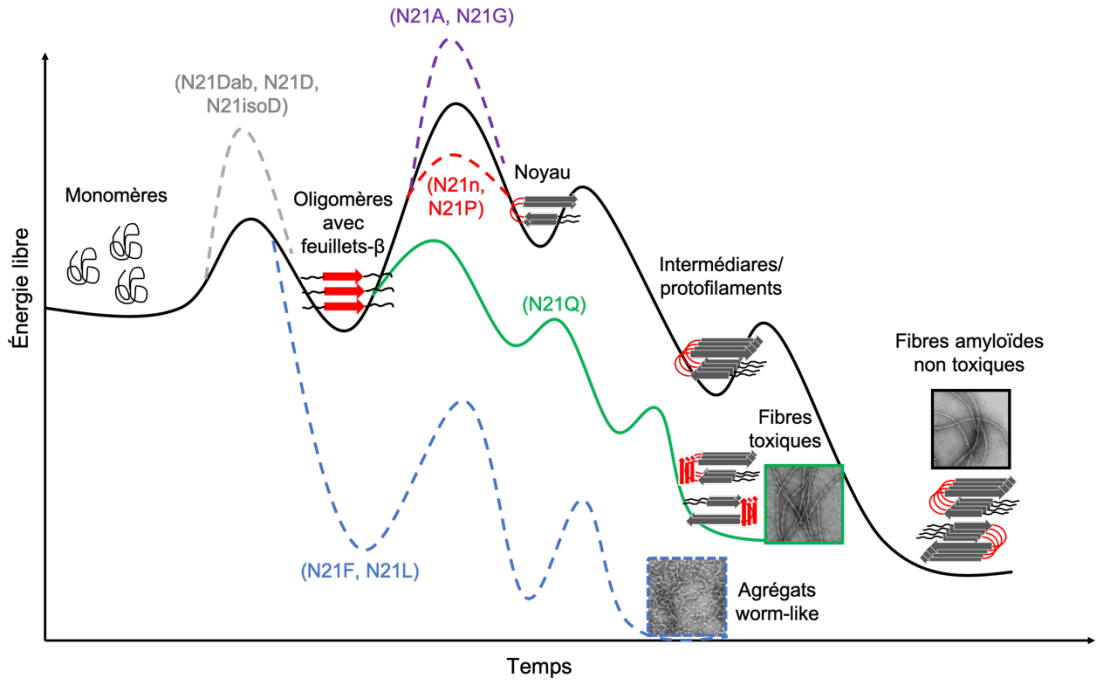


Figure 5.3 Représentation hypothétique du diagramme d'énergie de l'auto-assemblage de l'IAPP et des différents dérivés.

Les brins-β sont présentés en flèches grises et la région 20-29 est représentée en rouge.

Les propriétés *oligomer-like* peuvent être conservées lors de l'élongation, conduisant à la formation d'assemblages fibrillaires toxiques

Les résultats concernant l'impact de la désamidation et les modifications à la position 21 montrent qu'il n'existe pas une corrélation directe entre la capacité à s'auto-assembler en fibres amyloïdes et la cytotoxicité des peptides. Ceci suggère que la cytotoxicité associée à l'IAPP émane plutôt d'une, ou plusieurs, structures quaternaires spécifiques. En conséquence, l'étude des conformations cytotoxiques est essentielle afin d'élucider les caractéristiques responsables de leur cytotoxicité. L'effet surprenant de l'analogue N21Q, formant des fibres amyloïdes hautement cytotoxiques, longtemps

considérées bénignes pour les cellules, est donc un excellent candidat pour étudier ces caractéristiques.

Plusieurs études récentes ont montré des effets cytotoxiques importants pour des espèces oligomériques (Bemporad et Chiti, 2012; Benilova *et al.*, 2012 ; Fusco *et al.*, 2017). Ces espèces peuvent se former *on* - ou *off-pathway* au cours du processus de la formation des fibres amyloïdes (Lasagna-Reeves *et al.*, 2011; Stroud *et al.*, 2012), et peuvent être libérées par des fibres amyloïdes matures qui agissent comme réservoir d'espèces mal-repliées toxiques (Cremades *et al.*, 2012; Martins *et al.*, 2008). De ce fait, des efforts importants ont été déployés afin de caractériser les structures des oligomères et d'identifier des caractéristiques physicochimiques et structurales responsables de leur capacité à induire un dysfonctionnement cellulaire. Selon de nombreuses études, la taille des oligomères est considérée comme un facteur important expliquant leur forte pathogénicité ; la toxicité diminue généralement avec une augmentation de la taille des espèces peptidiques/protéiques (Ahmed *et al.*, 2010 ; Ladiwala *et al.*, 2011 ; Mannini *et al.*, 2014). L'hydrophobicité de surface joue également un rôle important pour la toxicité des oligomères, puisqu'elle facilite les interactions aberrantes avec les composantes cellulaires, particulièrement les bicouches lipidiques des membranes cellulaires (Bolognesi *et al.*, 2010; Campioni *et al.*, 2010). Une série d'études indépendantes sur les oligomères de plusieurs protéines amyloïdogéniques a montré que la toxicité des espèces corrèle non seulement à la taille et à l'exposition des résidus hydrophobes, mais aussi au degré de désordre des agrégats (*compact/molten*) (Krishnan *et al.*, 2012). En résumé, d'après ces nombreuses études récentes, la toxicité des assemblages augmente avec un poids moléculaire faible, une hydrophobicité élevée et un degré de désordre important.

Les assemblages fibrillaires de l'analogue N21Q sont hautement toxiques et induisent l'apoptose via l'activation des caspase-3. Cette observation suggère que la toxicité des assemblages pourrait être indépendante de la taille. Cette hypothèse est renforcée par

certaines études indiquant que la taille des assemblages n'est pas corrélée avec la toxicité sous-jacente et que deux assemblages de taille similaire pourraient afficher une toxicité différente (De *et al.*, 2019 ; Ladiwala *et al.*, 2012). Le polymorphisme des fibres amyloïdes est souvent observé pour les assemblages préparés *in vitro* (Fitzpatrick *et al.*, 2013; Kodali *et al.*, 2010; Meinhardt *et al.*, 2009) et chez des amyloïdes extraites de patients ou d'animal (Annamalai *et al.*, 2016 ; Annamalai *et al.*, 2017; Fitzpatrick *et al.*, 2017). Dans les préparations fibrillaires d'IAPP et de N21Q, deux types de fibres sont observés : des fibres plates en ruban et des fibres torsadées. La prévalence des fibres torsadées dans l'échantillon N21Q est plus importante que celle de l'IAPP sauvage. La morphologie torsadée a été observée dans des échantillons extraits de patients atteints d'Alzheimer et la pertinence du caractère torsadé dans les maladies amyloïdogéniques a été suggérée (Periole *et al.*, 2018 ; Qiang *et al.*, 2017 ; Turner *et al.*, 2003). En effet, la conformation mésoscopique torsadée apparaitrait lorsque les oligomères, probablement en feuillet-β, commencent à s'aligner en protofilaments, fibres non matures et plus flexibles. Ce caractère est une conséquence de la tendance à optimiser le nombre de contacts hydrophobe (Auer *et al.*, 2008; Turner *et al.*, 2003). Ce mécanisme de torsion serait modulé par la présence d'interactions supplémentaires, telles que les répulsions stériques ou la liaison hydrogène de la chaîne latérale, qui sont hautement spécifiques à la séquence. En substituant l'Asn-21 par une Gln, la formation de liaisons hydrogènes semble être favorisée et, en conséquence, la morphologie torsadée des fibres pourrait prédominer. La différence entre l'Asn et la Gln est que le groupement amide se situe en position ε- pour la Gln comparativement à γ- pour l'Asn. En outre, il a été démontré que l'interaction de liaisons hydrogène est renforcée lorsque le groupement amide est en position ε (Yamamoto *et al.*, 1999).

La conversion des monomères/oligomères en fibre amyloïdes est plus rapide pour N21Q que pour l'IAPP (Figure 3.4). De plus, les fibres de N21Q possèdent une hydrophobicité de surface plus élevée que celle des fibres d'IAPP (Figure 3.2), ce qui pourrait favoriser la formation des fibres torsadées, tel que mentionné ci-dessus. Ces

caractéristiques (phase de nucléation réduite et hydrophobicité élevée) pourraient conduire à l'exposition de domaines hydrophobes aberrants, qui pourraient être responsables de la toxicité. En considérant notre modèle de barrière énergétique de l'auto-assemblage de l'IAPP (Figure 5.3), la première association *on-pathway* des monomères d'IAPP implique la région 20-29, qui est hautement hydrophobe, afin de former des oligomères riches en feuillets-β parallèles. Ces oligomères sont connus pour être cytotoxiques (Birol *et al.*, 2018; Buchanan *et al.*, 2013 ; Wiltzius *et al.*, 2008). Cette conformation oligomérique se transforme ensuite en structure amyloïde dans laquelle le segment 20-29 forme une boucle dynamique. Les résultats obtenus pour l'analogue N21Q suggèrent que la conformation oligomérique, impliquant la région 20-29, pourrait être maintenue durant la phase d'élongation et demeurée exposée dans les fibres matures. Cette hypothèse est supportée par l'exposition au solvant du résidu Phe-23 tout au long du processus de formation des fibres amyloïdes (Figure 3.5D). De plus, la prémisse que la conformation oligomérique soit présente et exposée dans les fibres de N21Q est supportée par la reconnaissance par des anticorps de conformations (A11: anti-oligomère, 4G8/LOC : anti-fibre amyloïde). En effet, les essais de *dot blot* et d'immunomarquage aux particules d'or montrent que les fibres de N21Q sont reconnues spécifiquement par l'anticorps A11 (Figure 3.5A et figure S3.10). En outre, la co-reconnaissance des assemblages N21Q par les anti-oligomères (A11) et les anti-amyloïdes (4G8) a été révélée par un essai d'immunomarquage croisé, où les fibres sont incubées avec un mélange de ces deux anticorps conformationnels. Cohérent à cette hypothèse, nos premières analyses structurales des protofilaments du N21Q par cryo-EM ont montré le mélange de conformation *β-hairpin* et de conformation *flat β-sheet*, qui a été suggérée d'être la conformation des oligomères d'IAPP (Buchanan *et al.*, 2013) (Figure 5.4).

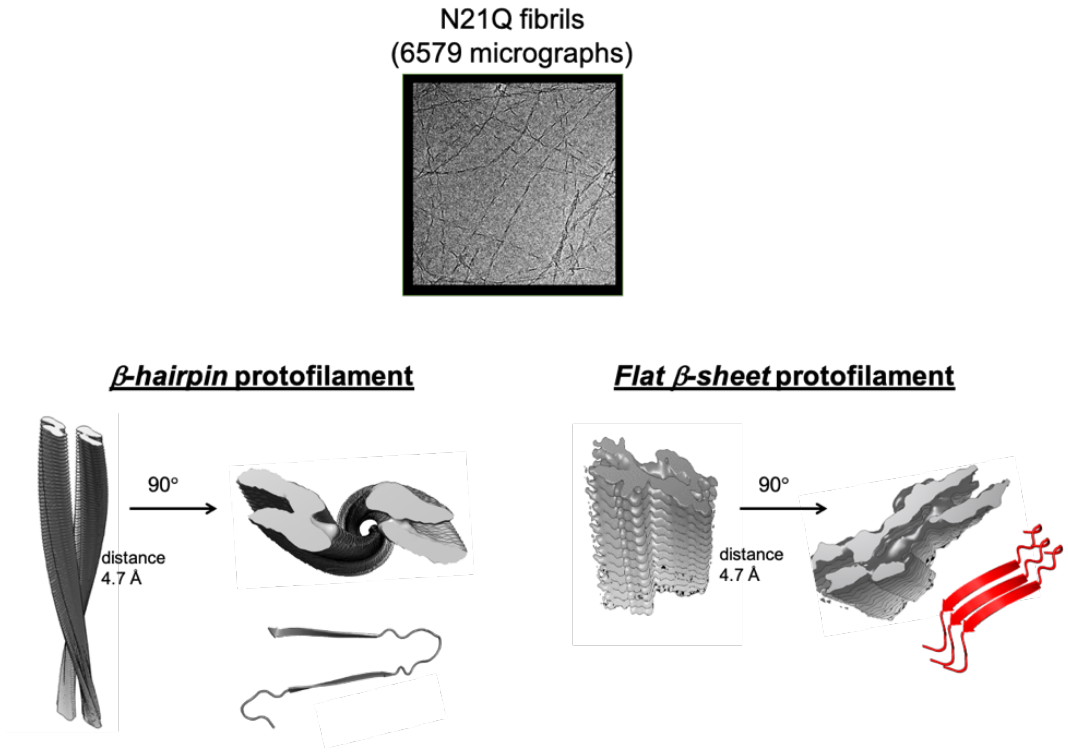


Figure 5.4 Structure des fibres du variant N21Q analysée par cryo-EM.

Dû à l'exposition du domaine oligomérique 20-29, les fibres N21Q empruntent un mécanisme de toxicité similaire à celui des oligomères d'IAPP, soit l'arrachement de la membrane plasmique (effet de détergent, ou *carpet-like*) (Raleigh *et al.*, 2017). Ces fibres N21Q dites « oligomériques » peuvent agir comme des noyaux de fibres et conduisent l'IAPP sauvage à adopter une conformation fibrillaire hautement toxique reconnue par les anti-oligomères et affichant une hydrophobicité de surface élevée (Figure 3.7). Ceci suggère qu'il existe une voie alternative d'auto-assemblage menant à des assemblages pathogéniques (Figure 5.3) et que cela peut se dès la phase de nucléation primaire (Chatani et Yamamoto, 2018).

Les dendrimères anioniques protègent les cellules face à la toxicité des oligomères en accélérant l'auto-assemblage amyloïde.

Bien que la corrélation entre les dépôts amyloïdes d'IAPP dans les îlots de Langerhans et la gravité et la progression du diabète de type II soit établie (Akter *et al.*, 2016), il n'existe actuellement aucune approche thérapeutique ciblant la cascade amyloïdogénique pancréatique. Plusieurs composés, y compris de petites molécules riches en aromatiques (Cheng *et al.*, 2013; Hassanpour *et al.*, 2014 ; Jesus *et al.*, 2014; Meng *et al.*, 2010a ; Meng *et al.*, 2010b ; Tomiyama *et al.*, 1997), des dérivés de peptides N-méthylés (Yan *et al.*, 2006), des petites molécules dérivées du N-phényle-N'-(2-éthyle) urées (Fortin *et al.*, 2016) et des glycosaminoglycanes sulfatés (GAG) (De Carufel *et al.*, 2013 ; Jha *et al.*, 2011), peuvent moduler l'auto-assemblage de l'IAPP *in vitro* et réduire la cytotoxicité associée. L'IAPP est un polypeptide nativement désordonné et doit subir une série de réarrangements conformationnels secondaires et quaternaires transitoires afin de s'auto-assembler en fibres amyloïdes. Néanmoins et tel que décrit plus haut, ces conversions structurales complexes ne sont que partiellement caractérisées. Par conséquent, la conception rationnelle de composés ciblant des conformations particulières, impliquées dans le processus de formation des fibres et responsables de la toxicité, demeure extrêmement difficile. Nos résultats ont mis en évidence certaines caractéristiques physicochimiques et conformationelles de l'auto-assemblage telles que des interactions électrostatiques importantes, une position charnière dans la formation de fibres et une conformation quaternaire cytotoxique (due à la présence de caractéristiques oligomériques). Dans ce contexte, nous avons évalué la modulation de l'auto-assemblage et de la cytotoxicité de l'IAPP par des composés chimiques dendritiques multi-fonctionnalisés. Quelques études ont rapporté que les dendrimères peuvent moduler la formation des fibres amyloïdes à partir de peptides amyloïdogéniques, incluant des dérivés du peptide Aβ, des fragments de protéines de prion et de l'IAPP, et ce, soit en accélérant ou en inhibant leur auto-assemblage (Benseny-Cases *et al.*, 2012; Gurzov *et al.*, 2016). Nous avons étudié les relations

structure-activité des dendrimères avec différentes fonctions chimiques : polyhydroxyle, polyamine, polycarboxylate et polysulfate (Figure 4.1B). Ces molécules dendritiques ont été conçues pour être hautement flexibles afin de cibler un large ensemble de conformations de l'IAPP. Nous avons identifié que le dendrimère modifié avec 4 groupes sulfate (1 d) inhibe la fibrillisation de l'IAPP (Figure 4.2 et figure 4.3) en empêchant sa conversion conformationnelle (Figure 4.4). Cela suggère que le composé 1d interagit avec l'IAPP dans sa structure nativement désordonnée, empêchant son agrégation. Les groupements sulfatés, qui sont chargés négativement, interagissent fort probablement avec les chaînes latérales chargées positivement (Lys-1, Arg-11, His-18). De ce fait, l'interaction entre le composé sulfaté 1d et l'IAPP pourrait prévenir les interactions inter-peptides qui initient l'auto-reconnaissance de l'IAPP. Toutefois, l'augmentation du nombre d'unités sulfatées (composé 2 d, 3 d et 4 d) par molécule a entraîné une accélération de la formation d'amyloïdes, très probablement par un mécanisme basé sur le recrutement des monomères et/ou oligomères, tels que suggérés pour les GAGs hautement sulfatés. En outre la surface sulfatée des GAGs interagirait avec les peptides (monomériques ou oligomériques) par le biais d'interactions électrostatiques, augmentant ainsi la concentration locale des peptides et/ou en les orientant de manière à accélérer la conversion structurale du noyau en structures amyloïdes (Bourgault *et al.*, 2011b; De Carufel *et al.*, 2013 ; Jha *et al.*, 2011).

Les essais de viabilité cellulaire ont montré que les composés polysulfatés atténuent la toxicité de l'IAPP (Figure 4.5). L'effet protecteur observé pour les dendrimères polysulfatés contre la toxicité induite par l'IAPP met en évidence que la séquestration d'espèces protéotoxiques de la cascade amyloïdogénique, soit par l'inhibition de la conversion structurale (composé 1d), soit par l'accélération de la formation de fibres (composé 2 d, 3 d et 4 d), constitue une stratégie thérapeutique pour réduire la toxicité pancréatique associée aux amyloïdes.

CONCLUSION ET PERSPECTIVES

Nonobstant les importants progrès récents concernant les structures amyloïdes, plusieurs interrogations perdurent quant au mécanisme de formation des fibres amyloïdes ainsi que des effets toxiques sous-jacents. Bien que plusieurs mécanismes de l'amyloïdogénèse aient été proposés, le débat demeure toujours vif en ce qui concerne la conformation protéotoxique des assemblages amyloïdes. La question globale de ce travail de recherche était ; est-ce que le caractère amyloïdogène de l'IAPP est influencé par : *i*) les modifications post-traductionnelles non-enzymatique, telles que la désamidation d'asparagine ; *ii*) les modifications chimiques ciblées ainsi que *iii)* les inhibiteurs/modulateurs dendritiques. Les travaux effectués consistent à étudier les déterminants moléculaires modulant l'auto-assemblage amyloïde de l'IAPP afin de mieux comprendre les caractéristiques physicochimiques et conformationnels de ce processus et des espèces quaternaires cytotoxiques.

Les principales conclusions émanant des travaux de recherche de cette thèse sont :

1. La désamidation d'asparagine module l'amyloïdogénèse de l'IAPP et tout particulièrement, lorsque celle-ci affecte les résidus Asn-14 et l'Asn-21.

2. La désamidation d'asparagine n'affecte pas la cytotoxicité de l'IAPP.

3. Le résidu Asn-21 agit comme une charnière moléculaire qui module tant l'auto-assemblage de l'IAPP que sa cytotoxicité sous-jacente.

4. L'IAPP passe d'abord par un intermédiaire impliquant la région hydrophobe ^{23}FGAIL^{27} sous forme de brin-β avant de se replier dans la conformation fibrillaire en *β-hairpin* dans laquelle cette région 20-29 se

retrouve en boucle. Ces deux conformations sont séparées par une barrière énergétique élevée qui est responsable du temps de latence observé avant la formation de fibres amyloïdes. En ciblant cette barrière énergétique, l'amyloïdogénèse et la toxicité de l'IAPP peuvent être efficacement modulées.

5. D'autres voies alternatives d'auto-assemblage émanant de la première nucléation existent et celles-ci peuvent mener à des conformations cytotoxiques.

6. Les caractéristiques des oligomères toxiques peuvent être conservées tout au long du processus d'amyloïdogénèse, menant à la formation des fibres toxiques.

7. Les caractéristiques qui modulent la cytotoxicité des assemblages fibrillaires pourraient inclure une organisation supramoléculaire torsadée et une hydrophobicité de surface élevée.

8. Les dendrimères polysulfatés modulent la formation des fibres et protègent les cellules soit en inhibant la conversion structurale des monomères en oligomères, soit en accélérant la formation de fibres amyloïdes non-toxiques. Ces deux mécanismes constituent des stratégies thérapeutiques de choix pour réduire la perte de cellules pancréatiques associée à l'auto-assemblage et à la déposition tissulaire de l'IAPP.

Dans l'ensemble, ces éléments fournissent de nouveaux indices sur la sensibilité et la spécificité des interactions inter-résidus, les déterminants moléculaires et les modulateurs, qui contribuent à l'amyloïdogénèse et la cytotoxicité des assemblages

d'IAPP. Nos travaux se dirigent vers de nouvelles études de relation structure-toxicité avec le nouvel outil, les fibres *oligomer-like* N21Q.

Pour des projets futurs, l'effet cytotoxique des fibres N21Q est très intéressant et nécessiterait des études plus approfondies. Nous avons proposé que la conformation oligomérique pourrait être conservée dans la suprastructure fibrillaire. De plus, cette conformation oligomérique impliquerait une exposition élevée de la région 20-29 sous forme de brins-β parallèles. Conséquemment, les fibres toxiques N21Q devraient avoir un mélange de feuillets-β parallèles et antiparallèles. De plus, une étude récente du groupe de recherche de Matsuzaki a montré que les fibres d'Aβ, qui possèdent un mélange de feuillets-β parallèles et antiparallèles, sont cytotoxiques (Okada *et al.*, 2019). Ainsi, des études sur la structure atomistique des fibres d'IAPP et de N21Q par cryo-EM en parallèle avec la RMN à l'état solide permettraient d'observer en détail le niveau d'organisation moléculaire à l'intérieur des fibres. D'autre part, les modèles animaux offrent la possibilité de valider les hypothèses générées à partir des travaux effectués *in vitro*. Le caractère toxique de l'analogue N21Q se conservera-t-il *in vivo* ? La surexpression pancréatique de l'analogue N21Q chez des souris transgéniques suivie de l'évaluation des effets induits par cet analogue seront utiles pour répondre à cette question. D'après les résultats de cette thèse, l'effet protecteur observé pour les dendrimères polysulfatés contre la toxicité induite par l'IAPP se fait par l'empêchement de la conversion structurale et par l'accélération de la formation des fibres. Alors, de la même façon, est-ce que ces dendrimères polysulfatés protègeront les cellules pancréatiques de la toxicité induite par l'analogue N21Q ? Pour répondre à ces questions, il est nécessaire de réaliser des études biophysiques et biologiques approfondies. Les études futures offriront sans doute un développement dans la compréhension détaillée de la nature pathologique des assemblages amyloïdes. De plus, ces travaux permettront d'acquérir des connaissances solides qui seront d'une grande valeur pour la conception rationnelle de nouvelles stratégies thérapeutiques ciblant le diabète de type 2.

BIBLIOGRAPHIE

Abedini A, Meng F et Raleigh DP (2007) A single-point mutation converts the highly amyloidogenic human islet amyloid polypeptide into a potent fibrillization inhibitor. *J Am Chem Soc 129*: 11300-11311.

Abedini A, Plesner A, Cao P, Ridgway Z, Zhang J, Tu LH, Middleton CT, Chao B, Sartori DJ, Meng F, et al. (2016) Time-resolved studies define the nature of toxic IAPP intermediates, providing insight for anti-amyloidosis therapeutics. *Elife 5*: 12977.

Abedini A et Raleigh DP (2005) Incorporation of pseudoproline derivatives allows the facile synthesis of human IAPP, a highly amyloidogenic and aggregation-prone polypeptide. *Org Lett 7*: 693-696.

Abedini A et Raleigh DP (2009) A critical assessment of the role of helical intermediates in amyloid formation by natively unfolded proteins and polypeptides. *PEDS 22*: 453-459.

Abedini A et Schmidt AM (2013) Mechanisms of islet amyloidosis toxicity in type 2 diabetes. *FEBS Lett 587*: 1119-1127.

Abedini A, Singh G et Raleigh DP (2006) Recovery and purification of highly aggregation-prone disulfide-containing peptides: application to islet amyloid polypeptide. *Anal Biochem 351*: 181-186.

Adams D, Ando Y, Beirao JM, Coelho T, Gertz MA, Gillmore JD, Hawkins PN, Lousada I, Suhr OB et Merlini G (2020) Expert consensus recommendations to improve diagnosis of ATTR amyloidosis with polyneuropathy. *J Neurol.* DOI: 10.1007/s00415-00019-09688-00410.

Adams D, Koike H, Slama M et Coelho T (2019) Hereditary transthyretin amyloidosis: a model of medical progress for a fatal disease. *Nat Rev Neuro 15*: 387-404.

Adav SS, Gallart-Palau X, Tan KH, Lim SK, Tam JP et Sze SK (2016) Dementia-linked amyloidosis is associated with brain protein deamidation as revealed by proteomic profiling of human brain tissues. *Mol Brain 9*: 20.

Aerts J, Kuo CL, Lelieveld LT, Boer DEC, van der Lienden MJC, Overkleeft HS et Artola M (2019) Glycosphingolipids and lysosomal storage disorders as illustrated by gaucher disease. *Curr Opin Chem Biol 53*: 204-215.

Aguzzi A et Lakkaraju AKK (2016) Cell Biology of Prions and Prionoids: A Status Report. *Trends Cell Biol 26*: 40-51.

Ahmed M, Davis J, Aucoin D, Sato T, Ahuja S, Aimoto S, Elliott JI, Van Nostrand WE et Smith SO (2010) Structural conversion of neurotoxic amyloid-beta(1-42) oligomers to fibrils. *Nat Struct Mol Biol 17*: 561-567.

Aisen PS, Gauthier S, Vellas B, Briand R, Saumier D, Laurin J et Garceau D (2007) Alzhemed: a potential treatment for Alzheimer's disease. *Curr Alzheimer Res 4*: 473-478.

Akkermans C, Venema P, van der Goot AJ, Gruppen H, Bakx EJ, Boom RM et van der Linden E (2008) Peptides are building blocks of heat-induced fibrillar protein aggregates of beta-lactoglobulin formed at pH 2. *Biomacromolecules 9*: 1474-1479.

Akter R, Cao P, Noor H, Ridgway Z, Tu L-H, Wang H, Wong AG, Zhang X, Abedini A, Schmidt AM, et al. (2016) Islet Amyloid Polypeptide: Structure, Function, and Pathophysiology. *Journal of Diabetes Research 2016*: 2798269.

Al-Shehah A, Al-Rajhi A et Alkatan H (2010) Amyloid corneal deposition in corneal buttons of congenital hereditary endothelial dystrophy (CHED) - A clinical and histopathological case series. *Saudi journal of ophthalmology 24*: 111-118.

Alexandrescu AT (2005) Amyloid accomplices and enforcers. *Protein Sci 14*: 1-12.

Aliyan A, Cook NP et Marti AA (2019) Interrogating Amyloid Aggregates using Fluorescent Probes. *Chem Rev 119*: 11819-11856.

Almstedt K, Nyström S, Nilsson KPR et Hammarström P (2009) Amyloid fibrils of human prion protein are spun and woven from morphologically disordered aggregates. *Prion 3*: 224-235.

Alvarez-Arellano L, Pedraza-Escalona M, Blanco-Ayala T, Camacho-Concha N, Cortes-Mendoza J, Perez-Martinez L et Pedraza-Alva G (2018) Autophagy impairment by caspase-1-dependent inflammation mediates memory loss in response to beta-Amyloid peptide accumulation. *J Neurosci Res 96*: 234-246.

American Diabetes A (2015) Standards of medical care in diabetes-2015 abridged for primary care providers. *Clinical diabetes : a publication of the American Diabetes Association 33*: 97-111.

Andley UP (2009) Effects of alpha-crystallin on lens cell function and cataract pathology. *Curr Mol Med 9*: 887-892.

Annamalai K, Liberta F, Vielberg MT, Close W, Lilie H, Guhrs KH, Schierhorn A, Koehler R, Schmidt A, Haupt C, et al. (2017) Common Fibril Structures Imply Systemically Conserved Protein Misfolding Pathways In Vivo. *Angew Chem Int Ed Engl 56*: 7510-7514.

Apostolidou M, Jayasinghe SA et Langen R (2008) Structure of alpha-helical membrane-bound human islet amyloid polypeptide and its implications for membrane-mediated misfolding. *The Journal of biological chemistry 283*: 17205-17210.

Armstrong AH, Chen J, McKoy AF et Hecht MH (2011) Mutations that replace aromatic side chains promote aggregation of the Alzheimer's Abeta peptide. *Biochemistry 50*: 4058-4067.

Arosio P, Knowles TP et Linse S (2015) On the lag phase in amyloid fibril formation. *Phys Chem 17*: 7606-7618.

Ashburn TT et Lansbury PT (1993) Interspecies sequence variations affect the kinetics and thermodynamics of amyloid formation: peptide models of pancreatic amyloid. *JACS 115*: 11012-11013.

Aspinwall CA, Brooks SA, Kennedy RT et Lakey JR (1997) Effects of intravesicular H+ and extracellular H+ and Zn2+ on insulin secretion in pancreatic beta cells. *J Biol Chem 272*: 31308-31314.

Asthana S, Mallick B, Alexandrescu AT et Jha S (2018) IAPP in type II diabetes: Basic research on structure, molecular interactions, and disease mechanisms suggests potential intervention strategies. *BBA 1860*: 1765-1782.

Aswad DW, Paranandi MV et Schurter BT (2000) Isoaspartate in peptides and proteins: formation, significance, and analysis. *J Pharm Biomed Anal 21*: 1129-1136.

Auer S, Meersman F, Dobson CM et Vendruscolo M (2008) A generic mechanism of emergence of amyloid protofilaments from disordered oligomeric aggregates. *PLoS Computational Biology 4*: e1000222.

Augner K, Eichler J, Utz W et Pischetsrieder M (2014) Influence of nonenzymatic posttranslational modifications on constitution, oligomerization and receptor binding of S100A12. *PLoS ONE 9*: e113418.

Azriel R et Gazit E (2001) Analysis of the minimal amyloid-forming fragment of the islet amyloid polypeptide. An experimental support for the key role of the phenylalanine residue in amyloid formation. *J Biol Chem 276*: 34156-34161.

Bakou M, Hille K, Kracklauer M, Spanopoulou A, Frost CV, Malideli E, Yan LM, Caporale A, Zacharias M et Kapurniotu A (2017) Key aromatic/hydrophobic amino acids controlling a cross-amyloid peptide interaction versus amyloid self-assembly. *J Biol Chem 292*: 14587-14602.

Barnhart MM et Chapman MR (2006) Curli biogenesis and function. *Annu Rev Microbiol 60*: 131-147.

Bauerlein FJB, Saha I, Mishra A, Kalemanov M, Martinez-Sanchez A, Klein R, Dudanova I, Hipp MS, Hartl FU, Baumeister W, et al. (2017) In situ architecture and cellular interactions of polyQ inclusions. *Cell 171*: 179-187.e110.

Baxa U, Cheng N, Winkler DC, Chiu TK, Davies DR, Sharma D, Inouye H, Kirschner DA, Wickner RB et Steven AC (2005) Filaments of the Ure2p prion protein have a cross-beta core structure. *J Struct Biol 150*: 170-179.

Bedrood S, Li Y, Isas JM, Hegde BG, Baxa U, Haworth IS et Langen R (2012) Fibril structure of human islet amyloid polypeptide. *J Biol Chem 287*: 5235-5241.

Bell ET (1959) Hyalinization of the islets of Langerhans in nondiabetic individuals. *The American Journal of Pathology 35*: 801-805.

Bemporad F et Chiti F (2012) Protein misfolded oligomers: experimental approaches, mechanism of formation, and structure-toxicity relationships. *Chem Biol 19*: 315-327.

Benilova I, Karran E et De Strooper B (2012) The toxic Abeta oligomer and Alzheimer's disease: an emperor in need of clothes. *Nat Neurosci 15*: 349-357.

Benseny-Cases N, Klementieva O et Cladera J (2012) Dendrimers antiamyloidogenic potential in neurodegenerative diseases. *New Journal of Chemistry 36*: 211-216.

Benson MD, Buxbaum JN, Eisenberg DS, Merlini G, Saraiva MJM, Sekijima Y, Sipe JD et Westermark P (2018) Amyloid nomenclature 2018: recommendations by the International Society of Amyloidosis (ISA) nomenclature committee. *Amyloid 25*: 215-219.

Benson MD, Liepnieks JJ, Yazaki M, Yamashita T, Hamidi Asl K, Guenther B et Kluve-Beckerman B (2001) A new human hereditary amyloidosis: the result of a stop-codon mutation in the apolipoprotein AII gene. *Genomics 72*: 272-277.

Bergman P, Roan NR, Römling U, Bevins CL et Münch J (2016) Amyloid formation: functional friend or fearful foe? *Journal of Internal Medicine 280*: 139-152.

Betsholtz C, Christmansson L, Engstrom U, Rorsman F, Svensson V, Johnson KH et Westermark P (1989) Sequence divergence in a specific region of islet amyloid polypeptide (IAPP) explains differences in islet amyloid formation between species. *FEBS Lett 251*: 261-264.

Bhattacharyya AM, Thakur AK et Wetzel R (2005) polyglutamine aggregation nucleation: thermodynamics of a highly unfavorable protein folding reaction. *Proc Natl Acad Sci U S A 102*: 15400-15405.

Bieschke J, Russ J, Friedrich RP, Ehrnhoefer DE, Wobst H, Neugebauer K et Wanker EE (2010) EGCG remodels mature alpha-synuclein and amyloid-beta fibrils and reduces cellular toxicity. *Proc Natl Acad Sci U S A 107*: 7710-7715.

Birol M, Kumar S, Rhoades E et Miranker AD (2018) Conformational switching within dynamic oligomers underpins toxic gain-of-function by diabetes-associated amyloid. *Nat Commun 9*: 1312.

Blanco LP, Evans ML, Smith DR, Badtke MP et Chapman MR (2012) Diversity, biogenesis and function of microbial amyloids. *Trends Microbiol 20*: 66-73.

Bolarinwa O, Li C, Khadka N, Li Q, Wang Y, Pan J et Cai J (2020) γ-AApeptides–based small molecule ligands that disaggregate human Islet Amyloid Polypeptide. *Sci Rep 10*: 95.

Bolognesi B, Kumita JR, Barros TP, Esbjorner EK, Luheshi LM, Crowther DC, Wilson MR, Dobson CM, Favrin G et Yerbury JJ (2010) ANS Binding Reveals Common Features of Cytotoxic Amyloid Species. *ACS Chem Biol 5*: 735-740.

Bourgault S, Choi S, Buxbaum JN, Kelly JW, Price JL et Reixach N (2011a) Mechanisms of transthyretin cardiomyocyte toxicity inhibition by resveratrol analogs. *Biochem Biophys Res Commun 410*: 707-713.

Bourgault S, Solomon JP, Reixach N et Kelly JW (2011b) Sulfated glycosaminoglycans accelerate transthyretin amyloidogenesis by quaternary structural conversion. *Biochemistry 50*: 1001-1015.

Bower RL et Hay DL (2016) Amylin structure-function relationships and receptor pharmacology: implications for amylin mimetic drug development. *Br J Pharmacol 173*: 1883-1898.

Bram Y, Frydman-Marom A, Yanai I, Gilead S, Shaltiel-Karyo R, Amdursky N et Gazit E (2014) Apoptosis induced by islet amyloid polypeptide soluble oligomers is neutralized by diabetes-associated specific antibodies. *Sci Rep 4*: 4267.

Brender JR, Durr UH, Heyl D, Budarapu MB et Ramamoorthy A (2007) Membrane fragmentation by an amyloidogenic fragment of human Islet Amyloid Polypeptide detected by solid-state NMR spectroscopy of membrane nanotubes. *BBA 1768*: 2026-2029.

Brender JR, Hartman K, Nanga RPR, Popovych N, de la Salud Bea R, Vivekanandan S, Marsh ENG et Ramamoorthy A (2010) Role of zinc in human Islet Amyloid

Polypeptide aggregation. *Journal of the American Chemical Society 132*: 8973-8983.

Brender JR, Krishnamoorthy J, Messina GM, Deb A, Vivekanandan S, La Rosa C, Penner-Hahn JE et Ramamoorthy A (2013) Zinc stabilization of prefibrillar oligomers of human islet amyloid polypeptide. *Chem Commun (Camb) 49*: 3339-3341.

Brender JR, Salamekh S et Ramamoorthy A (2012) Membrane disruption and early events in the aggregation of the diabetes related peptide IAPP from a molecular perspective. *Accounts of chemical research 45*: 454-462.

Brennan TV et Clarke S (1995) Effect of adjacent histidine and cysteine residues on the spontaneous degradation of asparaginyl- and aspartyl-containing peptides. *Int J Pept Protein Res 45*: 547-553.

Brettschneider J, Del Tredici K, Lee VM et Trojanowski JQ (2015) Spreading of pathology in neurodegenerative diseases: a focus on human studies. *Nat Rev Neurosci 16*: 109-120.

Bucciantini M, Calloni G, Chiti F, Formigli L, Nosi D, Dobson CM et Stefani M (2004) Prefibrillar amyloid protein aggregates share common features of cytotoxicity. *J Biol Chem 279*: 31374-31382.

Bucciantini M, Giannoni E, Chiti F, Baroni F, Formigli L, Zurdo J, Taddei N, Ramponi G, Dobson CM et Stefani M (2002) Inherent toxicity of aggregates implies a common mechanism for protein misfolding diseases. *Nature 416*: 507-511.

Buchanan LE, Dunkelberger EB, Tran HQ, Cheng P-N, Chiu C-C, Cao P, Raleigh DP, de Pablo JJ, Nowick JS et Zanni MT (2013) Mechanism of IAPP amyloid fibril formation involves an intermediate with a transient β-sheet. *Proceedings of the National Academy of Sciences 110*: 19285-19290.

Bugiani O, Giaccone G, Rossi G, Mangieri M, Capobianco R, Morbin M, Mazzoleni G, Cupidi C, Marcon G, Giovagnoli A, et al. (2010) Hereditary cerebral hemorrhage with amyloidosis associated with the E693K mutation of APP. *Arch Neurol 67*: 987-995.

Bulawa CE, Connelly S, Devit M, Wang L, Weigel C, Fleming JA, Packman J, Powers ET, Wiseman RL, Foss TR, et al. (2012) Tafamidis, a potent and selective transthyretin kinetic stabilizer that inhibits the amyloid cascade. *Proc Natl Acad Sci U S A 109*: 9629-9634.

Campioni S, Mannini B, Zampagni M, Pensalfini A, Parrini C, Evangelisti E, Relini A, Stefani M, Dobson CM, Cecchi C, et al. (2010) A causative link between the structure of aberrant protein oligomers and their toxicity. *Nat Chem Biol 6*: 140-147.

Cao P, Marek P, Noor H, Patsalo V, Tu LH, Wang H, Abedini A et Raleigh DP (2013) Islet amyloid: from fundamental biophysics to mechanisms of cytotoxicity. *FEBS Lett 587*: 1106-1118.

Cao P et Raleigh DP (2012) Analysis of the inhibition and remodeling of islet amyloid polypeptide amyloid fibers by flavanols. *Biochemistry 51*: 2670-2683.

Cao P, Tu L-H, Abedini A, Levsh O, Akter R, Patsalo V, Schmidt AM et Raleigh DP (2012) Sensitivity of amyloid formation by human Islet Amyloid Polypeptide to mutations at residue-20. *J Mol Biol 421*: 282-295.

Cao Q, Boyer DR, Sawaya MR, Ge P et Eisenberg DS (2020) Cryo-EM structure and inhibitor design of human IAPP (amylin) fibrils. *Nat Struct Mol Biol 27*: 653-659.

Carrell RW et Lomas DA (1997) Conformational disease. *Lancet 350*: 134-138.

Casalone C et Hope J (2018) Atypical and classic bovine spongiform encephalopathy. *Handb Clin Neurol 153*: 121-134.

Casas S, Gomis R, Gribble FM, Altirriba J, Knuutila S et Novials A (2007) Impairment of the ubiquitin-proteasome pathway is a downstream endoplasmic reticulum stress response induced by extracellular human Islet Amyloid Polypeptide and contributes to pancreatic β-cell apoptosis. *Diabetes 56*: 2284-2294.

Casas S, Novials A, Reimann F, Gomis R et Gribble FM (2008) Calcium elevation in mouse pancreatic beta cells evoked by extracellular human Islet Amyloid Polypeptide involves activation of the mechanosensitive ion channel TRPV4. *Diabetologia 51*: 2252-2262.

Castellano LM et Shorter J (2012) The surprising role of amyloid fibrils in HIV infection. *Biology 1*: 58-80.

Cerf E, Sarroukh R, Tamamizu-Kato S, Breydo L, Derclaye S, Dufrene YF, Narayanaswami V, Goormaghtigh E, Ruysschaert JM et Raussens V (2009) Antiparallel beta-sheet: a signature structure of the oligomeric amyloid beta-peptide. *Biochem J 421*: 415-423.

Chan B et Adam DN (2018) A review of Fabry disease. *Skin Therapy Lett 23*: 4-6.

Chan GK, Witkowski A, Gantz DL, Zhang TO, Zanni MT, Jayaraman S et Cavigiolio G (2015) Myeloperoxidase-mediated methionine oxidation promotes an amyloidogenic outcome for apolipoprotein A-I. *J Biol Chem 290*: 10958-10971.

Chan JC, Oyler NA, Yau WM et Tycko R (2005) Parallel beta-sheets and polar zippers in amyloid fibrils formed by residues 10-39 of the yeast prion protein Ure2p. *Biochemistry 44*: 10669-10680.

Chapman MR, Robinson LS, Pinkner JS, Roth R, Heuser J, Hammar M, Normark S et Hultgren SJ (2002) Role of Escherichia coli curli operons in directing amyloid fiber formation. *Science 295*: 851-855.

Chapter MC, White CM, DeRidder A, Chadwick W, Martin B et Maudsley S (2010) Chemical modification of class II G protein-coupled receptor ligands: frontiers in the development of peptide analogs as neuroendocrine pharmacological therapies. *Pharmacol Ther 125*: 39-54.

Charidimou A, Boulouis G, Gurol ME, Ayata C, Bacskai BJ, Frosch MP, Viswanathan A et Greenberg SM (2017) Emerging concepts in sporadic cerebral amyloid angiopathy. *Brain 140*: 1829-1850.

Chatani E et Yamamoto N (2018) Recent progress on understanding the mechanisms of amyloid nucleation. *Biophysical reviews 10*: 527-534.

Chaudhuri TK et Paul S (2006) Protein-misfolding diseases and chaperone-based therapeutic approaches. *FEBS J 273*: 1331-1349.

Cheignon C, Tomas M, Bonnefont-Rousselot D, Faller P, Hureau C et Collin F (2018) Oxidative stress and the amyloid beta peptide in Alzheimer's disease. *Redox biology 14*: 450-464.

Chen L, Magliano DJ et Zimmet PZ (2011) The worldwide epidemiology of type 2 diabetes mellitus--present and future perspectives. *Nat Rev Endocrinol 8*: 228-236.

Chen SW, Drakulic S, Deas E, Ouberai M, Aprile FA, Arranz R, Ness S, Roodveldt C, Guilliams T, De-Genst EJ, et al. (2015) Structural characterization of toxic oligomers that are kinetically trapped during alpha-synuclein fibril formation. *Proc Natl Acad Sci U S A 112*: E1994-2003.

Chen Y-C, Taylor AJ et Verchere CB (2018) Islet prohormone processing in health and disease. *Diabetes, Obesity and Metabolism 20*: 64-76.

Chen YR et Glabe CG (2006) Distinct early folding and aggregation properties of Alzheimer amyloid-beta peptides Abeta40 and Abeta42: stable trimer or tetramer formation by Abeta42. *J Biol Chem 281*: 24414-24422.

Cheng B, Gong H, Li X, Sun Y, Chen H, Zhang X, Wu Q, Zheng L et Huang K (2013) Salvianolic acid B inhibits the amyloid formation of human islet amyloid polypeptide and protects pancreatic beta-cells against cytotoxicity. *Proteins 81*: 613-621.

Cheng B, Gong H, Li X, Sun Y, Zhang X, Chen H, Liu X, Zheng L et Huang K (2012) Silibinin inhibits the toxic aggregation of human islet amyloid polypeptide. *Biochem Biophys Res Commun 419*: 495-499.

Cheng B, Liu X, Gong H, Huang L, Chen H, Zhang X, Li C, Yang M, Ma B, Jiao L, et al. (2011) Coffee components inhibit amyloid formation of human islet amyloid polypeptide in vitro: possible link between coffee consumption and diabetes mellitus. *J Agric Food Chem 59*: 13147-13155.

Chimon S, Shaibat MA, Jones CR, Calero DC, Aizezi B et Ishii Y (2007) Evidence of fibril-like β-sheet structures in a neurotoxic amyloid intermediate of Alzheimer's β-amyloid. *Nature Structural & Molecular Biology 14*: 1157-1164.

Chiti F, Calamai M, Taddei N, Stefani M, Ramponi G et Dobson CM (2002) Studies of the aggregation of mutant proteins in vitro provide insights into the genetics of amyloid diseases. *Proc Natl Acad Sci U S A 99 Suppl 4*: 16419-16426.

Chiti F et Dobson CM (2006) Protein misfolding, functional amyloid, and human disease. *Annu Rev Biochem 75*: 333-366.

Chiti F et Dobson CM (2009) Amyloid formation by globular proteins under native conditions. *Nat Chem Biol 5*: 15-22.

Chiti F et Dobson CM (2017) Protein Misfolding, Amyloid Formation, and Human Disease: A Summary of Progress Over the Last Decade. *Annu Rev Biochem 86*: 27-68.

Cho YM, Kim M, Park KS, Kim SY et Lee HK (2003) S20G mutation of the amylin gene is associated with a lower body mass index in Korean type 2 diabetic patients. *Diabetes Res Clin Pract 60*: 125-129.

Christ-Crain M, Bichet DG, Fenske WK, Goldman MB, Rittig S, Verbalis JG et Verkman AS (2019) Diabetes insipidus. *Nat Rev Dis Primers 5*: 54.

Christopoulos G, Perry KJ, Morfis M, Tilakaratne N, Gao Y, Fraser NJ, Main MJ, Foord SM et Sexton PM (1999) Multiple amylin receptors arise from receptor activity-modifying protein interaction with the calcitonin receptor gene product. *Mol Pharmacol 56*: 235-242.

Chuang E, Hori AM, Hesketh CD et Shorter J (2018) Amyloid assembly and disassembly. *J Cell Sci 131*: 1-18.

Claessen D, Rink R, de Jong W, Siebring J, de Vreugd P, Boersma FG, Dijkhuizen L et Wosten HA (2003) A novel class of secreted hydrophobic proteins is involved in aerial hyphae formation in Streptomyces coelicolor by forming amyloid-like fibrils. *Genes Dev 17*: 1714-1726.

Cloe AL, Orgel JP, Sachleben JR, Tycko R et Meredith SC (2011) The Japanese mutant Abeta (DeltaE22-Abeta(1-39)) forms fibrils instantaneously, with low-thioflavin T fluorescence: seeding of wild-type Abeta(1-40) into atypical fibrils by DeltaE22-Abeta(1-39). *Biochemistry 50*: 2026-2039.

Coelho T, Merlini G, Bulawa CE, Fleming JA, Judge DP, Kelly JW, Maurer MS, Plante-Bordeneuve V, Labaudiniere R, Mundayat R, et al. (2016) Mechanism of Action and Clinical Application of Tafamidis in Hereditary Transthyretin Amyloidosis. *Neurol Ther 5*: 1-25.

Cohen E, Bieschke J, Perciavalle RM, Kelly JW et Dillin A (2006) Opposing activities protect against age-onset proteotoxicity. *Science 313*: 1604-1610.

Cohen FE et Kelly JW (2003) Therapeutic approaches to protein-misfolding diseases. *Nature 426*: 905-909.

Cohen SI, Linse S, Luheshi LM, Hellstrand E, White DA, Rajah L, Otzen DE, Vendruscolo M, Dobson CM et Knowles TP (2013) Proliferation of amyloid-beta42 aggregates occurs through a secondary nucleation mechanism. *Proc Natl Acad Sci U S A 110*: 9758-9763.

Cooper GJ, Willis AC, Clark A, Turner RC, Sim RB et Reid KB (1987) Purification and characterization of a peptide from amyloid-rich pancreases of type 2 diabetic patients. *Proc Natl Acad Sci U S A 84*: 8628-8632.

Cooper ME, McNally PG, Phillips PA et Johnston CI (1995) Amylin Stimulates Plasma Renin Concentration in Humans. *Hypertension 26*: 460-464.

Courtade JA, Wang EY, Yen P, Dai DL, Soukhatcheva G, Orban PC et Verchere CB (2017) Loss of prohormone convertase 2 promotes beta cell dysfunction in a rodent transplant model expressing human pro-islet amyloid polypeptide. *Diabetologia 60*: 453-463.

Cremades N, Cohen SI, Deas E, Abramov AY, Chen AY, Orte A, Sandal M, Clarke RW, Dunne P, Aprile FA, et al. (2012) Direct observation of the interconversion of normal and toxic forms of alpha-synuclein. *Cell 149*: 1048-1059.

De Carufel CA, Nguyen PT, Sahnouni S et Bourgault S (2013) New insights into the roles of sulfated glycosaminoglycans in islet amyloid polypeptide amyloidogenesis and cytotoxicity. *Biopolymers 100*: 645-655.

De Carufel CA, Quittot N, Nguyen PT et Bourgault S (2015) Delineating the Role of Helical Intermediates in Natively Unfolded Polypeptide Amyloid Assembly and Cytotoxicity. *Angew Chem Int Ed Engl 54*: 14383-14387.

de Rosa M, Bemporad F, Pellegrino S, Chiti F, Bolognesi M et Ricagno S (2014) Edge strand engineering prevents native-like aggregation in Sulfolobus solfataricus acylphosphatase. *FEBS J 281*: 4072-4084.

De S, Wirthensohn DC, Flagmeier P, Hughes C, Aprile FA, Ruggeri FS, Whiten DR, Emin D, Xia Z, Varela JA, et al. (2019) Different soluble aggregates of Abeta42 can give rise to cellular toxicity through different mechanisms. *Nat Commun 10*: 1541.

DeFronzo RA (2004) Pathogenesis of type 2 diabetes mellitus. *Med Clin North Am 88*: 787-835, ix.

DePas WH et Chapman MR (2012) Microbial manipulation of the amyloid fold. *Res Microbiol 163*: 592-606.

DeWitt DA, Silver J, Canning DR et Perry G (1993) Chondroitin sulfate proteoglycans are associated with the lesions of Alzheimer's disease. *Exp Neurol 121*: 149-152.

Domanov YA et Kinnunen PK (2008) Islet amyloid polypeptide forms rigid lipid-protein amyloid fibrils on supported phospholipid bilayers. *J Mol Biol 376*: 42-54.

Doran TM, Kamens AJ, Byrnes NK et Nilsson BL (2012) Role of amino acid hydrophobicity, aromaticity, and molecular volume on IAPP(20-29) amyloid self-assembly. *Proteins 80*: 1053-1065.

Drisaldi B, Colnaghi L, Fioriti L, Rao N, Myers C, Snyder AM, Metzger DJ, Tarasoff J, Konstantinov E, Fraser PE, et al. (2015) SUMOylation Is an Inhibitory Constraint that Regulates the Prion-like Aggregation and Activity of CPEB3. *Cell Rep 11*: 1694-1702.

Dunkelberger EB, Buchanan LE, Marek P, Cao P, Raleigh DP et Zanni MT (2012) Deamidation accelerates amyloid formation and alters amylin fiber structure. *JACS 134*: 12658-12667.

Dupuis NF, Wu C, Shea JE et Bowers MT (2009) Human islet amyloid polypeptide monomers form ordered beta-hairpins: a possible direct amyloidogenic precursor. *JACS 131*: 18283-18292.

Dupuis NF, Wu C, Shea JE et Bowers MT (2011) The amyloid formation mechanism in human IAPP: dimers have beta-strand monomer-monomer interfaces. *JACS 133*: 7240-7243.

Dzwolak W et Pecul M (2005) Chiral bias of amyloid fibrils revealed by the twisted conformation of Thioflavin T: an induced circular dichroism/DFT study. *FEBS Lett 579*: 6601-6603.

Eakin CM, Attenello FJ, Morgan CJ et Miranker AD (2004) Oligomeric assembly of native-like precursors precedes amyloid formation by beta-2 microglobulin. *Biochemistry 43*: 7808-7815.

Eakin CM, Berman AJ et Miranker AD (2006) A native to amyloidogenic transition regulated by a backbone trigger. *Nat Struct Mol Biol 13*: 202-208.

Eanes ED et Glenner GG (1968) X-ray diffraction studies on amyloid filaments. *J Histochem Cytochem 16*: 673-677.

Easterhoff D, Ontiveros F, Brooks LR, Kim Y, Ross B, Silva JN, Olsen JS, Feng C, Hardy DJ, Dunman PM, et al. (2013) Semen-derived enhancer of viral infection (SEVI) binds bacteria, enhances bacterial phagocytosis by macrophages, and can protect against vaginal infection by a sexually transmitted bacterial pathogen. *Antimicrobial Agents and Chemotherapy 57*: 2443.

Ehrlich JC et Ratner IM (1961) Amyloidosis of the islets of Langerhans. A restudy of islet hyalin in diabetic and non-diabetic individuals. *The American Journal of Pathology 38*: 49-59.

Ehrnhoefer DE, Bieschke J, Boeddrich A, Herbst M, Masino L, Lurz R, Engemann S, Pastore A et Wanker EE (2008) EGCG redirects amyloidogenic polypeptides into unstructured, off-pathway oligomers. *Nat Struct Mol Biol 15*: 558-566.

Eisenberg D et Jucker M (2012) The amyloid state of proteins in human diseases. *Cell 148*: 1188-1203.

Eizirik DL, Cardozo AK et Cnop M (2008) The role for endoplasmic reticulum stress in diabetes mellitus. *Endocr Rev 29*: 42-61.

Evangelisti E, Cascella R, Becatti M, Marrazza G, Dobson CM, Chiti F, Stefani M et Cecchi C (2016) Binding affinity of amyloid oligomers to cellular membranes is a generic indicator of cellular dysfunction in protein misfolding diseases. *Sci Rep 6*: 32721.

Ewald M, Henry S, Lambert E, Feuillie C, Bobo C, Cullin C, Lecomte S et Molinari M (2019) High speed atomic force microscopy to investigate the interactions between toxic Abeta1-42 peptides and model membranes in real time: impact of the membrane composition. *Nanoscale 11*: 7229-7238.

Família C, Dennison SR, Quintas A et Phoenix DA (2015) Prediction of peptide and protein propensity for amyloid formation. *PloS ONE 10*: e0134679-e0134679.

Fändrich M, Nyström S, Nilsson KPR, Böckmann A, LeVine H, 3rd et Hammarström P (2018) Amyloid fibril polymorphism: a challenge for molecular imaging and therapy. *Journal of internal medicine 283*: 218-237.

Fitzpatrick AW, Debelouchina GT, Bayro MJ, Clare DK, Caporini MA, Bajaj VS, Jaroniec CP, Wang L, Ladizhansky V, Muller SA, et al. (2013) Atomic structure and hierarchical assembly of a cross-beta amyloid fibril. *Proc Natl Acad Sci U S A 110*: 5468-5473.

Flagmeier P, Meisl G, Vendruscolo M, Knowles TP, Dobson CM, Buell AK et Galvagnion C (2016) Mutations associated with familial Parkinson's disease alter the initiation and amplification steps of alpha-synuclein aggregation. *Proc Natl Acad Sci U S A 113*: 10328-10333.

Flaugh SL, Mills IA et King J (2006) Glutamine deamidation destabilizes human gammaD-crystallin and lowers the kinetic barrier to unfolding. *J Biol Chem 281*: 30782-30793.

Fonseca SG, Burcin M, Gromada J et Urano F (2009) Endoplasmic reticulum stress in beta-cells and development of diabetes. *Curr Opin Pharmacol 9*: 763-770.

Fortin JS et Benoit-Biancamano MO (2015) Wildlife sequences of islet amyloid polypeptide (IAPP) identify critical species variants for fibrillization. *Amyloid 22*: 194-202.

Fortin JS, Benoit-Biancamano MO et R CG (2016) Discovery of ethyl urea derivatives as inhibitors of islet amyloid polypeptide fibrillization and cytotoxicity. *Can J Physiol Pharmacol 94*: 341-346.

Foster MC, Leapman RD, Li MX et Atwater I (1993) Elemental composition of secretory granules in pancreatic islets of Langerhans. *Biophys J 64*: 525-532.

Fox A, Snollaerts T, Casanova CE, Calciano A, Nogaj LA et Moffet DA (2010a) Selection for non-amyloidogenic mutants of Islet Amyloid Polypeptide (IAPP) identifies an extended region for amyloidogenicity. *Biochemistry 49*: 7783-7789.

Fox A, Snollaerts T, Errecart Casanova C, Calciano A, Nogaj LA et Moffet DA (2010b) Selection for nonamyloidogenic mutants of islet amyloid polypeptide (IAPP) identifies an extended region for amyloidogenicity. *Biochemistry 49*: 7783-7789.

Fu Z, Aucoin D, Davis J, Van Nostrand WE et Smith SO (2015) Mechanism of nucleated conformational conversion of Abeta42. *Biochemistry 54*: 4197-4207.

Fusco G, Chen SW, Williamson PTF, Cascella R, Perni M, Jarvis JA, Cecchi C, Vendruscolo M, Chiti F, Cremades N, et al. (2017) Structural basis of membrane disruption and cellular toxicity by alpha-synuclein oligomers. *Science 358*: 1440-1443.

Gallardo R, Iadanza MG, Xu Y, Heath GR, Foster R, Radford SE et Ranson NA (2020) Fibril structures of diabetes-related amylin variants reveal a basis for surface-templated assembly. *Nat Struct Mol Biol 27*: 1048-1056.

Gaspar R, Meisl G, Buell AK, Young L, Kaminski CF, Knowles TPJ, Sparr E et Linse S (2017) Secondary nucleation of monomers on fibril surface dominates α-synuclein aggregation and provides autocatalytic amyloid amplification. *Quarterly Reviews of Biophysics 50*: e6.

Gasparotto J, Girardi CS, Somensi N, Ribeiro CT, Moreira JCF, Michels M, Sonai B, Rocha M, Steckert AV, Barichello T, et al. (2018) Receptor for advanced glycation end products mediates sepsis-triggered amyloid-beta accumulation, Tau phosphorylation, and cognitive impairment. *J Biol Chem 293*: 226-244.

Gazit E (2002) A possible role for pi-stacking in the self-assembly of amyloid fibrils. *FASEB J 16*: 77-83.

Gebbink MF, Claessen D, Bouma B, Dijkhuizen L et Wosten HA (2005) Amyloids--a functional coat for microorganisms. *Nat Rev Microbiol 3*: 333-341.

Geiger T et Clarke S (1987) Deamidation, isomerization, and racemization at asparaginyl and aspartyl residues in peptides. Succinimide-linked reactions that contribute to protein degradation. *J Biol Chem 262*: 785-794.

Ghosh D, Sahay S, Ranjan P, Salot S, Mohite GM, Singh PK, Dwivedi S, Carvalho E, Banerjee R, Kumar A, et al. (2014) The newly discovered Parkinson's disease associated Finnish mutation (A53E) attenuates alpha-synuclein aggregation and membrane binding. *Biochemistry 53*: 6419-6421.

Gilead S, Wolfenson H et Gazit E (2006) Molecular mapping of the recognition interface between the islet amyloid polypeptide and insulin. *Angew Chem Int Ed Engl 45*: 6476-6480.

Glenner GG, Eanes ED et Wiley CA (1988) Amyloid fibrils formed from a segment of the pancreatic islet amyloid protein. *Biochem Biophys Res Commun 155*: 608-614.

Glenner GG et Wong CW (1984) Alzheimer's disease: initial report of the purification and characterization of a novel cerebrovascular amyloid protein. *Biochem Biophys Res Commun 120*: 885-890.

Godin E, Nguyen PT, Zottig X et Bourgault S (2019) Identification of a hinge residue controlling islet amyloid polypeptide self-assembly and cytotoxicity. *J Biol Chem 294*: 8452-8463.

Goodchild SC, Sheynis T, Thompson R, Tipping KW, Xue W-F, Ranson NA, Beales PA, Hewitt EW et Radford SE (2014) β2-Microglobulin amyloid fibril-induced Membrane Disruption Is Enhanced by Endosomal Lipids and Acidic pH. *PLoS ONE 9*: e104492.

Greenberg SM, Bacskai BJ, Hernandez-Guillamon M, Pruzin J, Sperling R et van Veluw SJ (2020) Cerebral amyloid angiopathy and Alzheimer disease - one peptide, two pathways. *Nat Rev Neurol 16*: 30-42.

Griese M, Kappler M, Gaggar A et Hartl D (2008) Inhibition of airway proteases in cystic fibrosis lung disease. *Eur Respir J 32*: 783-795.

Griffiths JM, Ashburn TT, Auger M, Costa PR, Griffin RG et Lansbury PT (1995) Rotational Resonance Solid-State NMR Elucidates a structural model of pancreatic amyloid. *JACS 117*: 3539-3546.

Gu M et Viles JH (2016) Methionine oxidation reduces lag-times for amyloid-beta(1-40) fiber formation but generates highly fragmented fibers. *BBA 1864*: 1260-1269.

Gurlo T, Ryazantsev S, Huang C-j, Yeh MW, Reber HA, Hines OJ, O'Brien TD, Glabe CG et Butler PC (2010) Evidence for proteotoxicity in β Cells in type 2 diabetes : Toxic Islet Amyloid Polypeptide oligomers form intracellularly in the secretory pathway. *The American Journal of Pathology 176*: 861-869.

Gurzov EN, Wang B, Pilkington EH, Chen P, Kakinen A, Stanley WJ, Litwak SA, Hanssen EG, Davis TP, Ding F, et al. (2016) Inhibition of hIAPP amyloid aggregation and pancreatic beta-Cell toxicity by OH-terminated PAMAM dendrimer. *Small 12*: 1615-1626.

Han BH, Zhou M-L, Johnson AW, Singh I, Liao F, Vellimana AK, Nelson JW, Milner E, Cirrito JR, Basak J, et al. (2015) Contribution of reactive oxygen species to cerebral amyloid angiopathy, vasomotor dysfunction, and microhemorrhage in aged Tg2576 mice. *Proc Natl Acad Sci U S A 112*: E881-E890.

Han S, Kollmer M, Markx D, Claus S, Walther P et Fändrich M (2017) Amyloid plaque structure and cell surface interactions of β-amyloid fibrils revealed by electron tomography. *Scientific Reports 7*: 43577.

Hardy J et Allsop D (1991) Amyloid deposition as the central event in the aetiology of Alzheimer's disease. *Trends Pharmacol Sci 12*: 383-388.

Harigaya Y, Saido TC, Eckman CB, Prada CM, Shoji M et Younkin SG (2000) Amyloid beta protein starting pyroglutamate at position 3 is a major component of the amyloid deposits in the Alzheimer's disease brain. *Biochem Biophys Res Commun 276*: 422-427.

Hassanpour A, De Carufel CA, Bourgault S et Forgione P (2014) Synthesis of 2,5-diaryl-substituted thiophenes as helical mimetics: towards the modulation of islet amyloid polypeptide (IAPP) amyloid fibril formation and cytotoxicity. *Chemistry 20*: 2522-2528.

Hatami A, Monjazeb S, Milton S et Glabe CG (2017) Familial Alzheimer's disease mutations within the amyloid precursor protein alter the aggregation and conformation of the amyloid-beta peptide. *J Biol Chem 292*: 3172-3185.

Hay DL, Poyner DR et Sexton PM (2006) GPCR modulation by RAMPs. *Pharmacol Ther 109*: 173-197.

Head E (2013) A canine model of human aging and Alzheimer's disease. *BBA 1832*: 1384-1389.

Hebda JA et Miranker AD (2009) The interplay of catalysis and toxicity by amyloid intermediates on lipid bilayers: insights from type II diabetes. *Annu Rev Biophys 38*: 125-152.

Hebda JA, Saraogi I, Magzoub M, Hamilton AD et Miranker AD (2009) A peptidomimetic approach to targeting pre-amyloidogenic states in Type II diabetes. *Chemistry & Biology 16*: 943-950.

Heegaard PM, Boas U et Otzen DE (2007) Dendrimer effects on peptide and protein fibrillation. *Macromol Biosci 7*: 1047-1059.

Hekman C, DeMond W, Dixit T, Mauch S, Nuechterlein M, Stepanenko A, Williams JD et Ye M (1998) Isolation and identification of peptide degradation products of heat stressed pramlintide injection drug product. *Pharm Res 15*: 650-659.

Hekman CM, DeMond WS, Kelley PJ, Mauch SF et Williams JD (1999) Isolation and identification of cyclic imide and deamidation products in heat stressed pramlintide injection drug product. *J Pharm Biomed Anal 20*: 763-772.

Heneka MT, Carson MJ, El Khoury J, Landreth GE, Brosseron F, Feinstein DL, Jacobs AH, Wyss-Coray T, Vitorica J, Ransohoff RM, et al. (2015) Neuroinflammation in Alzheimer's disease. *Lancet Neurol 14*: 388-405.

Herczenik E et Gebbink MF (2008) Molecular and cellular aspects of protein misfolding and disease. *FASEB J 22*: 2115-2133.

Hieronymus L et Griffin S (2015) Role of amylin in type 1 and type 2 diabetes. *Diabetes Educ 41*: 47s-56s.

Höppener JWM, Oosterwijk C, Visser-Vernooy HJ, Lips CJM et Jansz HS (1992) Characterization of the human islet amyloid polypeptide/amylin gene transcripts: Identification of a new polyadenylation site. *Bioch and Biophys Res Commun 189*: 1569-1577.

Hoshi M, Sato M, Matsumoto S, Noguchi A, Yasutake K, Yoshida N et Sato K (2003) Spherical aggregates of beta-amyloid (amylospheroid) show high neurotoxicity and activate tau protein kinase I/glycogen synthase kinase-3beta. *Proc Natl Acad Sci U S A 100*: 6370-6375.

Howie AJ, Brewer DB, Howell D et Jones AP (2008) Physical basis of colors seen in Congo red-stained amyloid in polarized light. *Lab Invest 88*: 232-242.

Hsu YH, Chen YW, Wu MH et Tu LH (2019) Protein glycation by glyoxal promotes amyloid formation by Islet Amyloid Polypeptide. *Biophys J 116*: 2304-2313.

Hubbard JA, Martin SR, Chaplin LC, Bose C, Kelly SM et Price NC (1991) Solution structures of calcitonin-gene-related-peptide analogues of calcitonin-gene-related peptide and amylin. *The Biochemical journal 275 (Pt 3)*: 785-788.

Hull RL, Zraika S, Udayasankar J, Aston-Mourney K, Subramanian SL et Kahn SE (2009) Amyloid formation in human IAPP transgenic mouse islets and pancreas, and human pancreas, is not associated with endoplasmic reticulum stress. *Diabetologia 52*: 1102-1111.

Hunter S et Brayne C (2018) Understanding the roles of mutations in the amyloid precursor protein in Alzheimer disease. *Molecular Psychiatry 23*: 81-93.

Hutton JC (1994) Insulin secretory granule biogenesis and the proinsulin-processing endopeptidases. *Diabetologia 37 Suppl 2*: S48-56.

Iadanza MG, Jackson MP, Hewitt EW, Ranson NA et Radford SE (2018) A new era for understanding amyloid structures and disease. *Nat Rev Mol Cell Biol 19*: 755-773.

Ilitchev AI, Giammona MJ, Schwarze JN, Buratto SK et Bowers MT (2018) Zinc-induced conformational transitions in human Islet Amyloid Polypeptide and their role in the inhibition of amyloidosis. *J Phys Chem B 122*: 9852-9859.

Jaikaran ET, Nilsson MR et Clark A (2004) Pancreatic beta-cell granule peptides form heteromolecular complexes which inhibit islet amyloid polypeptide fibril formation. *Biochem J 377*: 709-716.

Jaikaran ETAS, Higham CE, Serpell LC, Zurdo J, Gross M, Clark A et Fraser PE (2001) Identification of a novel human islet amyloid polypeptide β-sheet domain and factors influencing fibrillogenesis11Edited by F. E. Cohen. *Journal of Molecular Biology 308*: 515-525.

Janson J, Ashley RH, Harrison D, McIntyre S et Butler PC (1999) The mechanism of islet amyloid polypeptide toxicity is membrane disruption by intermediate-sized toxic amyloid particles. *Diabetes 48*: 491-498.

Jarrett JT, Berger EP et Lansbury PT, Jr. (1993) The carboxy terminus of the beta amyloid protein is critical for the seeding of amyloid formation: implications for the pathogenesis of Alzheimer's disease. *Biochemistry 32*: 4693-4697.

Jeong HR et An SS (2015) Causative factors for formation of toxic islet amyloid polypeptide oligomer in type 2 diabetes mellitus. *Clin Interv Aging 10*: 1873-1879.

Jesus AR, Dias C, Matos AM, de Almeida RF, Viana AS, Marcelo F, Ribeiro RT, Macedo MP, Airoldi C, Nicotra F, et al. (2014) Exploiting the therapeutic potential of 8-beta-d-glucopyranosylgenistein: synthesis, antidiabetic activity, and molecular interaction with islet amyloid polypeptide and amyloid beta-peptide (1-42). *J Med Chem 57*: 9463-9472.

Jha S, Patil SM, Gibson J, Nelson CE, Alder NN et Alexandrescu AT (2011) Mechanism of amylin fibrillization enhancement by heparin. *J Biol Chem 286*: 22894-22904.

Jha S, Sellin D, Seidel R et Winter R (2009) Amyloidogenic propensities and conformational properties of ProIAPP and IAPP in the presence of lipid bilayer membranes. *J Mol Biol 389*: 907-920.

Jha S, Snell JM, Sheftic SR, Patil SM, Daniels SB, Kolling FW et Alexandrescu AT (2014) pH dependence of amylin fibrillization. *Biochemistry 53*: 300-310.

Jiang P, Li W, Shea J-E et Mu Y (2011) Resveratrol inhibits the formation of multiple-layered β-sheet oligomers of the human islet amyloid polypeptide segment 22-27. *Biophys J 100*: 1550-1558.

Jiang P, Xu W et Mu Y (2009) Amyloidogenesis abolished by proline substitutions but enhanced by lipid binding. *PLoS Comput Biol 5*: e1000357.

Jiao L, Zhang X, Huang L, Gong H, Cheng B, Sun Y, Li Y, Liu Q, Zheng L et Huang K (2013) Proanthocyanidins are the major anti-diabetic components of cinnamon water extract. *Food Chem Toxicol 56*: 398-405.

Kad NM, Thomson NH, Smith DP, Smith DA et Radford SE (2001) Beta(2)-microglobulin and its deamidated variant, N17D form amyloid fibrils with a range of morphologies in vitro. *J Mol Biol 313*: 559-571.

Kahn SE (2003) The relative contributions of insulin resistance and beta-cell dysfunction to the pathophysiology of Type 2 diabetes. *Diabetologia 46*: 3-19.

Kajava AV, Aebi U et Steven AC (2005) The parallel superpleated beta-structure as a model for amyloid fibrils of human amylin. *J Mol Biol 348*: 247-252.

Kao PY, Green E, Pereira C, Ekimura S, Juarez D, Whyte T, Arhar T, Malaspina B, Nogaj LA et Moffet DA (2015) Inhibition of toxic IAPP amyloid by extracts of common fruits. *J Funct Foods 12*: 450-457.

Kapurniotu A, Schmauder A et Tenidis K (2002) Structure-based design and study of non-amyloidogenic, double N-methylated IAPP amyloid core sequences as inhibitors of IAPP amyloid formation and cytotoxicity. *J Mol Biol 315*: 339-350.

Karle IL (2001) Controls exerted by the Aib residue: helix formation and helix reversal. *Biopolymers 60*: 351-365.

Kayed R, Head E, Sarsoza F, Saing T, Cotman CW, Necula M, Margol L, Wu J, Breydo L, Thompson JL, et al. (2007) Fibril specific, conformation dependent antibodies recognize a generic epitope common to amyloid fibrils and fibrillar oligomers that is absent in prefibrillar oligomers. *Mol Neurodegener 2*: 18.

Kayed R, Head E, Thompson JL, McIntire TM, Milton SC, Cotman CW et Glabe CG (2003) Common structure of soluble amyloid oligomers implies common mechanism of pathogenesis. *Science 300*: 486-489.

Kayed R, Pensalfini A, Margol L, Sokolov Y, Sarsoza F, Head E, Hall J et Glabe C (2009) Annular protofibrils are a structurally and functionally distinct type of amyloid oligomer. *J Biol Chem 284*: 4230-4237.

Kayed R, Sokolov Y, Edmonds B, McIntire TM, Milton SC, Hall JE et Glabe CG (2004) Permeabilization of lipid bilayers is a common conformation-dependent activity of soluble amyloid oligomers in protein misfolding diseases. J *Biol Chem 279*: 46363-46366.

Kelenyi G (1967) On the histochemistry of azo group-free thiazole dyes. *J Histochem Cytochem 15*: 172-180.

Kelly JW (1998) The alternative conformations of amyloidogenic proteins and their multi-step assembly pathways. *Curr Opin Struct Biol 8*: 101-106.

Khemtemourian L, Domenech E, Doux JP, Koorengevel MC et Killian JA (2011) Low pH acts as inhibitor of membrane damage induced by human islet amyloid polypeptide. *J Am Chem Soc 133*: 15598-15604.

Khemtemourian L, Guillemain G, Foufelle F et Killian JA (2017) Residue specific effects of human islet polypeptide amyloid on self-assembly and on cell toxicity. *Biochimie 142*: 22-30.

Kim AC, Lim S et Kim YK (2018) Metal Ion Effects on Aβ and Tau Aggregation. *International journal of molecular sciences 19*: 128.

King CY, Tittmann P, Gross H, Gebert R, Aebi M et Wuthrich K (1997) Prion-inducing domain 2-114 of yeast Sup35 protein transforms in vitro into amyloid-like filaments. *Proc Natl Acad Sci U S A 94*: 6618-6622.

Klajnert B, Wasiak T, Ionov M, Fernandez-Villamarin M, Sousa-Herves A, Correa J, Riguera R et Fernandez-Megia E (2012) Dendrimers reduce toxicity of A beta 1-28 peptide during aggregation and accelerate fibril formation. *Nanomedicine-Nanotechnology Biology and Medicine 8*: 1372-1378.

Klementieva O, Aso E, Filippini D, Benseny-Cases N, Carmona M, Juves S, Appelhans D, Cladera J et Ferrer I (2013) Effect of poly(propylene imine) glycodendrimers on beta-amyloid aggregation in vitro and in APP/PS1 transgenic mice, as a model of brain amyloid deposition and Alzheimer's disease. *Biomacromolecules 14*: 3570-3580.

Klementieva O, Benseny-Cases N, Gella A, Appelhans D, Voit B et Cladera J (2011) Dense shell glycodendrimers as potential nontoxic anti-amyloidogenic agents in Alzheimer's disease. Amyloid-dendrimer aggregates morphology and cell toxicity. *Biomacromolecules 12*: 3903-3909.

Knight JD, Hebda JA et Miranker AD (2006) Conserved and cooperative assembly of membrane-bound alpha-helical states of islet amyloid polypeptide. *Biochemistry 45*: 9496-9508.

Knight JD et Miranker AD (2004) Phospholipid catalysis of diabetic amyloid assembly. *J Mol Biol 341*: 1175-1187.

Knowles TP, Vendruscolo M et Dobson CM (2014) The amyloid state and its association with protein misfolding diseases. *Nat Rev Mol Cell Biol 15*: 384-396.

Knowles TP, Waudby CA, Devlin GL, Cohen SI, Aguzzi A, Vendruscolo M, Terentjev EM, Welland ME et Dobson CM (2009) An analytical solution to the kinetics of breakable filament assembly. *Science 326*: 1533-1537.

Kodali R, Williams AD, Chemuru S et Wetzel R (2010) Abeta(1-40) forms five distinct amyloid structures whose beta-sheet contents and fibril stabilities are correlated. *J Mol Biol 401*: 503-517.

Koo BW, Hebda JA et Miranker AD (2008) Amide inequivalence in the fibrillar assembly of islet amyloid polypeptide. *Protein Eng Des Sel 21*: 147-154.

Koo BW et Miranker AD (2005) Contribution of the intrinsic disulfide to the assembly mechanism of islet amyloid. *Protein Sci 14*: 231-239.

Krishnan R, Goodman JL, Mukhopadhyay S, Pacheco CD, Lemke EA, Deniz AA et Lindquist S (2012) Conserved features of intermediates in amyloid assembly determine their benign or toxic states. *Proc Natl Acad Sci U S A 109*: 11172-11177.

Krotee P, Rodriguez JA, Sawaya MR, Cascio D, Reyes FE, Shi D, Hattne J, Nannenga BL, Oskarsson ME, Philipp S, et al. (2017) Atomic structures of fibrillar segments of hIAPP suggest tightly mated beta-sheets are important for cytotoxicity. *Elife 6*:

Kumar S, Birol M, Schlamadinger DE, Wojcik SP, Rhoades E et Miranker AD (2016) Foldamer-mediated manipulation of a pre-amyloid toxin. *Nat Commun 7*: 11412.

Kumar S, Brown MA, Nath A et Miranker AD (2014) Folded small molecule manipulation of islet amyloid polypeptide. *Chem Biol 21*: 775-781.

Kumar S et Miranker AD (2013) A foldamer approach to targeting membrane bound helical states of islet amyloid polypeptide. *Chem Commun (Camb) 49*: 4749-4751.

Ladiwala ARA, Dordick JS et Tessier PM (2011) Aromatic small molecules remodel toxic soluble oligomers of amyloid beta through three independent pathways. *J Biol Mol 286*: 3209-3218.

Ladiwala ARA, Litt J, Kane RS, Aucoin DS, Smith SO, Ranjan S, Davis J, Van Nostrand WE et Tessier PM (2012) Conformational differences between two amyloid β oligomers of similar size and dissimilar toxicity. *J Biol Mol 287*: 24765-24773.

Ladner CL, Chen M, Smith DP, Platt GW, Radford SE et Langen R (2010) Stacked sets of parallel, in-register beta-strands of beta2-microglobulin in amyloid fibrils revealed by site-directed spin labeling and chemical labeling. *J Biol Mol chemistry 285*: 17137-17147.

Lam YPY, Wootton CA, Hands-Portman I, Wei J, Chiu CKC, Romero-Canelon I, Lermyte F, Barrow MP et O'Connor PB (2018) Does deamidation of islet amyloid polypeptide accelerate amyloid fibril formation? *Chem Commun 54*: 13853-13856.

Larson JL et Miranker AD (2004) The mechanism of insulin action on islet amyloid polypeptide fiber formation. *J Mol Biol 335*: 221-231.

Lasagna-Reeves CA, Glabe CG et Kayed R (2011) Amyloid-β annular protofibrils evade fibrillar fate in Alzheimer disease brain. *J Mol Biol 286*: 22122-22130.

Last NB et Miranker AD (2013) Common mechanism unites membrane poration by amyloid and antimicrobial peptides. *Proc Natl Acad Sci U S A 110*: 6382-6387.

Law E, Lu S, Kieffer TJ, Warnock GL, Ao Z, Woo M et Marzban L (2010) Differences between amyloid toxicity in alpha and beta cells in human and mouse islets and the role of caspase-3. *Diabetologia 53*: 1415-1427.

Lee M, Kim JI, Na S et Eom K (2018) Metal ions affect the formation and stability of amyloid beta aggregates at multiple length scales. *Phys Chem Chem Phys 20*: 8951-8961.

Lee SC, Hashim Y, Li JK, Ko GT, Critchley JA, Cockram CS et Chan JC (2001) The islet amyloid polypeptide (amylin) gene S20G mutation in Chinese subjects: evidence for associations with type 2 diabetes and cholesterol levels. *Clin Endocrinol (Oxf) 54*: 541-546.

Lesne S, Koh MT, Kotilinek L, Kayed R, Glabe CG, Yang A, Gallagher M et Ashe KH (2006) A specific amyloid-beta protein assembly in the brain impairs memory. *Nature 440*: 352-357.

LeVine H (1995) Thioflavine T interaction with amyloid β-sheet structures. *Amyloid 2*: 1-6.

LeVine H, 3rd (1993) Thioflavine T interaction with synthetic Alzheimer's disease beta-amyloid peptides: detection of amyloid aggregation in solution. *Protein Sci 2*: 404-410.

LeVine H, 3rd (1997) Stopped-flow kinetics reveal multiple phases of thioflavin T binding to Alzheimer beta (1-40) amyloid fibrils. *Arch Biochem Biophys 342*: 306-316.

Li SC, Goto NK, Williams KA et Deber CM (1996) Alpha-helical, but not beta-sheet, propensity of proline is determined by peptide environment. *Proc Natl Acad Sci U S A 93*: 6676-6681.

Li X, Ma L, Zheng W et Chen T (2014) Inhibition of islet amyloid polypeptide fibril formation by selenium-containing phycocyanin and prevention of beta cell apoptosis. *Biomaterials 35*: 8596-8604.

Li Y, Xu W, Mu Y et Zhang JZH (2013) Acidic pH retards the fibrillization of human islet amyloid polypeptide due to electrostatic repulsion of histidines. *J Chem Phys 139*: 055102.

Lim KH, Dasari AKR, Hung I, Gan Z, Kelly JW, Wright PE et Wemmer DE (2016) Solid-state NMR studies reveal native-like β-Sheet structures in Transthyretin amyloid. *Biochemistry 55*: 5272-5278.

Lin CY, Gurlo T, Kayed R, Butler AE, Haataja L, Glabe CG et Butler PC (2007) Toxic human islet amyloid polypeptide (h-IAPP) oligomers are intracellular, and vaccination to induce anti-toxic oligomer antibodies does not prevent h-IAPP-induced beta-cell apoptosis in h-IAPP transgenic mice. *Diabetes 56*: 1324-1332.

Lindquist SL et Kelly JW (2011) Chemical and biological approaches for adapting proteostasis to ameliorate protein misfolding and aggregation diseases: progress and prognosis. *Cold Spring Harb Perspect Biol 3*: a034108.

Liu G, Prabhakar A, Aucoin D, Simon M, Sparks S, Robbins KJ, Sheen A, Petty SA et Lazo ND (2010) Mechanistic studies of peptide self-assembly: transient alpha-helices to stable beta-sheets. *JACS 132*: 18223-18232.

Liu G, Robbins KJ, Sparks S, Selmani V, Bilides KM, Gomes EE et Lazo ND (2012) Helix-dipole effects in peptide self-assembly to amyloid. *Biochemistry 51*: 4167-4174.

Lo AW, Moonens K et Remaut H (2013) Chemical attenuation of pilus function and assembly in Gram-negative bacteria. *Curr Opin Microbiol 16*: 85-92.

Logovinsky V, Satlin A, Lai R, Swanson C, Kaplow J, Osswald G, Basun H et Lannfelt L (2016) Safety and tolerability of BAN2401--a clinical study in

Alzheimer's disease with a protofibril selective Aβ antibody. *Alzheimer's research & therapy 8*: 14-14.

Loksztejn A et Dzwolak W (2008) Chiral bifurcation in aggregating insulin: an induced circular dichroism study. *J Mol Biol 379*: 9-16.

Lopes DH, Attar A, Nair G, Hayden EY, Du Z, McDaniel K, Dutt S, Bravo-Rodriguez K, Mittal S, Klarner FG, et al. (2015) Molecular tweezers inhibit islet amyloid polypeptide assembly and toxicity by a new mechanism. *ACS Chem Biol 10*: 1555-1569.

Lorenzo A, Razzaboni B, Weir GC et Yankner BA (1994) Pancreatic islet cell toxicity of amylin associated with type-2 diabetes mellitus. *Nature 368*: 756-760.

Louros NN, Tsiolaki PL, Zompra AA, Pappa EV, Magafa V, Pairas G, Cordopatis P, Cheimonidou C, Trougakos IP, Iconomidou VA, et al. (2015) Structural studies and cytotoxicity assays of "aggregation-prone" IAPP(8-16) and its non-amyloidogenic variants suggest its important role in fibrillogenesis and cytotoxicity of human amylin. *Biopolymers 104*: 196-205.

Luca S, Yau W-M, Leapman R et Tycko R (2007) Peptide conformation and supramolecular organization in amylin fibrils: constraints from solid-state NMR. *Biochemistry 46*: 13505-13522.

Luedtke NW, Dexter RJ, Fried DB et Schepartz A (2007) Surveying polypeptide and protein domain conformation and association with FlAsH and ReAsH. *Nat Chem Biol 3*: 779-784.

Lutz TA (2010) The role of amylin in the control of energy homeostasis. *Am J Physiol Regul Integr Comp Physiol 298*: R1475-1484.

Maji SK, Perrin MH, Sawaya MR, Jessberger S, Vadodaria K, Rissman RA, Singru PS, Nilsson KPR, Simon R, Schubert D, et al. (2009) Functional amyloids as natural storage of peptide hormones in pituitary secretory granules. *Science 325*: 328.

Mallamace D, Fazio E, Mallamace F et Corsaro C (2018) The role of hydrogen bonding in the folding/unfolding process of hydrated lysozyme: A review of

recent NMR and FTIR results. *International journal of molecular sciences 19*: 3825.

Marek P, Abedini A, Song B, Kanungo M, Johnson ME, Gupta R, Zaman W, Wong SS et Raleigh DP (2007) Aromatic interactions are not required for amyloid fibril formation by islet amyloid polypeptide but do influence the rate of fibril formation and fibril morphology. *Biochemistry 46*: 3255-3261.

Marek P, Mukherjee S, Zanni MT et Raleigh DP (2010) Residue-specific, real-time characterization of lag-phase species and fibril growth during amyloid formation: a combined fluorescence and IR study of p-cyanophenylalanine analogs of islet amyloid polypeptide. *J Mol Biol 400*: 878-888.

Marinelli P, Navarro S, Graña-Montes R, Bañó-Polo M, Fernández MR, Papaleo E et Ventura S (2018) A single cysteine post-translational oxidation suffices to compromise globular proteins kinetic stability and promote amyloid formation. *Redox biology 14*: 566-575.

Martinez A, Kapas S, Miller MJ, Ward Y et Cuttitta F (2000) Coexpression of receptors for adrenomedullin, calcitonin gene-related peptide, and amylin in pancreatic beta-cells. *Endocrinology 141*: 406-411.

Martinez-Naharro A, Baksi AJ, Hawkins PN et Fontana M (2020) Diagnostic imaging of cardiac amyloidosis. *Nat Rev Cardiol*.

Martins IC, Kuperstein I, Wilkinson H, Maes E, Vanbrabant M, Jonckheere W, Van Gelder P, Hartmann D, D'Hooge R, De Strooper B, et al. (2008) Lipids revert inert Abeta amyloid fibrils to neurotoxic protofibrils that affect learning in mice. *The EMBO journal 27*: 224-233.

Marzban L, Rhodes CJ, Steiner DF, Haataja L, Halban PA et Verchere CB (2006) Impaired NH2-terminal processing of human proislet amyloid polypeptide by the prohormone convertase PC2 leads to amyloid formation and cell death. *Diabetes 55*: 2192-2201.

Marzban L, Tomas A, Becker TC, Rosenberg L, Oberholzer J, Fraser PE, Halban PA et Verchere CB (2008) Small interfering RNA-mediated suppression of proislet amyloid polypeptide expression inhibits islet amyloid formation and enhances survival of human islets in culture. *Diabetes 57*: 3045-3055.

Marzban L, Trigo-Gonzalez G et Verchere CB (2005) Processing of pro-Islet Amyloid Polypeptide in the constitutive and regulated secretory pathways of β Cells. *Molecular Endocrinology 19*: 2154-2163.

Marzban L, Trigo-Gonzalez G, Zhu X, Rhodes CJ, Halban PA, Steiner DF et Verchere CB (2004) Role of beta-cell prohormone convertase (PC)1/3 in processing of pro-islet amyloid polypeptide. *Diabetes 53*: 141-148.

Masel J, Jansen VAA et Nowak MA (1999) Quantifying the kinetic parameters of prion replication. *Biophysical Chemistry 77*: 139-152.

Masters SL, Dunne A, Subramanian SL, Hull RL, Tannahill GM, Sharp FA, Becker C, Franchi L, Yoshihara E, Chen Z, et al. (2010) Activation of the NLRP3 inflammasome by islet amyloid polypeptide provides a mechanism for enhanced IL-1β in type 2 diabetes. *Nat Immunol 11*: 897-904.

Mazor Y, Gilead S, Benhar I et Gazit E (2002) Identification and characterization of a novel molecular-recognition and self-assembly domain within the islet amyloid polypeptide. *J Mol Biol 322*: 1013-1024.

McAllister SR et Floudas CA (2009) Enhanced bounding techniques to reduce the protein conformational search space. *Optimization methods & software 24*: 837-855.

McLatchie LM, Fraser NJ, Main MJ, Wise A, Brown J, Thompson N, Solari R, Lee MG et Foord SM (1998) RAMPs regulate the transport and ligand specificity of the calcitonin-receptor-like receptor. *Nature 393*: 333-339.

McLaurin J, Franklin T, Zhang X, Deng J et Fraser PE (1999) Interactions of Alzheimer amyloid-beta peptides with glycosaminoglycans effects on fibril nucleation and growth. *Eur J Biochem 266*: 1101-1110.

Mehra S, Sahay S et Maji SK (2019) alpha-Synuclein misfolding and aggregation: Implications in Parkinson's disease pathogenesis. *Biochim Biophys Acta Proteins Proteom 1867*: 890-908.

Meier DT, Entrup L, Templin AT, Hogan MF, Mellati M, Zraika S, Hull RL et Kahn SE (2016) The S20G substitution in hIAPP is more amyloidogenic and cytotoxic than wild-type hIAPP in mouse islets. *Diabetologia 59*: 2166-2171.

Meinhardt J, Sachse C, Hortschansky P, Grigorieff N et Fandrich M (2009) Abeta(1-40) fibril polymorphism implies diverse interaction patterns in amyloid fibrils. *J Mol Biol 386*: 869-877.

Meisl G, Yang X, Hellstrand E, Frohm B, Kirkegaard JB, Cohen SI, Dobson CM, Linse S et Knowles TP (2014) Differences in nucleation behavior underlie the contrasting aggregation kinetics of the Abeta40 and Abeta42 peptides. *Proc Natl Acad Sci U S A 111*: 9384-9389.

Meng F, Abedini A, Plesner A, Middleton CT, Potter KJ, Zanni MT, Verchere CB et Raleigh DP (2010a) The sulfated triphenyl methane derivative acid fuchsin is a potent inhibitor of amyloid formation by human islet amyloid polypeptide and protects against the toxic effects of amyloid formation. *J Mol Biol 400*: 555-566.

Meng F, Abedini A, Plesner A, Verchere CB et Raleigh DP (2010b) The flavanol (-)-epigallocatechin 3-gallate inhibits amyloid formation by islet amyloid polypeptide, disaggregates amyloid fibrils, and protects cultured cells against IAPP-induced toxicity. *Biochemistry 49*: 8127-8133.

Meng F et Raleigh DP (2011) Inhibition of glycosaminoglycan-mediated amyloid formation by islet amyloid polypeptide and proIAPP processing intermediates. *J Mol Biol 406*: 491-502.

Meng F, Raleigh DP et Abedini A (2010c) Combination of kinetically selected inhibitors in trans leads to highly effective inhibition of amyloid formation. *J Am Chem Soc 132*: 14340-14342.

Merlini G, Dispenzieri A, Sanchorawala V, Schonland SO, Palladini G, Hawkins PN et Gertz MA (2018) Systemic immunoglobulin light chain amyloidosis. *Nat Rev Dis Primers 4*: 38.

Milanesi L, Sheynis T, Xue WF, Orlova EV, Hellewell AL, Jelinek R, Hewitt EW, Radford SE et Saibil HR (2012) Direct three-dimensional visualization of membrane disruption by amyloid fibrils. *Proc Natl Acad Sci U S A 109*: 20455-20460.

Mirecka EA, Feuerstein S, Gremer L, Schröder GF, Stoldt M, Willbold D et Hoyer W (2016) β-Hairpin of Islet Amyloid Polypeptide Bound to an Aggregation Inhibitor. *Sci Reps 6*: 33474.

Mirzabekov TA, Lin MC et Kagan BL (1996) Pore formation by the cytotoxic islet amyloid peptide amylin. *J Biol Chem 271*: 1988-1992.

Mishra A, Misra A, Sri Vaishnavi T, Thota C, Gupta M, Ramakumar S et Chauhan VS (2013) Conformationally restricted short peptides inhibit human islet amyloid polypeptide (hIAPP) fibrillization. *Chem Commun 49*: 2688-2690.

Montane J, Klimek-Abercrombie A, Potter KJ, Westwell-Roper C et Bruce Verchere C (2012) Metabolic stress, IAPP and islet amyloid. *Diabetes, Obesity and Metabolism 14*: 68-77.

Morgan AA et Rubenstein E (2013) Proline: the distribution, frequency, positioning, and common functional roles of proline and polyproline sequences in the human proteome. *PloS ONE 8*: e53785-e53785.

Moriarty DF et Raleigh DP (1999) Effects of Sequential Proline Substitutions on Amyloid Formation by Human Amylin20-29. *Biochemistry 38*: 1811-1818.

Morita S, Sakagashira S, Shimajiri Y, Eberhardt NL, Kondo T, Kondo T et Sanke T (2011) Autophagy protects against human islet amyloid polypeptide-associated apoptosis. *Journal of diabetes investigation 2*: 48-55.

Morris Kyle L, Rodger A, Hicks Matthew R, Debulpaep M, Schymkowitz J, Rousseau F et Serpell Louise C (2013) Exploring the sequence–structure relationship for amyloid peptides. *Biochemical Journal 450*: 275-283.

Mosselman S, Hoppener JW, Lips CJ et Jansz HS (1989) The complete islet amyloid polypeptide precursor is encoded by two exons. *FEBS Lett 247*: 154-158.

Mosselman S, Hoppener JW, Zandberg J, van Mansfeld AD, Geurts van Kessel AH, Lips CJ et Jansz HS (1988) Islet amyloid polypeptide: identification and chromosomal localization of the human gene. *FEBS Lett 239*: 227-232.

Motamedi-Shad N, Monsellier E, Torrassa S, Relini A et Chiti F (2009) Kinetic analysis of amyloid formation in the presence of heparan sulfate: faster unfolding and change of pathway. *J Biol Chem 284*: 29921-29934.

Muff R, Buhlmann N, Fischer JA et Born W (1999) An amylin receptor is revealed following co-transfection of a calcitonin receptor with receptor activity modifying proteins-1 or -3. *Endocrinology 140*: 2924-2927.

Murphy C, Eulitz D, Weiss D et Solomon A (2011) Light chain deamidation in ALlambda amyloid-associated protein. *Amyloid 18 Suppl 1*: 27-28.

Murphy MP et LeVine H, 3rd (2010) Alzheimer's disease and the amyloid-beta peptide. *J Alzheimers Dis 19*: 311-323.

Nagel-Steger L, Owen MC et Strodel B (2016) An Account of Amyloid Oligomers: Facts and Figures Obtained from Experiments and Simulations. *Chem Bio Chem 17*: 657-676.

Naiki H, Higuchi K, Hosokawa M et Takeda T (1989) Fluorometric determination of amyloid fibrils in vitro using the fluorescent dye, thioflavin T1. *Anal Biochem 177*: 244-249.

Naiki H, Higuchi K, Matsushima K, Shimada A, Chen WH, Hosokawa M et Takeda T (1990) Fluorometric examination of tissue amyloid fibrils in murine senile amyloidosis: use of the fluorescent indicator, thioflavine T. *Lab Invest 62*: 768-773.

Naiki H, Higuchi K, Nakakuki K et Takeda T (1991) Kinetic analysis of amyloid fibril polymerization in vitro. *Lab Invest 65*: 104-110.

Nanga RP, Brender JR, Vivekanandan S et Ramamoorthy A (2011) Structure and membrane orientation of IAPP in its natively amidated form at physiological pH in a membrane environment. *BBA 1808*: 2337-2342.

Nayer A (2014) Amyloid A amyloidosis: frequently neglected renal disease in injecting drug users. *Journal of nephropathology 3*: 26-28.

Nedumpully-Govindan P, Kakinen A, Pilkington EH, Davis TP, Chun Ke P et Ding F (2016) Stabilizing off-pathway oligomers by polyphenol nanoassemblies for IAPP aggregation inhibition. *Sci Reps 6*: 19463.

Nekooki-Machida Y, Kurosawa M, Nukina N, Ito K, Oda T et Tanaka M (2009) Distinct conformations of in vitro and in vivo amyloids of huntingtin-exon1 show different cytotoxicity. *Proc Natl Acad Sci U S A 106*: 9679-9684.

Nelson PT, Alafuzoff I, Bigio EH, Bouras C, Braak H, Cairns NJ, Castellani RJ, Crain BJ, Davies P, Del Tredici K, et al. (2012) Correlation of Alzheimer disease neuropathologic changes with cognitive status: a review of the literature. *J Neuropathol Exp Neurol 71*: 362-381.

Nelson R, Sawaya MR, Balbirnie M, Madsen AO, Riekel C, Grothe R et Eisenberg D (2005) Structure of the cross-beta spine of amyloid-like fibrils. *Nature 435*: 773-778.

Nguyen PT, Andraka N, De Carufel CA et Bourgault S (2015) Mechanistic contributions of biological cofactors in Islet Amyloid Polypeptide amyloidogenesis. *Journal of Diabetes Research 2015*: 13.

Nguyen PT, Sharma R, Rej R, De Carufel CA, Roy R et Bourgault S (2016) Low generation anionic dendrimers modulate islet amyloid polypeptide self-assembly and inhibit pancreatic β-cell toxicity. *RSC Advances 6*: 76360-76369.

Nguyen PT, Zottig X, Sebastiao M et Bourgault S (2017) Role of site-specific asparagine deamidation in Islet Amyloid Polypeptide amyloidogenesis: Key contributions of residues 14 and 21. *Biochemistry 56*: 3808-3817.

Nilsberth C, Westlind-Danielsson A, Eckman CB, Condron MM, Axelman K, Forsell C, Stenh C, Luthman J, Teplow DB, Younkin SG, et al. (2001) The 'Arctic' APP mutation (E693G) causes Alzheimer's disease by enhanced Aβ protofibril formation. *Nat Neurosci 4*: 887-893.

Nilsson MR (2004) Techniques to study amyloid fibril formation in vitro. *Methods 34*: 151-160.

Nilsson MR (2008) Post-translational chemical modifications in amyloid fibril formation. *Amyloid Proteins Wiley-VCH Verlag GmbH*: 81-109.

Nilsson MR, Driscoll M et Raleigh DP (2002) Low levels of asparagine deamidation can have a dramatic effect on aggregation of amyloidogenic peptides: implications for the study of amyloid formation. *Protein Sci 11*: 342-349.

Nilsson MR et Raleigh DP (1999) Analysis of amylin cleavage products provides new insights into the amyloidogenic region of human amylin. *J Mol Biol 294*: 1375-1385.

Nishi M, Sanke T, Seino S, Eddy RL, Fan YS, Byers MG, Shows TB, Bell GI et Steiner DF (1989) Human islet amyloid polypeptide gene: complete nucleotide sequence, chromosomal localization, and evolutionary history. *Mol Endocrinol 3*: 1775-1781.

Noji M, Sasahara K, Yamaguchi K, So M, Sakurai K, Kardos J, Naiki H et Goto Y (2019) Heating during agitation of beta2-microglobulin reveals that supersaturation breakdown is required for amyloid fibril formation at neutral pH. *J Biol Chem 294*: 15826-15835.

O'Brien TD, Westermark P et Johnson KH (1990) Islet amyloid polypeptide and calcitonin gene-related peptide immunoreactivity in amyloid and tumor cells of canine pancreatic endocrine tumors. *Vet Pathol 27*: 194-198.

O'Nuallain B, Freir DB, Nicoll AJ, Risse E, Ferguson N, Herron CE, Collinge J et Walsh DM (2010) Amyloid beta-protein dimers rapidly form stable synaptotoxic protofibrils. *J Neurosci 30*: 14411-14419.

Obasse I, Taylor M, Fullwood NJ et Allsop D (2017) Development of proteolytically stable N-methylated peptide inhibitors of aggregation of the amylin peptide implicated in type 2 diabetes. *Interface Focus 7*: 20160127.

Odani H, Oyama R, Titani K, Ogawa H et Saito A (1990) Purification and complete amino acid sequence of novel beta 2-microglobulin. *Biochem Biophys Res Commun 168*: 1223-1229.

Ohishi H, Skinner M, Sato-Araki N, Okuyama T, Gejyo F, Kimura A, Cohen AS et Schmid K (1990) Glycosaminoglycans of the hemodialysis-associated carpal synovial amyloid and of amyloid-rich tissues and fibrils of heart, liver, and spleen. *Clin Chem 36*: 88-91.

Okada Y, Okubo K, Ikeda K, Yano Y, Hoshino M, Hayashi Y, Kiso Y, Itoh-Watanabe H, Naito A et Matsuzaki K (2019) Toxic Amyloid Tape: A Novel Mixed Antiparallel/Parallel beta-Sheet Structure Formed by Amyloid beta-Protein on GM1 Clusters. *ACS Chem Neurosci 10*: 563-572.

Olofsson A, Ippel JH, Wijmenga SS, Lundgren E et Ohman A (2004) Probing solvent accessibility of transthyretin amyloid by solution NMR spectroscopy. *J Biol Chem 279*: 5699-5707.

Olzscha H, Schermann SM, Woerner AC, Pinkert S, Hecht MH, Tartaglia GG, Vendruscolo M, Hayer-Hartl M, Hartl FU et Vabulas RM (2011) Amyloid-like aggregates sequester numerous metastable proteins with essential cellular functions. *Cell 144*: 67-78.

Opie EL (1901) The relation oe diabetes mellitus to lesions of the pancreas. Hyaline degeneration of the islands oe langerhans. *The Journal of experimental medicine 5*: 527-540.

Owen MC, Gnutt D, Gao M, Wärmländer SKTS, Jarvet J, Gräslund A, Winter R, Ebbinghaus S et Strodel B (2019) Effects of in vivo conditions on amyloid aggregation. *Chemical Society Reviews 48*: 3946-3996.

Pacini F, Castagna MG, Cipri C et Schlumberger M (2010) Medullary thyroid carcinoma. *Clin Oncol (R Coll Radiol) 22*: 475-485.

Paravastu AK, Leapman RD, Yau WM et Tycko R (2008) Molecular structural basis for polymorphism in Alzheimer's beta-amyloid fibrils. *Proc Natl Acad Sci U S A 105*: 18349-18354.

Park J, Egolum U, Parker S, Andrews E, Ombengi D et Ling H (2019) Tafamidis: A First-in-Class Transthyretin Stabilizer for Transthyretin Amyloid Cardiomyopathy. *Ann Pharmacother* 1060028019888489.

Park YJ, Lee S, Kieffer TJ, Warnock GL, Safikhan N, Speck M, Hao Z, Woo M et Marzban L (2012) Deletion of Fas protects islet beta cells from cytotoxic effects of human islet amyloid polypeptide. *Diabetologia 55*: 1035-1047.

Parman Y, Adams D, Obici L, Galan L, Guergueltcheva V, Suhr OB et Coelho T (2016) Sixty years of transthyretin familial amyloid polyneuropathy (TTR-FAP) in Europe: where are we now? A European network approach to defining the epidemiology and management patterns for TTR-FAP. *Curr Opin Neurol 29 Suppl 1*: S3-s13.

Patil SM, Xu S, Sheftic SR et Alexandrescu AT (2009) Dynamic alpha-helix structure of micelle-bound human amylin. *J Mol Biol 284*: 11982-11991.

Paulsson JF, Benoit-Biancamano MO, Schaffer L et Dahl K (2011) Ferret islet amyloid polypeptide (IAPP): characterization of in vitro and in vivo amyloidogenicity. *Amyloid 18*: 222-228.

Paxinos G, Chai SY, Christopoulos G, Huang XF, Toga AW, Wang HQ et Sexton PM (2004) In vitro autoradiographic localization of calcitonin and amylin binding sites in monkey brain. *J Chem Neuroanat 27*: 217-236.

Pease LF, 3rd, Sorci M, Guha S, Tsai D-H, Zachariah MR, Tarlov MJ et Belfort G (2010) Probing the nucleus model for oligomer formation during insulin amyloid fibrillogenesis. *Biophys J 99*: 3979-3985.

Peduzzo A, Linse S et Buell AK (2020) The properties of alpha-synuclein secondary nuclei are dominated by the solution conditions rather than the seed fibril strain. *ACS Chem Neurosci 11(6)*: 909-918.

Petkova AT, Leapman RD, Guo Z, Yau WM, Mattson MP et Tycko R (2005) Self-propagating, molecular-level polymorphism in Alzheimer's beta-amyloid fibrils. *Science 307*: 262-265.

Pieri L, Madiona K, Bousset L et Melki R (2012) Fibrillar alpha-synuclein and huntingtin exon 1 assemblies are toxic to the cells. *Biophys J 102*: 2894-2905.

Pleyer C, Flesche J et Saeed F (2015) Lysozyme amyloidosis - a case report and review of the literature. *Clinical nephrology Case studies 3*: 42-45.

Porat Y, Mazor Y, Efrat S et Gazit E (2004) Inhibition of Islet Amyloid Polypeptide Fibril Formation: A Potential Role for Heteroaromatic Interactions. *Biochemistry 43*: 14454-14462.

Potter KJ, Scrocchi LA, Warnock GL, Ao Z, Younker MA, Rosenberg L, Lipsett M, Verchere CB et Fraser PE (2009) Amyloid inhibitors enhance survival of cultured human islets. *BBA 1790*: 566-574.

Prokaeva T, Akar H, Spencer B, Havasi A, Cui H, O'Hara CJ, Gursky O, Leszyk J, Steffen M, Browning S, et al. (2017) Hereditary renal amyloidosis associated with a novel apolipoprotein A-II variant. *Kidney international reports 2*: 1223-1232.

Prusiner SB (2013) Biology and genetics of prions causing neurodegeneration. *Annu Rev Genet 47*: 601-623.

Qiang W, Yau W-M, Lu J-X, Collinge J et Tycko R (2017) Structural variation in amyloid-β fibrils from Alzheimer's disease clinical subtypes. *Nature 541*: 217-221.

Quittot N, Sebastiao M, Al-Halifa S et Bourgault S (2018) Kinetic and conformational insights into Islet Amyloid Polypeptide self-assembly using a biarsenical fluorogenic probe. *Bioconjugate Chemistry 29*: 517-527.

Radovan D, Opitz N et Winter R (2009) Fluorescence microscopy studies on islet amyloid polypeptide fibrillation at heterogeneous and cellular membrane interfaces and its inhibition by resveratrol. *FEBS Lett 583*: 1439-1445.

Radovan D, Smirnovas V et Winter R (2008) Effect of pressure on islet amyloid polypeptide aggregation: revealing the polymorphic nature of the fibrillation process. *Biochemistry 47*: 6352-6360.

Rafeeq MM et Murad HAS (2017) Cystic fibrosis: current therapeutic targets and future approaches. *Journal of translational medicine 15*: 84-84.

Raimundo AF, Ferreira S, Martins IC et Menezes R (2020) Islet Amyloid Polypeptide: A partner in crime with Aβ in the pathology of Alzheimer's disease. *Frontiers in molecular neuroscience 13*: 35-35.

Raleigh D, Zhang X, Hastoy B et Clark A (2017) The beta-cell assassin: IAPP cytotoxicity. *J Mol Endocrinol 59*: R121-r140.

Reddy AS, Wang L, Singh S, Ling YL, Buchanan L, Zanni MT, Skinner JL et de Pablo JJ (2010) Stable and metastable states of human amylin in solution. *Biophys J 99*: 2208-2216.

Reixach N, Deechongkit S, Jiang X, Kelly JW et Buxbaum JN (2004) Tissue damage in the amyloidoses: Transthyretin monomers and nonnative oligomers are the major cytotoxic species in tissue culture. *Proc Natl Acad Sci U S A 101*: 2817-2822.

Rigacci S, Guidotti V, Bucciantini M, Parri M, Nediani C, Cerbai E, Stefani M et Berti A (2010) Oleuropein aglycon prevents cytotoxic amyloid aggregation of human amylin. *J Nutr Biochem 21*: 726-735.

Rivera JF, Gurlo T, Daval M, Huang CJ, Matveyenko AV, Butler PC et Costes S (2011) Human-IAPP disrupts the autophagy/lysosomal pathway in pancreatic beta-cells: protective role of p62-positive cytoplasmic inclusions. *Cell Death Differ 18*: 415-426.

Roan NR, Sandi-Monroy N, Kohgadai N, Usmani SM, Hamil KG, Neidleman J, Montano M, Ständker L, Röcker A, Cavrois M, et al. (2017) Semen amyloids participate in spermatozoa selection and clearance. *eLife 6*: e24888.

Robinson AB et Robinson LR (1991) Distribution of glutamine and asparagine residues and their near neighbors in peptides and proteins. *Proc Natl Acad Sci U S A 88*: 8880-8884.

Robinson NE et Robinson AB (2001) Deamidation of human proteins. *Proc Natl Acad Sci U S A 98*: 12409-12413.

Robinson NE, Robinson ML, Schulze SE, Lai BT et Gray HB (2009) Deamidation of alpha-synuclein. *Protein Sci 18*: 1766-1773.

Roden M et Shulman GI (2019) The integrative biology of type 2 diabetes. *Nature 576*: 51-60.

Röder C, Kupreichyk T, Gremer L, Schäfer LU, Pothula KR, Ravelli RBG, Willbold D, Hoyer W et Schröder GF (2020) Cryo-EM structure of islet amyloid polypeptide fibrils reveals similarities with amyloid-β fibrils. *Nat Struct Mol Biol 27*: 660-667.

Roher AE, Lowenson JD, Clarke S, Wolkow C, Wang R, Cotter RJ, Reardon IM, Zurcher-Neely HA, Heinrikson RL, Ball MJ, et al. (1993) Structural alterations in the peptide backbone of beta-amyloid core protein may account for its deposition and stability in Alzheimer's disease. *J Biol Chem 268*: 3072-3083.

Roy R et Shiao TC (2015) Glyconanosynthons as powerful scaffolds and building blocks for the rapid construction of multifaceted, dense and chiral dendrimers. *Chem Soc Rev 44*: 3924-3941.

Sadakane Y et Kawahara M (2018) Implications of metal binding and asparagine deamidation for amyloid formation. *International journal of molecular sciences 19*: 2449.

Sakagashira S, Hiddinga HJ, Tateishi K, Sanke T, Hanabusa T, Nanjo K et Eberhardt NL (2000) S20G mutant amylin exhibits increased in vitro amyloidogenicity and increased intracellular cytotoxicity compared to wild-type amylin. *The American Journal of Pathology 157*: 2101-2109.

Sakagashira S, Sanke T, Hanabusa T, Shimomura H, Ohagi S, Kumagaye KY, Nakajima K et Nanjo K (1996) Missense mutation of amylin gene (S20G) in Japanese NIDDM patients. *Diabetes 45*: 1279-1281.

Saraogi I, Hebda JA, Becerril J, Estroff LA, Miranker AD et Hamilton AD (2010) Synthetic alpha-helix mimetics as agonists and antagonists of islet amyloid polypeptide aggregation. *Angew Chem Int Ed Engl 49*: 736-739.

Saridaki T, Zampagni M, Mannini B, Evangelisti E, Taddei N, Cecchi C et Chiti F (2012) Glycosaminoglycans (GAGs) suppress the toxicity of HypF-N prefibrillar aggregates. *J Mol Biol 421*: 616-630.

Scarpioni R, Ricardi M, Albertazzi V, De Amicis S, Rastelli F et Zerbini L (2016) Dialysis-related amyloidosis: challenges and solutions. *International journal of nephrology and renovascular disease 9*: 319-328.

Schenk D (2002) Amyloid-beta immunotherapy for Alzheimer's disease: the end of the beginning. *Nat Rev Neurosci 3*: 824-828.

Sebastiao M, Quittot N et Bourgault S (2017) Thioflavin T fluorescence to analyse amyloid formation kinetics: Measurement frequency as a factor explaining irreproducibility. *Anal Biochem 532*: 83-86.

Seeliger J, Weise K, Opitz N et Winter R (2012) The effect of Abeta on IAPP aggregation in the presence of an isolated beta-cell membrane. *J Mol Biol 421*: 348-363.

Seino S (2001) S20G mutation of the amylin gene is associated with Type II diabetes in Japanese. Study Group of Comprehensive Analysis of Genetic Factors in Diabetes Mellitus. *Diabetologia 44*: 906-909.

Serio TR, Cashikar AG, Kowal AS, Sawicki GJ, Moslehi JJ, Serpell L, Arnsdorf MF et Lindquist SL (2000) Nucleated conformational conversion and the replication of conformational information by a prion determinant. *Science 289*: 1317-1321.

Serra-Batiste M, Ninot-Pedrosa M, Bayoumi M, Gairí M, Maglia G et Carulla N (2016) Aβ42 assembles into specific β-barrel pore-forming oligomers in membrane-mimicking environments. *Proc Natl Acad Sci U S A 113*: 10866-10871.

Serrano AL, Lomont JP, Tu LH, Raleigh DP et Zanni MT (2017) A free energy barrier caused by the refolding of an oligomeric intermediate controls the lag time of amyloid formation by hIAPP. *JACS 139*: 16748-16758.

Shankar GM, Li S, Mehta TH, Garcia-Munoz A, Shepardson NE, Smith I, Brett FM, Farrell MA, Rowan MJ, Lemere CA, et al. (2008) Amyloid-beta protein dimers isolated directly from Alzheimer's brains impair synaptic plasticity and memory. *Nat med 14*: 837-842.

Sharma R, Kottari N, Chabre YM, Abbassi L, Shiao TC et Roy R (2014) A highly versatile convergent/divergent "onion peel" synthetic strategy toward potent multivalent glycodendrimers. *Chem Commun (Camb) 50*: 13300-13303.

Sharma R, Zhang I, Abbassi L, Rej R, Maysinger D et Roy R (2015) A fast track strategy toward highly functionalized dendrimers with different structural layers: an "onion peel approach". *Polymer Chemistry 6*: 1436-1444.

Sharma R, Zhang I, Shiao TC, Pavan GM, Maysinger D et Roy R (2016) Low generation polyamine dendrimers bearing flexible tetraethylene glycol as nanocarriers for plasmids and siRNA. *Nanoscale 8*: 5106-5119.

Shi Y, Rhodes NR, Abdolvahabi A, Kohn T, Cook NP, Marti AA et Shaw BF (2013) Deamidation of asparagine to aspartate destabilizes Cu, Zn superoxide dismutase, accelerates fibrillization, and mirrors ALS-linked mutations. *JACS 135*: 15897-15908.

Shigihara N, Fukunaka A, Hara A, Komiya K, Honda A, Uchida T, Abe H, Toyofuku Y, Tamaki M, Ogihara T, et al. (2014) Human IAPP–induced pancreatic β cell toxicity and its regulation by autophagy. *The Journal of Clinical Investigation 124*: 3634-3644.

Shimizu T, Fukuda H, Murayama S, Izumiyama N et Shirasawa T (2002) Isoaspartate formation at position 23 of amyloid beta peptide enhanced fibril formation and deposited onto senile plaques and vascular amyloids in Alzheimer's disease. *Journal of Neuroscience Research 70*: 451-461.

Shimizu T, Matsuoka Y et Shirasawa T (2005) Biological significance of isoaspartate and its repair system. *Biol Pharm Bull 28*: 1590-1596.

Silverman GA, Pak SC et Perlmutter DH (2013) Disorders of protein misfolding: alpha-1-antitrypsin deficiency as prototype. *The Journal of pediatrics 163*: 320-326.

Sninate I et Bennana A (2018) Literature review regarding the impact of population aging on healthcare expenditure growth: Organisation for economic co-operation and development member countries and Morocco. *The Pan African medical journal 31*: 142-142.

Solomon JP, Bourgault S, Powers ET et Kelly JW (2011) Heparin binds 8 kDa gelsolin cross-beta-sheet oligomers and accelerates amyloidogenesis by hastening fibril extension. *Biochemistry 50*: 2486-2498.

Soto C (2003) Unfolding the role of protein misfolding in neurodegenerative diseases. *Nat Rev Neurosci 4*: 49-60.

Sparks S, Liu G, Robbins KJ et Lazo ND (2012) Curcumin modulates the self-assembly of the islet amyloid polypeptide by disassembling alpha-helix. *Biochem Biophys Res Commun 422*: 551-555.

Srivastava OP, Srivastava K, Chaves JM et Gill AK (2017) Post-translationally modified human lens crystallin fragments show aggregation in vitro. *Biochemistry and biophysics reports 10*: 94-131.

Stefani M (2010) Biochemical and biophysical features of both oligomer/fibril and cell membrane in amyloid cytotoxicity. *FEBS J 277*: 4602-4613.

Stefani M (2012) Structural features and cytotoxicity of amyloid oligomers: implications in Alzheimer's disease and other diseases with amyloid deposits. *Prog Neurobiol 99*: 226-245.

Stroud JC, Liu C, Teng PK et Eisenberg D (2012) Toxic fibrillar oligomers of amyloid-β have cross-β structure. *Proc Natl Acad Sci U S A 109*: 7717.

Stsiapura VI, Maskevich AA, Kuzmitsky VA, Turoverov KK et Kuznetsova IM (2007) Computational study of thioflavin T torsional relaxation in the excited state. *J Phys Chem A 111*: 4829-4835.

Subramanian SL, Hull RL, Zraika S, Aston-Mourney K, Udayasankar J et Kahn SE (2012) cJUN N-terminal kinase (JNK) activation mediates islet amyloid-induced beta cell apoptosis in cultured human islet amyloid polypeptide transgenic mouse islets. *Diabetologia 55*: 166-174.

Sudharsan R et Beltran WA (2019) Progress in Gene Therapy for Rhodopsin Autosomal Dominant Retinitis Pigmentosa. *Adv Exp Med Biol 1185*: 113-118.

Sunde M et Blake C (1997) The structure of amyloid fibrils by electron microscopy and X-ray diffraction. *Adv Protein Chem 50*: 123-159.

Thakarakkattil Narayanan Nair A, Donnelly LA, Dawed AY, Gan S, Anjana RM, Viswanathan M, Palmer CNA et Pearson ER (2020) The impact of phenotype, ethnicity and genotype on progression of type 2 diabetes mellitus. *Endocrinology, diabetes & metabolism 3*: e00108-e00108.

Tipping KW, van Oosten-Hawle P, Hewitt EW et Radford SE (2015) Amyloid fibres: Inert end-stage aggregates or key players in disease? *Trends Biochem Sci 40*: 719-727.

Tomiyama T, Kaneko H, Kataoka K, Asano S et Endo N (1997) Rifampicin inhibits the toxicity of pre-aggregated amyloid peptides by binding to peptide fibrils and preventing amyloid-cell interaction. *Biochem J 322 (Pt 3)*: 859-865.

Tomiyama T, Nagata T, Shimada H, Teraoka R, Fukushima A, Kanemitsu H, Takuma H, Kuwano R, Imagawa M, Ataka S, et al. (2008) A new amyloid beta variant favoring oligomerization in Alzheimer's-type dementia. *Ann Neurol 63*: 377-387.

Tornquist M, Michaels TCT, Sanagavarapu K, Yang X, Meisl G, Cohen SIA, Knowles TPJ et Linse S (2018) Secondary nucleation in amyloid formation. *Chem Commun (Camb) 54*: 8667-8684.

Tracz SM, Abedini A, Driscoll M et Raleigh DP (2004) Role of aromatic interactions in amyloid formation by peptides derived from human Amylin. *Biochemistry 43*: 15901-15908.

Trikha S et Jeremic AM (2011) Clustering and internalization of toxic amylin oligomers in pancreatic cells require plasma membrane cholesterol. *J Biol Chem 286*: 36086-36097.

Tsigelny IF, Sharikov Y, Wrasidlo W, Gonzalez T, Desplats PA, Crews L, Spencer B et Masliah E (2012) Role of α-synuclein penetration into the membrane in the mechanisms of oligomer pore formation. *FEBS J 279*: 1000-1013.

Tu L-H et Raleigh DP (2013a) The role of aromatic interactions in amyloid formation by islet amyloid polypeptide. *Biochemistry 52*: 333-342.

Tu L-H, Serrano Arnaldo L, Zanni Martin T et Raleigh Daniel P (2014a) Mutational analysis of preamyloid intermediates: The role of His-Tyr interactions in Islet Amyloid Formation. *Biophysl J 106*: 1520-1527.

Tu LH, Noor H, Cao P et Raleigh DP (2014b) Aspirin, diabetes, and amyloid: re-examination of the inhibition of amyloid formation by aspirin and ketoprofen. *ACS Chem Biol 9*: 1632-1637.

Tu LH et Raleigh DP (2013b) Role of aromatic interactions in amyloid formation by islet amyloid polypeptide. *Biochemistry 52*: 333-342.

Tucker S, Moller C, Tegerstedt K, Lord A, Laudon H, Sjodahl J, Soderberg L, Spens E, Sahlin C, Waara ER, et al. (2015) The murine version of BAN2401 (mAb158) selectively reduces amyloid-beta protofibrils in brain and cerebrospinal fluid of tg-ArcSwe mice. *J Alzheimers Dis 43*: 575-588.

Turner MS, Briehl RW, Ferrone FA et Josephs R (2003) Twisted protein aggregates and disease: the stability of sickle hemoglobin fibers. *Phys Rev Lett 90*: 128103.

Tycko R (2015) Amyloid polymorphism: structural basis and neurobiological relevance. *Neuron 86*: 632-645.

Tycko R et Wickner RB (2013) Molecular structures of amyloid and prion fibrils: consensus versus controversy. *Acc Chem Res 46*: 1487-1496.

Ueda M, Yamashita T, Misumi Y, Masuda T et Ando Y (2018) Origin of sporadic late-onset hereditary ATTR Val30Met amyloidosis in Japan. *Amyloid 25*: 143-147.

Uttara B, Singh AV, Zamboni P et Mahajan RT (2009) Oxidative stress and neurodegenerative diseases: a review of upstream and downstream antioxidant therapeutic options. *Curr Neuropharmacol 7*: 65-74.

Uversky VN, Li J et Fink AL (2001) Evidence for a partially folded intermediate in alpha-synuclein fibril formation. *J Biol Chem 276*: 10737-10744.

Vassar PS et Culling CF (1959) Fluorescent stains, with special reference to amyloid and connective tissues. *Arch Pathol 68*: 487-498.

Vignaud H, Cullin C et Bouchecareilh M (2015) [Alpha-1 antitrypsin deficiency: A model of alteration of protein homeostasis or proteostasis]. *Rev Mal Respir 32*: 1059-1071.

Vivoli Vega M, Cascella R, Chen SW, Fusco G, De Simone A, Dobson CM, Cecchi C et Chiti F (2019) The toxicity of misfolded protein oligomers is independent of their secondary structure. *ACS Chem Biol 14*: 1593-1600.

Voropai ES, Samtsov MP, Kaplevskii KN, Maskevich AA, Stepuro VI, Povarova OI, Kuznetsova IM, Turoverov KK, Fink AL et Uverskii VN (2003) Spectral properties of thioflavin T and its complexes with amyloid fibrils. *Journal of Applied Spectroscopy 70*: 868-874.

Wang H, Shu Q, Frieden C et Gross ML (2017) Deamidation slows curli amyloid-protein aggregation. *Biochemistry 56*: 2865-2872.

Wang J, Xu J, Finnerty J, Furuta M, Steiner DF et Verchere CB (2001) The prohormone convertase enzyme 2 (PC2) is essential for processing pro-islet amyloid polypeptide at the NH2-terminal cleavage site. *Diabetes 50*: 534-539.

Wang L, Ilitchev AI, Giammona MJ, Li F, Buratto SK et Bowers MT (2016) Human Islet Amyloid Polypeptide assembly: The key role of the 8-20 fragment. *J Phys Chem B 120*: 11905-11911.

Wang L, Li Y, Lu T et Li F (2014a) The effects of organic solvents on the membrane-induced fibrillation of human islet amyloid polypeptide and on the inhibition of the fibrillation. *BBA 1838*: 3162-3170.

Wang Q, Guo J, Jiao P, Liu H et Yao X (2014b) Exploring the influence of EGCG on the β-Sheet-rich oligomers of human Islet Amyloid Polypeptide (hIAPP1–37) and identifying its possible binding sites from molecular dynamics simulation. *PLoS ONE 9*: e94796.

Wang Z, Natte R, Berliner JA, van Duinen SG et Vinters HV (2000) Toxicity of Dutch (E22Q) and Flemish (A21G) mutant amyloid beta proteins to human cerebral microvessel and aortic smooth muscle cells. *Stroke 31*: 534-538.

Wasiak T, Ionov M, Nieznanski K, Nieznanska H, Klementieva O, Granell M, Cladera J, Majoral JP, Caminade AM et Klajnert B (2012) Phosphorus dendrimers affect Alzheimer's (Abeta1-28) peptide and MAP-Tau protein aggregation. *Mol Pharm 9*: 458-469.

Watt B, van Niel G, Fowler DM, Hurbain I, Luk KC, Stayrook SE, Lemmon MA, Raposo G, Shorter J, Kelly JW, et al. (2009) N-terminal domains elicit formation of functional Pmel17 amyloid fibrils. *J Biol Chem 284*: 35543-35555.

Watt B, van Niel G, Raposo G et Marks MS (2013) PMEL: a pigment cell-specific model for functional amyloid formation. *Pigment Cell Melanoma Res 26*: 300-315.

Wei L, Jiang P, Xu W, Li H, Zhang H, Yan L, Chan-Park MB, Liu XW, Tang K, Mu Y, et al. (2011) The molecular basis of distinct aggregation pathways of islet amyloid polypeptide. *J Biol Chem 286*: 6291-6300.

Westermark P (1972) Quantitative studies on amyloid in the islets of Langerhans. *Ups J Med Sci 77*: 91-94.

Westermark P (2011) Amyloid in the islets of Langerhans: thoughts and some historical aspects. *Ups J Med Sci 116*: 81-89.

Westermark P, Andersson A et Westermark GT (2011) Islet amyloid polypeptide, islet amyloid, and diabetes mellitus. *Physiol Rev 91*: 795-826.

Westermark P, Engström U, Johnson KH, Westermark GT et Betsholtz C (1990) Islet amyloid polypeptide: pinpointing amino acid residues linked to amyloid fibril formation. *Proc Natl Acad Sci U S A 87*: 5036-5040.

Westermark P, Li ZC, Westermark GT, Leckstrom A et Steiner DF (1996) Effects of beta cell granule components on human islet amyloid polypeptide fibril formation. *FEBS Lett 379*: 203-206.

Westermark P, Wernstedt C, Wilander E, Hayden DW, O'Brien TD et Johnson KH (1987) Amyloid fibrils in human insulinoma and islets of Langerhans of the diabetic cat are derived from a neuropeptide-like protein also present in normal islet cells. *Proc Natl Acad Sci U S A 84*: 3881-3885.

Westwell-Roper C, Dai DL, Soukhatcheva G, Potter KJ, van Rooijen N, Ehses JA et Verchere CB (2011) IL-1 blockade attenuates islet amyloid polypeptide-induced proinflammatory cytokine release and pancreatic islet graft dysfunction. *J Immunol 187*: 2755-2765.

Williamson JA, Loria JP et Miranker AD (2009) Helix stabilization precedes aqueous and bilayer-catalyzed fiber formation in islet amyloid polypeptide. *J Mol Biol 393*: 383-396.

Williamson JA et Miranker AD (2007) Direct detection of transient alpha-helical states in islet amyloid polypeptide. *Protein Sci 16*: 110-117.

Wiltzius JJ, Sievers SA, Sawaya MR, Cascio D, Popov D, Riekel C et Eisenberg D (2008) Atomic structure of the cross-beta spine of islet amyloid polypeptide (amylin). *Protein Sci 17*: 1467-1474.

Wiltzius JJW, Sievers SA, Sawaya MR et Eisenberg D (2009) Atomic structures of IAPP (amylin) fusions suggest a mechanism for fibrillation and the role of insulin in the process. *Protein Sci 18*: 1521-1530.

Wimalawansa SJ (1997) Amylin, calcitonin gene-related peptide, calcitonin, and adrenomedullin: a peptide superfamily. *Crit Rev Neurobiol 11*: 167-239.

Wineman-Fisher V, Tudorachi L, Nissim E et Miller Y (2016) The removal of disulfide bonds in amylin oligomers leads to the conformational change of the 'native' amylin oligomers. *Phys Chem Chem Phys 18*: 12438-12442.

Winklhofer KF et Haass C (2010) Mitochondrial dysfunction in Parkinson's disease. *BBA 1802*: 29-44.

Winklhofer KF, Tatzelt J et Haass C (2008) The two faces of protein misfolding: gain- and loss-of-function in neurodegenerative diseases. *EMBO J 27*: 336-349.

Winner B, Jappelli R, Maji SK, Desplats PA, Boyer L, Aigner S, Hetzer C, Loher T, Vilar M, Campioni S, et al. (2011) In vivo demonstration that alpha-synuclein oligomers are toxic. *Proc Natl Acad Sci U S A 108*: 4194-4199.

Wobst HJ, Sharma A, Diamond MI, Wanker EE et Bieschke J (2014) The green tea polyphenol (-)-epigallocatechin gallate prevents the aggregation of tau protein into toxic oligomers at substoichiometric ratios. *FEBS Lett 589(1)*: 77-83.

Wong AG, Wu C, Hannaberry E, Watson MD, Shea J-E et Raleigh DP (2016) Analysis of the amyloidogenic potential of pufferfish (Takifugu rubripes) islet amyloid polypeptide highlights the limitations of thioflavin-T assays and the difficulties in defining amyloidogenicity. *Biochemistry 55*: 510-518.

Wu C, Lei H, Wang Z, Zhang W et Duan Y (2006) Phenol red interacts with the protofibril-like oligomers of an amyloidogenic hexapeptide NFGAIL through both hydrophobic and aromatic contacts. *Biophys J 91*: 3664-3672.

Wu C et Shea J-E (2013) Structural similarities and differences between amyloidogenic and non-amyloidogenic islet amyloid polypeptide (IAPP) sequences and implications for the dual physiological and pathological activities of these peptides. *PLoS computational biology 9*: e1003211-e1003211.

Wu L, Rosa-Neto P, Hsiung GY, Sadovnick AD, Masellis M, Black SE, Jia J et Gauthier S (2012) Early-onset familial Alzheimer's disease (EOFAD). *Can J Neurol Sci 39*: 436-445.

Wu Y, Ding Y, Tanaka Y et Zhang W (2014) Risk factors contributing to type 2 diabetes and recent advances in the treatment and prevention. *Int J Med Sci 11*: 1185-1200.

Wyant KJ, Ridder AJ et Dayalu P (2017) Huntington's Disease-Update on Treatments. *Curr Neurol Neurosci Rep 17*: 33.

Xu F, Fu Z, Dass S, Kotarba AE, Davis J, Smith SO et Van Nostrand WE (2016) Cerebral vascular amyloid seeds drive amyloid β-protein fibril assembly with a distinct anti-parallel structure. *Nat Commun 7*: 13527.

Yamamoto Y, Kurihara N, Egawa T, Shimada H et Ishimura Y (1999) Hydrogen bonding interaction of the amide group of Asn and Gln at distal E7 of bovine myoglobin with bound-ligand and its functional consequences. *BBA 1433*: 27-44.

Yan LM, Tatarek-Nossol M, Velkova A, Kazantzis A et Kapurniotu A (2006) Design of a mimic of nonamyloidogenic and bioactive human islet amyloid polypeptide (IAPP) as nanomolar affinity inhibitor of IAPP cytotoxic fibrillogenesis. *Proc Natl Acad Sci U S A 103*: 2046-2051.

Yang G, Wu L, Chen G et Jiang M (2016) Precise protein assembly of array structures. *Chem Commun 52*: 10595-10605.

Yang T, Li S, Xu H, Walsh DM et Selkoe DJ (2017) Large soluble oligomers of amyloid β-protein from Alzheimer brain are far less neuroactive than the smaller oligomers to which they dissociate. *The Journal of neuroscience 37*: 152-163.

Yazaki M, Liepnieks JJ, Barats MS, Cohen AH et Benson MD (2003) Hereditary systemic amyloidosis associated with a new apolipoprotein AII stop codon mutation Stop78Arg. *Kidney Int 64*: 11-16.

Yonemoto IT, Kroon GJA, Dyson HJ, Balch WE et Kelly JW (2008) Amylin proprotein processing generates progressively more amyloidogenic peptides that initially sample the helical state. *Biochemistry 47*: 9900-9910.

Young ID, Ailles L, Narindrasorasak S, Tan R et Kisilevsky R (1992) Localization of the basement membrane heparan sulfate proteoglycan in islet amyloid deposits in type II diabetes mellitus. *Arch Pathol Lab Med 116*: 951-954.

Young LM, Cao P, Raleigh DP, Ashcroft AE et Radford SE (2014) Ion mobility spectrometry-mass spectrometry defines the oligomeric intermediates in amylin amyloid formation and the mode of action of inhibitors. *JACS 136*: 660-670.

Youssef SA, Capucchio MT, Rofina JE, Chambers JK, Uchida K, Nakayama H et Head E (2016) Pathology of the aging brain in domestic and laboratory animals,

and animal models of human neurodegenerative diseases. *Veterinary Pathology 53*: 327-348.

Zaman M, Khan AN, Wahiduzzaman, Zakariya SM et Khan RH (2019) Protein misfolding, aggregation and mechanism of amyloid cytotoxicity: An overview and therapeutic strategies to inhibit aggregation. *Int J Biol Macromol 134*: 1022-1037.

Zandomeneghi G, Krebs MR, McCammon MG et Fandrich M (2004) FTIR reveals structural differences between native beta-sheet proteins and amyloid fibrils. *Protein Sci 13*: 3314-3321.

Zhang J, Tan J, Pei R et Ye S (2020) Acidic environment significantly alters aggregation pathway of human Islet Amyloid Polypeptide at negative lipid membrane. *Langmuir 36*: 1530-1537.

Zhang S, Liu H, Yu H et Cooper GJ (2008) Fas-associated death receptor signaling evoked by human amylin in islet beta-cells. *Diabetes 57*: 348-356.

Zhang X, St Clair JR, London E et Raleigh DP (2017) Islet Amyloid Polypeptide membrane interactions: Effects of membrane composition. *Biochemistry 56*: 376-390.

Zhen DB, Swiecicki PL, Zeldenrust SR, Dispenzieri A, Mauermann ML et Gertz MA (2015) Frequencies and geographic distributions of genetic mutations in transthyretin- and non-transthyretin-related familial amyloidosis. *Clin Genet 88*: 396-400.

Zottig X, Al-Halifa S, Babych M, Quittot N, Archambault D et Bourgault S (2019) Guiding the morphology of amyloid assemblies by electrostatic capping: from polymorphic twisted fibrils to uniform nanorods. *Small 15*: e1901806.

Zuniga RN, Tolkach A, Kulozik U et Aguilera JM (2010) Kinetics of formation and physicochemical characterization of thermally-induced beta-lactoglobulin aggregates. *J Food Sci 75*: E261-268.

ANNEXE I

Low generation anionic dendrimers modulate islet amyloid polypeptide self-assembly and inhibit pancreatic β-cell toxicity

Phuong T. Nguyen[a,b], Rishi Sharma[a], Rabindra Rej[a], Carole Anne De Carufel[a,b], René Roy*[a] and Steve Bourgault*[a,b]

[a]*Department of Chemistry, Pharmaqam, University of Québec in Montreal, Montreal, QC, Canada, H3C 3P8*
[b]*Quebec Network for Research on Protein Function, Structure, and Engineering, PROTEO*

***Corresponding authors**:

Pr. Steve Bourgault

Université du Québec à Montréal

C.P. 8888, Succursale Centre-Ville

Montréal (Québec), H3C 3P8, Canada

1-514-987-3000 (5161)

bourgault.steve@uqam.ca

Pr. René Roy

Université du Québec à Montréal

C.P. 8888, Succursale Centre-Ville

Montréal (Québec), H3C 3P8, Canada

1-514-987-3000 (2546)

roy.rene@uqam.ca

General approach for synthesis of low generation dendrimers:

All reactions in organic medium were performed in standard oven dried glassware under an inert atmosphere of nitrogen using freshly distilled solvents. Solvents and reagents were deoxygenated when necessary by purging with nitrogen. Water used for lyophilization of final dendrimers was nanopure grade, purified through Barnstead NANOPure II Filter with Barnstead MegOhm-CM Sybron meter. All reagents were used as supplied without prior purification unless otherwise stated, and obtained from Sigma-Aldrich Chemical Co. Ltd. Reactions were monitored by analytical thin-layer chromatography using silica gel 60 F254 precoated plates (E. Merck). Purifications were performed by flash column chromatography using silica gel from Silicycle (60 Å, 40-63 μm) with the indicated eluent.

^{1}H NMR and ^{13}C NMR spectra were recorded at 300 or 600 MHz and 75 or 150 MHz, respectively, on a Bruker spectrometer (300 MHz) and (600 MHz). All NMR spectra were measured at 25°C in indicated deuterated solvents. Proton and carbon chemical shifts (δ) are reported in ppm and coupling constants (J) are reported in Hertz (Hz). The resonance multiplicity in the ^{1}H NMR spectra are described as “s” (singlet), “d” (doublet), “t” (triplet), “quint” (quintuplet) and “m” (multiplet) and broad resonances are indicated by “br”. Residual protic solvent of $CDCl_3$ (^{1}H, δ 7.27 ppm; ^{13}C, δ 77.0 ppm (central resonance of the triplet)), D_2O (^{1}H, δ 4.79 ppm and 30.9 ppm for CH_3 of Acetone for ^{13}C spectra), MeOD (^{1}H, δ 3.31 ppm and ^{13}C, δ 49.0 ppm). 2D Homonuclear correlation 1H-1H COSY experiments were used to confirm NMR peak assignments. Fourier transform infrared (FTIR) spectra were obtained with Thermo-scientific, Nicolet model 6700 equipped with ATR. The absorptions are given in wavenumbers (cm^{-1}). The intensity of the bands is described as s (strong), m (medium) or w (weak).

Accurate mass measurements (HRMS) were performed on a LC-MSD-ToF instrument from Agilent Technologies in positive electrospray mode. Low-resolution mass spectra were performed on the same apparatus or on a LCQ Advantage ion trap instrument from Thermo Fisher Scientific in positive electrospray mode (Plateforme analytique pour molécules organiques (Université du Québec à Montréal), Québec, Canada). Either protonated molecular ions $[M+nH]^{n+}$ or adducts $[M+nX]^{n+}$ (X = Na, K, NH_4) were used for empirical formula confirmation. MALDI-TOF experiments were performed on an Autoflex III from Brucker Smarteam in linear positive mode (Mass Spectrometry Laboratory (McGill University)) to afford adducts $[M+nX]^{n+}$ (X = Na, K or Li). Samples were solubilized in H_2O for a final concentration of 6 mg/mL. Dihydroxybenzoic acid (DHB) was used as the matrix. Cationization was eased by the use of the corresponding sodium salt (2mg/mL).

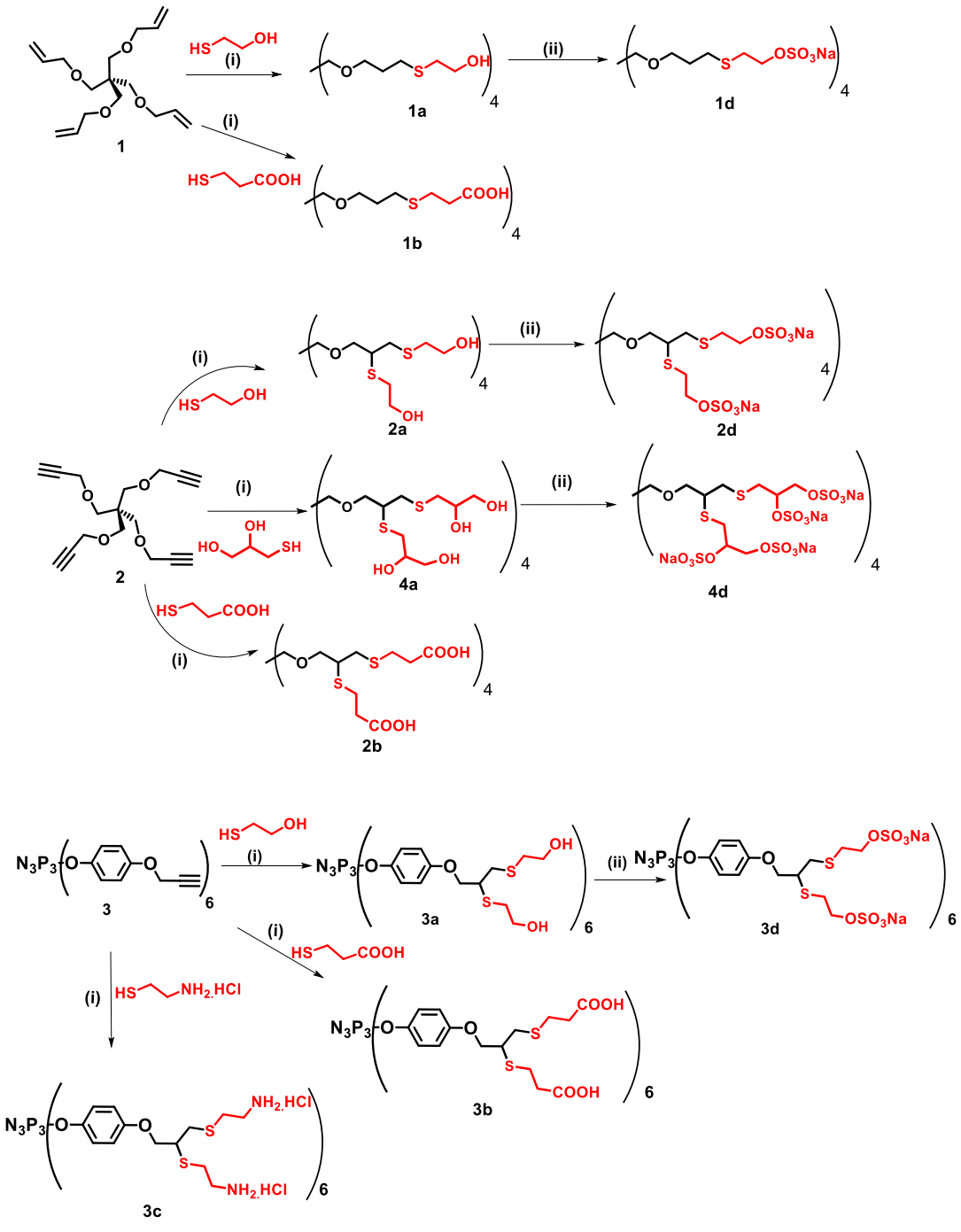
Results and discussion of low generation dendrimers synthesis:

Starting from tetrakis-allylpentaerythritol core (1; Scheme 1), we first performed radical induced photolytic addition of 2-mercaptoethanol under standard thiol-ene click conditions to obtain compound (**1a**) (Sharma *et al.*, 2014). The reaction of (1) with 3-mercaptopropionic acid using similar conditions provided tetra-carboxylic acid derivative (**1b**) in decent yield (78%). In the NMR spectrum of the product (**1b**) signals analogous to allylic group from parent core molecule disappeared completely and a singlet was observed corresponding to carboxylic acid around 11.36 δ which confirming the 100% completion of the reaction. I.R spectrum also showed strong O-H stretching band in at 2800-3000 cm^{-1}. Tetrahydroxylated compound (**1a**) was further subjected to sulfation using sulphur trioxide pyridine complex in DMF at 60°C for 24 h. The resulting tetra-sulfated compound (**1d**) was isolated in 71% yield; after purification of the reaction mixture by dialysis. The ^1H NMR spectrum of (**1d**) showed a downfield shift from 3.74 to 4.25 ppm for -CH_2- peak present adjacent to hydroxyl

group. HRMS (ESI-MS) also confirmed the desired product with a sharp dominant peak at 1016.0075 (calculated 1016.0095).

For the enhancement of number of surface groups we further utilized thiol-yne click reaction to build dendrimers. Thiol-yne click is radical initiated hydrothiolation reaction where two thiols are added over an alkyne bond; and due to this advantage it is an effective tool for rapid construction of complex macromolecules. The photoaddition of 2-mercaptoethanol , 1-thioglycerol and 3-mercaptopropionic acid to tetrapropargylated pentaerythritol (2) yielded G1 dendrimers **2a**(Sharma *et al.*, 2014), **4a**, **2b** harboring 8,16 hydroxyl groups and 8 carboxylic acids, respectively. The ^{1}H NMR spectra clearly illustrated completion of click reaction by entire disappearance of propargyl function from core around 2.5 ppm. Hydroxyl terminated dendrimers **2a** and **4a** were finally transformed into sulfates 2d and 4d using sulphur trioxide pyridine complex. Degree of sulfation was calculated with the help of ^{1}H NMR spectra. We observed for dendrimer **2d** which consists of 8 hydroxyl groups, only six were converted to sulfates. The CH_2 which are alpha to hydroxyl group shifted downfield from 3.79 to 4.21 ppm but this downfield shift is experienced by only 12 protons. It is observed that two CH_2 are still unmoved or unchanged from their previous position. In the case of dendrimer **4d** we found that only 12 hydroxyl groups are transformed into sulfates and leaving 4 of the secondary OHs are not transformed to sulfates as we observed downfield signal at 4.70 ppm corresponding to 4 protons (CH-OH).

We further selected rigid hexapropargyl cyclotriphosphazene core for our next series of (G1) dendrimers. Once again thiol-yne reaction was performed using commercially available 2-mercaptoethanol, 3-mercaptopropionic acid and cysteamine hydrochloride which provided us dendrimers with 12 peripheral hydroxyl (**3a**), carboxylic acid (**3b**)(Sharma *et al.*, 2014) and amine (**3c**) groups in decent yields. Upon completion signals due to propargyllic protons were not found in any case which confirmed defect free products. Moreover a singlet was observed in ^{13}P NMR of these products which determines the monodispersity of these dendrimers. High resolution mass spectrometry (ESI) confirmed the formation of products with dominant signal at calculated values. Finally polyhydroxy (**G1**) dendrimer **3a** was subjected to sulfation using excess of SO_3.Py in DMF for 36 hours to yield sulfated dendrimer (**3d**). ^1H NMR spectrum suggests that only 9-10 OH groups were converted to sulfates as we observed 2 to 3 – CH_2- groups still unmoved from their previous position of 3.70 δ. All the dendrimers were achieved rapidly in decent yields with ease, bypassing any protection /deprotection steps without intensive purification procedures. The additional advantage of these hydroxyl, carboxylic acid and amine based dendrimers comes from the fact that all the dendrimers have terminal reactive functionalities on the surface which can be easily utilised as a platform for the preparation of highly branched dendritic structures. This work is under investigation and will be covered in future.



Scheme 1 Reaction conditions and reagents: (i) DMPAP (10 mol%),UV 365 nm, DMF, rt, 12 h; (ii) SO3.Py,DMF, 60^{o}C, 24-36 h.

Synthesis and characterization of low generation dendrimers:

General procedure for thiol-ene, thiol-yne click reaction and sulfation:

Procedure A for thiol-ene:

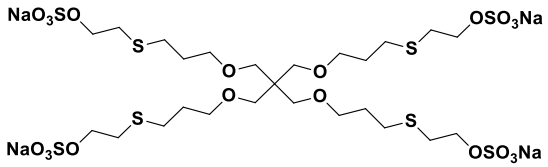
To a stirred solution of alkene derivative (1.0 eq.), 2,2'-dimethoxy-2-phenylacetophenone (DMPA) (10 mol %) in dry DMF (0.2 ml/mmol) was added thiol derivative (excess per alkene) under nitrogen. The vial was then purged with N_2 for 10 min and irradiated for 12 hrs using UV lamp at room temperature *(classical glassware, UV lamp (365 nm, Model UVGL-58 MINERALIGHT® LAMP) in a cardboard box)*. Upon completion of the reaction, the solvent was removed under vacuum and the residue was subsequently washed three times with diethyl ether to remove excess of thiol and disulphide formed during the reaction, affording a clear viscous liquid. The crude product was further purified by column chromatography over silica gel or through dialysis.

Procedure B for thiol-yne:

To a stirred solution of alkyne derivative (1.0 eq.), 2,2'-dimethoxy-2-phenylacetophenone (DMPA) (10 mol %) in dry DMF (0.2 ml/mmol) was added thiol derivative (excess per alkyne) under nitrogen. The vial was then purged with N_2 for 10 min and irradiated for 12 hrs using UV lamp at room temperature *(classical glassware, UV lamp (365 nm, Model UVGL-58 MINERALIGHT® LAMP) in a cardboard box)*. Upon completion of the reaction, the solvent was removed under vacuum and the residue was subsequently washed three times with diethyl ether to remove excess of thiol and disulphide formed during the reaction, affording a clear viscous liquid. The crude product was further purified by column chromatography over silica gel or through dialysis.

Procedure C for Sulfation:

To a solution of polyhydroxy compound in 10 ml dry DMF, sulfur trioxide pyridine complex (6 eq. per hydroxyl) was added, and the mixture was stirred over 24- 36 h at 60 ^{o} C. After removal of the solvent, crude mixture was redissolved in distilled water and 1M NaOH solution was added until a pH of 10 was reached. Crude mixture was further purified by dialysis in water (MWCO: 500-2000 based on M.Wt). Dialysed products were lyophilized.



Synthesis of compound 1d:

Compound **1a** (500mg, 0.821 mmol) and sulfur trioxide pyridine complex (2612mg, 16.42 mmol, 5 eq. per hydroxyl) were reacted together following the procedure C. Crude mixture was further purified by dialysis against water using 500 molecular weight cut-off dialysis tubing. Dialysed product was lyophilized to yield compound **1d,** yield**:** 71%.

^{1}H NMR (300 MHz, D_2O): δ (ppm) 4.32 - 4.16 (m, 8H), 3.68 – 3.57 (m, 8H), 3.47 (br s, 8H), 2.94 (t, *J* = 5.7 Hz, 8H), 2.74 (d, *J* = 6.1 Hz, 8H), 1.95 (d, *J* = 6.7 Hz, 8H).

^{13}C NMR (151 MHz, D_2O): δ (ppm): 70.4, 68.3, 63.0, 31.2, 29.1, 28.8.
HRMS (ESI^{+}-TOF): Calculated for $C_{25}H_{48}Na_4O_{20}S_8$: 1016.0095, found: 1016.0075.
IR (cm^{-1}): 3459, 2920, 2863, 1634, 1107, 1067, 973, 883, 750.

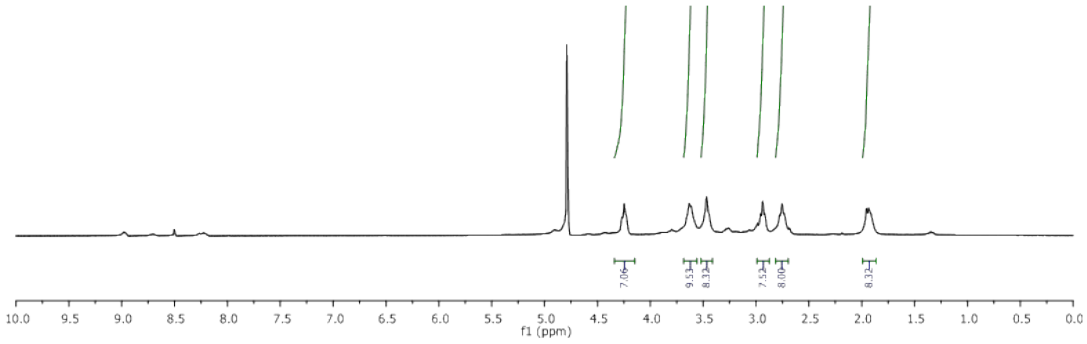


Figure S1. ^{1}HNMR spectrum of compound **1d** (D_2O, 300 MHz).

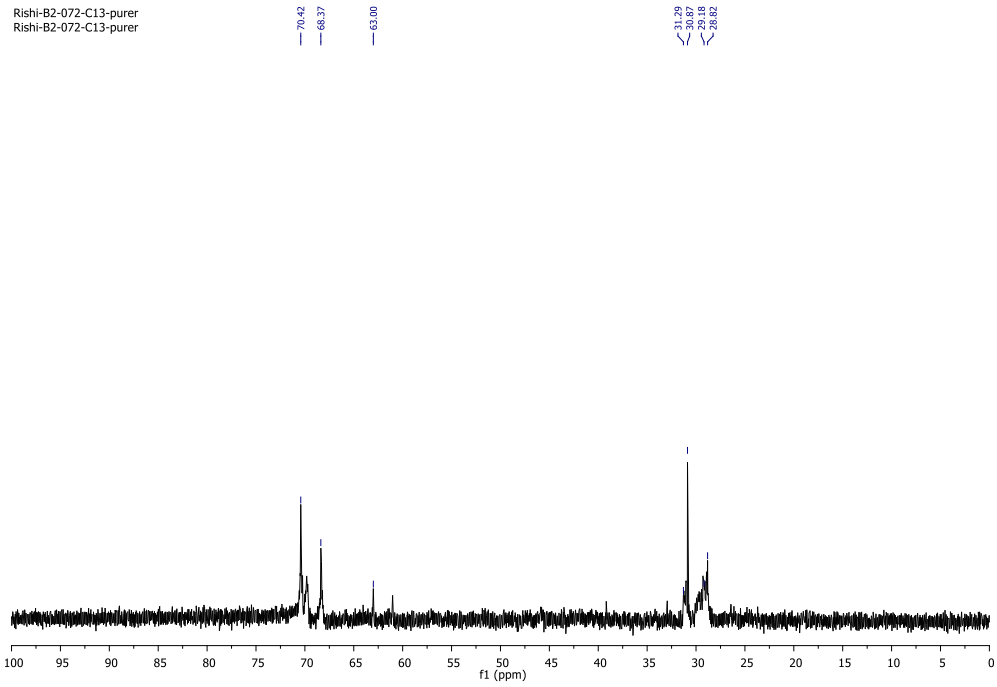


Figure S2. ^{13}CNMR spectrum of compound **1d** (D_2O, 151 MHz).

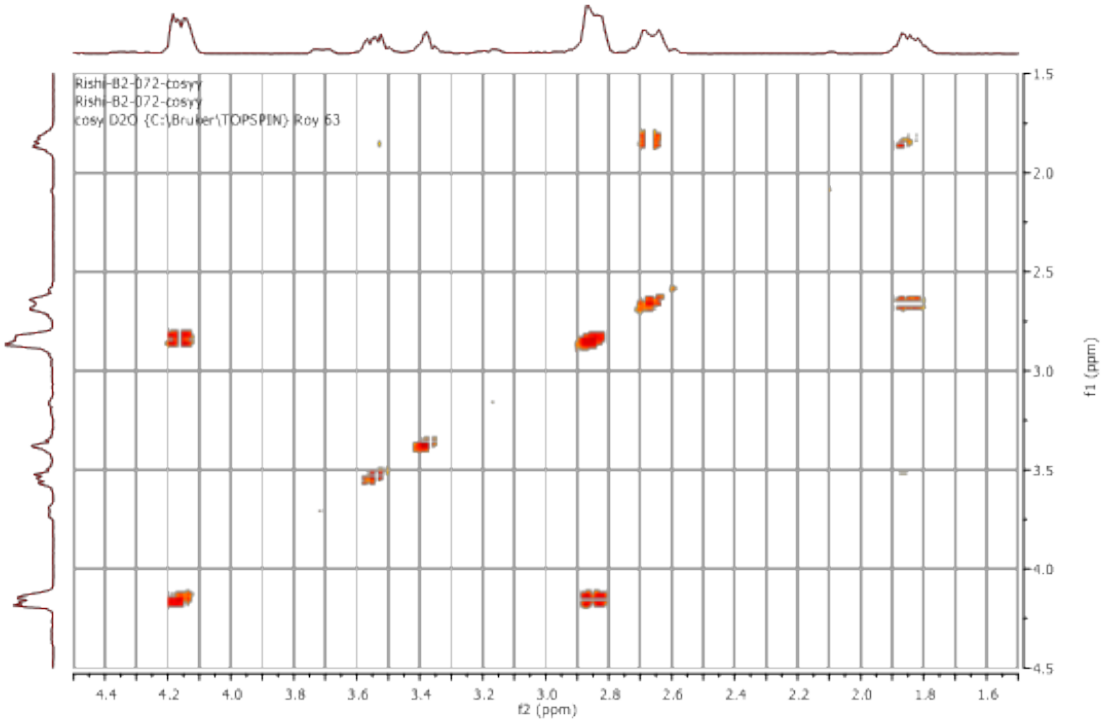


Figure S3. COSY spectrum of compound **1d.**

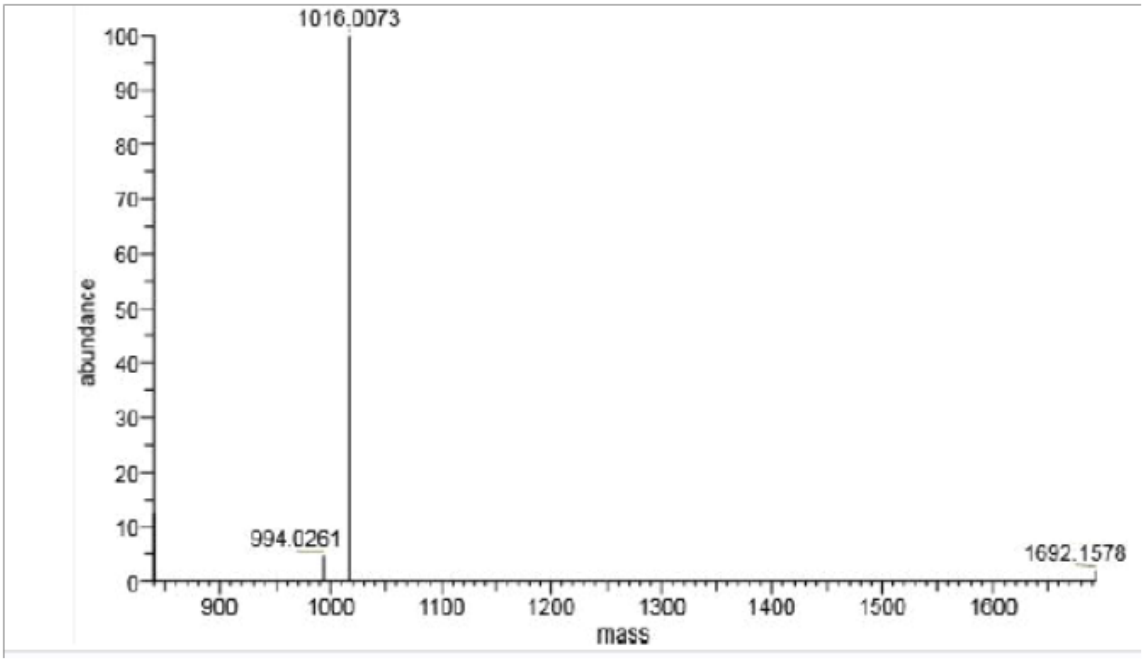


Figure S4. HRMS analysis (ESI^+) for compound **1d.**

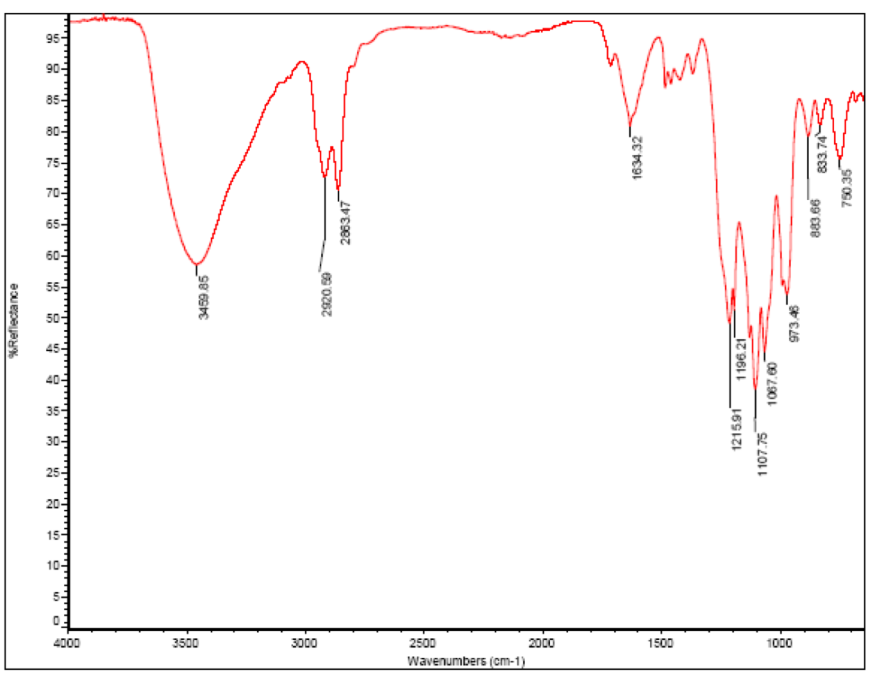
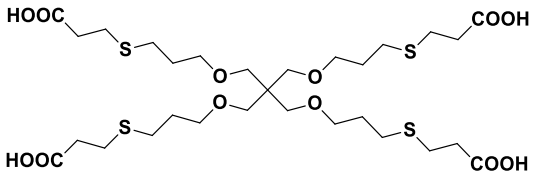


Figure S5. IR spectrum of compound **1d.**



Synthesis of compound 1b:
Tetraallyl pentaerythritol **1** (500 mg, 1.68 mmol) and 3-mercaptopropanoic acid (2.9 ml, 33.7mmol, 5 eq. per site) were reacted according to procedure **A**. Crude mixture was purified by passing through a column of silica gel using 4-8% MeOH in DCM as eluents. The final compound was recovered as white solid. (yield:78%).
^{1}H NMR (300 MHz, $CDCl_3$) δ 11.36 (s, 4H), 3.46 (t, *J* = 5.5 Hz, 8H), 3.36 (d, *J* = 8.0 Hz, 8H), 2.85 – 2.72 (m, 8H), 2.71 – 2.54 (m,16H), 1.91 – 1.71 (m, 8H,).
^{13}C NMR (151 MHz, CDCl3): δ178.0, 69.8, 69.5, 45.4, 35.1, 29.6, 29.0, 26.8.
IR (cm^{-1}): 2934, 2871, 1655, 1420, 1108, 927.

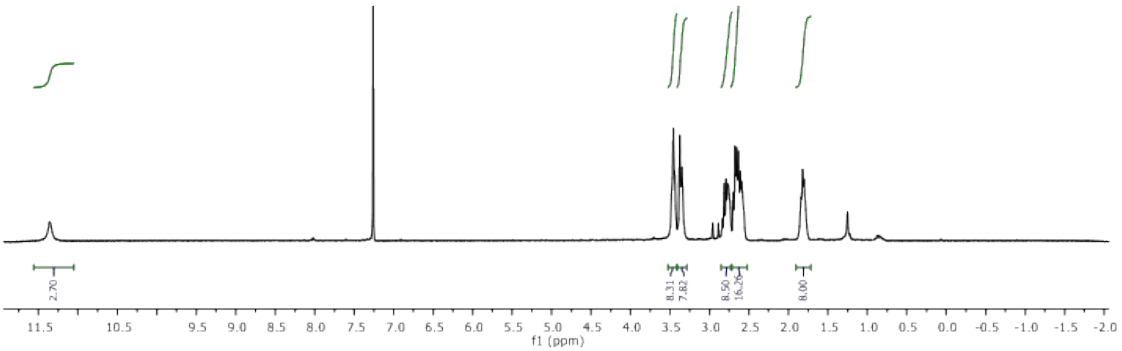


Figure S6 ^{1}HNMR spectrum of compound **1b** ($CDCl_3$, 300 MHz)

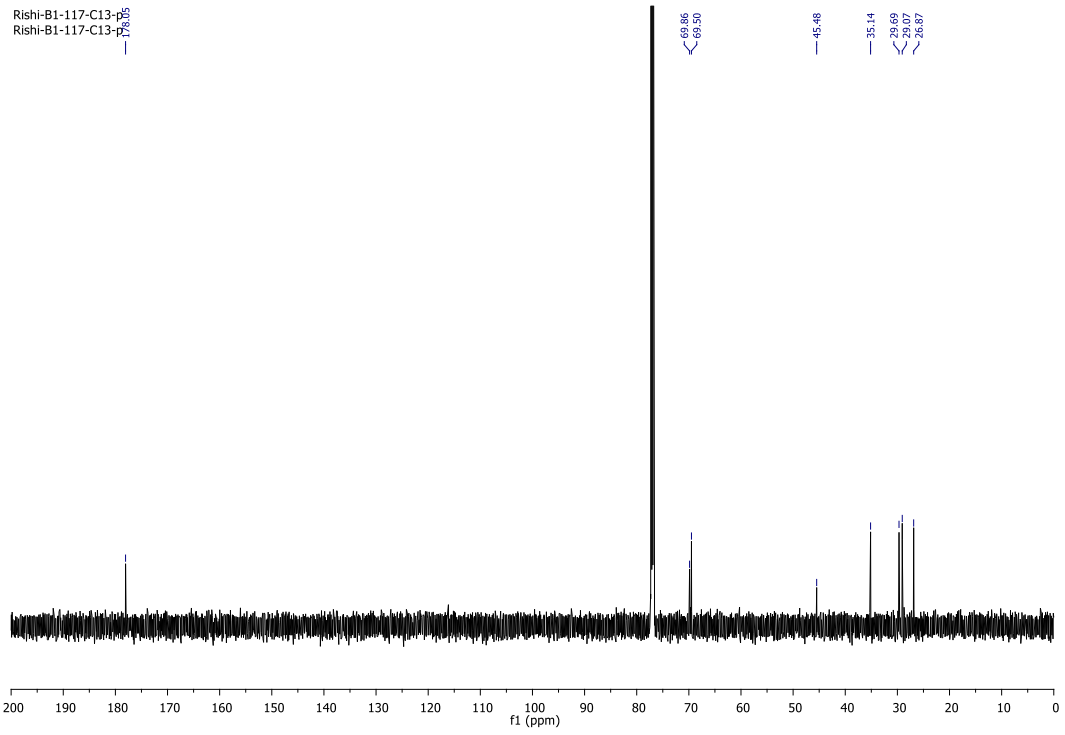


Figure S7. ^{13}C NMR spectrum of compound **1b** (CD_3Cl_3, 151 MHz)

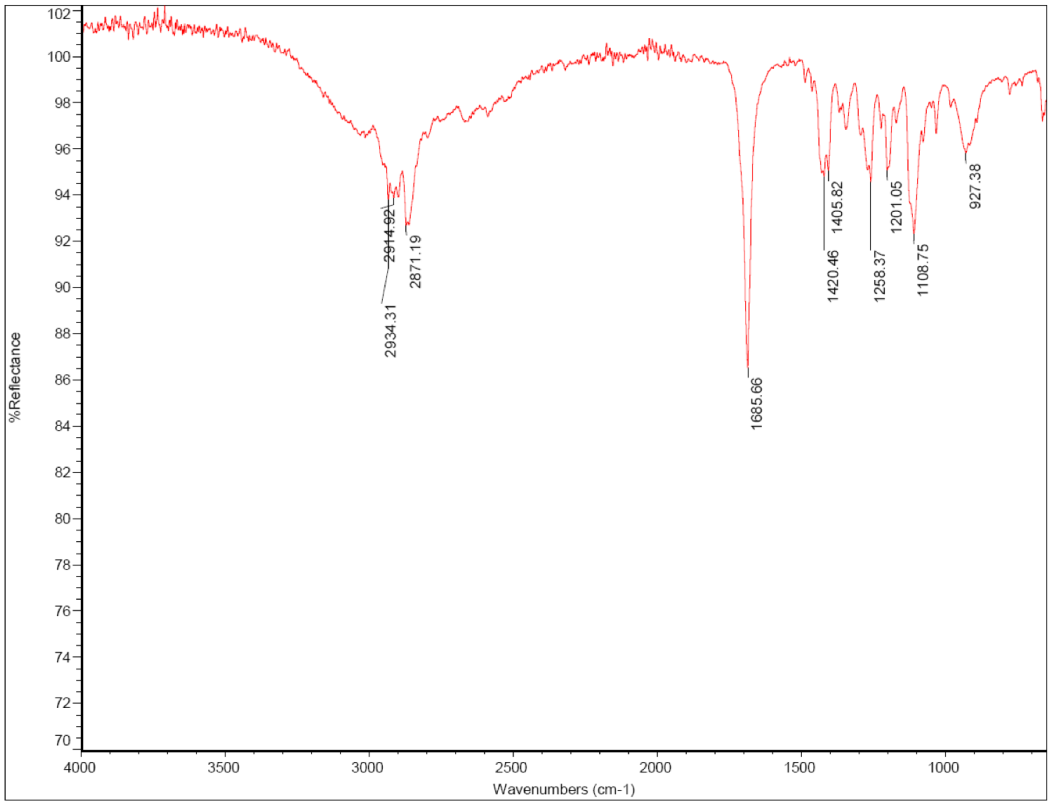
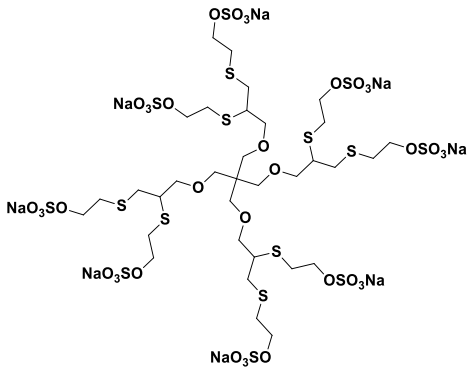


Figure S8. IR spectrum of compound **1b.**



Synthesis of compound 2d :

Polyhydroxyl dendrimer **2a** (220 mg, 0.240 mmol) and sulfur trioxide pyridine complex (1526mg, 9.60 mmol, 5 eq. per hydroxyl) were reacted together according to procedure **C**. Crude mixture was further purified by dialysis in water using dialysis

tubing of 1000 molecular weight cut-off. Dialysed product was lyophilized to yield pure product **2d**, **yield:** 74%

^{1}H NMR (300 MHz, D_2O) δ 4.21 (t, *J* = 6.0 Hz, 12H), 3.84 - 3.63 (m, 12H), 3.48 (s, 8H), 3.23 (s, 4H), 3.07 – 2.85 (m, 24H).

^{13}C NMR (75 MHz, D_2O): δ (ppm) 148.1, 142.0, 128.3, 73.5, 69.0, 46.2, 35.2, 32.2.
IR (cm^{-1}): 3468, 2922, 1634, 1417, 1223, 1115, 1070, 972.

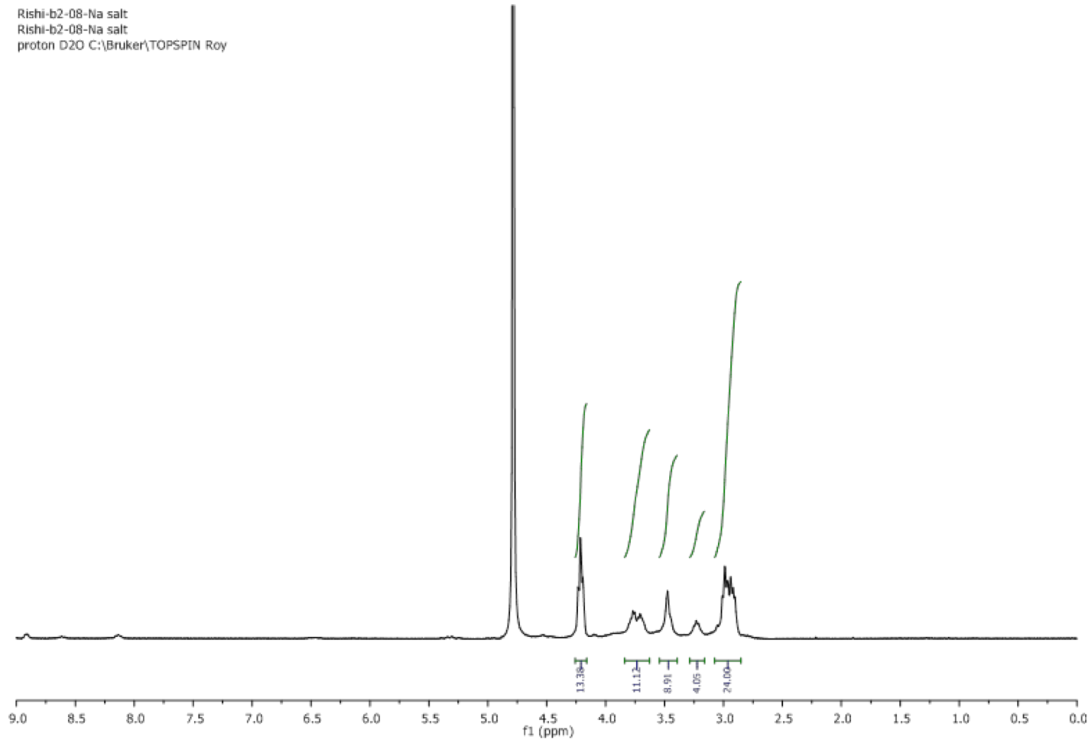


Figure S9. ^{1}HNMR spectrum of compound **2d** (D_2O, 300 MHz).

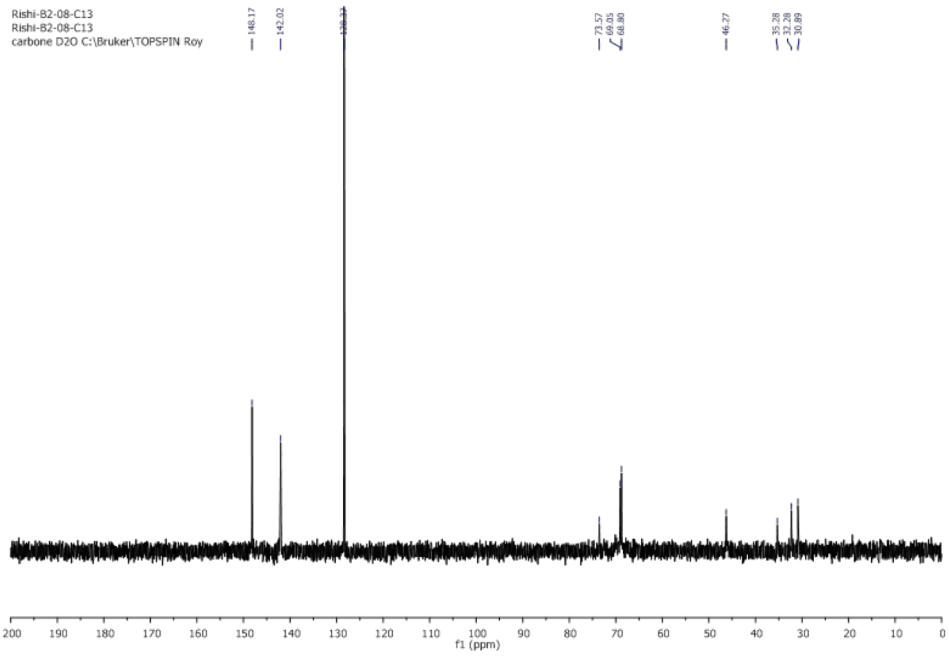


Figure S10. ^{13}CNMR spectrum of compound **2d** (D_2O, 75 MHz).

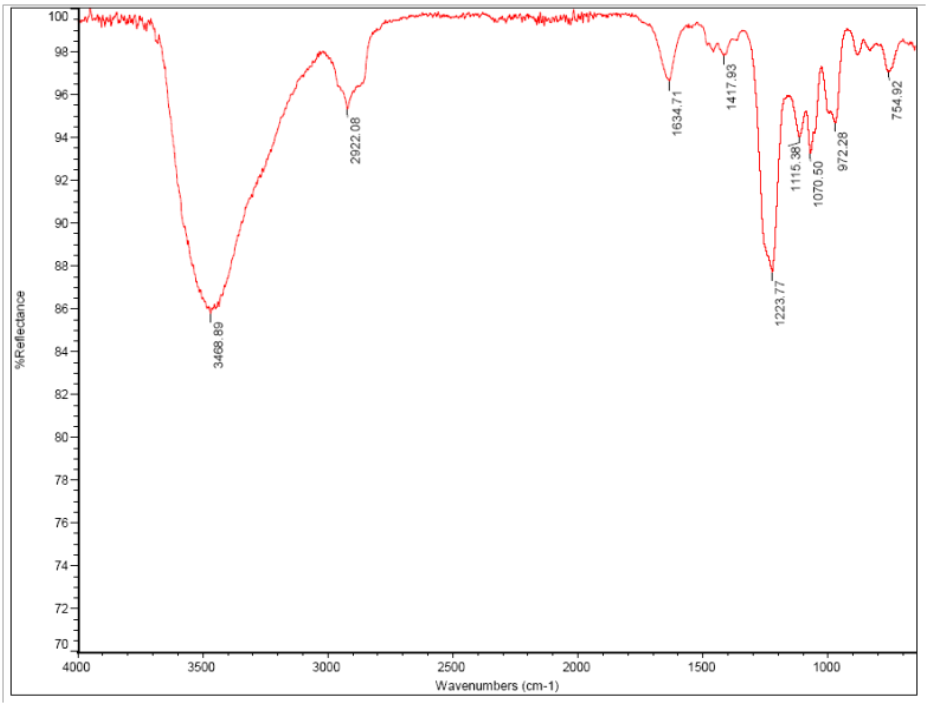
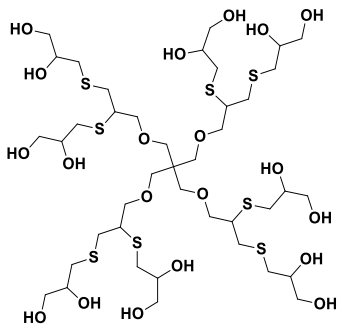


Figure S11. IR spectrum of compound **2d.**



Synthesis of compound 4a:

Tetrapropargyl pentaerythritol **(2)** (0.330 mg, 1.14 mmol), and 1-thioglycerol (4.2 ml, 48.5 mmol, 10.6 eq. per site) were reacted together according to **procedure B** to give crude mixture which was washed with diethyl ether. The residue was dissolved in 4 ml of water and washed with ethyl acetate (3x15 ml) and finally aqueous layer was lyophilized to obtain the pure product **4a** as an oil (yield: 990 mg; 75%).

^{1}H NMR (600 MHz, D2O) δ 3.90 – 3.82 (m, 8H), 3.81 – 3.72 (m, 4H), 3.72 – 3.64 (m, 12H), 3.60 – 3.54 (m, 8H), 3.48 (s, 8H), 3.21 – 3.13 (m, 4H,), 3.02 – 2.89 (m, 8H,), 2.87 – 2.76 (m, 8H,), 2.76 – 2.65 (m, 8H,).

^{13}C NMR (151 MHz, D2O) δ 73.3, 71.8, 71.7, 71.5, 69.9, 64.9, 46.3, 36.1, 35.4, 34.5.

IR : 3328.2 cm-1 (hydroxyl group)

HRMS (ESI^{+}-TOF): For $C_{41}H_{85}O_{20}S_8$ calculated: 1153.3394 found:1153.3393 (M+H).

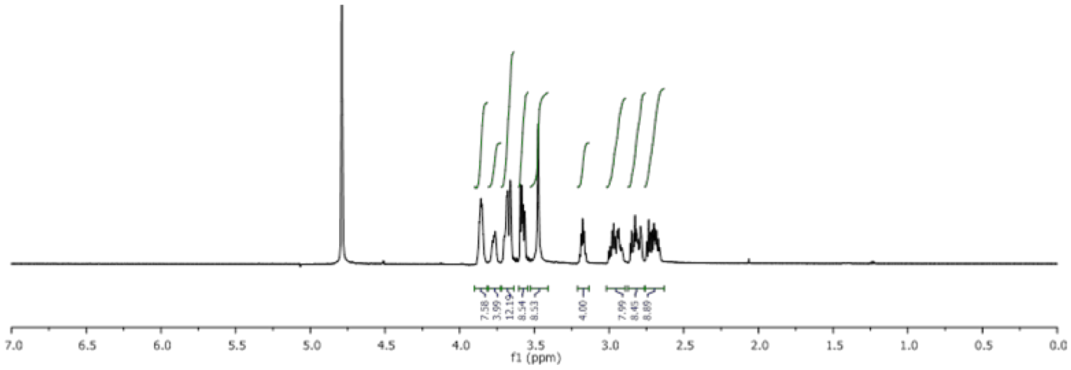


Figure S12 ^{1}HNMR spectrum of compound **4a** (D_2O, 600 MHz)

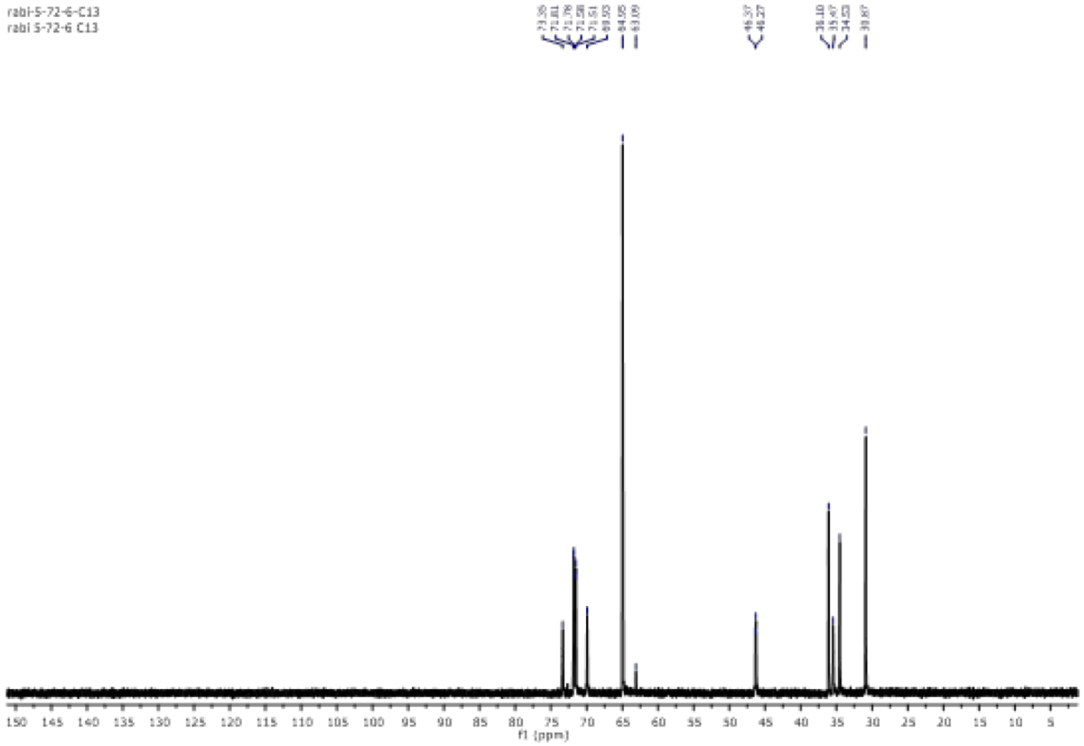


Figure S13 ^{13}C NMR spectrum of compound **4a** (D_2O, 151 MHz)

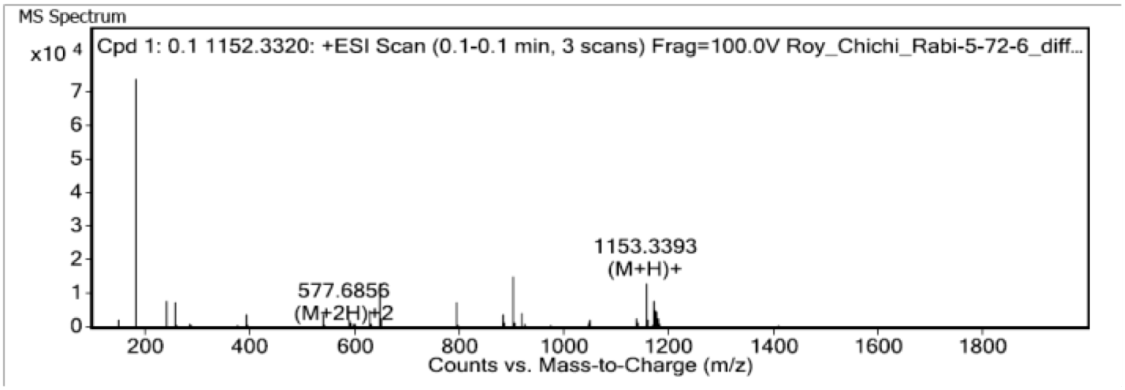


Figure S14 HRMS analysis (ESI^+) for compound **4a.**

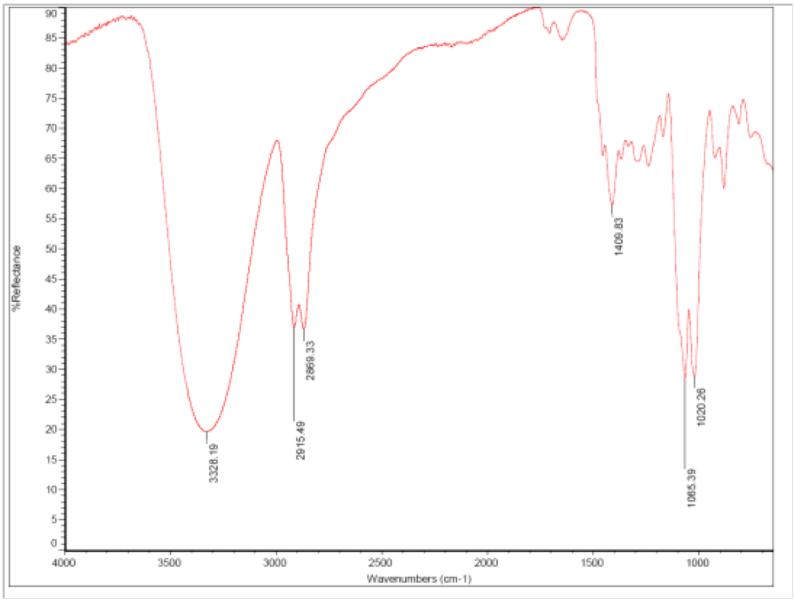
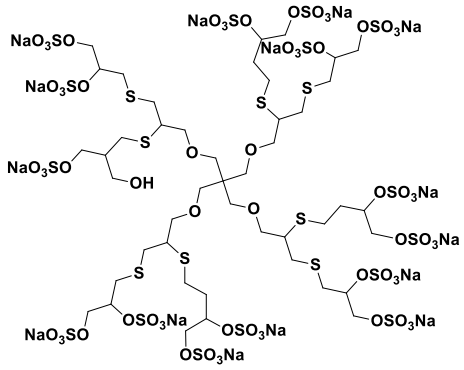


Figure S15. IR spectrum of compound **4a.**



Synthesis of compound 4d:

Polyhydroxy dendrimer **4a** (200 mg, 0.173 mmol) and sulfur trioxide pyridine complex (2.2 g, 13.84 mmol, 5 eq. per hydroxyl) were reacted together following the procedure C. Crude mixture was further purified by dialysis in water using 1000 cut-off dialysis tubing. Dialysed product was lyophilized to yield compound **4d**, y**ield:** 76%

^{1}H NMR (300 MHz, D_2O): δ (ppm) ^{1}H NMR (300 MHz, D_2O) δ 4.73-4.66 (m, 4H, HO-CH), 4.41-4.26 (m, 8H), 4.22-4.02 (m, 8H), 3.95 – 3.65 (m, 12H), 3.49 (s, 2H), 3.31-3.16 (m, 4H,), 3.12 – 2.67 (m, 24H,).

^{13}C NMR (75 MHz, D_2O): δ (ppm) ^{13}C NMR (75 MHz, D_2O) δ 76.8, 73.0, 70.9, 69.4, 69.1, 67.9, 46.2, 35.5, 34.0, 33.4, 31.7.

IR (cm^{-1}): 3443, 2917, 1636, 1216, 1063, 994, 918.

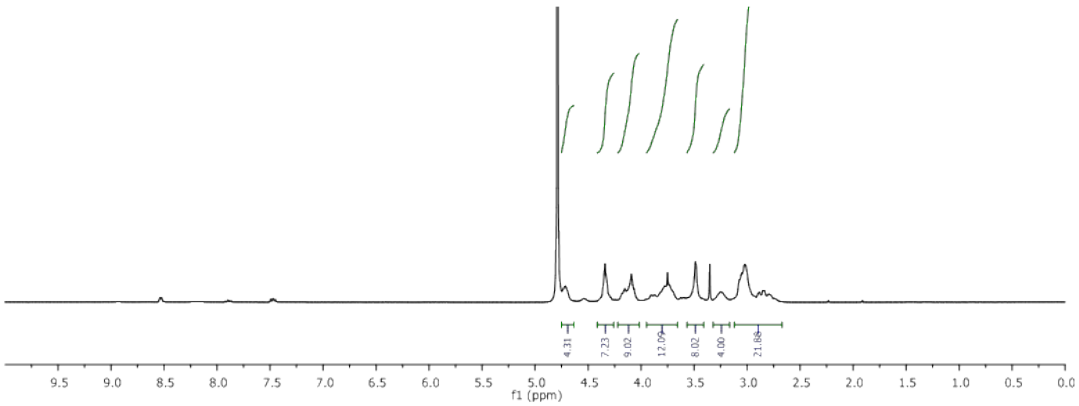


Figure S16 ^{1}HNMR spectrum of compound **4d** (D_2O, 300 MHz)

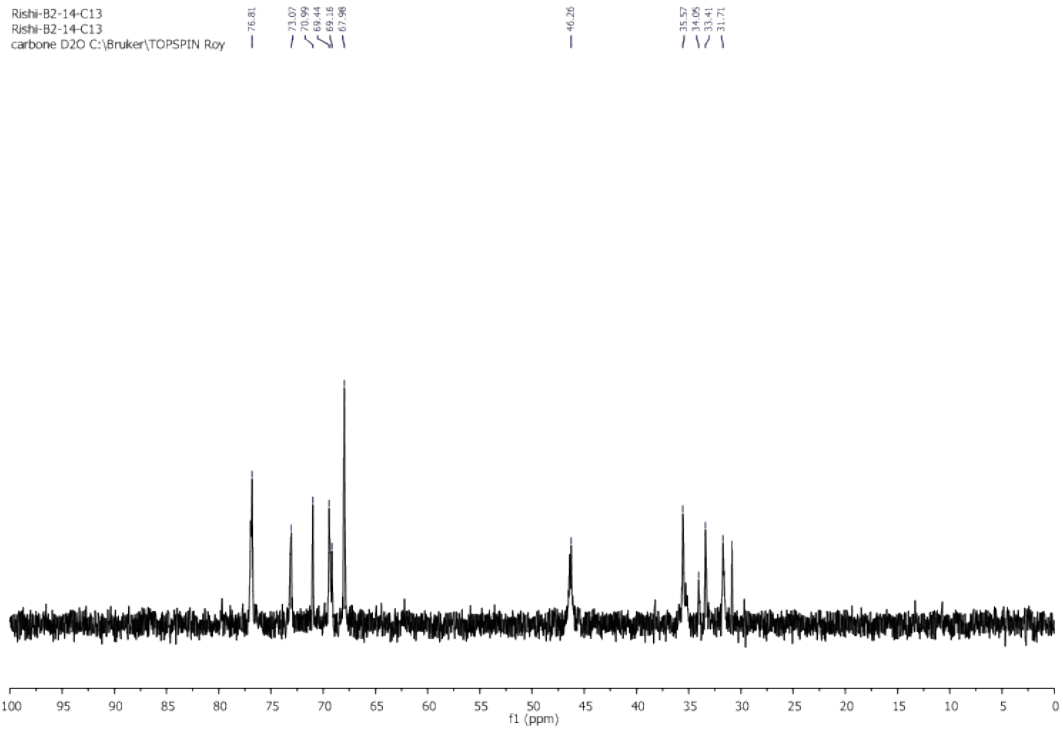


Figure S17 ^{13}C NMR spectrum of compound **4d** (D_2O, 75 MHz)

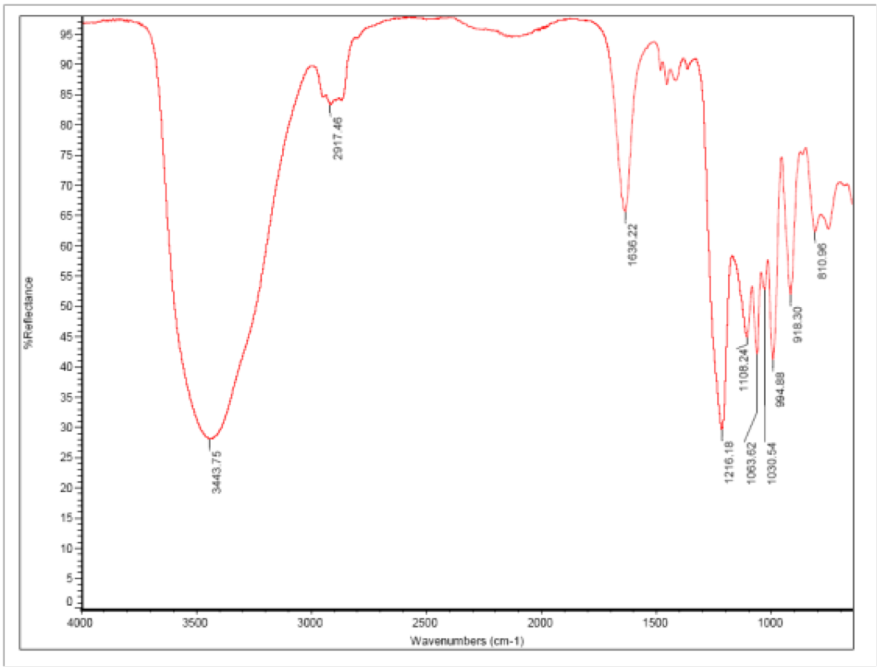
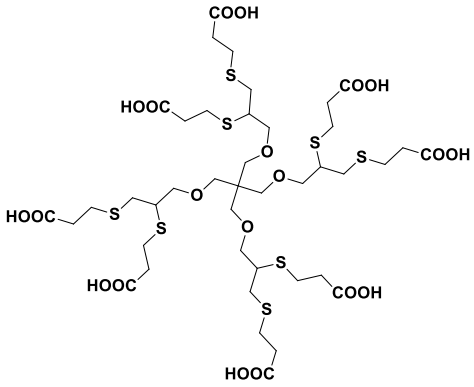


Figure S18. IR spectrum of compound **4d.**



Synthesis of compound 2b:
Tetrapropargyl pentaerythritol (**2)** (100mg, 0.347mmol) and 3-mercaptopropanoic acid (0.183ml, 13.888mmol, 5 eq. per site) were reacted according to procedure **B**. Crude mixture was passed through a silica coloumn and 5% methanol in DCM was used as an eluent to get rid of disulfide. The final compound (**2b**) was recovered using 10% H_2O in acetone as white solid. (yield:78%).
^{1}H NMR (300 MHz, D_2O) δ 3.83 – 3.63 (m, 8H), 3.49 (s, 8H), 3.21-3.11 (m, 4H), 3.01-2.83 (m, 24H), 2.67 (t, J = 7.0 Hz, 16H).

^{13}C NMR (75 MHz, D_2O) δ 178.11, 73.41, 69.85, 45.87, 36.28, 36.0, 34.80, 28.43, 26.98.
HRMS (ESI^+-TOF): For $C_{41}H_{68}NaO_{20}S_8$ found:1159.1963 $(M+Na)^+$; calculated: 1159.1961
IR (cm^{-1}): 3323, 2946, 2830, 1019.

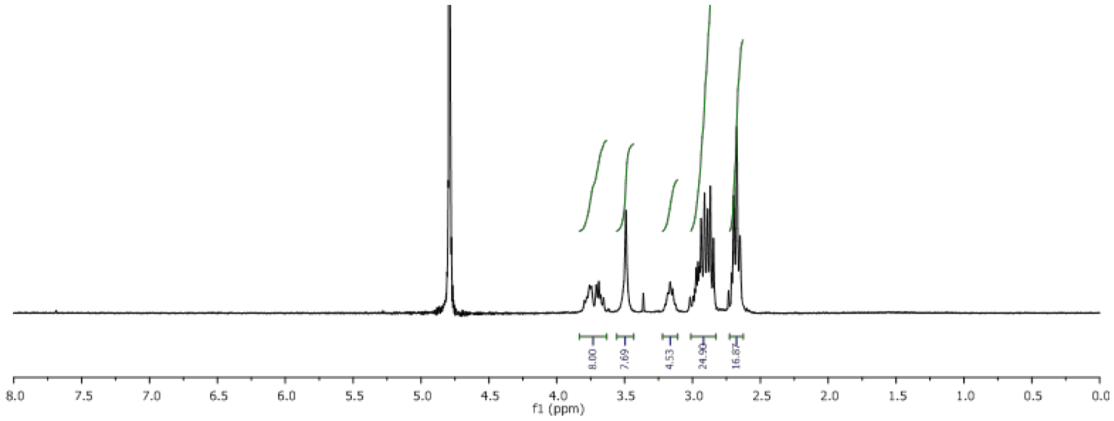


Figure S19 ^{1}HNMR spectrum of compound **2b** (D_2O, 300 MHz)

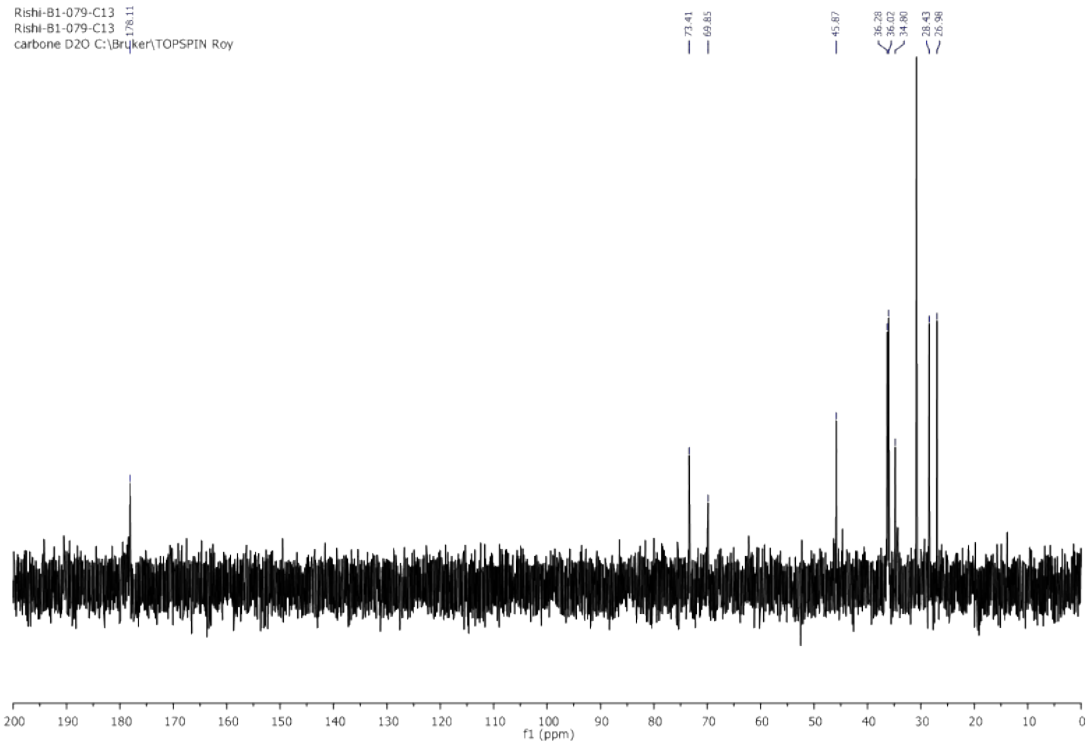


Figure S20 ^{13}C NMR spectrum of compound **2b** (D_2O, 75 MHz)

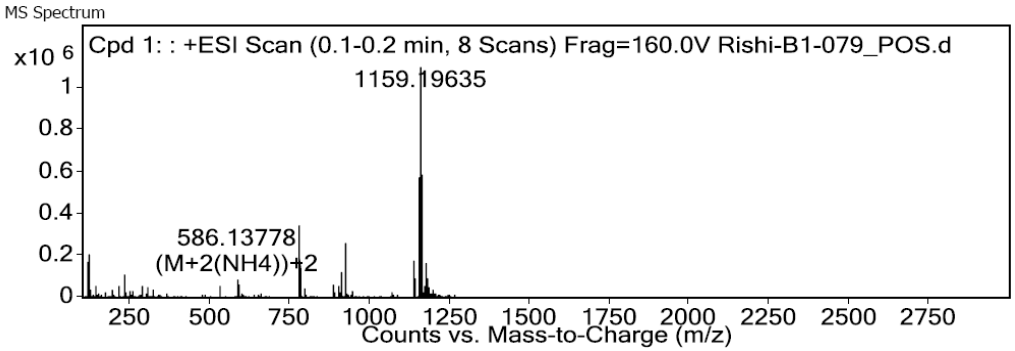


Figure S21 HRMS analysis (ESI^+) for compound **2b**

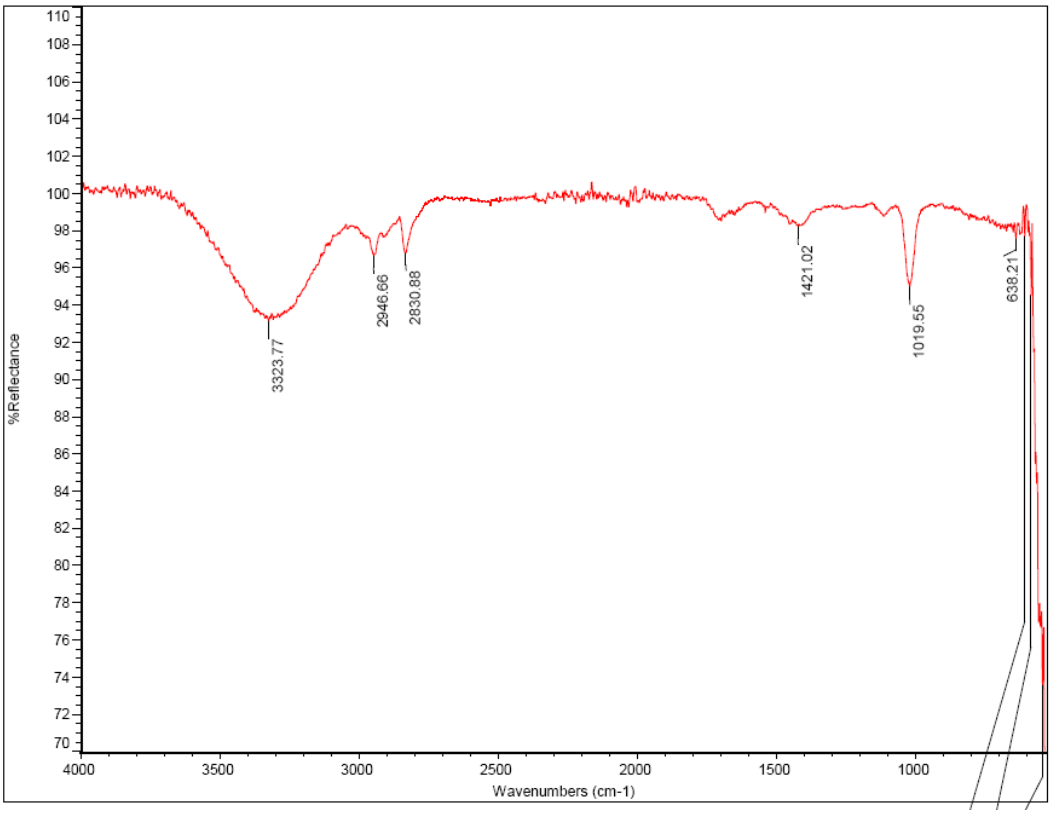
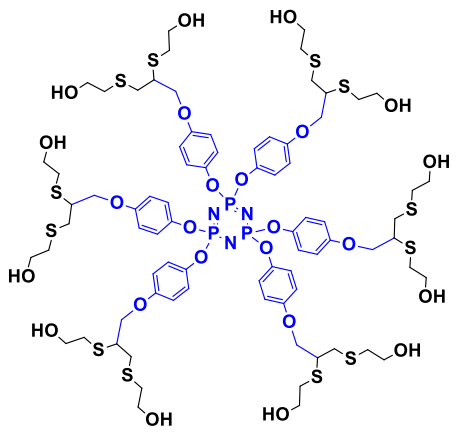


Figure S22. IR spectrum of compound **2b**



Synthesis of compound 3a:

Hexapropargylated P_3N_3 core **(3)** (100 mg, 0.0983 mmol, 1.0 eq.) 2-mercaptoethanol **(**0.413 ml, 5.89 mmol, 10 eq. per site) and AIBN (0.1 mmol, 15mg) were dissolved in methanol (2ml) and heated together at 70°C in a sealed tube for 10 hrs. Solvent was evaporated and crude mixture was washed with diethylether. The crude mixture was dissolved in minimum amount of methanol followed by dilution with water and placed in a dialysis bag of 1000 molecular weight cut-off. Dialysis was performed for 5-6 hrs and finally lyophilization afforded the compound **3a**, **yield: 83%**.

^{1}H NMR (300 MHz, CD_3OD) : δ 6.76 (dd, *J* = 20.5, 9.2 Hz,24H, ArH), 4.23 (ddd, *J* = 31.1, 9.7, 5.2 Hz, 12H, Ph-OCH_2), 3.72 (dt, *J* = 11.3, 6.6 Hz, 24H, OH-CH_2), 3.29 – 3.20 (m, 6H, CH), 3.06 – 2.96 (m, 12H, CH-CH_2), 2.83 (t, *J* = 6.6 Hz, 12H, SH-CH_2), 2.72 (t, *J* = 6.6 Hz, 12H, SH-CH_2).

^{31}P NMR (122 MHz, CD_3OD) δ 10.45 (s).

^{13}C NMR (151 MHz, CD_3OD): δ 157.8, 145.5, 123.0, 116.5, 71.3, 63.0, 62.6, 45.9, 36.3, 35.9, 35.2

HRMS (ESI^+-TOF): Calculated for $C_{78}H_{115}N_3O_{24}P_3S_{12}$ [M+H]$^+$: 1956.4467, found: 1956.3749 $(M+NH_4)^+$-(H_2O).

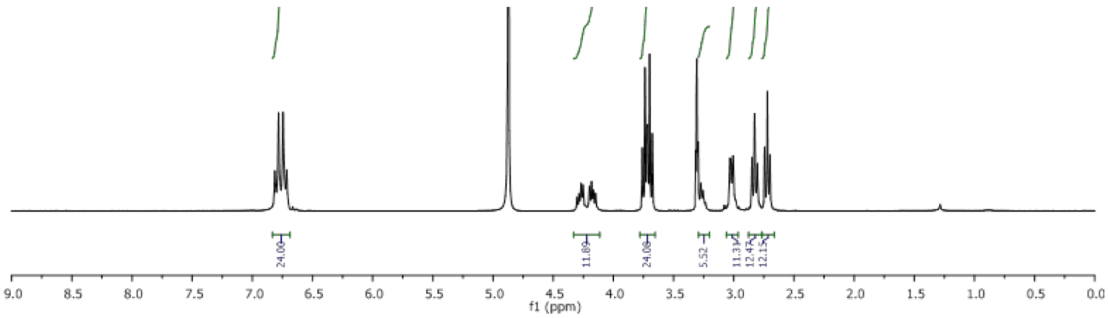


Figure S23. ^{1}HNMR spectrum of compound **3a** (CD_3OD, 300 MHz)

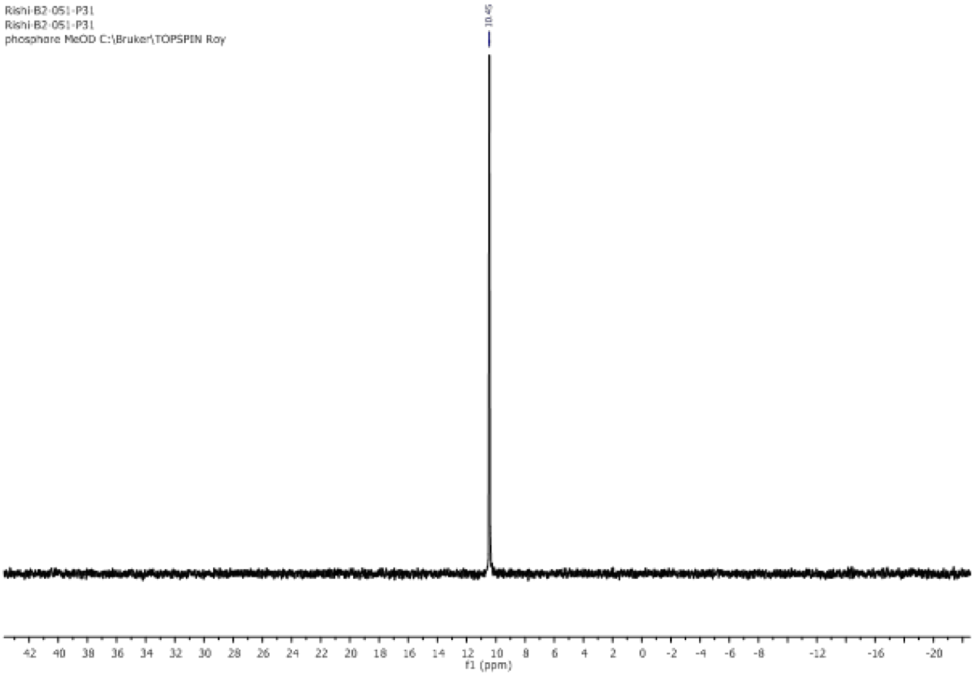


Figure S24. ^{13}P NMR spectrum of compound **3a** (122 MHz, CD_3OD).

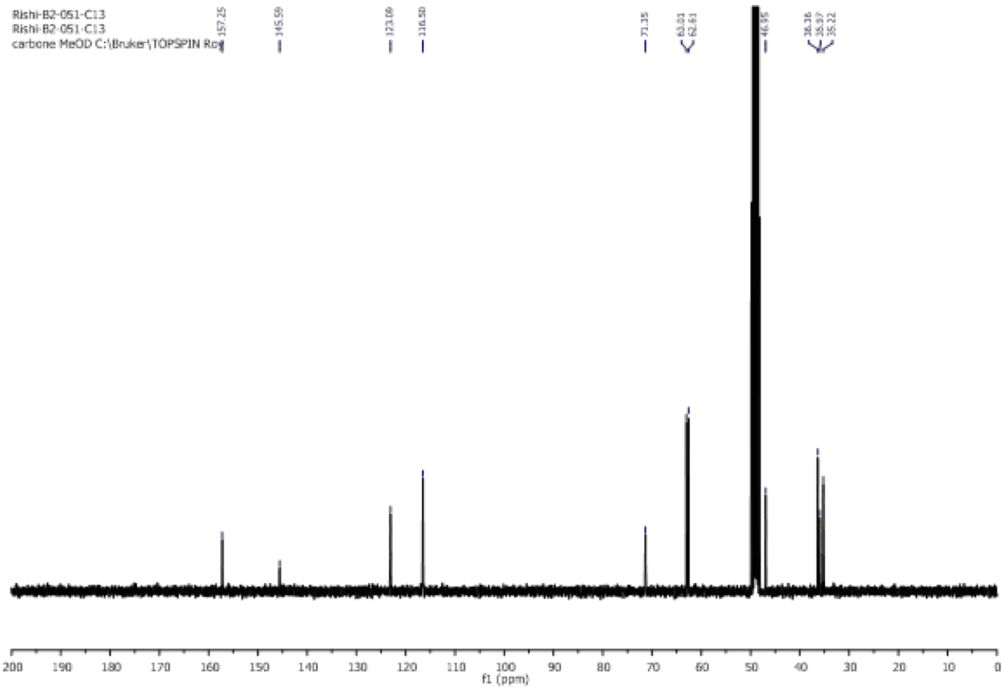


Figure S25 ^{13}C NMR spectrum of compound **3a** (CD_3OD, 75 MHz)

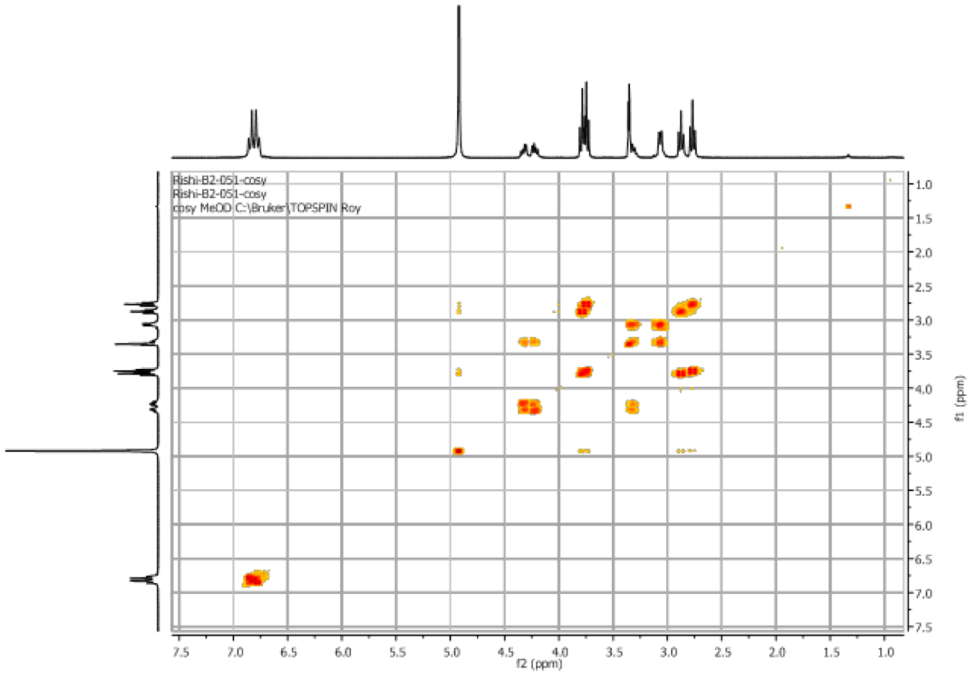


Figure S26. COSY spectrum of compound **3a**

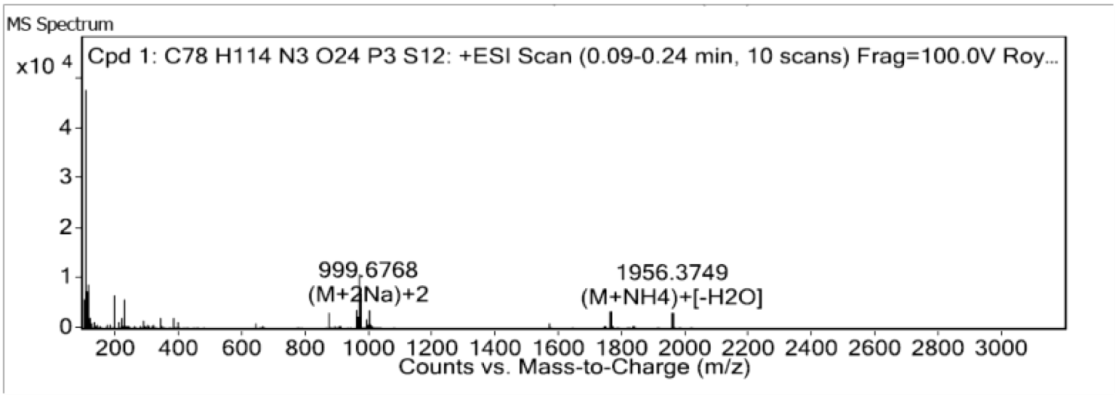
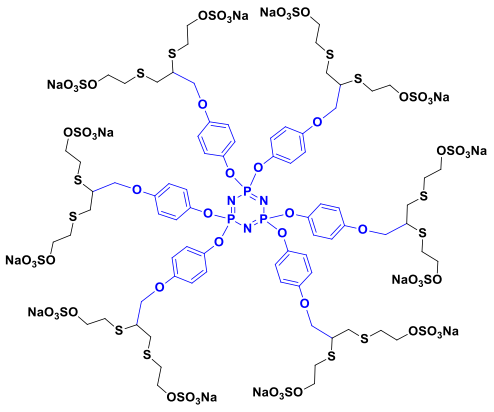


Figure S27. HRMS analysis (ESI^+) for compound **3a**



Synthesis of compound 3d:

Polyhydroxy dendrimer **3a** (100mg, 0.055 mmol) and sulfur trioxide pyridine complex (488mg, 3.06 mmol, 5 eq. per hydroxyl) were reacted together following the procedure **C**. Crude mixture was further purified by dialysis in water using dialysis tubing 1000 molecular weight cut-off. Dialysed product was lyophilized to yield compound **3d**, **yield:** 80%

^{1}H NMR (300 MHz, D_2O) : δ (ppm) 6.93-6.50 (m, 24H), 4.38-3.95 (m, 28H), 3.84-3.52 (m, 6H), 3.40-2.65 (m, 42H).

^{13}C NMR (75 MHz, D_2O): δ (ppm) 122.5, 116.2, 70.4, 68.8, 68.5, 45.6, 36.4, 34.8, 31.9.

^{31}P NMR (122 MHz, D_2O): δ 10.77 (s).

IR (cm^{-1}): 2981, 2937, 2865, 1634, 1500, 1461, 1220, 1188, 1167, 1053, 953, 880, 831.

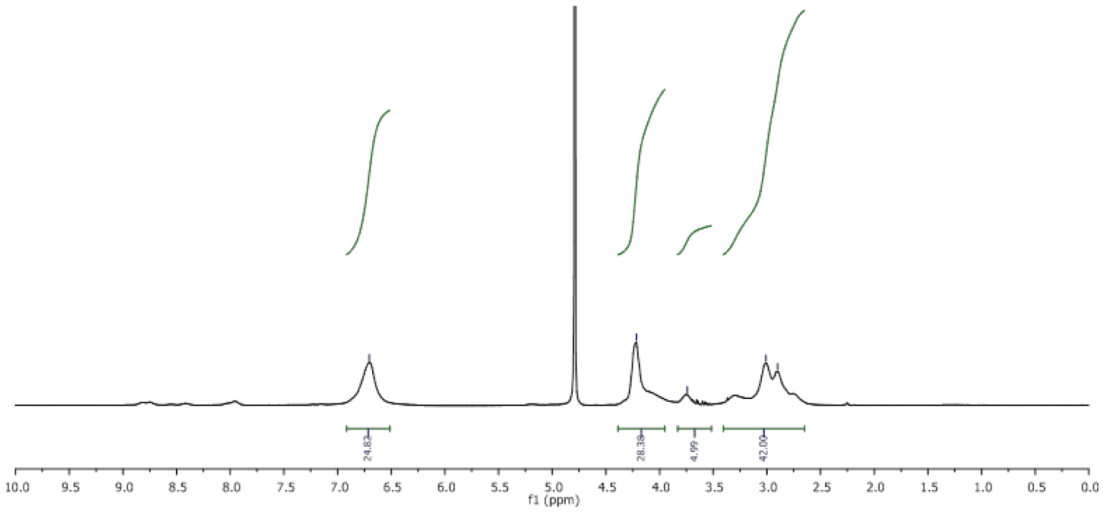


Figure S28. ^{1}HNMR spectrum of compound **3d** (D_2O, 300 MHz)

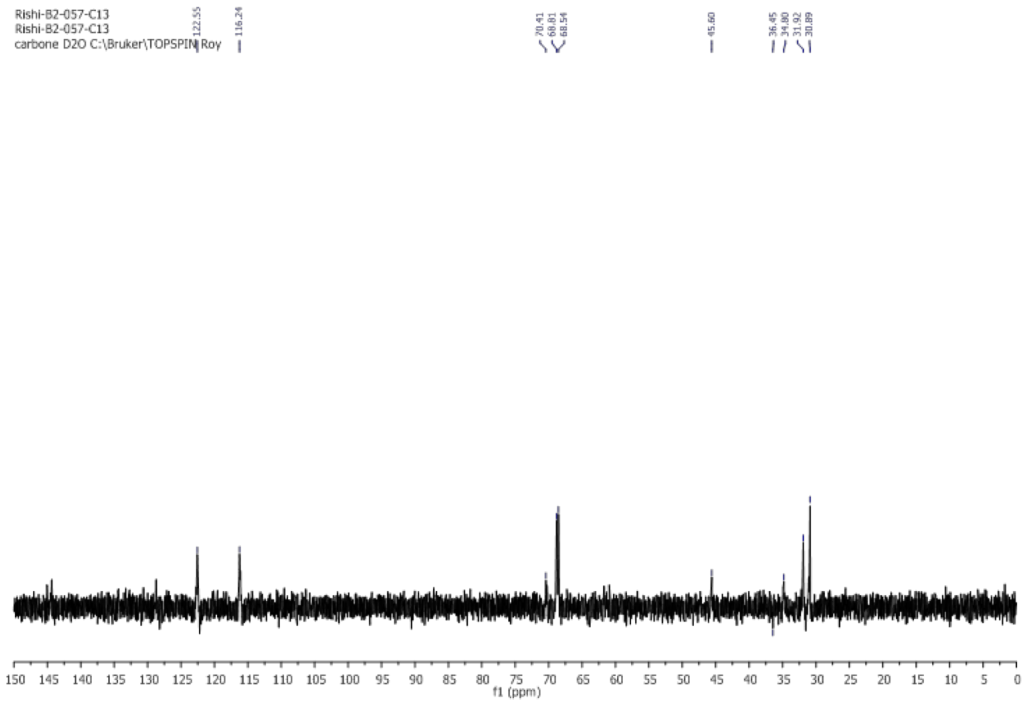


Figure S29.[13]CNMR spectrum of compound **3d** (D_2O, 75 MHz)

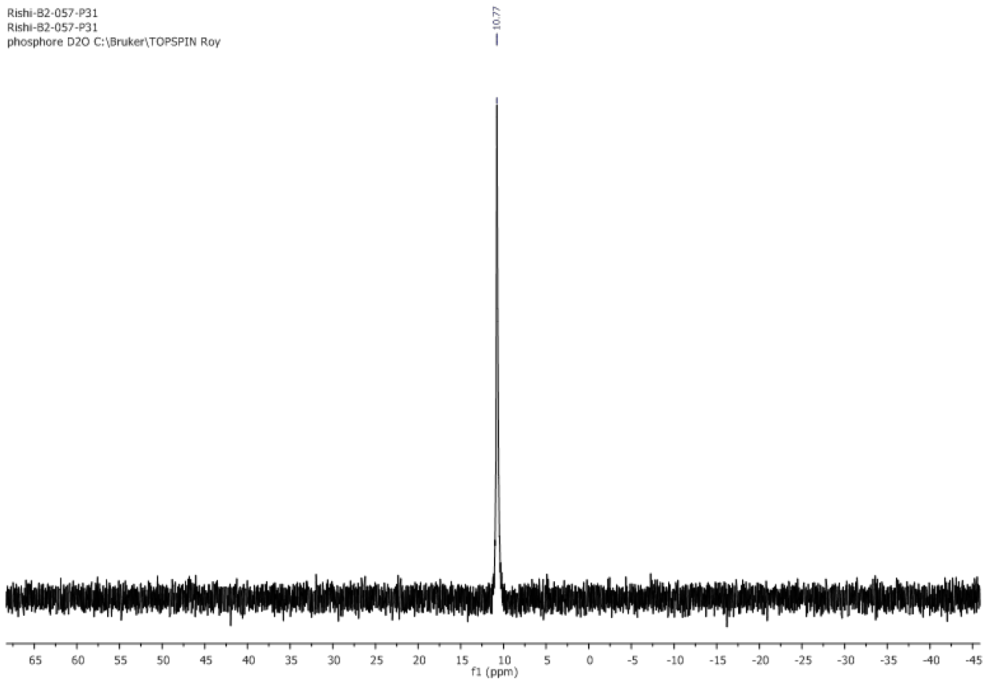


Figure S30. ^{13}PNMR spectrum of compound **3d** (D_2O, 122 MHz)

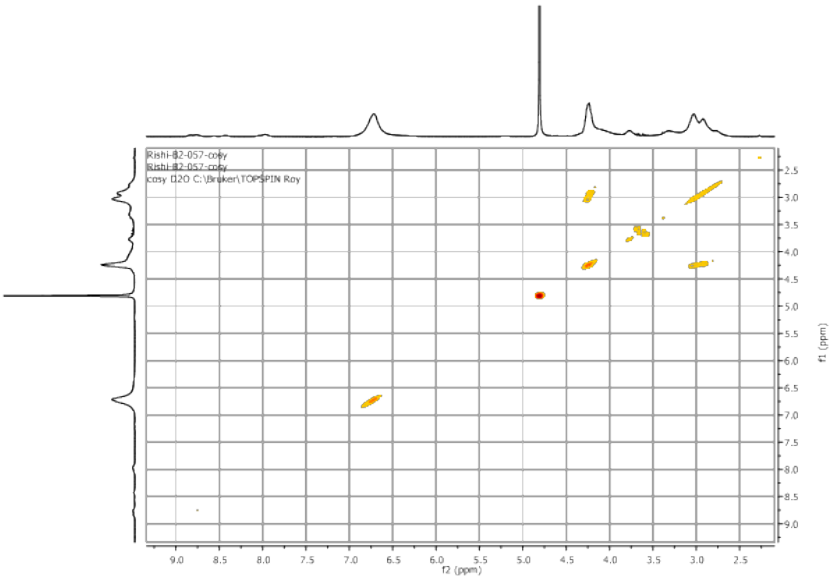


Figure S31. COSY spectrum of compound **3d**

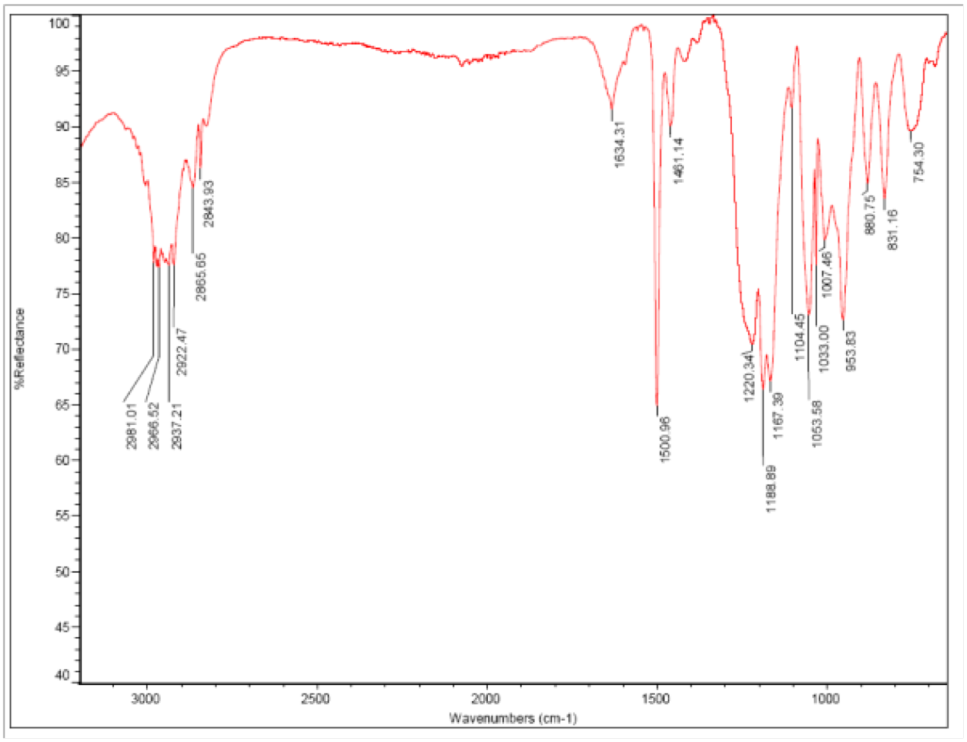
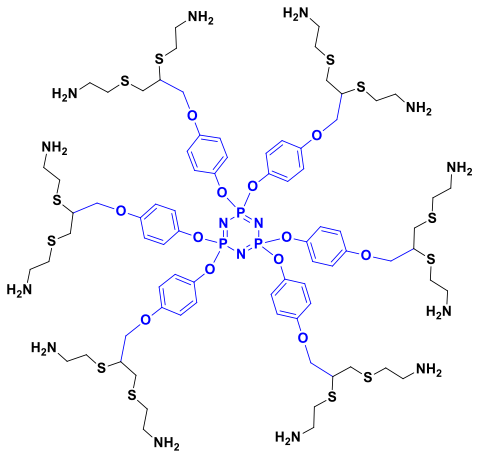


Figure S32. IR spectrum of compound **3d**



Synthesis of compound 3c:

Hexapropargylated P_3N_3 core **(3)** (100 mg, 0.0983 mmol, 1.0 eq.) 2-aminoethanethiol hydrochloride (0.804 mg, 7.0 mmol, 12 eq. per acetylene) and AIBN (0.196 mmol, 13 mg) were dissolved in methanol (2 ml) and heated together at 70°C in a sealed tube for 10 hrs. Solvent was evaporated and crude mixture was washed with diethyl ether. The crude mixture was dissolved in minimum volume of methanol followed by dilution with water and placed in a dialysis bag of 1000 molecular weight cut-off. Dialysis was performed for 8-10 hrs and finally lyophilization afforded the compound **3c**, **Yield: 69%**.

^{1}H NMR (300 MHz, D_2O): δ 6.91 (dd, *J* = 30.9, 8.7 Hz, 24H), 4.42 – 4.28 (m, 12H), 3.49 – 3.38 (m, 6H), 3.28 (dt, *J* = 10.7, 6.8 Hz, 24H), 3.15 – 3.00 (m, 24H), 2.95 (t, *J* = 6.8 Hz, 12H).
^{13}C NMR (75 MHz, D_2O): δ 122.6, 116.6, 70.5, 45.3, 39.7, 39.1, 34.1, 30.0, 28.9.
^{31}P NMR (122 MHz, D_2O): δ 10.59 (s).

HRMS (ESI$^+$-TOF): Calculated for $C_{78}H_{127}N_{15}O_{12}P_3S_{12}$ [M+H]$^+$: 1944.6296, found: 972.7893 (M+2)$^+$.

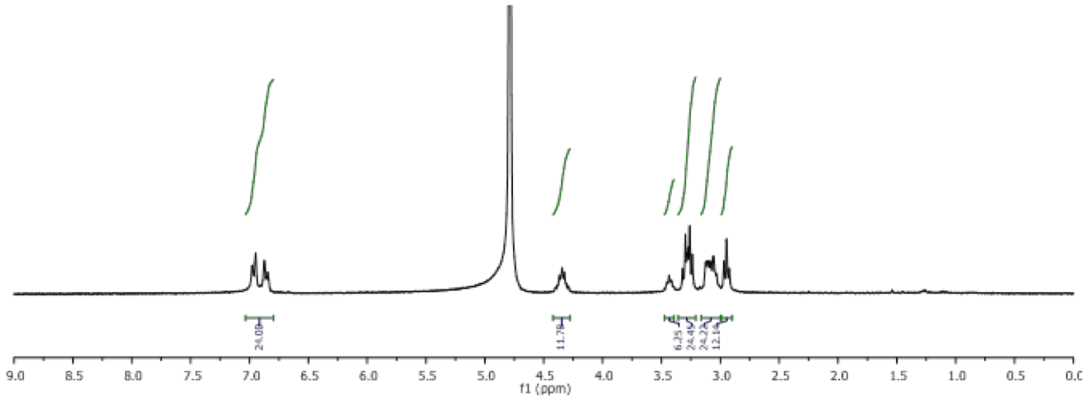


Figure S33. ^{1}HNMR spectrum of compound **3c** (D_2O, 300 MHz)

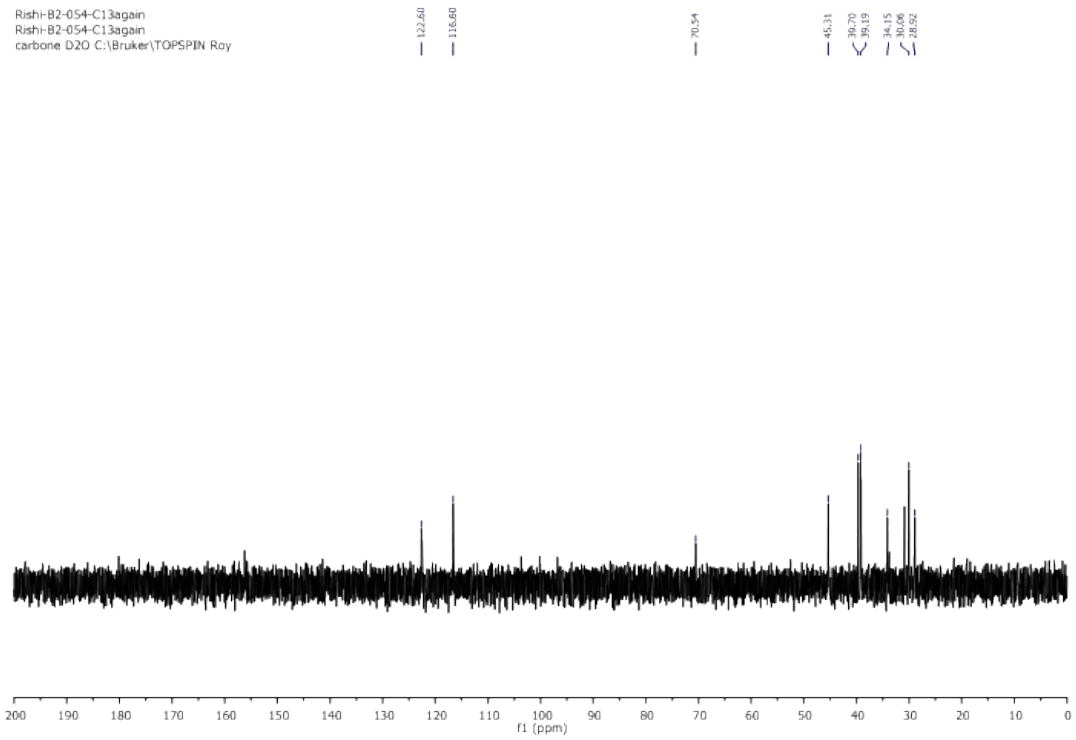


Figure S34.[13]CNMR spectrum of compound **3c** (D_2O, 75 MHz)

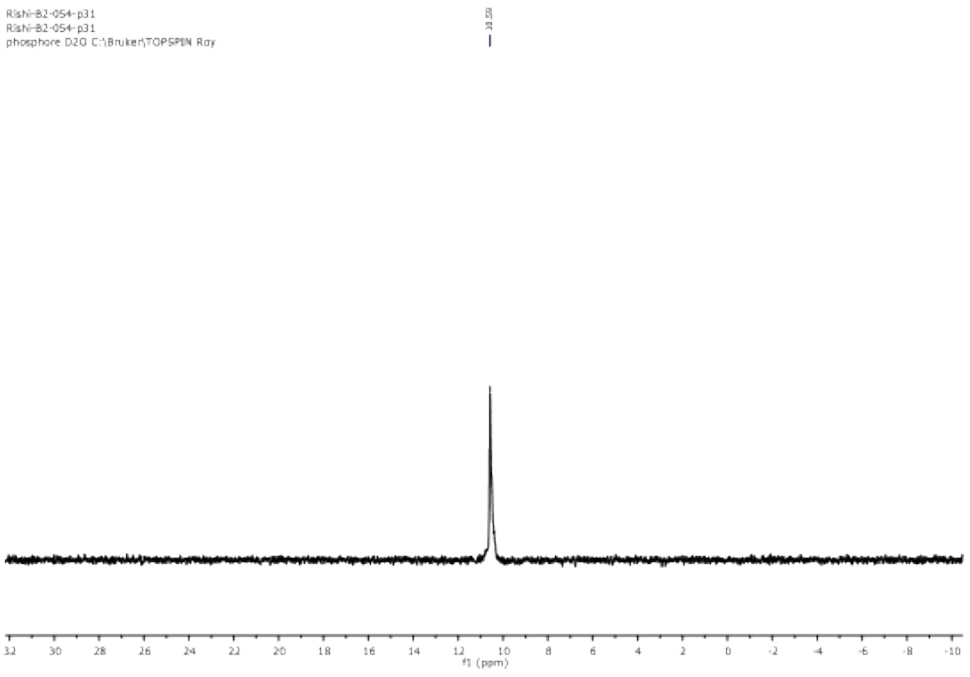


Figure S35. ^{13}PNMR spectrum of compound **3c** (D_2O, 122 MHz)

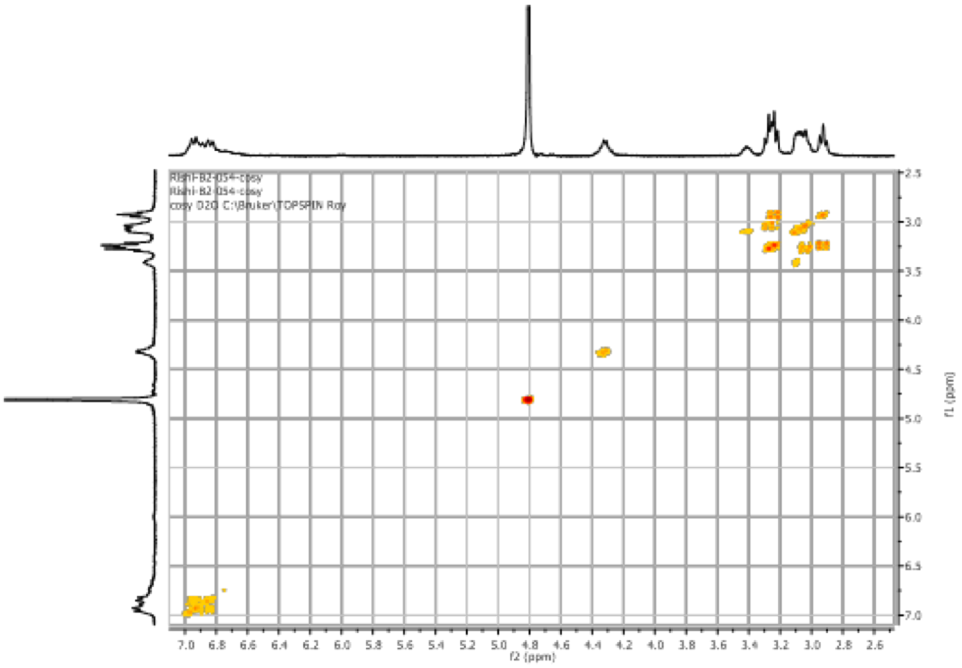
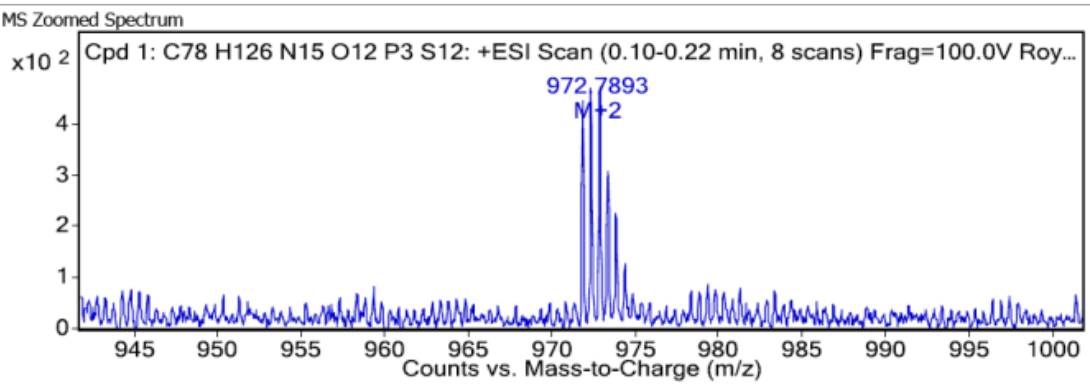


Figure S36. COSY spectrum of compound **3c**



MS Spectrum Peak List

m/z	*Calc m/z*	Diff(ppm)	z	Abund	Formula	Ion
358.1047				1095		
358.5083				15204		
358.7088				14595		
358.9088				14354		
359.1095				9555		
359.3088				5704		
359.5084				2919		
359.7088				1439		
362.1051				1153		
971.7846	971.7783	6.5	2	458	C78 H126 N15 O12 P3 S12	M+2

--- End Of Report ---

Figure S37. HRMS analysis (ESI^+) for compound **3c**

ANNEXE II

IDENTIFICATION OF A HINGE RESIDUE CONTROLLING ISLET AYMLOID POLYPEPTIDE SELF-ASSEMBLY AND CYTOTOXICITY

Elizabeth Godin*[1], Phuong Trang Nguyen*[1], Ximena Zottig[1] and Steve Bourgault[1]

[1]Department of Chemistry, Université du Québec à Montréal, Montréal, Qc, Canada

Manuscrit publié dans ***Journal of Biological Chemistry***, 294 : 8452-8463

DOI : 10.1074/jbc.RA118.006454

Identification of a hinge residue controlling islet amyloid polypeptide self-assembly and cytotoxicity

Received for publication, October 26, 2018, and in revised form, April 4, 2019 Published, Papers in Press, April 11, 2019, DOI 10.1074/jbc.RA118.006454

Elizabeth Godin[‡§1], **Phuong Trang Nguyen**[‡§1], **Ximena Zottig**[‡§], **and Steve Bourgault**[‡§2]

From the [‡]*Department of Chemistry, Pharmaqam, Université du Québec à Montréal, Montreal, Quebec H3C 3P8, Canada and the* [§]*Quebec Network for Research on Protein Function, Engineering, and Applications, PROTEO, Quebec G1V 0A6, Canada*

Edited by Paul E. Fraser

The islet amyloid polypeptide (IAPP) is a 37-residue peptide hormone whose deposition as amyloid fibrils in the pancreatic islets is associated with type 2 diabetes. Previous studies have suggested that residue Asn-21 plays a critical role in the *in vitro* self-assembly of IAPP. Herein, we studied structure–self-assembly relationships focusing on position 21 to gain detailed insights into the molecular mechanisms of IAPP self-assembly and to probe the conformational nature of the toxic assemblies associated with β-cell death. Thioflavin T (ThT) fluorescence, CD spectroscopy, and transmission EM analysis revealed that the Asn-21 amide side chain is not required for IAPP nucleation and amyloid elongation, as N21A and N21G variants assembled into prototypical fibrils. In contrast, Asn-21 substitution with the conformationally constrained and turn-inducing residue Pro accelerated IAPP self-assembly. Successive substitutions with hydrophobic residues led to the formation of ThT-negative β-sheet–rich aggregates having high surface hydrophobicity. Cell-based assays revealed no direct correlation between the *in vitro* amyloidogenicity of these variants and their toxicity. In contrast, leakage of anionic lipid vesicles disclosed that membrane disruption is closely associated with cytotoxicity. We observed that the N21F variant self-assembles into worm-like aggregates, causing loss of lipid membrane structural integrity and inducing β-cell apoptosis. These results indicate that specific intra- and intermolecular interactions involving Asn-21 promote IAPP primary nucleation events by modulating the conformational conversion of the oligomeric intermediates into amyloid fibrils. Our study identifies position 21 as a hinge residue that modulates IAPP amyloidogenicity and cytotoxicity.

The aggregation and tissue deposition of proteins into amyloid fibrils are the hallmark of numerous diseases, including Alzheimer's disease, type II diabetes, and various amyloidoses (1, 2). In over 90% of patients afflicted with type II diabetes, amyloid deposits are observed in the extracellular space of pancreatic islets of Langherhans (3–5). The main component of islet amyloids is the peptide hormone islet amyloid polypeptide (IAPP,[3] or amylin) (6, 7). The accumulation of IAPP-insoluble aggregates correlates closely with the duration and severity of the disease and with the loss of β-cell mass (4). The link between islet amyloid and type II diabetes initially led to the postulate that amyloid fibrils mediate β-cell degeneration. This hypothesis was reinforced by the early work of Lorenzo *et al.* (8), demonstrating the cytotoxicity of IAPP fibrils on pancreatic islet cells. However, most recent studies have indicated that oligomeric and nonfibrillar species cause cell death (9–11). Using time-resolved analysis, it has been observed that IAPP amyloid structures are nontoxic to INS-1 cells and that the toxic species are low-order oligomers, which lack a β-sheet structure and hydrophobic patches (12). Recently, IAPP fibrils have been shown to be toxic to RIN-5F cells, and it has been proposed that a quaternary structure characterized by pairs of β-sheets joined by a dry interface represents the toxic spine (13). The opposing conclusions between these two elegant studies (12, 13) are likely associated with differences in the experimental conditions (monomerization, buffer, aging time, cells, toxicity assays, etc.) and/or with the undetectable presence of toxic oligomers in the fibril preparation used by Krotee *et al.* (13). Thus, although a substantial number of studies have investigated the conformational nature of IAPP toxic species, the subject is still the matter of active debates.

IAPP is a 37-residue hormone that is co-expressed and co-secreted with insulin by pancreatic β-cells (14). The peptide exhibits, under its monomeric state, a conformational ensemble populated by disordered structures, although it diverges from an absolute random coil by the presence of transient helical conformations (15). In membrane mimetic environments, which are known to accelerate fibrillization, IAPP is mainly characterized by helical conformation (16, 17). A structure characterized with three antiparallel β-strands has been recently reported when the peptide is trapped into negatively charged lipid nanodiscs (18). Upon self-assembly into cross-β-sheet quaternary structure, each monomer adopts a U-shaped conformation with two β-strands connected by a loop. According to solid-state NMR, the β-strands comprise residues 8–17 and 28–37, and the loop involves residues 18–27 (19). In the EPR model, the two β-strands comprise residues 14–19 and

This work was supported by Natural Sciences and Engineering Research Council of Canada (NSERC) Grant 06209 (to S. B.). The authors declare that they have no conflicts of interest with the contents of this article.

This article contains Table S1 and Figs. S1–S17.

[1] Both authors contributed equally to this work.

[2] To whom correspondence should be addressed: Dept. of Chemistry, Université du Québec à Montréal, C.P. 8888, Succursale Centre-Ville, Montréal (Québec) H3C 3P8, Canada. Tel.: 514-987-3000 (ext. 5161); E-mail: bourgault.steve@uqam.ca.

[3] The abbreviations used are: IAPP, islet amyloid polypeptide; rIAPP, rodent IAPP; n, D-enantiomer of Asn; Dab, diaminobutyric acid; Aib, aminoisobutyric acid; ThT, thioflavin T; ANS, 8-anilino-1-napthalenesulfonic acid; TEM, transmission EM; LUV, large unilamellar vesicle; DOPC, dipalmitoylphosphatidylcholine; DOPG, dioleoylphosphatidylglycerol; RP, reverse-phase; Tricine, *N*-[2-hydroxy-1,1-bis(hydroxymethyl)ethyl]glycine.

© 2019 Godin et al. Published under exclusive license by The American Society for Biochemistry and Molecular Biology, Inc.

Downloaded from http://www.jbc.org/ at DUPONT-BALL LIBRARY on May 7, 2020

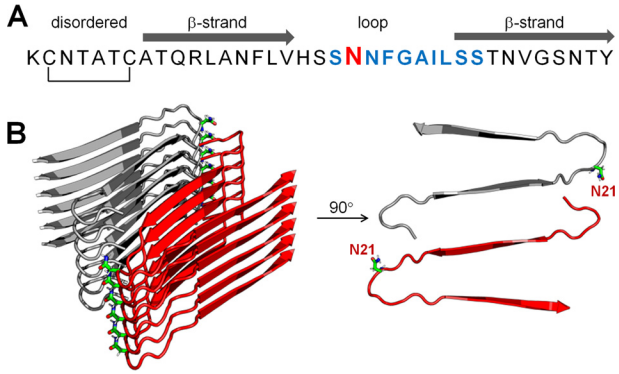


Figure 1. IAPP sequence and structural model of IAPP protofilament. *A*, primary sequence of human IAPP with Asn-21 residue in *red boldface type* and the amyloidogenic core in *blue*. IAPP has a disulfide between Cys-2 and Cys-7 and a C-α-amidated C terminus. The two β-sheets inferred from the solid-state NMR amyloid fibril model are indicated with *gray arrows*. *B*, solid-state NMR model of IAPP protofilament with the Asn-21 side chain indicated (19).

31–36 (20). Conformational changes associated with the transition of IAPP from its soluble state ensembles into ordered amyloids and the molecular interactions governing this transition remain elusive. Helical conformation has been proposed to be critical for self-recognition, as oligomerization could be thermodynamically linked with helix formation within the 5–20 segment (21, 22). In contrast, by using a helix-disrupting analog, it has been proposed that helical species are off-pathway and that preventing helical folding increases cytotoxicity (23). Moreover, it has been reported that helical conformations are mainly found in the monomeric state and could seed oligomer formation, although they are not mandatory for amyloid growth (24).

Elucidating the molecular determinants promoting oligomerization and the interactions initiating amyloidogenesis is critical to better define the nature of the toxic proteospecies. Studies have exploited residue-specific modifications to better define the driving forces of IAPP self-assembly (25–30). Sequence differences between human and mouse IAPP and mutational studies have initially indicated that the segment 20–29 dictates aggregation and toxicity (11). Nevertheless, substitutions outside the 20–29 amyloidogenic region, including A13E, V17C, and Y37L, have been shown to alter amyloid formation (27, 31). It has been shown that residue Asn-21 plays a key role in the *in vitro* self-assembly of IAPP, as its consecutive replacement by Leu, Ser, and Asp inhibits amyloid formation (25, 30). Position 21 is particularly intriguing because it is located in the disordered loop joining the two β-strands in the amyloid conformation (19, 20) (Fig. 1). The side chain of Asn-21 projects outward from the protofilament core; thus, it could participate in fibril packing. This position is also located at the intersection of the putative 5–20 helical segment and the 20–29 amyloidogenic core. Moreover, Asn-21 is adjacent to Ser-20, for which the Asian mutation S20G is known to increase amyloidogenicity and toxicity (32). These observations strongly suggest that this residue plays a critical role in the conformational conversion modulating oligomerization, nucleation, and/or amyloid growth.

Accordingly, we performed a structure–assembly relationship study focusing on position 21 by tuning the side-chain physicochemical properties and the local conformational freedom of the backbone. The data indicated that the introduction of a hydrophobic residue at this position locks the peptide into highly toxic β-sheet–rich aggregates, whereas a Pro hastens IAPP self-assembly into nontoxic amyloid fibrils. The present study reveals that Asn-21 acts as a molecular hinge modulating IAPP amyloid formation and cytotoxicity.

Results

Rational design of N21X mutants

To gain mechanistic insights into IAPP self-assembly and toxicity to β-cells, we prepared a library of analogs modified at Asn-21. We probed the contribution of the amide side chain by successively incorporating Ala and a negatively (Asp) and a positively (diaminobutyric acid (Dab)) charged residue. Dab was used instead of Lys to maintain the length of the side chain. Asn-21 was substituted with hydrophobic residues with high β-sheet propensity (Phe and Leu) and with Phe capable of π–π interactions. Conformational modifications were introduced to favor turn (Pro, Gly, and D-enantiomer). In fact, D-amino acids are known to promote and/or stabilize turn conformation (33, 34). The C-α-methylated aminoisobutyric acid (Aib) residue, known to promote helical folding (35), was incorporated. These substitutions (Pro, Gly, Asn, and Aib) modulate the local conformational freedom of the peptide backbone. Rodent IAPP (rIAPP), which contains three Pro residues and is less prone to aggregation and is nontoxic, was used as a negative control (36).

Substitutions at position 21 modulate kinetics of self-assembly

The effect of site-specific modifications on self-assembly was initially evaluated by thioflavin T (ThT) fluorescence. ThT is a small dye whose fluorescence emission increases sharply upon its binding to the cross-β-sheet quaternary structure (37). IAPP amyloid formation can be ascribed to a nucleated polymerization where the three distinctive phases (lag phase, elongation phase, saturation phase) are governed by different kinetics. Dynamic and transient oligomeric species are generated during the lag phase, which is the thermodynamic rate-limiting step. Upon formation of competent oligomer(s), or nuclei, the elongation phase begins, leading to the rapid growth of protofilaments and fibrils until equilibrium is reached. The sigmoidal curve obtained by measuring ThT fluorescence over time is fitted to a Boltzmann sigmoidal, and the lag time can be extracted. Under the conditions of the assay (20 mM Tris-HCl, pH 7.4, 40 μM ThT, 25 °C, nonbinding surface 96-well plates, 10-min interval between measurements, no agitation), a lag time of 8.6 ± 1.8 h was observed for IAPP at 12.5 μM (Fig. 2) and 4.2 ± 1.2 h at 25 μM (Fig. S1).

Introducing a hydrophobic side chain (N21F, N21L) at position 21 abolished the formation of ThT-positive assemblies (Fig. 2*A*). This is in agreement with the previous work of Miranker and colleagues (25). Interestingly, the presence of an amide group on the residue 21 side chain is not a prerequisite for the formation of a ThT-positive cross-β-sheet structure, as the substitution N21A led to a slight acceleration of self-assembly. This result is unexpected, considering that the mutant N21S has been previously shown to self-assemble into ThT-negative amorphous aggregates (25). Introducing a negative or

Downloaded from http://www.jbc.org/ at DUPONT-BALL LIBRARY on May 7, 2020

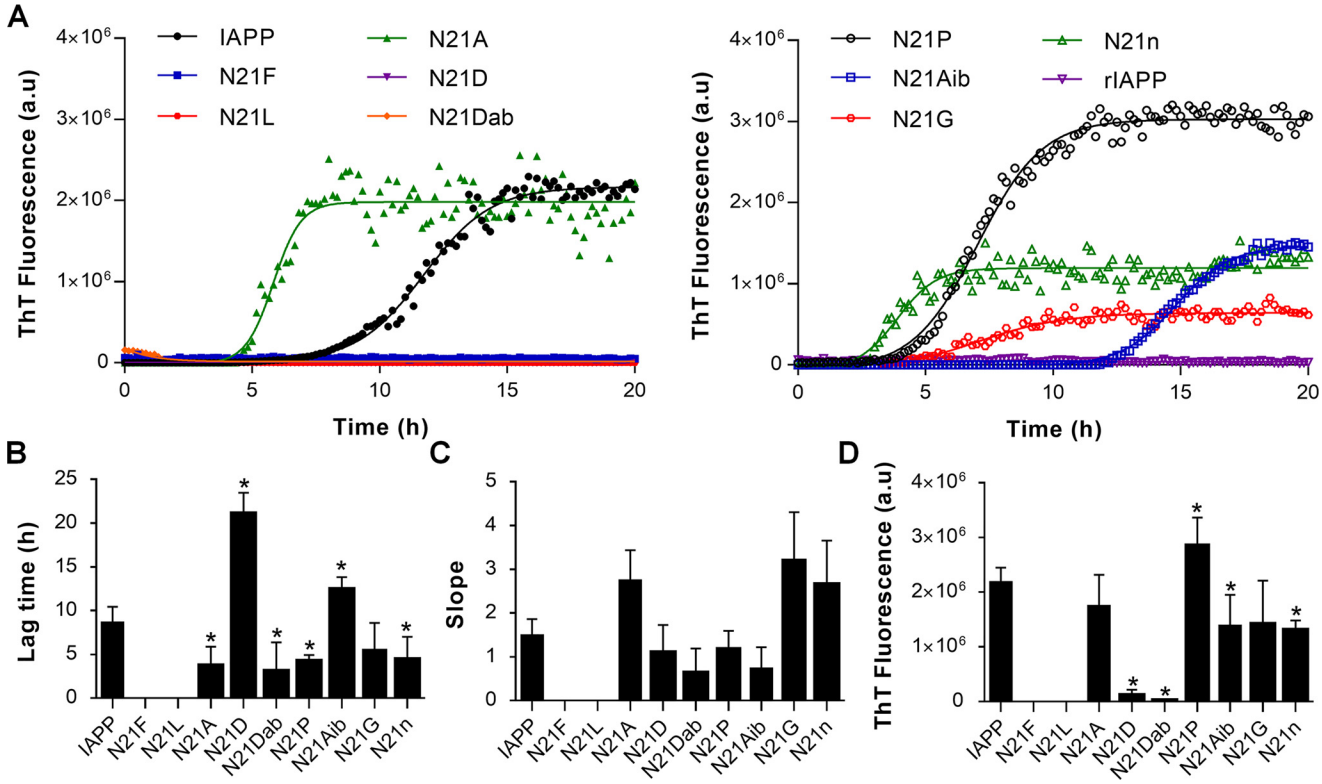


Figure 2. Effect of Asn-21 substitutions on the kinetics of IAPP amyloid formation. *A*, representative kinetic traces of amyloid assembly of IAPP and mutants monitored by ThT fluorescence. Peptides were incubated at 12.5 μM under quiescent conditions in 20 mM Tris-HCl buffer, pH 7.4, and the fluorescence of ThT (40 μM) was measured every 10 min with excitation at 440 nm and emission at 485 nm. The curves represent the best from the sigmoidal growth model. Shown are lag time (*B*), slope (*C*), and final ThT fluorescence (*D*) of the self-assembly kinetics. Data represent mean ± S.E. (*error bars*) of at least four experiments performed in triplicate. Results were analyzed using Student's *t* test, and statistically significant difference (between IAPP and analogs) was established at $p < 0.01$ (*). *B–D*, data are not shown for N21F and N21L because results could not be fitted to a sigmoidal curve. *a.u.*, arbitrary units.

a positive charge without altering the side chain length (N21D or N21Dab) inhibited the formation of ThT-positive species. These results indicate that IAPP amyloid formation tolerates the elimination of the position 21 amide group, although it does not allow the introduction of a charged or hydrophobic residue.

Considering that IAPP self-assembly occurs in the absence of the Asn-21 amide group, we investigated the role of backbone conformational entropy and side-chain chirality. Introducing the turn-inducing residue Pro led to an acceleration of amyloid assembly, with N21P displaying a lag time of 4.2 ± 0.8 h and a significant increase of ThT end-point fluorescence (Fig. 2*B*). This observation is intriguing, as a Pro residue is recognized to inhibit amyloid assembly (36, 38, 39). For instance, single-point mutation I26P has been shown to transform IAPP into a potent amyloid inhibitor (28). When Asn-21 was replaced by Aib, known to favor α-helix, amyloid assembly was slowed down to a lag time of over 12 h, with some ThT assays at 12.5 μM showing no increase of fluorescence over 20 h (Fig. S2). Increasing the conformational freedom by incorporating Gly led to kinetics somewhat similar to the N21A analog. It is worth mentioning that N21Aib, N21A, and N21G showed a somewhat high heterogeneity between ThT kinetic assays performed at 12.5 μM (Fig. S2). This observation suggests that the Asn-21 amide function facilitates the IAPP nucleation step through specific intra- or intermolecular hydrogen bonds. Substituting Asn-21 by its corresponding D-amino acid hastened amyloid formation, although it led to a lower fluorescence at the saturation phase. Similar trends were obtained with all peptides used at 25 μM (Fig. S1). These results show that modifications favoring turn conformation (Pro and D-Asn) hasten IAPP self-assembly, whereas restricting the local conformation to the helical space (Aib) delays amyloid formation.

Asn-21 modulates the conformational conversion associated with self-assembly

The effect of site-specific modifications on conformational transitions was evaluated by CD spectroscopy. Peptides were incubated at room temperature under quiescent conditions (20 mM Tris-HCl, pH 7.4, 50 μM IAPP), and far-UV CD spectra were recorded. As expected, immediately after solubilization of monomerized/lyophilized IAPP, a random coil CD spectrum was recorded (Fig. 3). No conformational shift was observed during the first 6 h incubation of WT IAPP, whereas a β-sheet secondary structure (single minimum at 220 nm) was observed upon 24 h. The presence of a hydrophobic group (Phe, Leu) confined IAPP into a β-sheet conformation immediately after solubilization. These β-sheet–rich species assembled under these conditions were also ThT-negative (Fig. S3). N21D and N21Dab remained in a random coil conformation, even after 48-h incubation. Although the N21A and N21G mutants showed a ThT-positive signal in the kinetic assays (Fig. 2), the two peptides remained in a random coil conformation after 24 h of incubation, and a β-sheet signal was observed only after 48 h of incubation. Moreover, under the conditions of the CD

Downloaded from http://www.jbc.org/ at DUPONT-BALL LIBRARY on May 7, 2020

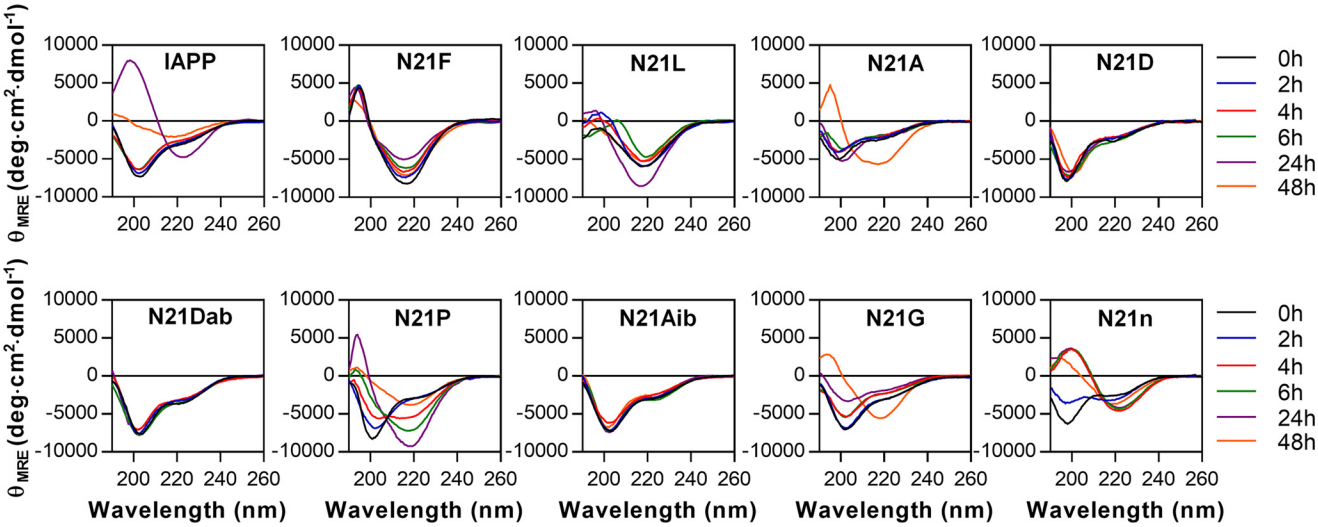


Figure 3. Effect of Asn-21 substitutions on the conformational transition of IAPP. Peptides were incubated under quiescent conditions in 20 mM Tris-HCl buffer, pH 7.4, at 50 μM. CD analysis was performed after incubation of 0, 2, 4, 6, 24, and 48 h. Far-UV CD spectra were recorded from 190 to 260 nm.

experiment, a low ThT fluorescence was measured for N21A and N21G (Fig. S3). Substitution of Asn-21 by an Aib abolished conformational transition. It is worth mentioning that time point measurements under quiescent conditions in a microcentrifuge tube (Fig. 3 and Fig. S3) cannot be directly compared with the microplate-based ThT kinetics (Fig. 2 and Figs. S1 and S2). We recently reported that, although the microplate kinetic assay is done under quiescent conditions (*i.e.* no agitation between each reading), the displacement of the microplate within the fluorimeter occurring during measurements is sufficient to accelerate amyloid formation (40). Thus, self-assembly of N21A, N21G, and N21Aib appears to be more dependent on agitation than the WT IAPP. The mechanical forces associated with agitation are known to enhance amyloid formation by promoting mass transport and amplifying the number of fibrils by fragmentation (secondary nucleation) (41).

Time point CD analysis of N21P and N21n mutants revealed their prompt random coil-to-β-sheet conformational conversion (Fig. 3), in agreement with ThT kinetics. A ThT-positive signal was measured for N21n at time 0 h (dead time of 3–4 min), confirming the prompt self-assembly of this analog (Fig. S3). In fact, short fibrils could even be observed by atomic force microscopy immediately after the solubilization of N21n, whereas no fibrillar aggregates were visible for WT (Fig. S4). Control rIAPP remained in a random coil conformation (Fig. S5).

The self-assembly of N21X derivatives was further characterized by measuring the formation of hydrophobic clusters using 8-anilino-1-napthalenesulfonic acid (ANS). The fluorescence intensity of ANS increases upon its binding to protein hydrophobic patches. Random coil ThT-negative WT IAPP species (0 h) did not induce any ANS fluorescence (Fig. 4). Upon 24-h incubation, a positive ANS signal was measured. This result indicates that the formation of ThT-positive β-sheet–rich assemblies (Fig. 3 and Fig. S3) is associated with the emergence of hydrophobic clusters (Fig. 4). Interestingly, N21F and N21L exhibited a strong signal of ANS fluorescence immediately after their solubilization. Thus, incorporation of a hydrophobic residue at position 21 prompts the formation of β-sheet–rich ThT-negative aggregates with high surface hydrophobicity. Successive substitution of Asn-21 with Asp and Dab precluded the formation of ANS-positive assemblies, whereas the Asn-to-Ala mutation reduced ANS fluorescence. As anticipated from the kinetic assays and time point CD analysis, incorporation of Pro and the inversion of Asn chirality led to a positive ANS signal. As observed for ThT (Fig. S3), freshly dissolved N21n showed an increase of ANS fluorescence (0 h; Fig. 4). The Asn-to-Gly mutation delayed time-dependent increase of ANS fluorescence, as observed for ThT fluorescence. Time point ANS fluorescence (Fig. 3) was plotted as a function of time point ThT fluorescence (Fig. S3), and we observed that the formation of ThT-positive assemblies is associated with the emergence of hydrophobic clusters for WT IAPP, N21n, and N21P (Fig. S6). The correlation between ANS and ThT signal was not present for N21F and N21L, whereas a low correlation was observed for N21G.

Asn-21 mutations modify the supramolecular architecture of assemblies

The mesoscopic architecture of the assembled proteospecies was analyzed by negative-stain transmission EM (TEM). Long, unbranched, and twisted fibrils were obtained for WT IAPP after 24 h of aging under the conditions of the time point analysis (Fig. 5). Amorphous aggregates were mainly observed for the N21F and N21L mutants, although short fibrils could be detected in some N21L samples (Fig. 5 and Fig. S7). TEM analysis validated that the addition of a charge at position 21 inhibits fibril formation, although fibril-like assemblies could be observed for N21Dab (Fig. S8). In sharp contrast, successive replacements of Asn-21 with Pro and its D-enantiomeric counterpart led to the formation of a dense network of fibrils. Although the time point CD and ThT analysis of N21A and N21G mutants suggested the absence of amyloid assemblies after 24 h of aging (Fig. 3 and Fig. S3), TEM analysis revealed the presence of fibrils for both peptides. Poorly defined fibrils could

Downloaded from http://www.jbc.org/ at DUPONT-BALL LIBRARY on May 7, 2020

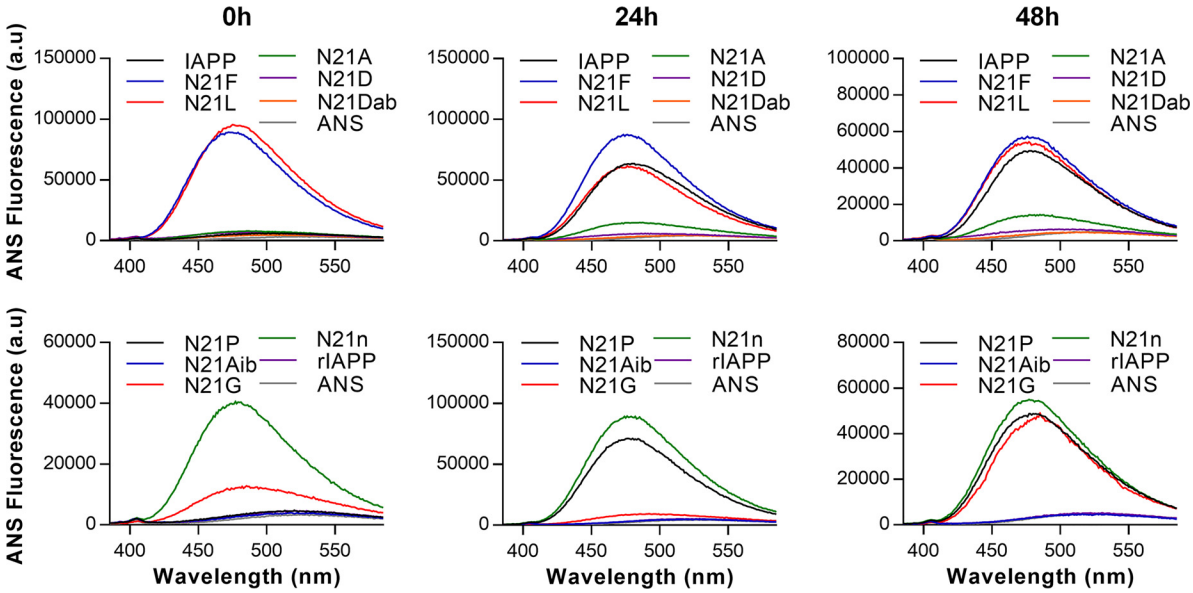


Figure 4. Effect of Asn-21 substitutions on surface hydrophobicity of IAPP assemblies. Peptides were incubated under quiescent conditions at 50 μM. After 0-, 24-, and 48-h incubation, the emission spectra of ANS was recorded from 385 to 585 nm with an excitation set at 355 nm. Data presented are the most representative spectra of at least three experiments performed in triplicate. *a.u.*, arbitrary units.

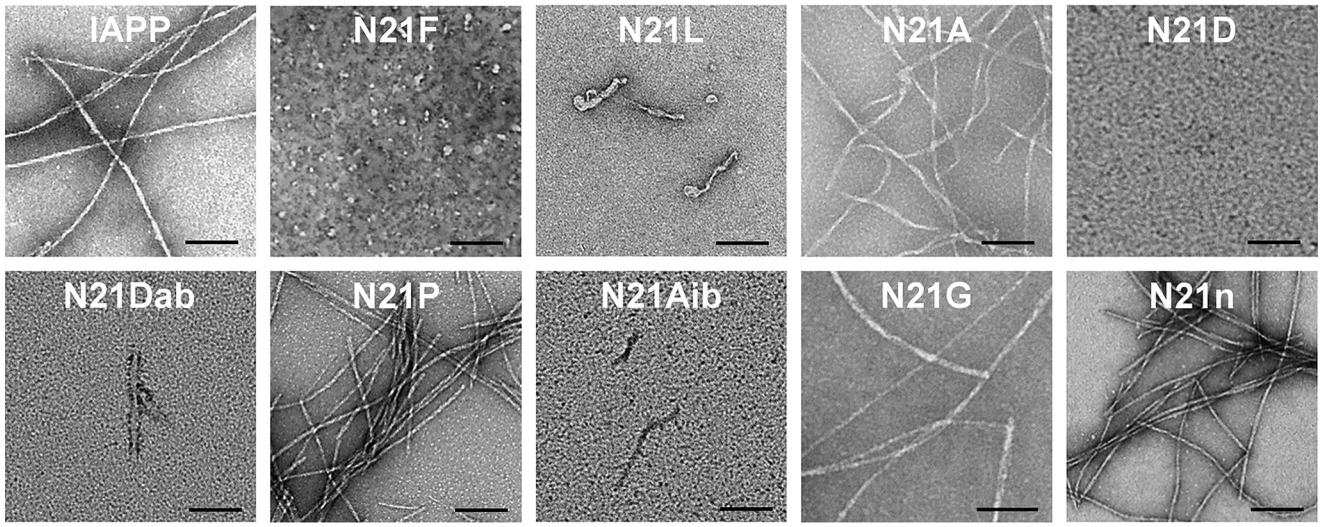


Figure 5. Effect of Asn-21 substitutions on the morphology of IAPP assemblies. Peptides were incubated in 20 mM Tris-HCl buffer, pH 7.4, for 24 h at 50 μM before TEM imaging. *Scale bars*, 100 nm.

be observed in some N21Aib preparations (Fig. 5 and Fig. S9), in agreement with the low reproducibility between ThT kinetics.

Toxicity of N21X mutants does not correlate with their in vitro amyloidogenicity

The relationships between the *in vitro* amyloidogenicity and the cytotoxicity of N21X analogs were investigated by evaluating the viability of INS-1 cells upon treatment with freshly dissolved monomerized peptides. As reported (12, 29, 42), a concentration-dependent decrease of viability was observed for IAPP, with a cell viability below 20% of control at 50 μM (Fig. 6). In contrast, the nonamyloidogenic rIAPP did not induce cell death, even at a concentration of 50 μM. N21A, N21P, and N21n mutants, which self-assembled into amyloids, reduced the viability of INS-1 cells as the WT peptide. Incorporation of a positive or a negative charge at position 21 reduced the toxicity of IAPP, although both analogs were toxic at 50 μM (Fig. 6). The hydrophobic-substituted derivatives were toxic to β-cells, although N21F and N21L did not form amyloids. These observations indicate that nonamyloidogenic IAPP derivatives (N21Dab, N21D, N21F, and N21L) can be toxic toward INS-1E cells. In contrast, N21Aib and N21G were nontoxic. Toxicity (Fig. 6) was plotted as a function of *in vitro* amyloidogenicity (Fig. 1) to evaluate the correlation between these two parameters. No direct correlation between *in vitro* amyloidogenicity and cytotoxicity was observed (Fig. S10), although mutagenesis at position 21 dramatically modulates both the cytotoxicity and the self-assembly of IAPP.

It was proposed that toxic IAPP species are mainly pre-amyloid intermediates that are transiently formed during the lag phase (12). Thus, the presence and distribution of oligomers populating the lag phase were evaluated for selected mutants using

Downloaded from http://www.jbc.org/ at DUPONT-BALL LIBRARY on May 7, 2020

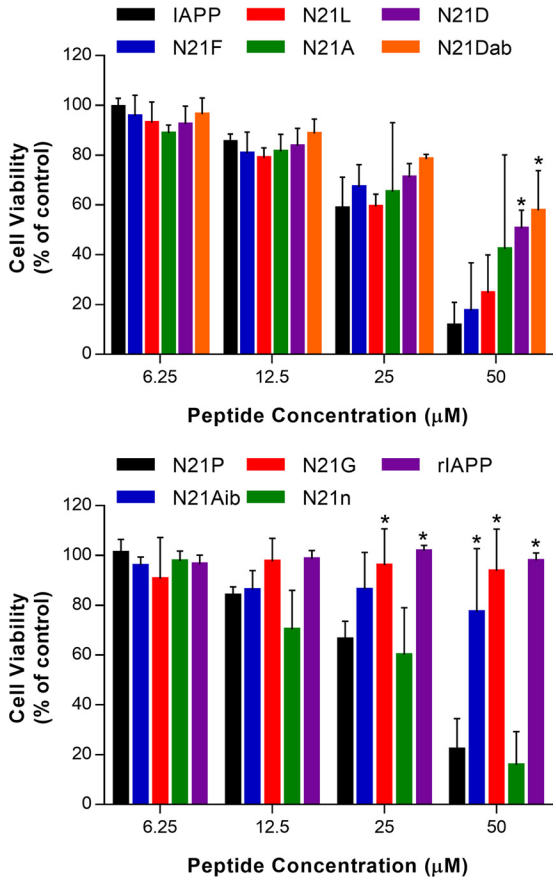


Figure 6. Effect of Asn-21 substitutions on IAPP cytotoxicity. INS-1E cells were treated with increasing concentration of freshly dissolved peptides for 24 h. Cell viability was measured using the resazurin reduction assay and compared with that of cells treated with vehicle. Data represent mean ± S.E. (*error bars*) of at least four experiments performed in triplicate. Results were analyzed using Student's *t* test, and statistically significant difference (between IAPP and mutants) was established at $p < 0.01$ (*).

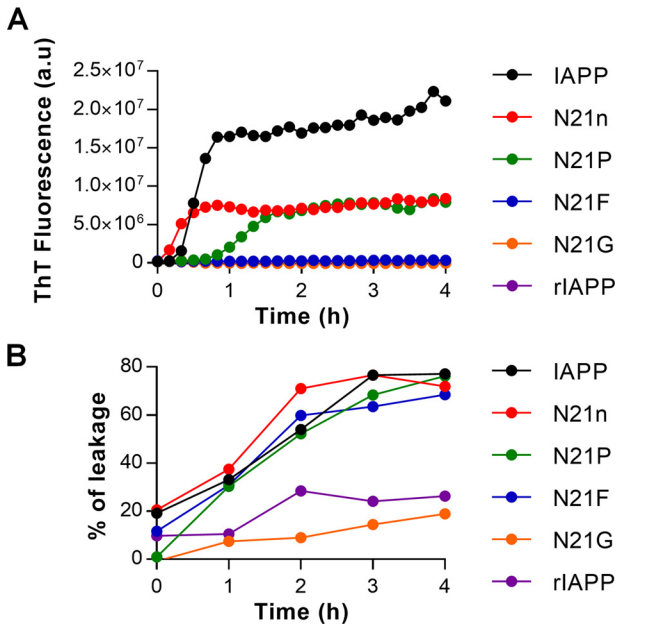


Figure 7. Effect of Asn-21 mutagenesis on membrane-induced amyloid formation and lipid vesicle disruption. *A*, representative kinetic traces of amyloid assembly in the presence of LUVs (DOPC/DOPG, 7:3) monitored by ThT (40 μM) fluorescence. Peptides (12.5 μM) and LUVs (500 μM) were incubated under quiescent conditions in 20 mM Tris-HCl, pH 7.4. *B*, membrane leakage of 500 μM DOPC/DOPG LUVs (7:3) by 50 μM peptides. *a.u.*, arbitrary units.

photoinduced cross-linking of unmodified proteins (PICUP) followed by SDS-PAGE analysis (43). As observed in Fig. S11, an essentially similar distribution of proteospecies, from monomers to hexamers, was obtained for WT, N21P, N21n, N21G, and rIAPP. In contrast, cross-linking of the ThT-negative and toxic N21F mutant only revealed monomers and dimers and an absence of higher oligomeric species. Considering that N21G (amyloidogenic) and rIAPP (nonamyloidogenic) are not cytotoxic (Fig. 6), the PICUP results indicate that toxicity is not necessarily associated with the *in vitro* aggregation propensity and that not all oligomers are toxic, as shown previously (12).

Mutagenesis of Asn-21 modulates lipid membrane disruption

The mechanism by which IAPP induces cell death is complex and is still the subject of active research (10, 44). One of the most accepted upstream events is disruption of the plasma membrane structural integrity by prefibrillar proteospecies (45, 46). In addition, lipid membranes are known to hasten amyloid formation and might change the pathway(s) by which IAPP self-assembles, compared with aqueous solution (45, 47). Thus, we sought to evaluate how mutagenesis at position 21 affects the kinetics of amyloid formation in the presence of lipid vesicles and the ability of IAPP to disrupt membranes. First, ThT fluorescence assays were performed in the presence of large unilamellar vesicles (LUVs) composed of phosphocholine/phosphoglycerol (DOPC/DOPG, 7:3). The presence of anionic vesicles dramatically hastened amyloid formation of WT, N21P, and N21n peptides, with a lag time under 30 min for N21n and WT and 90 min for N21P (Fig. 7*A*; peptide concentration of 12.5 μM). In contrast, no ThT signal was measured for the N21G and N21F mutants and rIAPP over the 4-h incubation time. Next, we examined the ability of these peptides to induce leakage of DOPC/DOPG vesicles. Calcein was encapsulated at high concentration within LUVs, leading to fluorescence self-quenching. Membrane disruption releases the dye, and the fluorescence is restored. LUVs loaded with calcein were incubated in the presence of 12.5 μM peptides, and fluorescence was measured for 4 h. For WT IAPP and the N21n and N21P mutants, an increase of fluorescence was observed over time with membrane leakage of 60–80% after 4 h (Fig. 7*B*). Strikingly, the nontoxic amyloidogenic N21G analog, which does not form ThT-positive species in the presence of LUVs, induced a low membrane leakage. Actually, N21G mutant shows a similar behavior in the presence of membrane vesicles as the nontoxic rIAPP (Fig. 7). Interestingly, although the N21F analog did not form ThT-positive signal in the presence of lipid vesicles, a high percentage of membrane leakage was measured. These results expose a certain association between cytotoxicity (Fig. 6) and membrane disruption (Fig. 7).

Residue 21 controls the assembly-dependent cytotoxicity of IAPP

Bearing in mind that Asn-21 mutagenesis modulates the morphology of the resulting assemblies (Fig. 5), we evaluated the toxicity of the proteospecies formed after a prolonged incu-

Downloaded from http://www.jbc.org/ at DUPONT-BALL LIBRARY on May 7, 2020

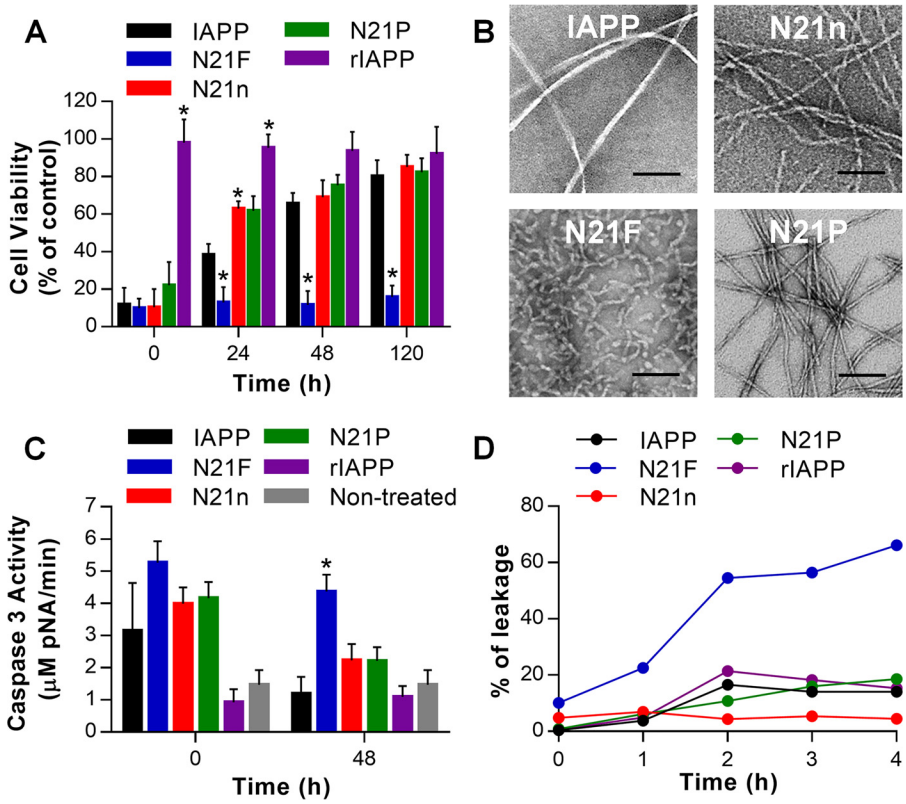


Figure 8. Effect of Asn-21 substitutions on cytotoxicity of IAPP proteospecies. *A* and *C*, INS-1E cells were treated for 24 h with 50 μM of pre-incubated peptides (0–120 h), and cell viability (*A*) and caspase-3 activation (*C*) were evaluated. *B*, TEM images of peptides incubated for 48 h under quiescent conditions at 150 μM. *Scale bars*, 100 nm. *D*, membrane leakage of 500 μM DOPC/DOPG LUVs (7:3) by 50 μM IAPP proteospecies (pre-incubated for 48 h at 150 μM). *A* and *C*, data represent mean ± S.E. (*error bars*) of at least three experiments performed in triplicate. Results were analyzed using Student's *t* test, and statistically significant difference (between IAPP and mutant) was established at $p < 0.01$ (*).

bation period. WT IAPP, N21F, N21P, N21n, and rIAPP were incubated at 150 μM under quiescent conditions at room temperature. At different incubation times, peptide solution was applied to INS-1E cells, and cellular viability was evaluated. As anticipated, all peptides, except for the rIAPP control, were highly toxic at time 0 h (Fig. 8*A*). N21P and N21n assemblies incubated for 24 h were significantly less toxic to cells compared with IAPP. The proteospecies generated after 120 h of aging for WT, N21P, and N21n were nontoxic. TEM images validated that IAPP, N21n, and N21P assembled into well-defined amyloid fibrils at 150 μM (Fig. 8*B*). These data support previous studies indicating that well-defined fibrils are poorly toxic. In sharp contrast, the Asn-to-Phe substitution locked IAPP into proteospecies, which remained highly toxic over time (Fig. 8*A*). As observed by TEM, N21F formed short and poorly defined wormlike fibrils when incubated at 150 μM for 48 h (Fig. 8*B*). Interestingly, immediately upon its solubilization at 150 μM, the N21F analog assembled into amorphous spherical aggregates that slowly evolved into short wormlike assemblies (Fig. S12).

IAPP-induced cytotoxicity is associated with numerous downstream cellular events, including oxidative stress, mitochondrial dysfunction, endoplasmic reticulum stress, and apoptosis (9, 44, 48). We evaluated the activation of caspase-3 upon cell treatment with the different proteospecies. As caspase-3 activation is an upstream event to cell death, cells were treated for 3 h with the proteospecies. All four peptides under their nonfibrillar states (0 h) induced a significant increase of caspase-3 activation (Fig. 8*C*). N21F short fibrillar species obtained after 48 h of aging strongly activated caspase-3, in contrast to IAPP, N21P, and N21n. Moreover, we measured the ability of the assemblies formed after 48 h of aging to induce membrane disruption using the calcein release assay. Interestingly, N21F wormlike aggregates disrupted anionic LUVs, whereas well-defined amyloid fibrils (WT, N21P, and N21n) had no significant effect on lipid membrane (Fig. 8*D*). We investigated whether the cytotoxicity and membrane leakage ability of N21F assemblies could be associated with the presence of remaining oligomers/monomers in solution. Accordingly, an N21F aggregation mixture (48 h; 150 μM) was centrifuged at 35,000 × *g* for 45 min, and the presence of soluble species in the supernatant was evaluated by analytical reverse-phase HPLC (RP-HPLC). As observed in Fig. S13, no N21F was detected by HPLC in the supernatant. These data indicate that N21F ThT-negative β-sheet–rich assemblies are highly toxic to pancreatic β-cells, increasing the complexity of identifying specific IAPP toxic species. Nonetheless, we cannot rule out the possibility that the N21F wormlike aggregates disassemble and release soluble species, which induce cell death.

Discussion

A complex network of specific intra- and intermolecular interactions, which give rise to off- and on-pathway intermediates, governs IAPP self-assembly from a disordered peptide into

Downloaded from http://www.jbc.org/ at DUPONT-BALL LIBRARY on May 7, 2020

highly ordered fibrils. Intermediate assemblies were identified as the most toxic species of the amyloidogenic cascade. Thus, it is important to pinpoint the chemical determinants governing these secondary and quaternary structural transitions. Whereas IAPP amyloid formation is somewhat tolerant to mutations, previous studies have revealed that self-assembly does not tolerate substitution at Asn-21 (25, 30). Herein, we performed a structure–assembly relationship study at position 21 to delineate the molecular mechanisms of self-assembly and to better define the conformational species associated with β-cell death.

In contrast to expected results based on previous studies, we showed that an Asn-21 amide group is not a prerequisite for nucleation and amyloid elongation. As shown in the kinetic assays, substitution by Ala led to a shorter lag time, and the N21A mutant formed well-defined fibrils. This result indicates that hydrogen-bonding interactions involving the Asn amide side chain are not mandatory for IAPP amyloid formation. Nonetheless, N21A amyloidogenesis was significantly delayed when assembly occurred in a test tube and was followed by time point ANS, ThT, and CD measurements. A similar trend was observed with the mutant N21G. N21A and N21G mutants show high heterogeneity between ThT kinetics in microplate assays. Microplate displacement within the fluorimeter induces significant agitation, hastening amyloid formation through mass transport and fibril fragmentation (secondary nucleation). Moreover, ThT kinetic assays are performed in nonbinding surface microplates, whereas the surface of microcentrifuge tubes is nontreated. It has been reported that hydrophobic surfaces, such as nonbinding coating, hasten amyloid formation by promoting the primary nucleation rate (41). These observations suggest that removing the amide group (*i.e.* N21A and N21G) prolongs the lag phase (delayed nucleation) under fully quiescent conditions and in the absence of a hydrophobic surface. In contrast, the nonbinding surface of the microplate and/or agitation within the fluorimeter counteract this effect by promoting primary and/or secondary nucleation events.

Interestingly, substitution of Asn-21 with the conformationally constrained and turn-inducing Pro accelerated amyloid formation. This result is surprising, considering that the incorporation of Pro within an amyloidogenic peptide is a common strategy to inhibit amyloid formation. This substitution constitutes the first *X*-to-Pro mutation within the amyloidogenic 20–29 segment promoting self-assembly. Inversing the chirality of Asn-21, a modification known to favor β-turn and to destabilize α-helix (34), dramatically hastened amyloid formation. Short ThT-positive fibrils were even observable immediately after solubilization of N21n. Previous studies have suggested that the segment 20–29 mediates initial self-recognition and that early oligomers contain stacks of parallel β-sheet within the ^{23}FGAIL^{27} region (24, 49, 50). However, below a critical concentration, IAPP self-recognition appears to be primarily initiated by the N-terminal region, which than propagates to the central domain (51). Regardless of the contacts initiating aggregation, a high-energy structural rearrangement within the 20–29 segment is necessary for the conversion from oligomers to fibrils. The energy barrier induced by the FGAIL β-sheet oligomers is predicted to slow down amyloid formation and to be at the origin of the lag phase (50). In the NMR and EPR atomistic structural models of amyloids, Asn-21 is located at the β-strand–loop interface, whereas in the oligomers, this residue is located close to the FGAIL β-sheet. Accordingly, the N21P mutation provides sufficient torsional driving forces to overcome the FGAIL β-sheet intermediate free energy barrier while not affecting the initial self-recognition events. This promotes primary nucleation by facilitating the structural conversion of the oligomer into the nuclei conformation.

Aromatic stacking and hydrophobic collapse are key driving forces for aggregation. IAPP self-recognition involving the 20–29 amyloidogenic core is mainly directed by hydrophobic interactions (52). It has been reported, using both the full-length peptide and IAPP(20–29), that the contributions of Phe-23 in amyloid formation are a function of its hydrophobicity and β-sheet propensity, whereas its ability to form π–π interactions is not critical (27, 53). In the present study, we observed that the successive substitutions of Asn-21 with Leu and Phe led to the prompt formation of ThT-negative β-sheet–rich aggregates with high surface hydrophobicity. Some short and poorly defined fibrils could also be observed for N21L and N21F when incubated for a long period at 50 and 150 μM, respectively. The increase of hydrophobicity and/or β-sheet propensity of the 20–29 segment induced by these mutations promote(s) the formation of low energy nonamyloid aggregates, most likely due to the propagation of the FGAIL parallel β-sheet. In sharp contrast, incorporation of a charge (*i.e.* Asp or Dab) inhibited amyloid assembly, probably due to electrostatic repulsion between monomers. It has been shown that the consecutive substitutions of the neighboring Asn-22 residue with Asp and Leu have a modest impact on IAPP amyloid formation (25, 30). This clearly indicates that Asn-21 plays a dictating role in IAPP self-assembly and is involved in specific intra- or intermolecular interactions controlling nucleation and/or elongation events, which is not the case for Asn-22.

Whereas the causative link between islet amyloids and type II diabetes was initially described over 100 years ago (3), the conformational nature of the proteotoxic species remains ambiguous. Whereas most studies have reported that soluble oligomers populating the lag phase are causing β-cell death (10, 12, 54), some earlier and current researches have proposed that amyloid fibrils could also be cytotoxic (8, 13). Considering that Asn-21 mutagenesis modulates the kinetics of self-assembly and the final supramolecular morphology, we evaluated the toxicity of freshly dissolved IAPPs (monomers/oligomers) and of assemblies generated after different aging periods. We observed a concentration-dependent β-cell toxicity for most N21X derivatives. Interestingly, although N21F and N21L did not self-assemble into amyloids, both mutants showed a high toxicity. In sharp contrast, N21G was nontoxic, although this mutant is prone to form amyloid fibrils. These results highlight that the relation between amyloidogenicity and cytotoxicity cannot be rationalized according to *in vitro* biophysical studies performed in homogeneous solution. Moreover, the nontoxic rIAPP and N21G mutant readily oligomerized, indicating that not all oligomers are cytotoxic and that specific structural and/or physicochemical properties are determining factors for

Downloaded from http://www.jbc.org/ at DUPONT-BALL LIBRARY on May 7, 2020

cellular toxicity (12, 55). Interestingly, the nontoxic mutant N21G induced low leakage of anionic LUVs, comparable with the rIAPP. This suggests the existence of a correlation between cytotoxicity and *in vitro* membrane disruption. However, this observation should be taken with caution, as it has been reported that there is no direct correlation between cell toxicity and the ability to disrupt model membranes (56). Besides, it has been shown using the N-terminal 1–19 fragment that membrane disruption can occur independently of amyloid formation (57) and that the capacity of hIAPP(1–19) to perturb membrane is associated with a specific transmembrane orientation of the peptide (58). Thus, differences between the membrane-induced conformation of the WT and the N21G variant can be related to the observed divergence effect on lipid membrane integrity.

Amyloid fibrils assembled from WT IAPP, N21P, and N21n were poorly toxic, whereas the N21F analog formed toxic wormlike aggregates, which induce disruption of anionic lipid membranes. N21F cytotoxic assemblies are ThT-negative, display a high β-sheet content, and have solvent-exposed hydrophobic patches. This is in agreement with previous studies stipulating that the toxicity of protein aggregates is associated with their surface hydrophobicity (59, 60). However, the structural and physico-chemical properties of N21F aggregates diverge substantially from those of the toxic IAPP intermediates reported by Abedini *et al.* (12), which lack extensive β-sheet structure and do not have persistent hydrophobic patches. Thus, it appears that multiple IAPP quaternary species could contribute to β-cell death, perhaps by using different upstream mechanisms. Consequently, it remains challenging to determine the specific conformational features of cytotoxic prefibrillar and/or amyloid assemblies.

Overall, the present work indicates that specific intra- and intermolecular interactions involving Asn-21 are governing nuclei formation and protofilament elongation. Asn-21 could promote IAPP primary nucleation by facilitating the conformational conversion of the FGAIL β-sheet intermediate into poorly toxic fibrillar quaternary structure. This study identifies position 21 as a hinge residue that controls both the amyloidogenicity and the cytotoxicity of IAPP, ultimately supporting the rational development of therapeutic strategies to arrest aggregation and IAPP-induced pancreatic β-cell loss.

Experimental procedures

Peptide synthesis and purification

Peptides were synthesized on solid support using Fmoc (fluorenylmethyloxycarbonyl chloride) chemistry. Oxazolidine dipeptide derivatives were used to facilitate synthesis (61). Peptides were cleaved from the Rink Amide AM resin with a mixture of TFA, ethanedithiol, phenol, and water. Crude peptides were precipitated with ethyl ether, solubilized in water, and lyophilized. Peptides were dissolved in 100% acetic acid and diluted to 35% to be purified by RP-HPLC on a C_{18} column. Fractions were analyzed by TOF MS using a LC/electrospray ionization-TOF (Table S1 and Fig. S14). Peptides were cyclized with 100% DMSO overnight and then diluted to 20% to be purified by RP-HPLC a second time. Fractions with purity higher than 95% were pooled and lyophilized (Figs. S15–S17).

IAPP monomerization and sample preparation

Aliquots of monomerized IAPP were prepared by dissolving the lyophilized and pure peptide in 100% hexafluoro-2-propanol to a concentration of 1 mg/ml. The solution was filtered through a 0.22-μm hydrophilic polyvinylidene difluoride filter and sonicated for 20 min before being lyophilized. The resulting peptide powder was solubilized for a second time in hexafluoro-2-propanol to a concentration of 1 mg/ml and sonicated for 20 min, and the solution was aliquoted and lyophilized again. Monomerized IAPP samples were kept dried at −80 °C until used, but not for longer than 4 weeks.

Kinetics of amyloid formation by ThT fluorescence

Solutions were prepared by dissolving the lyophilized peptide at a concentration of 50 μM in 20 mM Tris-HCl, pH 7.4. Assays were performed at 25 °C without stirring in sealed black-wall clear-bottom 96-well nonbinding surface plates with 100 μl/well. Final peptide concentrations were 12.5 and 25 μM, and ThT concentration was 40 μM. LUVs were added (or not) at a final concentration of 500 μM. Fluorescence, excitation at 440 nm and emission at 485 nm, was measured every 10 min. Data obtained from triplicate wells were averaged, corrected by subtracting the corresponding control reaction, and plotted as fluorescence *versus* time. Data of time dependence of ThT fluorescence were fitted to a sigmoidal Boltzmann model, where T_{50} is the time required to reach half of the fluorescence intensity, k is the apparent first-order constant, and Y_{max} and Y_0 are, respectively, the maximum and initial fluorescence values.

$$Y = \frac{Y_0 + (Y_{max} - Y_0)}{1 + e^{-(T - T_{50})}/k} \quad \text{(Eq. 1)}$$

The lag time is described as $T_{50} - 2/k$. Data (lag time and final ThT) of at least four different lots of peptides were averaged and were expressed as the mean ± S.D. Evaluation of the results was made using Student's t test, and statistically significant difference (between WT and mutants) was established at $p < 0.01$.

CD spectroscopy

Lyophilized aliquots of peptide were dissolved in 20 mM Tris-HCl, pH 7.4, at 50 μM and were incubated at room temperature without agitation. Samples were incorporated into a 1-mm path length quartz cell. Far-UV CD spectra were recorded from 190 to 260 nm using a Jasco J-815 CD spectropolarimeter at 25 °C. The wavelength step was set at 0.5 nm with an average time of 10 s/scan at each wavelength step. Each collected spectrum was background-subtracted with peptide-free buffer. The raw data were converted to mean residue ellipticity.

Time point fluorescence spectroscopy (ThT and ANS)

Solutions were prepared by dissolving the peptides at a concentration of 50 μM in 20 mM Tris-HCl, pH 7.4, and were incubated at room temperature without agitation. At the indicated time, peptide was diluted to a final concentration of 25 μM in

Downloaded from http://www.jbc.org/ at DUPONT-BALL LIBRARY on May 7, 2020

the presence of a final concentration of 40 μM ThT or 50 μM ANS. Fluorescence was measured in ultra-micro 10-mm length cells using a PTI QuantaMaster spectrofluorometer. For ThT, excitation wavelength was set at 440 nm, and the emission spectra from 450 to 550 nm was recorded. For ANS, the excitation wavelength was set at 355 nm, and the emission scan was recorded from 385 to 585 nm. For each experiment, control reactions (without IAPP) were carried out. Data obtained from at least three experiments were averaged.

Transmission EM

Peptide samples were solubilized in a 20 mM Tris-HCl buffer, pH 7.4, to a final concentration of 50 or 150 μM (for time-resolved toxicity assays) and incubated at room temperature under fully quiescent conditions. Samples were diluted to 10 μM before being applied on glow-discharged carbon films on 300-mesh copper grids. Peptides were adsorbed and were negatively stained with 1.5% uranyl formate for 45 s. Images were recorded using an FEI Tecnai 12 BioTwin microscope operating at 120 kV and equipped with an AMT XR80C CCD camera system.

Atomic force microscopy

Peptides were solubilized in a 20 mM Tris-HCl buffer, pH 7.4, to a concentration of 50 μM and incubated at room temperature without agitation. After the indicated time of incubation, the peptide was diluted in 1% acetic acid and immediately applied to freshly cleaved mica. The mica was washed twice with deionized water and air-dried for 24 h. Samples were analyzed using a Veeco/Bruker Multimode atomic force microscope using tapping mode with a silicon tip (2–12-nm tip radius, 0.4 newton/m force constant) on a nitride lever. Images were taken at 0.5 Hz and 1024 scans/min.

Photoinduced cross-linking

Peptides were incubated at 50 μM in 20 mM Tris-HCl, pH 7.4, at 25 °C for the indicated periods. Cross-linking solution was added to a final concentration of 70 μM Tris-(bipyridyl)Ru(II) and 1.4 mM ammonium persulfate. Aliquots were illuminated with a 150-watt incandescent bulb for 10 s. Reaction was quenched by the addition of 1 M DTT. Prefibrillar species were separated by SDS-PAGE using a 15% Tris-Tricine gel and visualized by silver staining.

Cell viability assay

Rat INS-1 cells were cultured in black-wall clear-bottom 96-well plates (tissue culture–treated) at a density of 20,000 cells/well (100 μl/well) in RPMI 1640 medium supplemented with 10% FBS, 100 units/ml penicillin, 100 mg/ml streptomycin, 10 mM HEPES, 1 mM sodium pyruvate, 50 mM β-mercaptoethanol. After a 48-h incubation at 37 °C in a 5% CO_2, cells were treated by the direct addition of 50 μl of peptide solutions (20 mM Tris-HCl, pH 7.4) at 3× final concentration. Cells were incubated another 24 h, and cellular viability was measured using the resazurin reduction assay. Cell viability (in percentage) was calculated from the ratio of the fluorescence of the treated sample to the control (vehicle-treated). Data of at least four assays (with different peptide lots) were averaged and were expressed as the mean ± S.D. Statistical analysis was performed with Prism version 6.0 software using Student's t test, and statistically significant difference (between WT and mutants) was established at $p < 0.01$.

Caspase-3 activity assay

Rat INS-1 β-cells were cultured in 12-well plates (tissue culture–treated) at a density of 400,000 cells/well in supplemented RPMI 1640 medium. After a 48-h incubation, cells were treated by the direct addition of peptide solution (50 μM) for 3 h. Cells were lysed on ice for 30 min followed by a centrifugation at 16,000 × g for 20 min. Protein extracts in supernatant were measured by a caspase-3 colorimetric assay (Sigma-Aldrich). Commercial caspase-3 enzyme provided with the kit was used as a positive control. Caspase-3 activity after a 2-h reaction was evaluated at 37 °C by measuring absorbance at 405 nm.

Large unilamellar vesicle preparation and membrane leakage

DOPC and DOPG lipids were solubilized in 100% chloroform at a ratio of 7:3, and solvent was evaporated. The lipid film was hydrated in 20 mM Tris-HCl, pH 7.4, buffer containing 70 mM calcein, or not, for 30 min. Solubility of calcein was increased with the dropwise addition of NaOH. The solution was freeze-thawed five times, and lipids were extruded through a 0.1-μm nucleopore membrane. Nonencapsulated calcein was removed using a 10-ml Sephadex G-25 column. Lipid concentration was determined using an P_i detection colorimetric assay. The size and homogeneity of LUVs were analyzed by dynamic light scattering, and an average diameter of 100 nm was obtained. For membrane leakage, 50 μM peptide was used, and concentration of LUVs was fixed at 500 μM. The excitation wavelength was set at 495 nm, and the emission scan was recorded from 500 to 540 nm in an ultra-micro cell. Fluorescence was measured over incubation time. The control used to determine 100% leakage (F_{max}) was calcein-LUVs with 0.2% Triton X-100. Dye leakage was reported using the following equation.

$$\%\ \text{of leakage} = (F - F_{baseline})/(F_{max} - F_{baseline}) \quad \text{(Eq. 2)}$$

Author contributions—E. G., P. T. N., and X. Z. conducted the experiments and analyzed the results. E. G., P. T. N., and S. B. wrote the paper and prepared the figures. S. B. supervised the project.

References

1. Chiti, F., and Dobson, C. M. (2017) Protein misfolding, amyloid formation, and human disease: a summary of progress over the last decade. *Annu. Rev. Biochem.* **86,** 27–68 CrossRef Medline
2. Cohen, F. E., and Kelly, J. W. (2003) Therapeutic approaches to protein-misfolding diseases. *Nature* **426,** 905–909 CrossRef Medline
3. Opie, E. L. (1901) On the relation of chronic interstitial pancreatitis to the islands of langerhans and to diabetes melutus. *J. Exp. Med.* **5,** 397–428 CrossRef Medline
4. Westermark, P., Andersson, A., and Westermark, G. T. (2011) Islet amyloid polypeptide, islet amyloid, and diabetes mellitus. *Physiol. Rev.* **91,** 795–826 CrossRef Medline
5. Höppener, J. W., Ahrén, B., and Lips, C. J. (2000) Islet amyloid and type 2 diabetes mellitus. *N. Engl. J. Med.* **343,** 411–419 CrossRef Medline

Downloaded from http://www.jbc.org/ at DUPONT-BALL LIBRARY on May 7, 2020

6. Cooper, G. J., Willis, A. C., Clark, A., Turner, R. C., Sim, R. B., and Reid, K. B. (1987) Purification and characterization of a peptide from amyloid-rich pancreases of type 2 diabetic patients. *Proc. Natl. Acad. Sci. U.S.A.* **84,** 8628–8632 CrossRef Medline
7. Westermark, P., Wernstedt, C., Wilander, E., Hayden, D. W., O'Brien, T. D., and Johnson, K. H. (1987) Amyloid fibrils in human insulinoma and islets of Langerhans of the diabetic cat are derived from a neuropeptide-like protein also present in normal islet cells. *Proc. Natl. Acad. Sci. U.S.A.* **84,** 3881–3885 CrossRef Medline
8. Lorenzo, A., Razzaboni, B., Weir, G. C., and Yankner, B. A. (1994) Pancreatic islet cell toxicity of amylin associated with type-2 diabetes mellitus. *Nature* **368,** 756–760 CrossRef Medline
9. Nguyen, P. T., Andraka, N., De Carufel, C. A., and Bourgault, S. (2015) Mechanistic contributions of biological cofactors in islet amyloid polypeptide amyloidogenesis. *J. Diabetes Res.* **2015,** 515307 CrossRef Medline
10. Raleigh, D., Zhang, X., Hastoy, B., and Clark, A. (2017) The beta-cell assassin: IAPP cytotoxicity. *J. Mol. Endocrinol.* **59,** R121–R140 CrossRef Medline
11. Cao, P., Marek, P., Noor, H., Patsalo, V., Tu, L. H., Wang, H., Abedini, A., and Raleigh, D. P. (2013) Islet amyloid: from fundamental biophysics to mechanisms of cytotoxicity. *FEBS Lett.* **587,** 1106–1118 CrossRef Medline
12. Abedini, A., Plesner, A., Cao, P., Ridgway, Z., Zhang, J., Tu, L. H., Middleton, C. T., Chao, B., Sartori, D. J., Meng, F., Wang, H., Wong, A. G., Zanni, M. T., Verchere, C. B., Raleigh, D. P., and Schmidt, A. M. (2016) Time-resolved studies define the nature of toxic IAPP intermediates, providing insight for anti-amyloidosis therapeutics. *Elife* **5,** e12977 CrossRef Medline
13. Krotee, P., Rodriguez, J. A., Sawaya, M. R., Cascio, D., Reyes, F. E., Shi, D., Hattne, J., Nannenga, B. L., Oskarsson, M. E., Philipp, S., Griner, S., Jiang, L., Glabe, C. G., Westermark, G. T., Gonen, T., and Eisenberg, D. S. (2017) Atomic structures of fibrillar segments of hIAPP suggest tightly mated beta-sheets are important for cytotoxicity. *Elife* **6,** e19273 CrossRef Medline
14. Zhu, S., Larkin, D., Lu, S., Inouye, C., Haataja, L., Anjum, A., Kennedy, R., Castle, D., and Arvan, P. (2016) Monitoring C-peptide storage and secretion in islet beta-cells *in vitro* and *in vivo*. *Diabetes* **65,** 699–709 CrossRef Medline
15. Williamson, J. A., and Miranker, A. D. (2007) Direct detection of transient α-helical states in islet amyloid polypeptide. *Protein Sci.* **16,** 110–117 CrossRef Medline
16. Patil, S. M., Xu, S., Sheftic, S. R., and Alexandrescu, A. T. (2009) Dynamic α-helix structure of micelle-bound human amylin. *J. Biol. Chem.* **284,** 11982–11991 CrossRef Medline
17. Nanga, R. P., Brender, J. R., Vivekanandan, S., and Ramamoorthy, A. (2011) Structure and membrane orientation of IAPP in its natively amidated form at physiological pH in a membrane environment. *Biochim. Biophys. Acta* **1808,** 2337–2342 CrossRef Medline
18. Rodriguez Camargo, D. C., Korshavn, K. J., Jussupow, A., Raltchev, K., Goricanec, D., Fleisch, M., Sarkar, R., Xue, K., Aichler, M., Mettenleiter, G., Walch, A. K., Camilloni, C., Hagn, F., Reif, B., and Ramamoorthy, A. (2017) Stabilization and structural analysis of a membrane-associated hIAPP aggregation intermediate. *Elife* **6,** e31226 CrossRef Medline
19. Luca, S., Yau, W. M., Leapman, R., and Tycko, R. (2007) Peptide conformation and supramolecular organization in amylin fibrils: constraints from solid-state NMR. *Biochemistry* **46,** 13505–13522 CrossRef Medline
20. Bedrood, S., Li, Y., Isas, J. M., Hegde, B. G., Baxa, U., Haworth, I. S., and Langen, R. (2012) Fibril structure of human islet amyloid polypeptide. *J. Biol. Chem.* **287,** 5235–5241 CrossRef Medline
21. Abedini, A., and Raleigh, D. P. (2009) A critical assessment of the role of helical intermediates in amyloid formation by natively unfolded proteins and polypeptides. *Protein Eng. Des. Sel.* **22,** 453–459 CrossRef Medline
22. Williamson, J. A., Loria, J. P., and Miranker, A. D. (2009) Helix stabilization precedes aqueous and bilayer-catalyzed fiber formation in islet amyloid polypeptide. *J. Mol. Biol.* **393,** 383–396 CrossRef Medline
23. De Carufel, C. A., Quittot, N., Nguyen, P. T., and Bourgault, S. (2015) Delineating the role of helical intermediates in natively unfolded polypeptide amyloid assembly and cytotoxicity. *Angew. Chem. Int. Ed. Engl.* **54,** 14383–14387 CrossRef Medline
24. Maj, M., Lomont, J. P., Rich, K. L., Alperstein, A. M., and Zanni, M. T. (2018) Site-specific detection of protein secondary structure using 2D IR dihedral indexing: a proposed assembly mechanism of oligomeric hIAPP. *Chem. Sci.* **9,** 463–474 CrossRef Medline
25. Koo, B. W., Hebda, J. A., and Miranker, A. D. (2008) Amide inequivalence in the fibrillar assembly of islet amyloid polypeptide. *Protein Eng. Des. Sel.* **21,** 147–154 CrossRef Medline
26. Koo, B. W., and Miranker, A. D. (2005) Contribution of the intrinsic disulfide to the assembly mechanism of islet amyloid. *Protein Sci.* **14,** 231–239 CrossRef Medline
27. Tu, L. H., and Raleigh, D. P. (2013) Role of aromatic interactions in amyloid formation by islet amyloid polypeptide. *Biochemistry* **52,** 333–342 CrossRef Medline
28. Abedini, A., Meng, F., and Raleigh, D. P. (2007) A single-point mutation converts the highly amyloidogenic human islet amyloid polypeptide into a potent fibrillization inhibitor. *J. Am. Chem. Soc.* **129,** 11300–11301 CrossRef Medline
29. Khemtemourian, L., Guillemain, G., Foufelle, F., and Killian, J. A. (2017) Residue specific effects of human islet polypeptide amyloid on self-assembly and on cell toxicity. *Biochimie* **142,** 22–30 CrossRef Medline
30. Nguyen, P. T., Zottig, X., Sebastiao, M., and Bourgault, S. (2017) Role of site-specific asparagine deamidation in islet amyloid polypeptide amyloidogenesis: key contributions of residues 14 and 21. *Biochemistry* **56,** 3808–3817 CrossRef Medline
31. Fox, A., Snollaerts, T., Errecart Casanova, C., Calciano, A., Nogaj, L. A., and Moffet, D. A. (2010) Selection for nonamyloidogenic mutants of islet amyloid polypeptide (IAPP) identifies an extended region for amyloidogenicity. *Biochemistry* **49,** 7783–7789 CrossRef Medline
32. Sakagashira, S., Hiddinga, H. J., Tateishi, K., Sanke, T., Hanabusa, T., Nanjo, K., and Eberhardt, N. L. (2000) S20G mutant amylin exhibits increased *in vitro* amyloidogenicity and increased intracellular cytotoxicity compared to wild-type amylin. *Am. J. Pathol.* **157,** 2101–2109 CrossRef Medline
33. Bourgault, S., Vaudry, D., Ségalas-Milazzo, I., Guilhaudis, L., Couvineau, A., Laburthe, M., Vaudry, H., and Fournier, A. (2009) Molecular and conformational determinants of pituitary adenylate cyclase-activating polypeptide (PACAP) for activation of the PAC1 receptor. *J. Med. Chem.* **52,** 3308–3316 CrossRef Medline
34. Hruby, V. J. (2002) Designing peptide receptor agonists and antagonists. *Nat. Rev. Drug. Discov.* **1,** 847–858 CrossRef Medline
35. Karle, I. L. (2001) Controls exerted by the Aib residue: helix formation and helix reversal. *Biopolymers* **60,** 351–365 CrossRef Medline
36. Westermark, P., Engström, U., Johnson, K. H., Westermark, G. T., and Betsholtz, C. (1990) Islet amyloid polypeptide: pinpointing amino acid residues linked to amyloid fibril formation. *Proc. Natl. Acad. Sci. U.S.A.* **87,** 5036–5040 CrossRef Medline
37. LeVine, H. (1995) Thioflavine T interaction with amyloid β-sheet structures. *Amyloid* **2,** 1–6 CrossRef
38. Kraus, A. (2016) Proline and lysine residues provide modulatory switches in amyloid formation: insights from prion protein. *Prion* **10,** 57–62 CrossRef Medline
39. Abedini, A., and Raleigh, D. P. (2006) Destabilization of human IAPP amyloid fibrils by proline mutations outside of the putative amyloidogenic domain: is there a critical amyloidogenic domain in human IAPP? *J. Mol. Biol.* **355,** 274–281 CrossRef Medline
40. Sebastiao, M., Quittot, N., and Bourgault, S. (2017) Thioflavin T fluorescence to analyse amyloid formation kinetics: measurement frequency as a factor explaining irreproducibility. *Anal. Biochem.* **532,** 83–86 CrossRef Medline
41. Grigolato, F., Colombo, C., Ferrari, R., Rezabkova, L., and Arosio, P. (2017) Mechanistic origin of the combined effect of surfaces and mechanical agitation on amyloid formation. *ACS Nano* **11,** 11358–11367 CrossRef Medline
42. De Carufel, C. A., Nguyen, P. T., Sahnouni, S., and Bourgault, S. (2013) New insights into the roles of sulfated glycosaminoglycans in islet amyloid

Downloaded from http://www.jbc.org/ at DUPONT-BALL LIBRARY on May 7, 2020

ASBMB

polypeptide amyloidogenesis and cytotoxicity. *Biopolymers* **100,** 645–655 CrossRef Medline
43. Bitan, G., and Teplow, D. B. (2004) Rapid photochemical cross-linking–a new tool for studies of metastable, amyloidogenic protein assemblies. *Acc. Chem. Res.* **37,** 357–364 CrossRef Medline
44. Abedini, A., and Schmidt, A. M. (2013) Mechanisms of islet amyloidosis toxicity in type 2 diabetes. *FEBS Lett.* **587,** 1119–1127 CrossRef Medline
45. Brender, J. R., Salamekh, S., and Ramamoorthy, A. (2012) Membrane disruption and early events in the aggregation of the diabetes related peptide IAPP from a molecular perspective. *Acc. Chem. Res.* **45,** 454–462 CrossRef Medline
46. Birol, M., Kumar, S., Rhoades, E., and Miranker, A. D. (2018) Conformational switching within dynamic oligomers underpins toxic gain-of-function by diabetes-associated amyloid. *Nat. Commun.* **9,** 1312 CrossRef Medline
47. Hebda, J. A., and Miranker, A. D. (2009) The interplay of catalysis and toxicity by amyloid intermediates on lipid bilayers: insights from type II diabetes. *Annu. Rev. Biophys.* **38,** 125–152 CrossRef Medline
48. Zhang, S., Liu, J., Dragunow, M., and Cooper, G. J. (2003) Fibrillogenic amylin evokes islet beta-cell apoptosis through linked activation of a caspase cascade and JNK1. *J. Biol. Chem.* **278,** 52810–52819 CrossRef Medline
49. Buchanan, L. E., Dunkelberger, E. B., Tran, H. Q., Cheng, P. N., Chiu, C. C., Cao, P., Raleigh, D. P., de Pablo, J. J., Nowick, J. S., and Zanni, M. T. (2013) Mechanism of IAPP amyloid fibril formation involves an intermediate with a transient beta-sheet. *Proc. Natl. Acad. Sci. U.S.A.* **110,** 19285–19290 CrossRef Medline
50. Serrano, A. L., Lomont, J. P., Tu, L. H., Raleigh, D. P., and Zanni, M. T. (2017) A free energy barrier caused by the refolding of an oligomeric intermediate controls the lag time of amyloid formation by hIAPP. *J. Am. Chem. Soc.* **139,** 16748–16758 CrossRef Medline
51. Brender, J. R., Krishnamoorthy, J., Sciacca, M. F., Vivekanandan, S., D'Urso, L., Chen, J., La Rosa, C., and Ramamoorthy, A. (2015) Probing the sources of the apparent irreproducibility of amyloid formation: drastic changes in kinetics and a switch in mechanism due to micellelike oligomer formation at critical concentrations of IAPP. *J. Phys. Chem. B* **119,** 2886–2896 CrossRef Medline
52. Wu, C., Lei, H., and Duan, Y. (2005) Elongation of ordered peptide aggregate of an amyloidogenic hexapeptide NFGAIL observed in molecular dynamics simulations with explicit solvent. *J. Am. Chem. Soc.* **127,** 13530–13537 CrossRef Medline
53. Doran, T. M., Kamens, A. J., Byrnes, N. K., and Nilsson, B. L. (2012) Role of amino acid hydrophobicity, aromaticity, and molecular volume on IAPP(20–29) amyloid self-assembly. *Proteins* **80,** 1053–1065 CrossRef Medline
54. Huang, C. J., Lin, C. Y., Haataja, L., Gurlo, T., Butler, A. E., Rizza, R. A., and Butler, P. C. (2007) High expression rates of human islet amyloid polypeptide induce endoplasmic reticulum stress mediated beta-cell apoptosis, a characteristic of humans with type 2 but not type 1 diabetes. *Diabetes* **56,** 2016–2027 CrossRef Medline
55. Young, L. M., Cao, P., Raleigh, D. P., Ashcroft, A. E., and Radford, S. E. (2014) Ion mobility spectrometry-mass spectrometry defines the oligomeric intermediates in amylin amyloid formation and the mode of action of inhibitors. *J. Am. Chem. Soc.* **136,** 660–670 CrossRef Medline
56. Cao, P., Abedini, A., Wang, H., Tu, L. H., Zhang, X., Schmidt, A. M., and Raleigh, D. P. (2013) Islet amyloid polypeptide toxicity and membrane interactions. *Proc. Natl. Acad. Sci. U.S.A.* **110,** 19279–19284 CrossRef Medline
57. Brender, J. R., Lee, E. L., Cavitt, M. A., Gafni, A., Steel, D. G., and Ramamoorthy, A. (2008) Amyloid fiber formation and membrane disruption are separate processes localized in two distinct regions of IAPP, the type-2-diabetes-related peptide. *J. Am. Chem. Soc.* **130,** 6424–6429 CrossRef Medline
58. Nanga, R. P., Brender, J. R., Xu, J., Veglia, G., and Ramamoorthy, A. (2008) Structures of rat and human islet amyloid polypeptide IAPP(1–19) in micelles by NMR spectroscopy. *Biochemistry* **47,** 12689–12697 CrossRef Medline
59. Mannini, B., Mulvihill, E., Sgromo, C., Cascella, R., Khodarahmi, R., Ramazzotti, M., Dobson, C. M., Cecchi, C., and Chiti, F. (2014) Toxicity of protein oligomers is rationalized by a function combining size and surface hydrophobicity. *ACS Chem. Biol.* **9,** 2309–2317 CrossRef Medline
60. Lorenzen, N., Nielsen, S. B., Buell, A. K., Kaspersen, J. D., Arosio, P., Vad, B. S., Paslawski, W., Christiansen, G., Valnickova-Hansen, Z., Andreasen, M., Enghild, J. J., Pedersen, J. S., Dobson, C. M., Knowles, T. P., and Otzen, D. E. (2014) The role of stable α-synuclein oligomers in the molecular events underlying amyloid formation. *J. Am. Chem. Soc.* **136,** 3859–3868 CrossRef Medline
61. Abedini, A., and Raleigh, D. P. (2005) Incorporation of pseudoproline derivatives allows the facile synthesis of human IAPP, a highly amyloidogenic and aggregation-prone polypeptide. *Org. Lett.* **7,** 693–696 CrossRef Medline

Downloaded from http://www.jbc.org/ at DUPONT-BALL LIBRARY on May 7, 2020

Identification of a hinge residue controlling islet amyloid polypeptide self-assembly and cytotoxicity

Elizabeth Godin, Phuong Trang Nguyen, Ximena Zottig and Steve Bourgault

J. Biol. Chem. 2019, 294:8452-8463.
doi: 10.1074/jbc.RA118.006454 originally published online April 11, 2019

Access the most updated version of this article at doi: 10.1074/jbc.RA118.006454

Alerts:
- When this article is cited
- When a correction for this article is posted

Click here to choose from all of JBC's e-mail alerts

This article cites 61 references, 12 of which can be accessed free at
http://www.jbc.org/content/294/21/8452.full.html#ref-list-1

Downloaded from http://www.jbc.org/ at DUPONT-BALL LIBRARY on May 7, 2020

Supporting info

Identification of a hinge residue controlling islet amyloid polypeptide self-assembly and cytotoxicity

Elizabeth Godin[a,b,*], Phuong Trang Nguyen[a,b,*], Ximena Zottig[a,b], Steve Bourgault[a,b,#]

[a]Department of Chemistry, Pharmaqam, University of Québec in Montreal, Montreal, QC, Canada, H3C 3P8, [b]Quebec Network for Research on Protein Function, Engineering, and Applications, PROTEO, Canada

Running title: *Self-assembly-toxicity relationships of islet amyloid polypeptide*

[*]These authors contributed equally to this work.

[#]To whom correspondence should be addressed: Prof. Steve Bourgault, Department of Chemistry, Université du Québec à Montréal, C.P. 8888, Succursale Centre-Ville, Montréal (Québec), H3C 3P8, Canada, Telephone: (514) 987-3000 (5161); e-mail: bourgault.steve@uqam.ca

Keywords: Amyloid, Islet amyloid polypeptide, Self-assembly, Cytotoxicity, Aggregation

Table of content

S1. Kinetics of amyloid formation at 25 μM……..……...…...….. 3

S2. Kinetics of amyloid formation of IAPP, N21A, N21G and N21Aib…..……... 4

S3. Time-point ThT fluorescence spectroscopy……...…. 5

S4. AFM images of N21n and IAPP at time 0……..…… 6

S5. Far-UV circular dichroism spectra of rIAPP ……..……...… 7

S6. Surface hydrophobicity of IAPP assemblies as a function of ThT fluorescence …… 8

S7. TEM images of N21L after 24h incubation……...……..… 9

S8. TEM images of N21Dab after 24h incubation……...……..… 10

S9. TEM images of N21Aib after 24h incubation……..…...…… 11

S10. Correlation between cytotoxicity and *in vitro* amyloidogenecity…….. 12

S11. Representative SDS-PAGE of photochemically cross-linked peptides……. 13

S12. AFM images of N21F aggregates…….…..... 14

S13. HPLC traces of N21F before and after incubation……. 15

Table S1. Mass spectrometry analysis of peptides……. 16

S14. Representative ESI-MS-TOF analysis of purified IAPP ……..... 17

S15. RP-HPLC chromatograms of IAPP and N21X mutants …… 18

S16. RP-HPLC chromatograms of N21X mutants …… 19

S17. RP-HPLC chromatograms of rIAPP and N21X mutants …….. 20

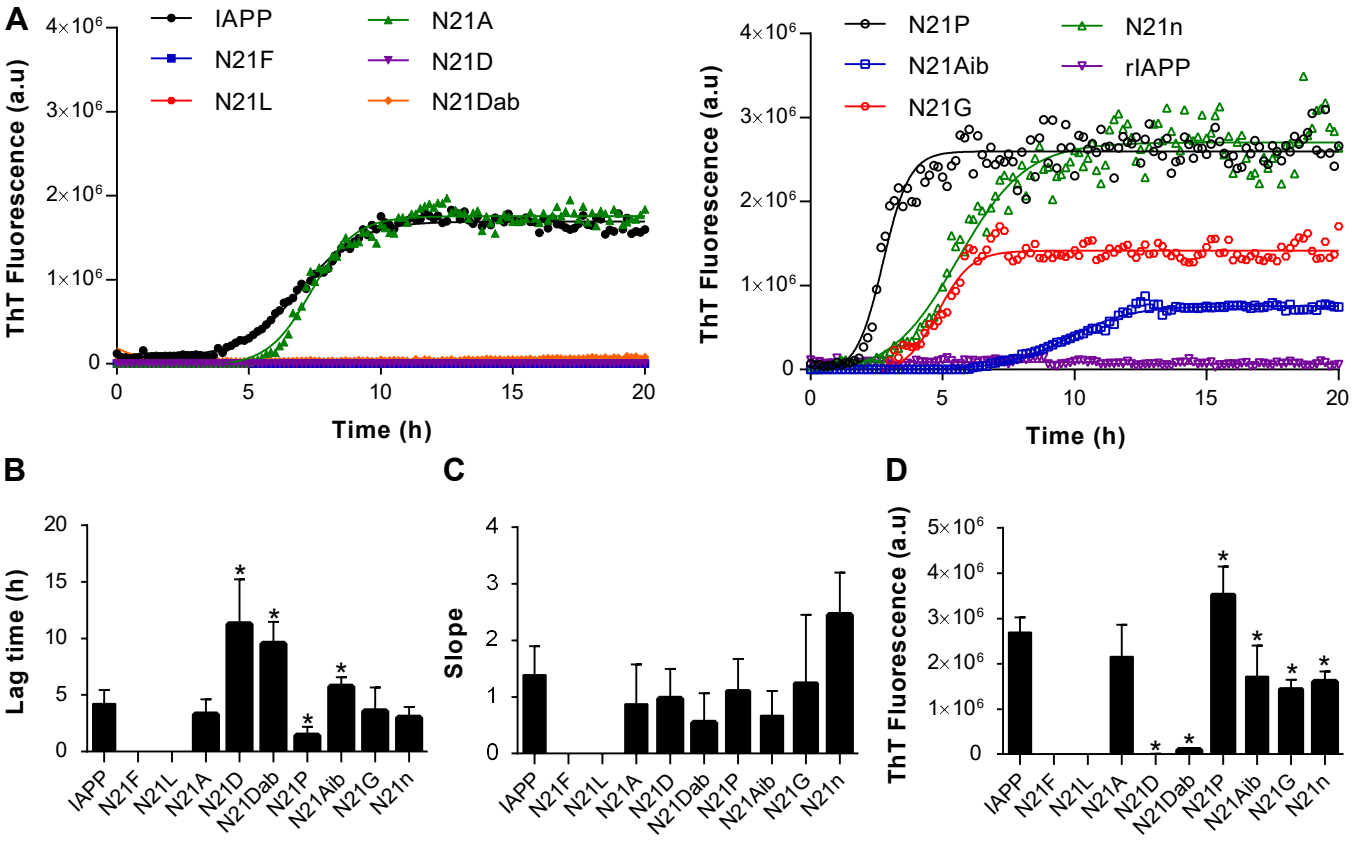


Figure S1. Kinetics of amyloid formation at 25 µM. (A) Representative kinetic traces of amyloid formation monitored by ThT fluorescence. Peptides were incubated at 25 µM under quiescent conditions in 20 mM Tris-HCl buffer, pH 7.4 and the fluorescence of ThT (40 µM) was measured every 10 min with excitation at 440 nm and emission at 485 nm. The curves represent the best from the sigmoidal growth model. (B) Lag time, (C) slope and (D) final ThT fluorescence of the self-assembly kinetics. Data represent mean ± S.D. of at least four experiments performed in triplicate. Results were analyzed using the student's t-test and statistical difference (between IAPP and analogs) was established at * $P < 0.01$. (B, C, D) Data are not shown for N21F and N21L because results could not be fitted to a sigmoidal curve. (A-D) n: D-enantiomer of Asn; Aib: aminoisobutyric acid; Dab: diaminobutyric acid.

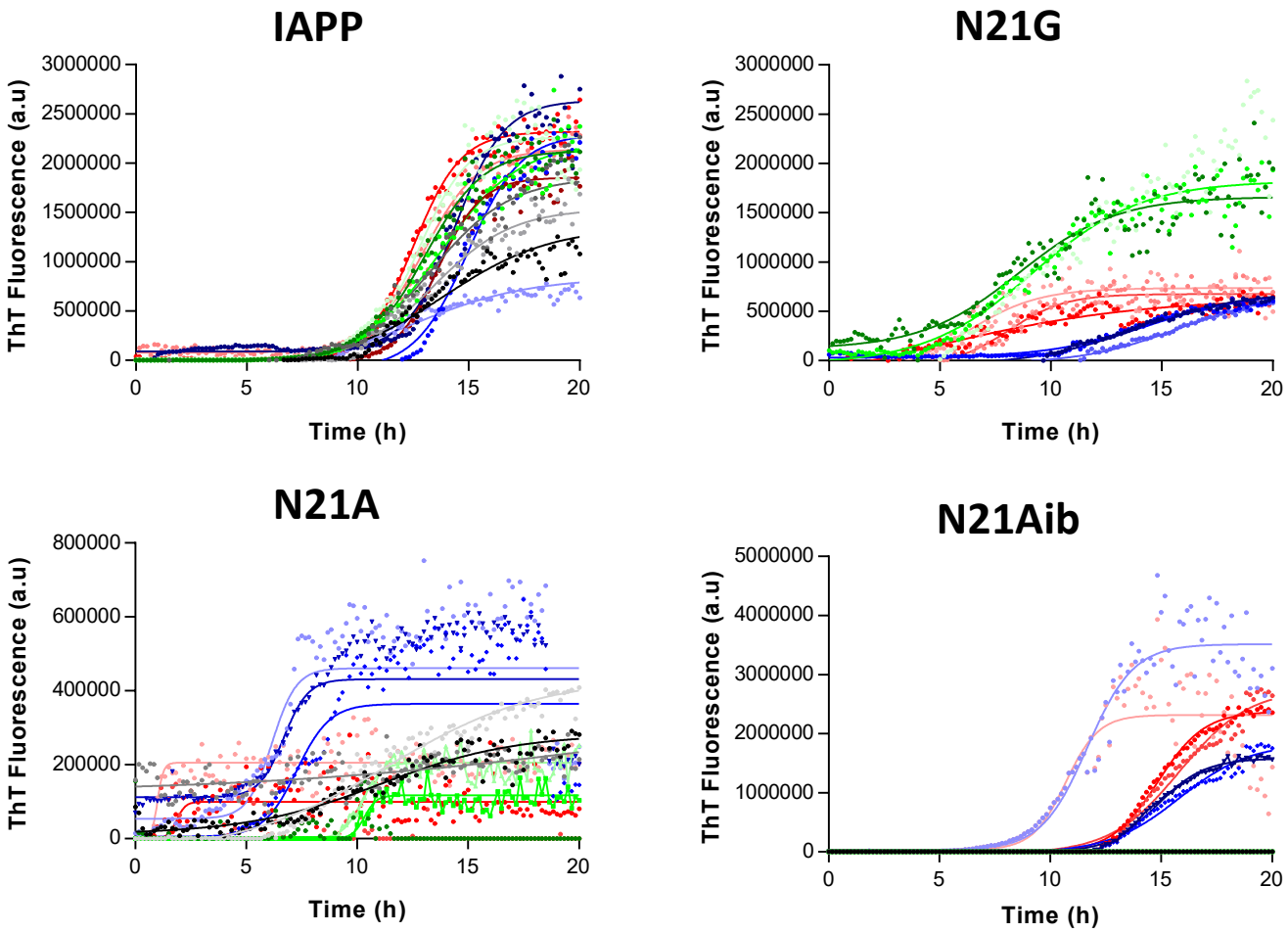


Figure S2. Kinetics of amyloid formation of IAPP, N21A, N21G and N21Aib. Raw kinetic traces (12 runs; 4 assays run in triplicate) of amyloid formation monitored by ThT fluorescence. Peptides were incubated at 12.5 μM under quiescent conditions in 20 mM Tris-HCl buffer, pH 7.4 and the fluorescence of ThT (40 μM) was measured every 10 min with excitation at 440 nm and emission at 485 nm.

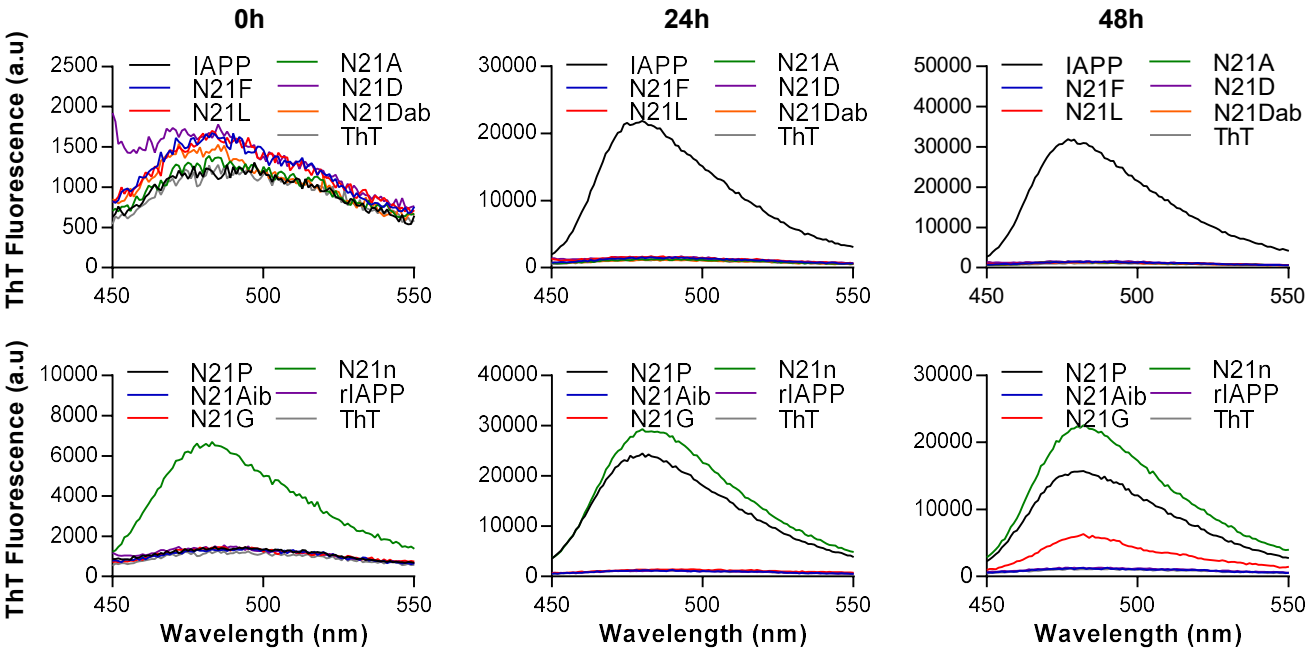


Figure S3. Time-point ThT fluorescence spectroscopy. Peptides were incubated under quiescent conditions in 20 mM Tris-HCl buffer, pH 7.4 at 50 µM. After 0, 24 and 48 h incubation, the emission spectra of ThT (40 µM) was recorded from 450 nm to 550 nm with an excitation set at 440 nm.

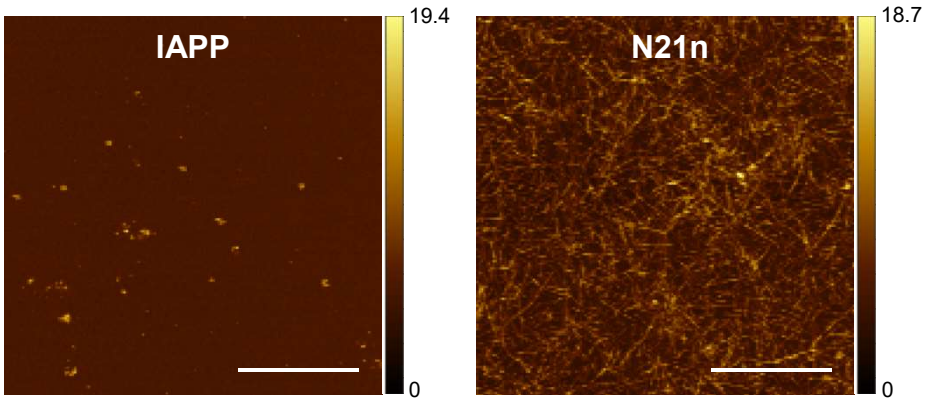


Figure S4. AFM images of N21n and IAPP at time 0. Peptides were solubilised in 20 mM Tris-HCl buffer, pH 7.4 at 50 µM immediately before AFM analysis. Scale bar represents 1 µm.

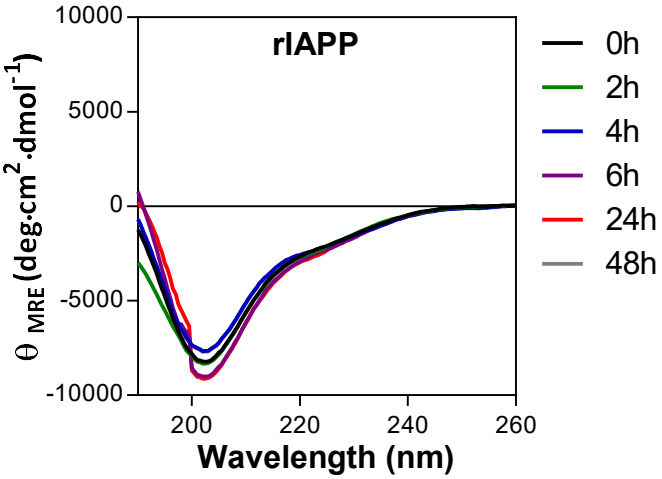


Figure S5. Far-UV circular dichroism spectra of rIAPP. rIAPP was incubated under quiescent conditions in 20 mM Tris-HCl buffer, pH 7.4 at 50 µM. CD analysis was performed after incubation of 0, 2, 4, 6, 24 and 48h. Far-UV CD spectrum was recorded from 190 to 260 nm.

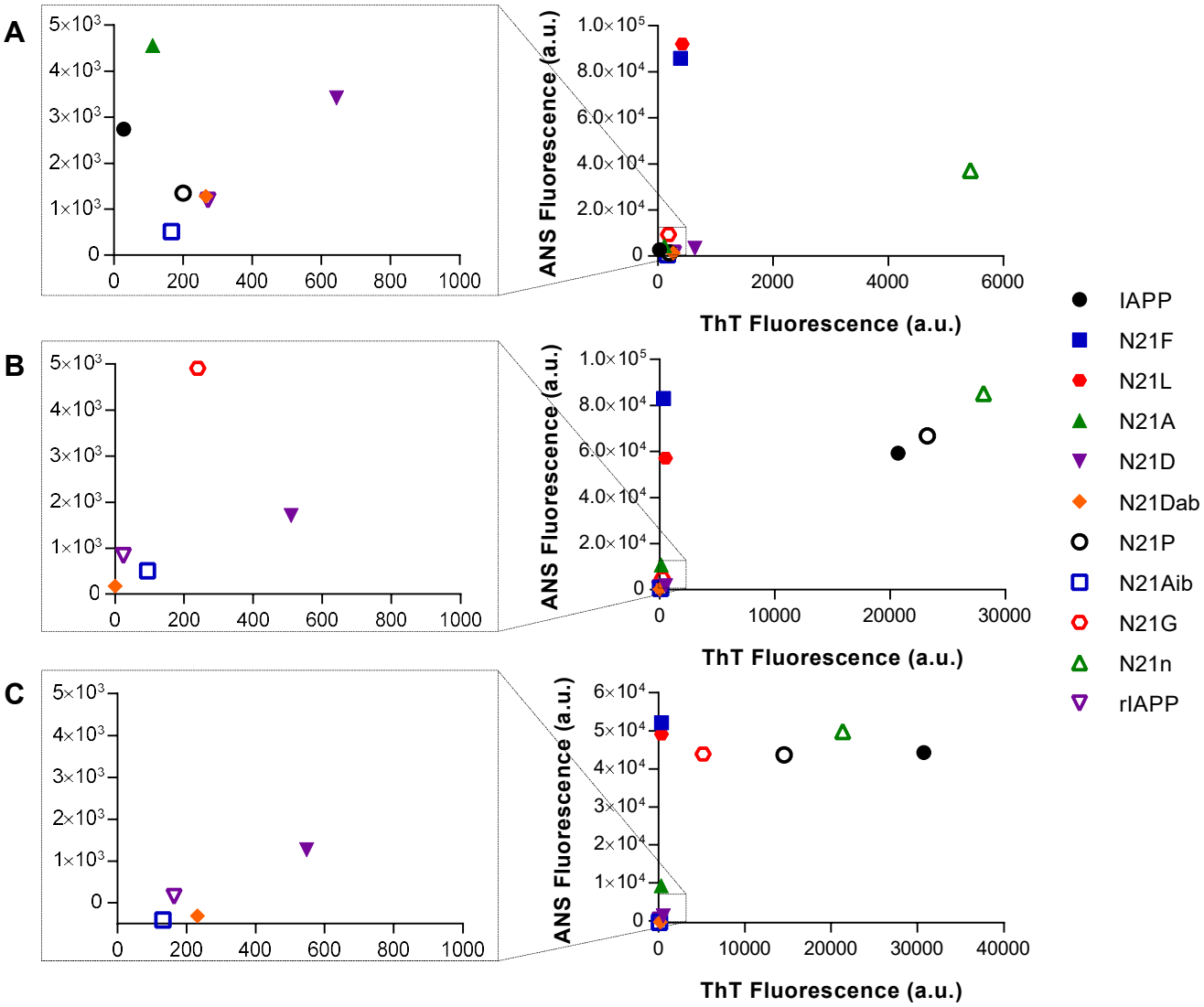


Figure S6. Surface hydrophobicity of IAPP assemblies as a function of ThT fluorescence. Maximal ANS fluorescence from peptide at 50 µM (**Fig. 4**) versus maximal ThT fluorescence from peptide at 50 µM (**Fig. S3**) after (A) 0, (B) 24 or (C) 48h of incubation.

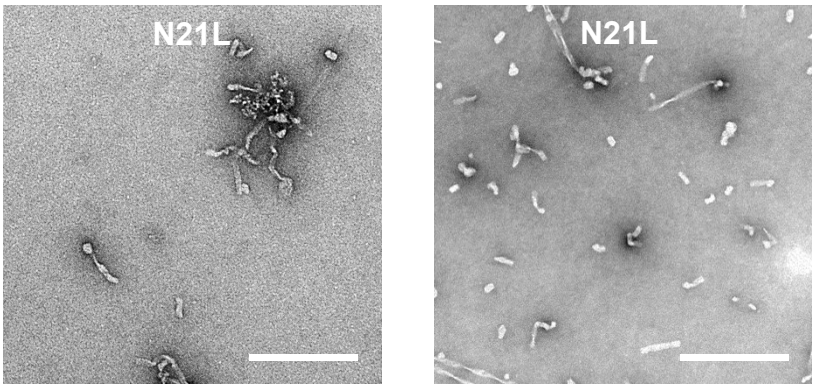


Figure S7. TEM images of N21L after 24h incubation. Peptide was incubated at 50 μM in 20 mM Tris-HCl buffer, pH 7.4 for 24h before TEM analysis. Scale bar represents 200 nm.

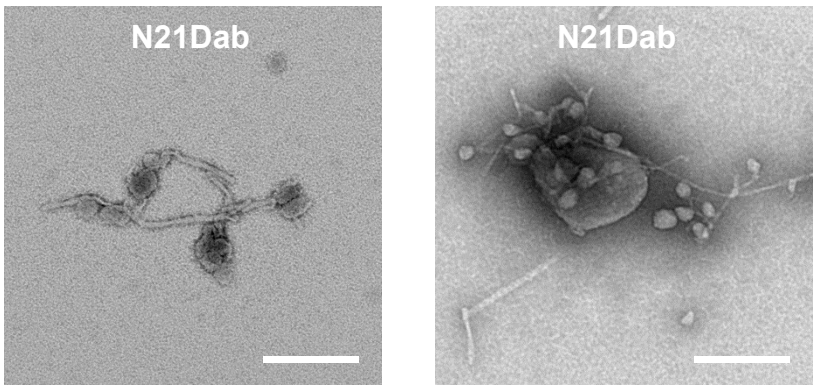


Figure S8. TEM images of N21Dab after 24h incubation. Peptide was incubated at 50 μM in 20 mM Tris-HCl buffer, pH 7.4 for 24h before TEM analysis. Scale bar represents 200 nm.

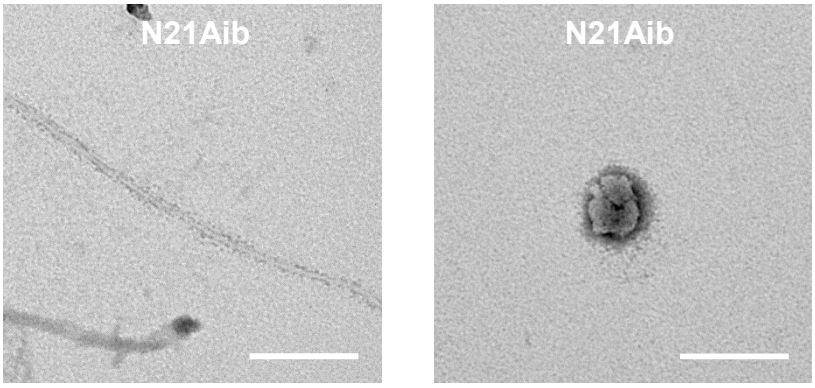


Figure S9. TEM images of N21Aib after 24h incubation. Peptide was incubated at 50 μM in 20 mM Tris-HCl buffer, pH 7.4 for 24h before TEM analysis. Scale bar represents 200 nm.

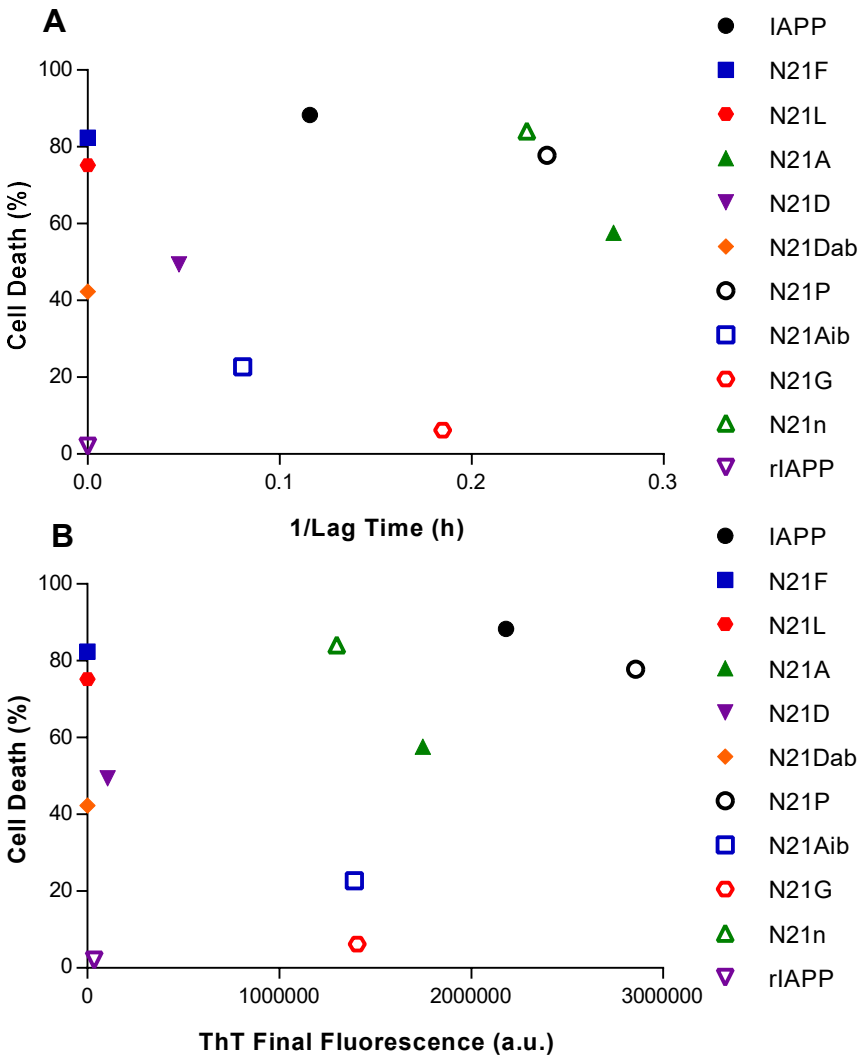


Figure S10. Correlation between cytotoxicity and *in vitro* amyloidogenecity. Percentage of cell death (50 µM) after 24h of incubation with INS-1E cells (**Fig. 6**) *vs* (A) the lag time and (B) the final ThT fluorescence of peptides at from kinetic assays (**Fig. 2**). The 1/lag time value for N21Dab, N21F, N21L and rIAPP was set at zero (no ThT positive signal).

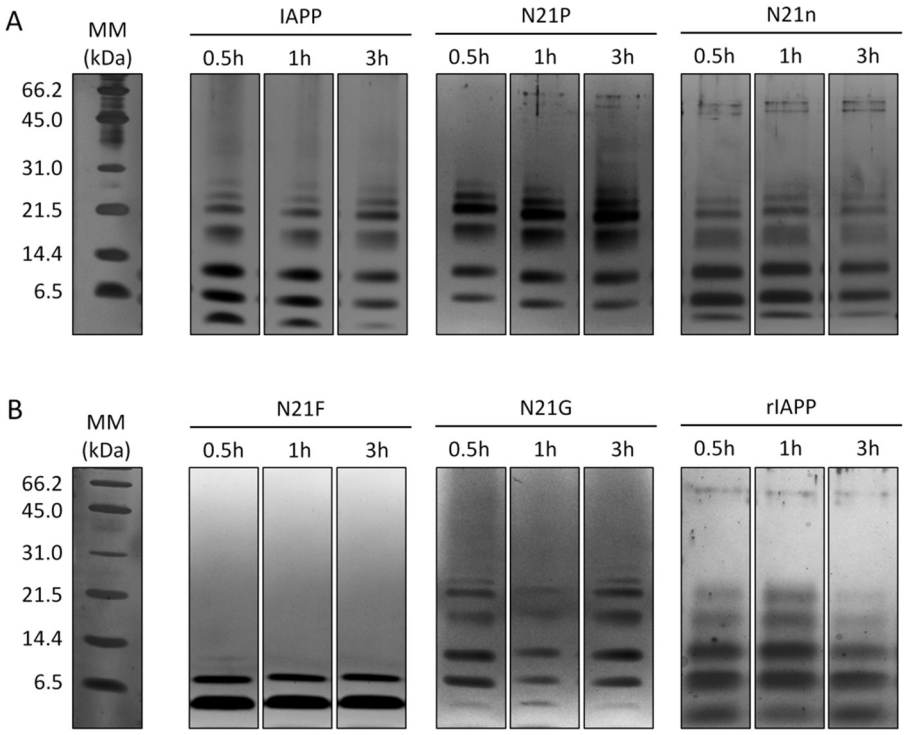


Figure S11. Representative SDS-PAGE of photochemically cross-linked prefibrillar species. Peptides were incubated under quiescent conditions at 25°C in 20 mM Tris-HCl buffer (pH 7.4) at 50 μM for 30 min, 1h and 3h before PICUP treatment. (A,B) MM: molecular weight marker.

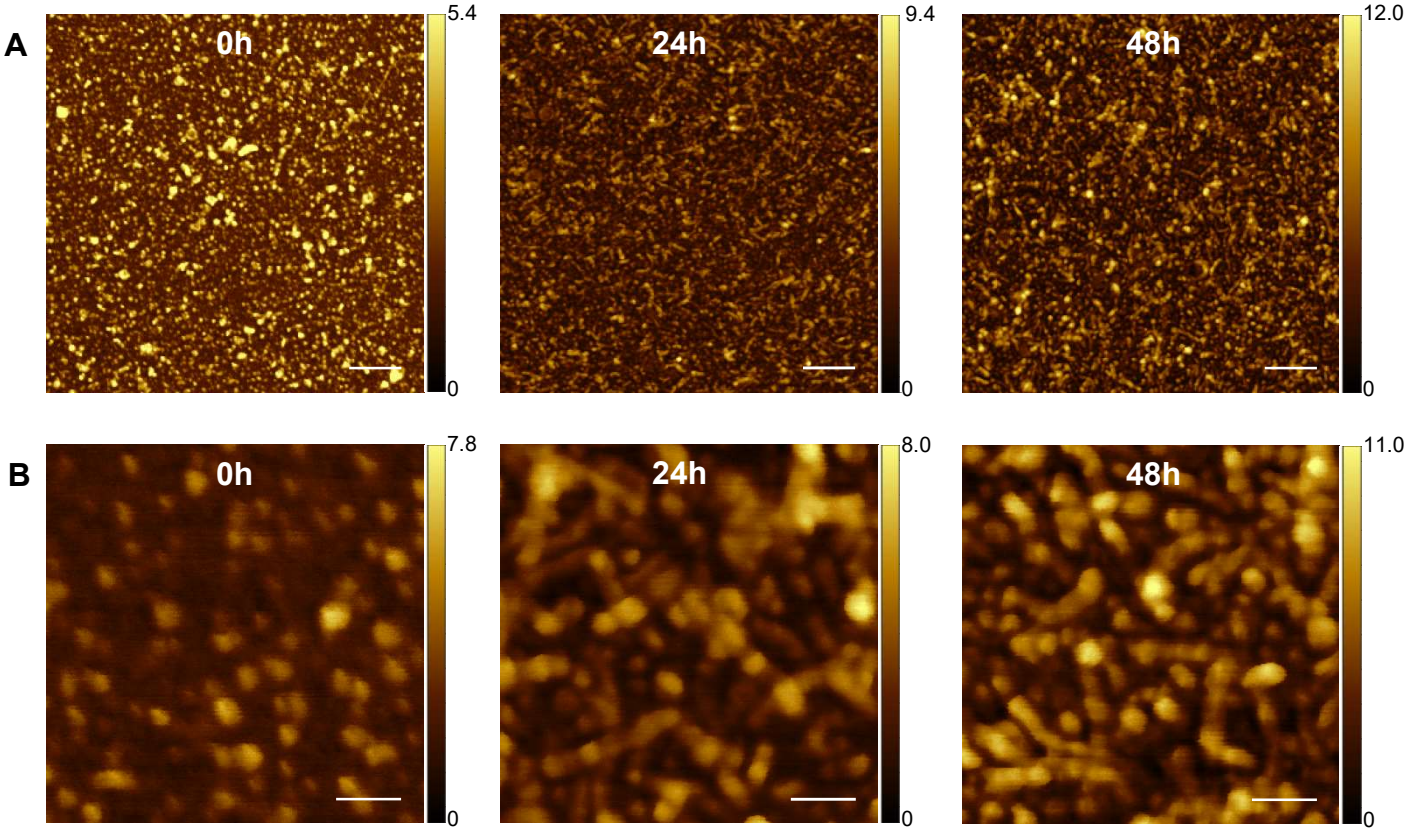


Figure S12. AFM images of N21F aggregates. N21F was incubated at 150 µM under quiescent conditions in 20 mM Tris-HCl buffer, pH 7.4 for 0, 24 and 48h before AFM analysis. Scale bars represent **(A)** 200 nm and **(B)** 50 nm.

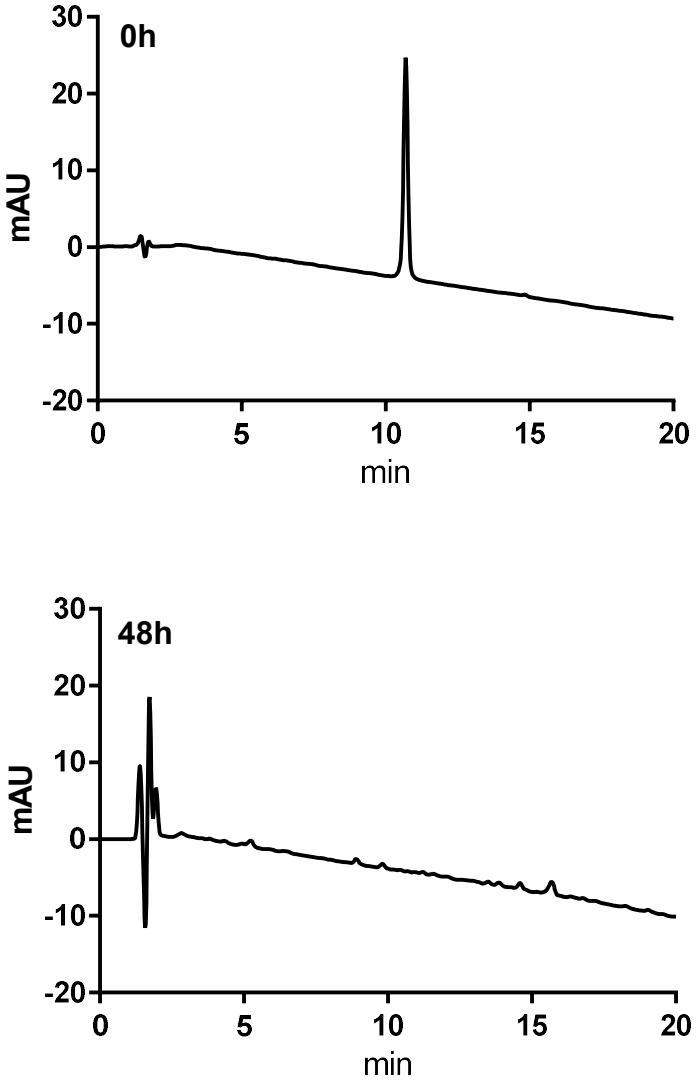


Figure S13. **HPLC traces of N21F.** HPLC chromatograms of freshly dissolved N21F (0h) and of the supernatant after 48h of incubation in 20 mM Tris-HCl buffer, pH 7.4 at a concentration of 150 μM. N21F fibrils (48h) were centrifuged at 35 000 g and 4°C for 45 minutes and the supernatant was analysed.

Table S1. Mass spectrometry analysis of peptides

Peptide	Formula	Exact mass (Da)	Adduct	Extraction mass (Da)	Found at mass (Da)
IAPP	$C_{165}H_{261}N_{51}O_{55}S_2$	3900,86	+3H	1301,29	1301,97
			+4H	976,22	976,69
			+5H	781,17	781,55
N21A	$C_{164}H_{260}N_{50}O_{54}S_2$	3857,86	+3H	1286,95	1287,63
			+4H	965,47	965,97
			+5H	772,57	772,98
N21Aib	$C_{165}H_{262}N_{50}O_{54}S_2$	3873,89	+3H	1292,29	1293,02
			+4H	969,47	970,03
			+5H	775,78	776,23
N21D	$C_{165}H_{260}N_{50}O_{56}S_2$	3901,85	+3H	1301,62	1302,30
			+4H	976,46	976,94
			+5H	781,37	781,75
N21Dab	$C_{165}H_{263}N_{51}O_{54}S_2$	3886,88	+3H	1296,63	1297,30
			+4H	972,72	973,19
			+5H	778,37	778,75
N21F	$C_{170}H_{264}N_{50}O_{54}S_2$	3933,89	+3H	1312,30	1312,91
			+4H	984,47	984,94
			+5H	787,78	788,16
N21G	$C_{163}H_{258}N_{50}O_{54}S_2$	3843,84	+3H	1282,28	1282,92
			+4H	961,96	962,45
			+5H	769,77	770,17
N21L	$C_{167}H_{266}N_{50}O_{54}S_2$	3899,90	+3H	1300,97	1301,61
			+4H	975,98	976,20
			+5H	780,98	781,38
N21n	$C_{165}H_{261}N_{51}O_{55}S_2$	3900,86	+3H	1301,29	1301,92
			+4H	976,22	976,70
			+5H	781,17	781,56
N21P	$C_{166}H_{262}N_{50}O_{54}S_2$	3883,87	+3H	1295,62	1296,30
			+4H	971,97	972,48
			+5H	777,77	778,20
rIAPP	$C_{167}H_{272}N_{52}O_{53}S_2$	3917,96	+3H	1306,99	1307,63
			+4H	980,48	980,98
			+5H	784,59	784,99

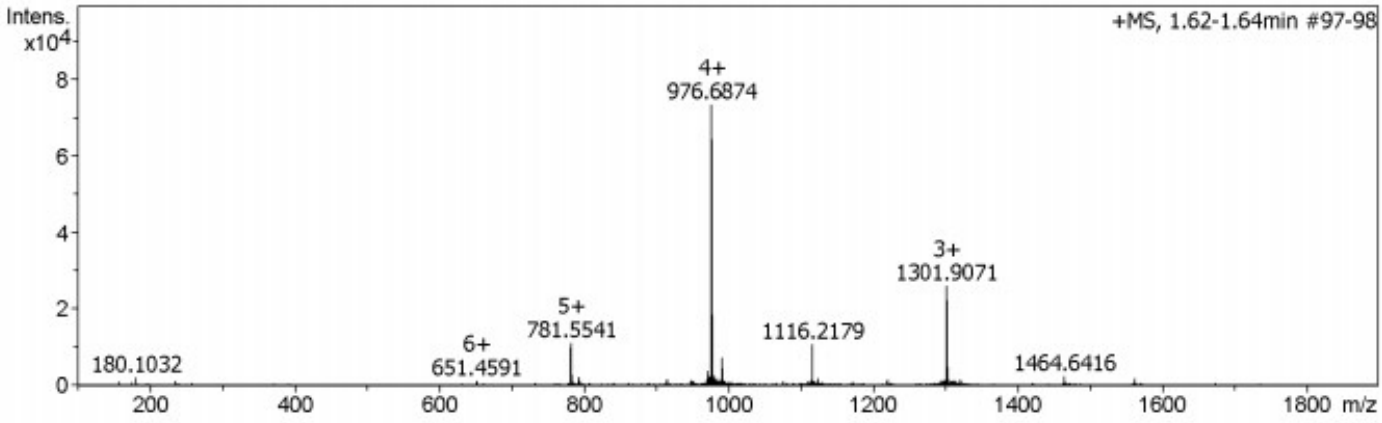


Figure S14. Representative ESI-MS-TOF analysis of purified IAPP. IAPP was analyzed by time-of-flight mass spectroscopy using a LC/ESI-TOF.

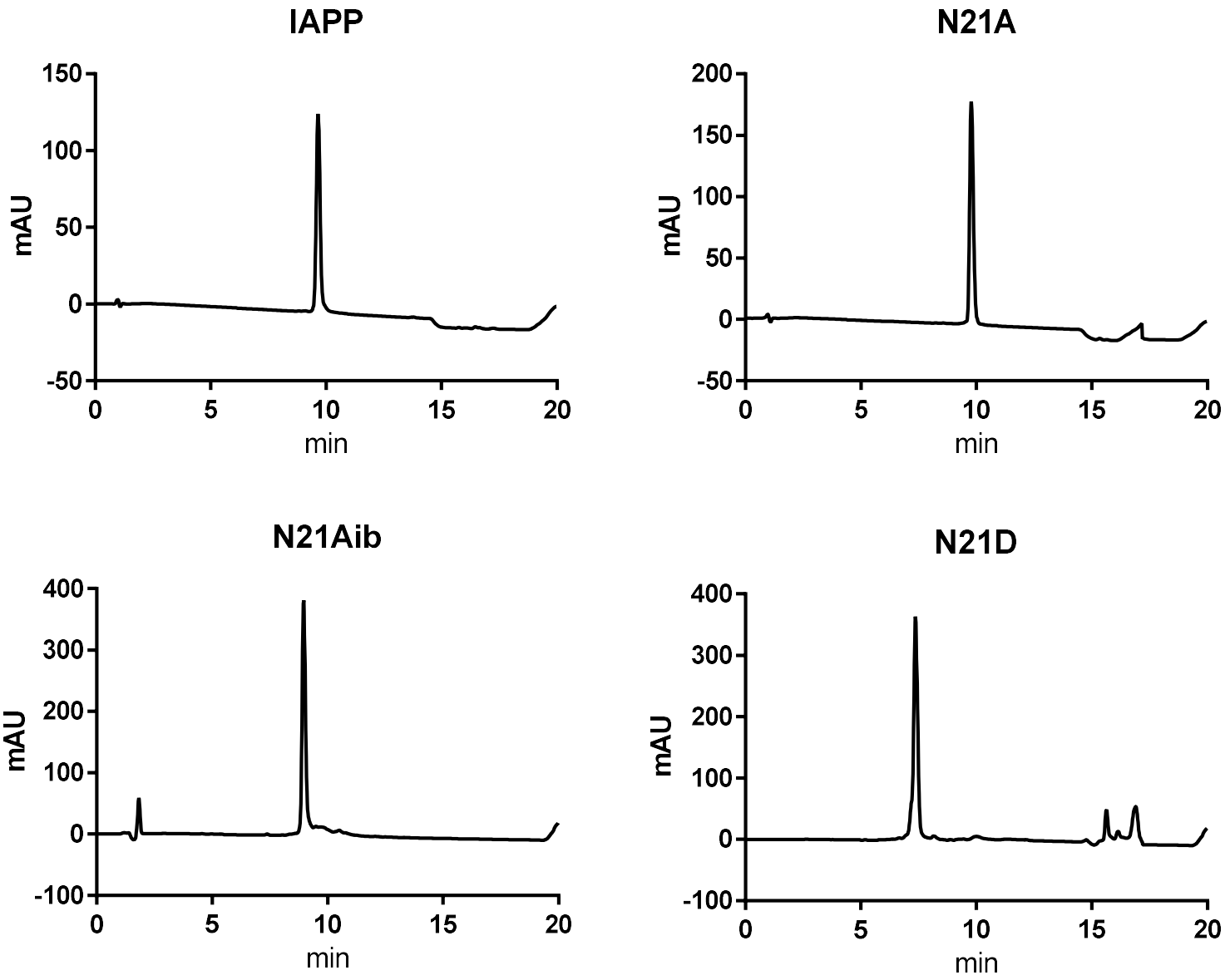


Figure S15. RP-HPLC chromatograms of IAPP and N21X mutants. Gradient of 20 to 60 % of acetonitrile in mixture of H_2O/TFA (0,06%) in 20 or 25 min. C_{18} column (5 µm, 150 x 4.6 mm or 3.5 µm, 100 x 4.6 mm). Absorbance monitored at 229 nm.

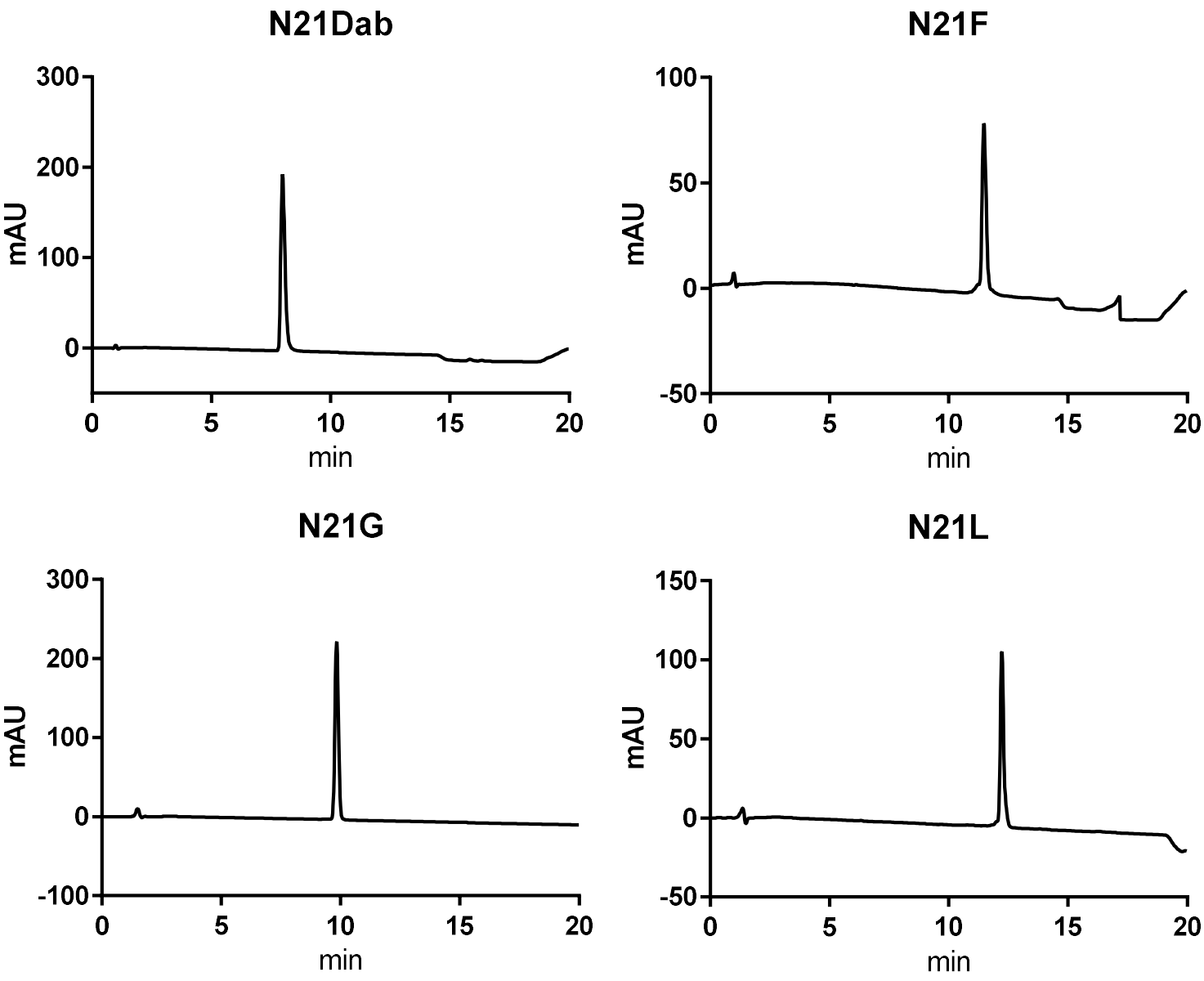


Figure S16. RP-HPLC chromatograms of N21X mutants. Gradient of 20 to 60 % of acetonitrile in mixture of H_2O/TFA (0,06%) in 20 or 25 min. C_{18} column (5 µm, 150 x 4.6 mm or 3.5 µm, 100 x 4.6 mm). Absorbance monitored at 229 nm.

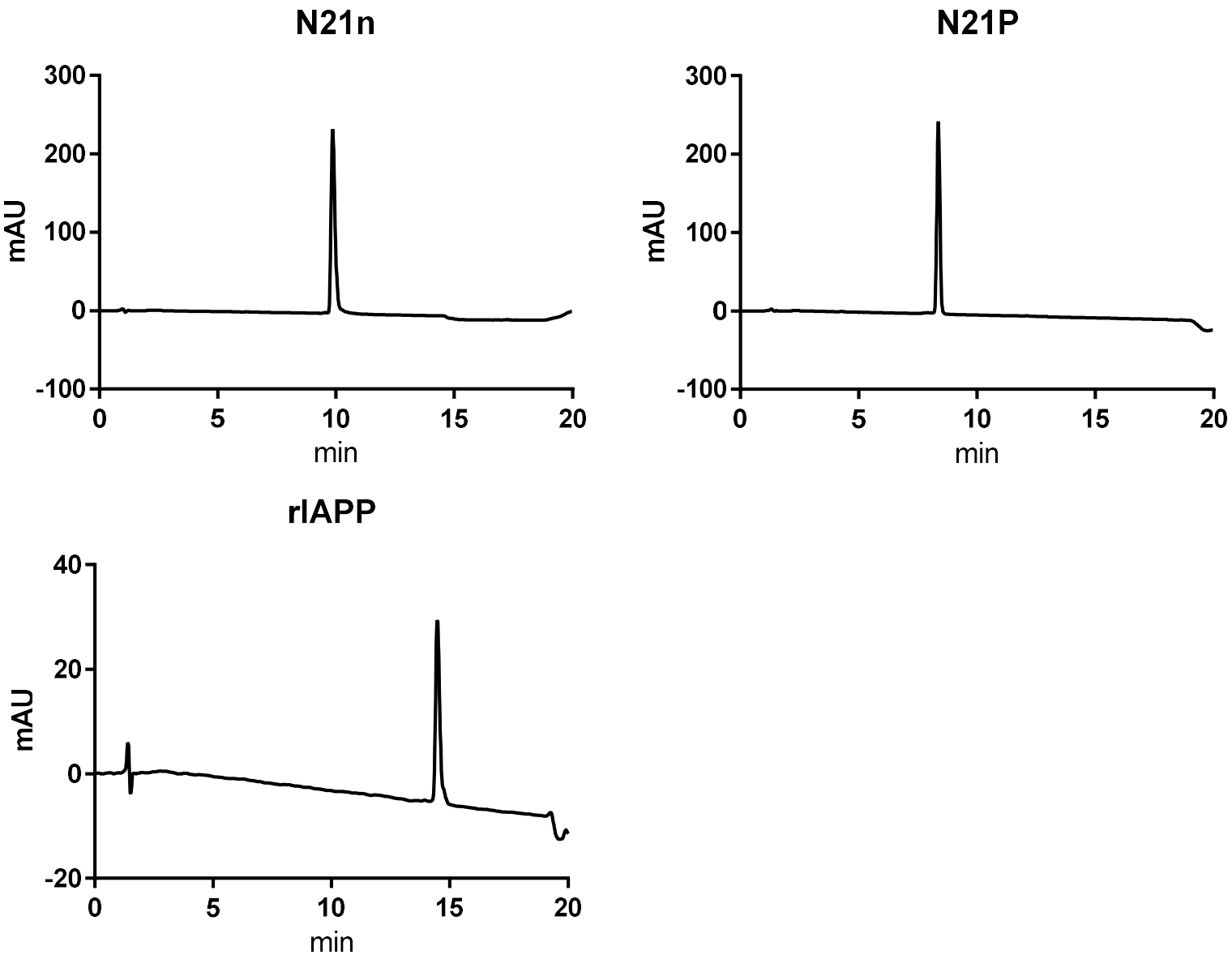


Figure S17. RP-HPLC chromatograms of rIAPP and N21X mutants. Gradient of 20 to 60 % of acetonitrile in mixture of H_2O/TFA (0,06%) in 20 or 25 min. C_{18} column (5 µm, 150 x 4.6 mm or 3.5 µm, 100 x 4.6 mm). Absorbance monitored at 229 nm.